

Dynamic response of an Offshore wind turbine using linear (LIM) and non-linear (NLIM) environmental interaction models

A Parametric study

Nischal Sehrawat
Student id: 4388518

Offshore and Dredging Engineering

Dynamic response of an Offshore wind turbine using linear (LIM) and non-linear (NLIM) environmental interaction models

A Parametric study

Nischal Sehrawat

Student id: 4388518

Date: 19th July, 2016

A thesis presented for the degree of
Master of Science
In
Offshore and Dredging Engineering



Thesis Committee

Prof. Dr. A.V. Metrikine

Dr.ir. K.N. van Dalen

Ir. P. van der Male

Ir. F.W. Renting

Delft University of Technology, The Netherlands

Abstract

The present state-of-the-art modelling tools (such as FAST, BLADED) used for modelling an offshore wind turbine (OWT) are too detailed and computationally expensive. These tools are required only at detailed design stages of a project. For the preliminary phase, however, a much simpler (yet reliable) 3D model can improve and speedup the design process.

Therefore, the aim of this thesis was to develop two different finite element models of an offshore wind turbine and compare their dynamic responses. In order to assess the extent of non-linearities in the environmental interactions arising due to structural motions, one model included the non-linear models of soil, hydrodynamic and aerodynamic loads (called NLIM henceforth) while the other used linearized expressions for modelling them (called LIM henceforth).

The soil was modelled as a series of non-linear (and linear) elastic springs using $p-y$ curves. The conventionally used Morison's equation was compared with MacCamy and Fuchs' equation for modelling the hydrodynamic loads on a large diameter pile. It was found that the MacCamy and Fuchs' equation is a better way of modelling the hydrodynamic loads on submerged cylinders than Morison's equation as it takes the wave diffraction effects into account. Several load cases were defined and the models were subjected to these load cases to check whether they are able to capture the physical behaviour of the OWT. The modal decomposition technique was used for reducing simulation time.

It was found that the model(s) adequately captured the physical behaviour of the OWT till a wind speed of 20 m/s. Its side-side plane physical behaviour needs further investigation for a constant wind speed of 24 m/s. The LIM and the NLIM compared well for most load cases. For the side-side plane responses, however, the LIM developed a phase lag. A strong coupling was found between the motions (rotations) in fore-aft plane and the motions about the yaw axis. The structural velocities were found to be very small to influence hydrodynamic drag terms. Also, the deflections of the pile in the soil were found to be too small suggesting that $p-y$ curves do not capture the non-linear behaviour of soil accurately.

Finally, a damping matrix resulting from the linearised aerodynamic forces was used for calculating the modal damping ratios related to different modes. The results were compared to the literature, with addition of side-side and yaw damping.

Declaration

I declare that this thesis, which I submit to TU Delft for examination in consideration of the award of Master of Science degree in Offshore and Dredging engineering is my own personal effort. Where any of the content presented is the result of input or data from a related source this is duly acknowledged in the text such that it is possible to ascertain how much of the work is my own. I have not already obtained a degree in TU Delft or elsewhere on the basis of this work. Furthermore, I took reasonable care to ensure that the work is original, and, to the best of my knowledge, does not breach copyright law, and has not been taken from other sources except where such work has been cited and acknowledged within the text.

Name: Nischal Sehrawat

Student Number: 4388518

Signed:

Date: 19th July, 2016

Acknowledgements

Firstly, I would like to express my sincere gratitude to Prof. Dr. A.V. Metrikine for giving the course on structural dynamics. The way he taught the course inclined me towards structural dynamics. The course Computational Dynamics started by him proved to be one of the best and the most helpful courses for completing my thesis well within the stipulated time.

Secondly, I would like to thank Dr.ir. K.N. (Karel) van Dalen who was always there to help me with my conceptual doubts. His ability to associate physical reality with mathematics is simply amazing.

Thirdly, I would like to thank my daily supervisor I.r. P. van der Male (Pim) for his invaluable guidance all throughout my thesis period. He was very patient with me, provided detailed feedbacks on my reports, helped me push my limits and strengthen my concepts.

I would like to thank all the friends at room 2.83 who lit up the atmosphere with all the wonderful conversations. Finally, I would thank my parents for respecting my decision to return back to the academia after a gap of 5 years of working at sea.

Thank you all.

Contents

List of symbols	ii
Greek symbols	v
List of Acronyms	vii
List of Figures	ix
List of Tables	xii
1 Introduction	1
1.1 Background	1
1.2 Problem Statement	2
1.3 Literature review	2
1.4 Research Questions	3
1.5 Approach	3
1.6 Report structure	4
2 Terminology	5
2.1 Introduction	5
2.2 Support structure terminology	5
2.2.1 Rotor and nacelle assembly	5
2.2.2 Tower	5
2.2.3 Transition Piece	5
2.2.4 Pile	6
2.3 Blade terminology	6
2.3.1 Aero-foil	6
2.3.2 Pitch angle (β_{pitch})	6
2.3.3 Angle of attack (α_{wind})	7
2.3.4 Angle of inflow (α_{in})	7
2.3.5 Twist angle (β_{twist})	7
2.3.6 Induction factor a_{in}	8
2.4 Blade discretization	9
3 Soil Modelling	11
3.1 Introduction	11
3.2 $p - y$ curves and reaction modulus E_{py}	11
3.2.1 Modification for cyclic loading	13
3.3 Deriving the $p-y$ curves	15
3.3.1 Experimentally	15
3.3.2 Empirically	15

3.4	Limitations of $p-y$ curves	15
3.5	Beam on a Winkler foundation	16
3.5.1	Advantages of the Winkler foundation approach	17
3.5.2	Dis-advantages of the Winkler foundation approach	17
3.6	Modelling soil springs	17
3.6.1	Non-linear springs	17
3.6.2	Linear springs	18
4	Hydrodynamic Loading	19
4.1	Introduction	19
4.2	Simulation - Wave time series	19
4.3	Morison's Equation (ME)	22
4.3.1	1-plane structural motions	22
4.3.2	Value of C_a and C_D	23
4.4	MacCamy and Fuchs' (MFE) linear diffraction theory	23
4.4.1	Corrected C_M	25
4.5	ME vs MFE	26
4.6	Two-plane structural motions	28
5	Aerodynamic Loading	29
5.1	Introduction	29
5.2	Wind profile	29
5.3	Turbulence spectra	29
5.4	Simulation - Wind time series	30
5.5	Aerodynamic forces	31
5.5.1	Aerodynamic loads Tower and Transition piece	31
5.5.2	Aerodynamic loads on rotor blades	32
6	Model Description	35
6.1	Introduction	35
6.2	Discretization	35
6.2.1	Support structure	35
6.3	Solution in time domain	38
6.4	An example	38
6.5	Mode displacement method (Modal Reduction)	40
6.5.1	Initial conditions	42
6.6	Selecting the number of modes	42
7	Results and Discussions	46
7.1	Introduction	46
7.2	Simple load case - Regular wave and constant wind	46
7.2.1	Discussions - Side-side (X-Z) plane motions and rotation about Y axis .	49
7.2.2	Discussions - Fore-aft (Y-Z) plane motions and rotation about X axis .	52
7.2.3	Discussions - Yaw motions	53
7.3	Advanced load cases	54
7.3.1	Integrated load case	54
7.3.2	Load case - Wind	60
7.3.3	Load case - Waves	63
7.3.4	Load case - Soil	65
7.4	Modal damping	67

8 Conclusions and Recommendations	69
8.1 Conclusions	69
8.2 Recommendations for further work	70
A Finite Element Formulation	71
A.1 Introduction	71
A.2 Timoshenko Beam Elements (single plane)	71
A.3 2-Plane bending with torsional capability	72
B Results-Regular wave-Constant wind	75
C Results-Integrated	79
D Results-Wind	83
E Results-Waves	87
F Results-Soil	90
G Aerodynamic model for blade loading	93
Bibliography	121

List of symbols

A_1 Amplitude of the wave [m]

$$a_1 \exp\left(-\frac{(\omega-\omega_0)^2}{2\sigma^2\omega_0^2}\right)$$

A_b Cross sectional area of the beam in [m^2]

L Length of the beam element in [m]

$E_p I_p$ Bending stiffness of the pile [Nm^2]

C_a Added mass coefficient

C_d Drag coefficient for wind

$C_{d,b}$ Drag coefficient for blade elements

C_D Drag coefficient for wave loading coefficient

C_M Inertia coefficient $1 + C_a$

D_{pile} Pile diameter [m]

$D_{t,tp}$ Diameter of Tower, Transition piece [m]

d_w Water depth [m]

E_{py} Soil reaction modulus [N/m^2]

$F_{d,b}$ Drag forces on blade element [N]

dF_{diff} Diffraction force per unit length acting on the pile element [N/m]

$dF_{drag,waves}$ Drag force per unit length due to waves acting on the pile element [N/m]

dF_{hydro} Total hydrodynamic force per unit length acting on the pile element [N/m]

$F_{i,b}$ Inertia forces on blade element

dF_{in} Inertia force per unit length acting on the pile element [N/m]

$f_{j,w}$ j^{th} wind frequency component [Hz]

dF_{fk} Froude Krylov force per unit length acting on the pile element [N/m]

$F_{l,b}$ Lift forces on blade element [N]

f_w Frequency of wind component [Hz]

g Acceleration due to gravity [m/s²]

G_s Shear modulus of steel [N/m²]

I_b Area moment of inertia of the cross section of beam [m⁴]

I_{ref} Expected value of the turbulence intensity at 15 m/s

J_b Polar mass moment of inertia of the beam [Kgm²]

k_1 Wave number of the wave [1/m]

K_l Linear soil spring stiffness [N/m²]

K_{nl} Non-linear soil spring stiffness [N/m²]

K_s Initial modulus of subgrade reaction [MPa/m]

L_p Natural deflection wavelength of the pile [m]

M_p Bending moment of the pile [Nm]

N_{f1} Number of frequencies in the wave spectrum

N_{f2} Number of frequencies in the wind spectrum

p Soil reaction per unit length [N/m]

P_{ax} Axial force acting on top of the beam element [N]

p_u Ultimate bearing capacity of sand at depth z_p [kN/m]

P_z Axial load on the pile [N]

r_g Radius of gyration of the beam [m]

r_{in} Internal radius of the circular beam cross section [m]

r_j Radius of the j^{th} blade segment measured from the hub center to its COG [m]

r_{ext} External radius of the circular beam cross section [m]

r_{pile} Radius of the pile [m]

$$L_{1,2v} \text{ Integral scale parameter [m]} = \begin{cases} 5.67z_a & \text{if } z_a < 60m; \\ 340.2 & \text{if } z_a > 60m; \end{cases}$$

$S_j(f_w)$ Spectral value of the j^{th} wind frequency component [(m/s)²/Hz]

S_i Spectral value of the i^{th} wave frequency component [m²s/rad]

$S(\omega)$ Spectral density [m²s/rad]

T_2 Simulation time for wind time series [s]

T_w Time period of a single wave component [s]

T_s Simulation time for wave spectra [s]

u Water particle velocity [m/s]

\dot{u} Water particle acceleration [m/s²]

\bar{V} Mean velocity of the time signal averaged over 10 minutes [m/s]

V_{hub} Wind velocity profile at the hub [m/s]

V_p Pile shear force [N]

k_i Wave number associated with the i^{th} frequency wave component [1/m]

y Lateral deflection of the pile at a point z_p along the length of the pile in soil [m]

\ddot{y}_2 Transverse acceleration of the pile element dZ_2 [m/s²]

\dot{y}_2 Transverse velocity of the pile element dZ_2 [m/s]

E Youngs modulus for steel in [N/m²]

z_a Height above the sea level [m]

z_w Distance along the pile below mean sea level upto sea-bed [m]

z_{hub} Hub height measured from sea level [m]

z_p Distance along the pile below sea-bed [m]

Greek symbols

α_1 Shape factor = 0.0081 for North Sea

α_2 0.14 for offshore locations

α_{wind} Wind angle of attack [Degree]

ϕ_{sand} Angle of friction for sand [Degree]

$$\Psi_j \text{ Azimuth for the } j^{th} \text{ blade segment [radians]} = \begin{cases} -\Omega t & \text{for } 1^{st} \text{ blade;} \\ -\Omega t - \frac{2\pi}{3} & \text{for } 2^{nd} \text{ blade;} \\ -\Omega t - \frac{4\pi}{3} & \text{for } 3^{rd} \text{ blade;} \end{cases}$$

ρ_a Density of air 1.225 [Kg/m³]

ρ_s Density of steel 7850 [kg/m³]

ρ_w Density of sea water 1025 [kg/m³]

Δf_w $2\pi/T_2$ Difference between successive harmonic frequencies [Hz]

$\Delta\omega$ Difference between successive harmonic wave frequency components = $2\pi/T_s$

$\eta(t)$ Time series of sea surface elevation [m]

γ_w Peak enhancement factor = 3.3

ω_i i^{th} frequency component [rad/s]

ω Wave circular frequency [rad/s]

ω_0 Dominant or peak wave circular frequency $\left(\frac{4g/\alpha_1}{\sqrt{5}H_s}\right)$ [rad/s]

ω_1 Circular frequency of the wave [rad/s]

ν Poisson's ratio

$\Phi_{wind(j)}$ Randomly generated phase angles between 0 and 2π [radians]

$\Phi_{waves(i)}$ Randomly generated phase angles between 0 and 2π [radians]

Ω Rotation speed of the rotor blades [rad/s]

γ_{sand} Effective weight of submerged sand [KN/m³]

σ_v Variance of the wind time signal with respect to its mean [m/s]

$$\sigma \text{ Peak width parameter} = \begin{cases} 0.07 & \text{if } \omega < \omega_0; \\ 0.09 & \text{if } \omega > \omega_0; \end{cases}$$

θ_{wave} Angle of approach of waves w.r.t the XZ plane [Degree]

θ_{wind} Angle of approach of the wind with respect to the XZ plane [Degrees]

ω_n Natural Frequency vector of the system

λ_w Wave length of the wave component [m]

List of Acronyms

API American Petroleum Institute

BEM Blade Element Momentum

CAE Computer Aided Engineering

COG Center of gravity

DNV Det Norske Veritas

DOF Degrees of freedom

ECS Element Coordinate System

FAST Fatigue, Aerodynamics, Structures, and Turbulence

FEM Finite Element Method

FFT Fast Fourier Transform

GCS Global Coordinate System

H_s Significant wave height

ITTC International Towing Tank Conference

JS Joint North Sea Wave Project

KC Keulegan-Carpenter number

KS Kaimal Spectrum

LCS Local Coordinate System

LIM Linear Interaction Model

MATLAB Matrix Laboratory

ME Morison's Equation

MFE MacCamy and Fuchs' Equation

MSL Mean Sea Level

NLIM Non-Linear Interaction Model

NREL National Renewable Energy Laboratory

ODE Ordinary Differential Equation

OWT Offshore Wind Turbine

PM Pierson Moskowitz

PSD Power Spectrum Density

Re Reynold's Number

T_p Spectral peak period

VKS Von Karman Spectra

w.r.t With Respect To

List of Figures

1.1	Simplified depiction of environmental interactions of an OWT [22]	2
2.1	OWT terminology [26]	6
2.2	Dimensions (in mm) and Global coordinate system	7
2.3	Aerofoil and chord length [29]	8
2.4	Blade angles defined [29]	9
2.5	Induction factor [29]	9
3.1	Pile equilibrium [24]	12
3.2	Stress distribution on a laterally loaded pile [24]	12
3.3	Typical $p - y$ curve & resulting soil modulus E_{py} (static loading) (re-created from [24])	13
3.4	Variation of soil lateral resistance p with depth z_p	13
3.5	Modified $p-y$ curve for cyclic loading	14
3.6	Mechanism of soil stiffness reduction [24]	14
3.7	Loading history considerations [3]	15
3.8	Beam on a Winkler foundation	16
3.9	Shallow & deep failure soil mechanisms [13]	17
4.1	Wave Spectrum	20
4.2	Wave time series for $H_s = 1.5m$	20
4.3	Velocity (a) and acceleration (b) time series	21
4.4	Example of Wheeler's stretching	22
4.5	Partially submerged pile	22
4.6	Different flow regimes [25]	24
4.7	Wave diffraction [25]	24
4.8	Variation of δ with $(k_1 r_{pile})$ [25]	25
4.9	Variation of C_M with (D_{pile/λ_w}) [25]	26
4.10	ME vs MFE vs ANSYS-AQWA	27
4.11	Top view of waves approaching a pile	28
5.1	The 3 turbulence components [28]	30
5.2	Wind Spectrum	31
5.3	Top view of wind approaching the tower	32
5.4	Drag coefficient vs Reynold's number	32
5.5	Corrected coefficients of the DU40 airfoil [17]	33
5.6	Coordinate systems for rotor blades	34
6.1	Discretization scheme (support structure)	36
6.2	Forces and nodes	37
6.3	Simplified model of an OWT	39

6.4	Frequency distribution	43
6.5	Mode shapes 1-6 (Horizontal axis-Modal displacement, Vertical axis-Height of the OWT [m])	44
6.6	Mode shapes 7-10 (Horizontal axis-Modal displacement, Vertical axis-Height of the OWT [m])	45
7.1	Top view-Regular wave, constant wind	46
7.2	Response of the OWT in side-side (X-Z) plane	48
7.3	Fixed rotor subjected to constant wind	49
7.4	Tower top deflection due to constant wind in side-side (X-Z) plane	50
7.5	Response of the OWT in fore-aft (Y-Z) plane	51
7.6	Tower top deflection due to constant wind in fore-aft (Y-Z) plane	52
7.7	Rotations about the yaw (θ_z) axis	53
7.8	Steady yaw moment resulting from a steady rotation about the X axis	54
7.9	Top view-Integrated model	55
7.10	Response of the OWT subjected to Load case-2 (Integrated model)	56
7.11	Frequency contents of load and responses (Load case-2, Integrated model)	57
7.12	PSD plots drawn to semi-log normal scale	58
7.13	Top view-(Wind model)	60
7.14	Response of the OWT subjected to Load case-1 (Wind Model)	61
7.15	Frequency contents of load and responses (Load case-1, Wind model)	62
7.16	Top view-(Waves-model)	63
7.17	Response of the OWT subjected Load case-1 (Waves model)	64
7.18	Response of the OWT subjected to Load case-1 (Soil Model)	66
7.19	E_{py} vs Deflection and maximum displacement of the 2 nd node (from sea bed in soil)	67
7.20	Modal damping ratios for different wind speeds	68
A.1	DOF of a beam element [15]	71
A.2	Beam element in 3D ECS [15]	73
A.3	Beam element with two plane motion and torsion capability	74
B.1	Response of the OWT subjected in X-Z (side-side) plane for different load cases (Regular wave-constant wind)	76
B.2	Response of the OWT subjected in Y-Z (fore-aft) plane for different load cases (Regular wave-constant wind)	77
B.3	Response of the OWT about the Yaw axis for different load cases (Regular wave-constant wind)	78
C.1	Response of the OWT subjected in X-Z plane for different load cases (Integrated model)	80
C.2	Response of the OWT subjected in Y-Z plane for different load cases (Integrated model)	81
C.3	Response of the OWT about the Yaw axis for different load cases (Integrated model)	82
D.1	Response of the OWT subjected in side-side (X-Z) plane for different load cases (Wind)	84
D.2	Response of the OWT subjected in fore-aft (Y-Z) plane for different load cases (Wind)	85
D.3	Response of the OWT about the Yaw axis for different load cases (Wind)	86

E.1	Response of the OWT subjected in side-side (X-Z) plane for different load cases (Waves)	88
E.2	Response of the OWT subjected in fore-aft (Y-Z) plane for different load cases (Waves)	89
F.1	Response of the OWT in side-side (X-Z) plane for different load cases (Soil) . .	91
F.2	Response of the OWT in fore-aft (Y-Z) plane for different load cases (Soil) . .	92

List of Tables

2.1	Properties of wind turbine and support structure	8
2.2	Properties of blade segments	10
3.1	Parameters for $p-y$ curve formulation	18
6.1	Number of elements in each section	36
6.2	Forces and node numbers	37
6.3	Position of forces and moments in the force vector	37
6.4	First 10 natural frequencies of the OWT [Hz]	43
7.1	Parameters - (Regular wave-constant wind)	47
7.2	Physical conditions (Regular wave, constant wind)	47
7.3	Parameters (Integrated model)	55
7.4	Physical conditions (Integrated model)	55
7.5	Parameters (Wind)	60
7.6	Physical Conditions (Wind)	60
7.7	Parameters (Waves)	63
7.8	Physical Conditions (Waves)	63
7.9	Parameters (Soil)	65
7.10	Physical Conditions (Soil)	65
7.11	Modal damping ratios for different planes for wind speed of 15 m/s	68

Chapter 1

Introduction

”But the real glory of science is that we can find a way of thinking such that the law is evident.”

— Richard Feynman, Physicist

1.1 Background

Harnessing the offshore wind economically presents greater challenges. Unlike its land based counterpart, a bottom-founded mono-pile based **OWT** operates under much arduous conditions. Apart from aerodynamic forces from wind, it is also subjected to hydrodynamic forces from waves while it operates in a highly corrosive environment. To add, wind-wave misalignments make the situation even worse. Because of the misalignment, aerodynamic damping is less effective at mitigating wave-induced loads. Consequently, fatigue becomes a major concern. To predict fatigue, accurate mathematical modelling of the environmental loads and physical behaviour of the wind turbine structure becomes vital.

Both wind and waves are stochastic in nature and in-fact highly correlated. Waves are generated by air-pressure fluctuations above the sea surface. These pressure fluctuations are in-turn caused by the wave-induced variations in the air flow just above the waves [12]. The interaction between the OWT and environmental conditions i.e. wind, waves and soil is very complicated and highly non-linear. A simplified depiction of these environmental interactions is shown in [Figure 1.1](#). Precise mathematical modelling of such an intricate system is a challenging task and various models exist that take these interactions into account. Existing 3D **CAE** modelling tools like **FAST**, **BLADED** are highly complicated and computationally expensive with very detailed aerodynamics which comes into picture only at advanced stages of a project.

At preliminary stages, however, such an exhaustive model is preferably not required. Hence a need for a simpler integrated model arises that can predict the response of the OWT without losing the precious details and can still be reliable.

A simpler 3D model that assumes linear interactions between the OWT structure and the environment is faster to solve. This swiftness in calculations, of course, comes at the cost of accuracy. On the other hand, a model that accounts for these non-linear interactions (arising due to structural motions) increases the accuracy¹, but becomes computationally

¹It is to be noted that if not modelled properly, even non-linear models can be physically incorrect.

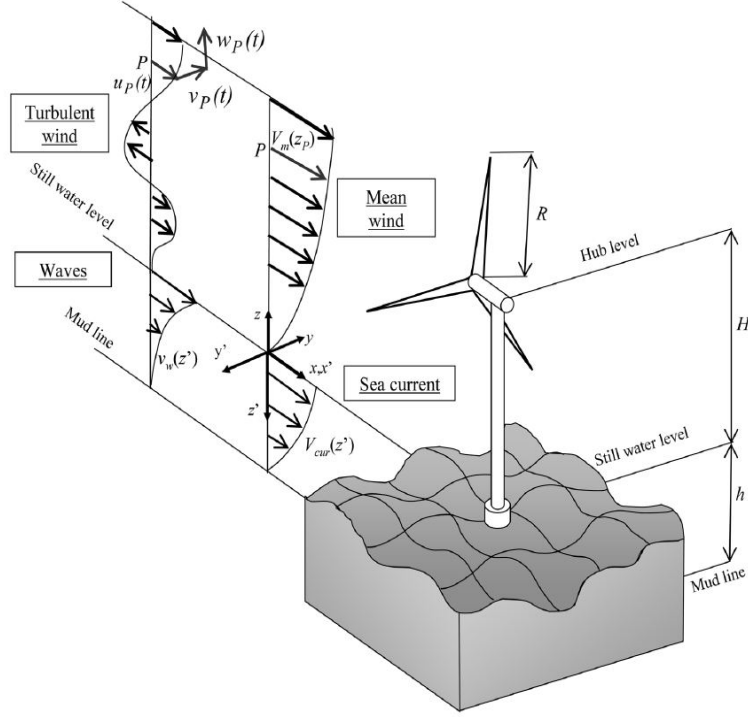


Figure 1.1: Simplified depiction of environmental interactions of an OWT [22]

expensive to solve in time domain. If the accuracy, error in response and the limits of application of the linear interaction model (**LIM**) can be assessed with respect to the non-linear interaction model (**NLIM**), significant computational resources can be saved as a LIM model can be solved more quickly in frequency domain.

Therefore, a parametric study is also required that compares the response of the OWT modelled with linear and non-linear environmental conditions.

1.2 Problem Statement

Develop an integrated NLIM and a LIM of a mono-pile based OWT and carry out a parametric study to evaluate the differences in their response. Also, find a range of environmental parameters in which they are in good agreement so that LIM can be used to obtain a quick estimation of the response within that range.

1.3 Literature review

A lot of parametric studies have been carried out on OWTs. Abhinav and Saha [1] had carried out a parametric study on a mono-pile based NREL-5MW OWT for varying soil conditions for mean wind speed of 12 m/s and sea state defined by $H_s = 4 \text{ m}$ and $T_p = 10 \text{ s}$. They had, however, disregarded any coupling between wind and wave loads and also neglected the aerodynamic loads on the tower. Bisoi and Haldar [4] carried out a parametric study of the effects of several parameters on the dynamic response of the OWT. To account for damping, they had considered a total damping of 12% (including 8% for material, 3.5% for aerodynamic and 0.15% for hydrodynamic damping). Bush and Manuel [6] had carried out a study using two different foundation models and studied their (foundation's) effects on the extreme loads that are needed during design. All the above studies were conducted considering single plane motions of the OWT structure.

To simulate an OWT more realistically, however, 2 plane motions of the OWT must be considered including the coupling that exists between them. This master thesis takes these coupling effects into account and will try to estimate the modal damping ratios resulting from the aerodynamic forces on the rotor blades.

1.4 Research Questions

The scope of this research project is limited to mono-pile based OWT structures. This master thesis shall try to answer the following questions.

1. Can a model, that assumes linear environmental interactions, simulate an OWT with reasonable accuracy?
2. If yes, what is the range of wind and wave loads till which it is effective.
3. What is the error introduced between a LIM and a NLIM when this range is exceeded.

1.5 Approach

Turbine and support structure definitions are adopted from [NREL-5](#) [17] and UpWind [27] technical reports. The following approach is adopted for building up the mathematical model of the OWT and investigating the effects of non-linear environmental interactions on its structural response.

Approach for NLIM :

1. The support structure is modelled as a finite element beam on a Winkler foundation capable of 2 plane motions and rotations about its longitudinal axis.
2. The soil is modelled as a series of non-linear springs using $p-y$ curves as suggested by the [DNV](#) guidelines.
3. The hydrodynamic forces are modelled including the structural velocities in force terms.
4. The aerodynamic forces are modelled including non-linearities arising due to structural displacements and velocities in force terms. The rotor blades are considered rigid. The aerodynamic loads resulting from the rotating rotor blades are applied at the top most node of the discretized support structure.

Approach for LIM :

1. The support structure is modelled as a finite element beam on a Winkler foundation capable of 2 plane motions and rotation about its longitudinal axis.
2. The soil is modelled as a series of linear springs whose stiffness increase with depth.
3. The hydrodynamic forces are modelled neglecting the structural velocities in force terms.
4. The aerodynamic forces are modelled by linearising terms containing structural displacements and velocities in force terms. The rotor blades are considered rigid. The aerodynamic loads resulting from the rotating rotor blades are applied at the top most node of the discretized support structure.

Morison Equation's Validity :

Morison's equation is the generally preferred method of computing forces on submerged cylindrical structures. However, it doesn't account for any diffraction effects due to the presence of the structure. OWTs have diameters ranging from 6 - 8 m and can therefore influence the incoming waves. Thus the validity of Morison's equation also needs to be checked for such large diameter structures.

Both these models (LIM and NLIM) are subjected to a chosen set of wind and wave loads and directions and their responses are calculated in time domain using MATLAB's ODE solvers and these responses are compared.

1.6 Report structure

The composition of this thesis is as follows. [Chapter 2](#) deals with the general terminology used to define support structure and blade cross-sections. The dimensions and other parameters required for modelling the OWT are also presented. [Chapter 3](#) describes the method used to model soil as linear and non-linear springs.

[Chapter 4](#) deals with generating wave time series for computing hydro-dynamic loads. It will deals with investigating the accuracy of Morison's equation with respect to Mac-Camy and Fuch's equation for calculating the wave inertia loads on cylindrical structures. [Chapter 5](#) deals with describing the method used to generate wind time series and calculating the wind loads on tower and rotating rotor blades.

[Chapter 6](#) describes the procedure used for integrating the soil, waves and wind conditions formulated in earlier chapters. It also describes the modal analysis technique used for reducing the model's simulation time.

[Chapter 7](#) describes the load cases used for comparing the two integrated models and discusses the results. [Chapter 8](#) is dedicated for conclusions and recommendations for further work.

Chapter 2

Terminology

2.1 Introduction

An OWT is a highly complicated mechanism that converts wind energy to electrical energy. The number of components constituting an OWT is quite large. However, since this thesis focuses on the structural response of the OWT to environmental loads, only the main structural components are introduced in this section.

2.2 Support structure terminology

The support structure of an offshore wind turbine can be defined as:

The structure that supports the turbine, holds it in place and transfers the loads from the turbine to the ground [27].

An OWT support structure with a monopile foundation is made of 4 major structural components. Their brief functions are defined below.

2.2.1 Rotor and nacelle assembly

The hub and the blades combined together are called rotor. The nacelle is a housing on top of the tower that houses gearbox, alternators and control system equipment.

2.2.2 Tower

It is a tubular member on top of which the rotor-nacelle assembly is mounted. Since the wind speed increases with height, taller towers enable wind turbines to harness more wind energy.

2.2.3 Transition Piece

It acts as a connection between the tower and the foundation pile. Its main functions are

1. Provides flange for connecting the tower and the foundation pile.
2. Correct for any misalignment while installation of the pile.
3. Provide space for boat landings, platform, ladder etc.

2.2.4 Pile

Piles are open-ended hollow tubular elements that are installed vertically. Their main function is to transmit lateral loads to the soil by activating the horizontal active soil pressure. The axial loads are taken by shaft friction and end bearing. All the 4 parts are shown in [Figure 2.1](#).

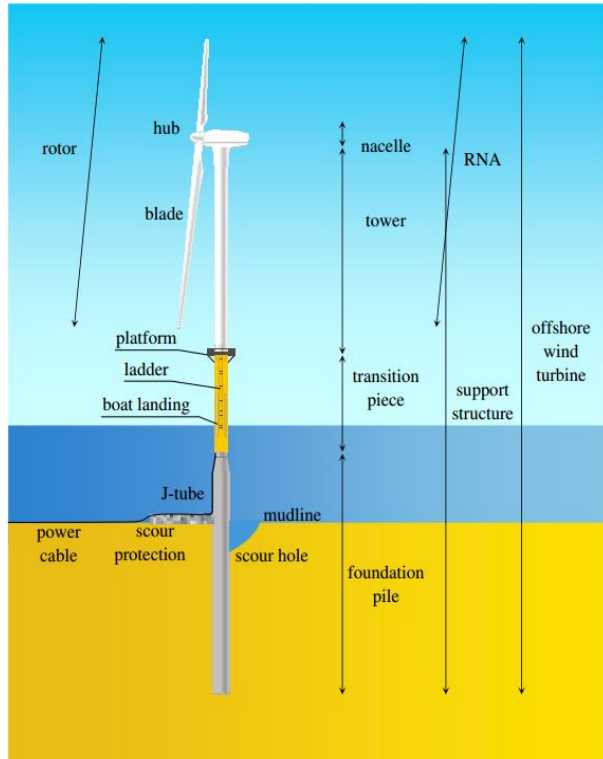


Figure 2.1: OWT terminology [26]

The global coordinate system used in this report is as shown in [Figure 2.2](#). The dimensions used for various parts of the support structure are shown in [Table 2.1](#).

2.3 Blade terminology

The basic terminology used for defining blade elements is explained in this section. The blades are assumed to be rigid in this thesis and their flexibility is ignored.

2.3.1 Aero-foil

An aerofoil is the cross section of an infinitely long straight wing. For this thesis, DU40 air foil is used for defining the blade elements' profile. The length of an imaginary straight line joining the leading and trailing edges of an aerofoil is called the ***chord length***. The chord length and the aero foil cross section are shown in [Figure 2.3](#).

2.3.2 Pitch angle (β_{pitch})

It is the angle between the chord line and the plane of rotation. It is used to keep the rotational speed of the wind turbine within operating limits. For example when the wind speed exceeds the allowable maximum wind speed, the pitch angle is increased so that the exposed surface area of the blade is minimised, reducing the torque acting on the blades and hence the rotational speed decreases (***feathering***).

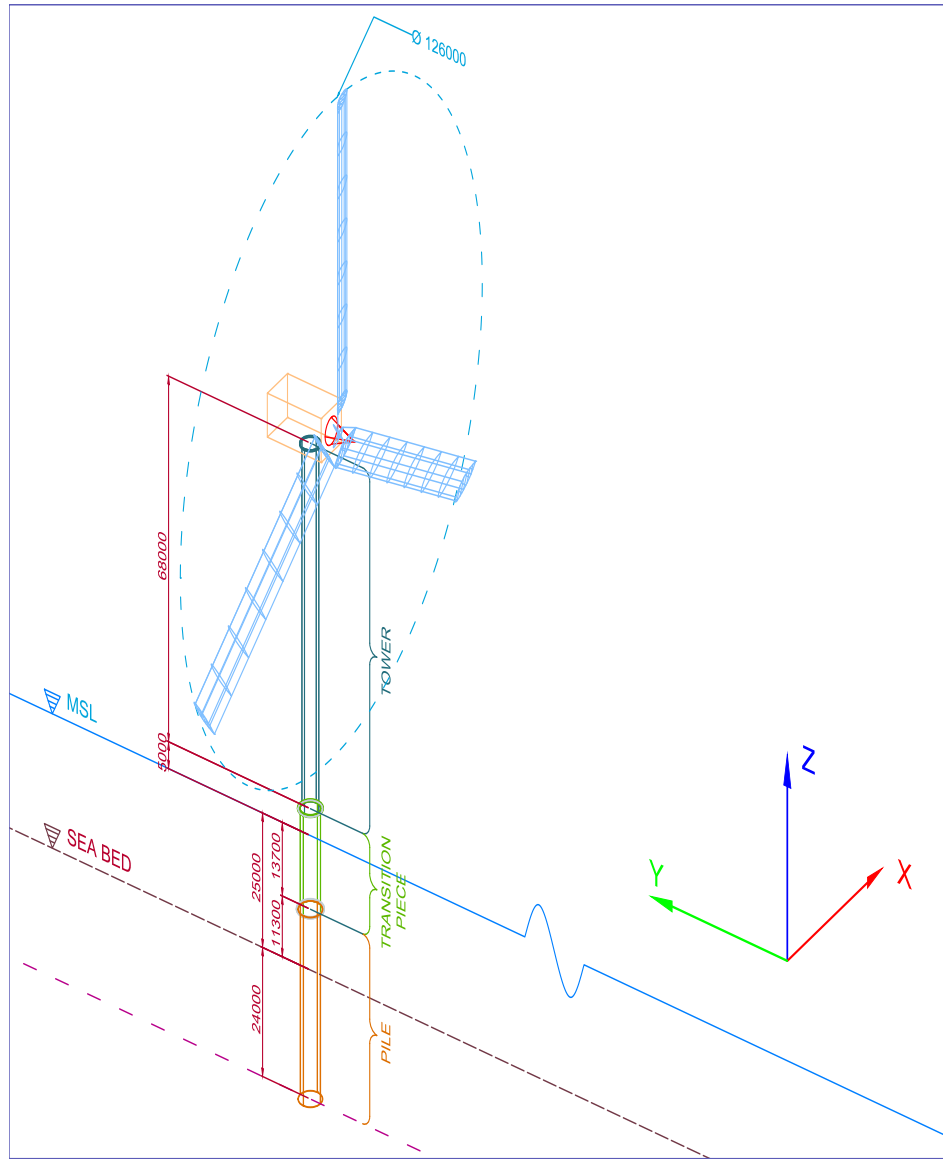


Figure 2.2: Dimensions (in mm) and Global coordinate system

2.3.3 Angle of attack (α_{wind})

It is the angle of approach of the wind as experienced by the blade element. In other words, it is the angle between the chord line and the relative wind velocity.

2.3.4 Angle of inflow (α_{in})

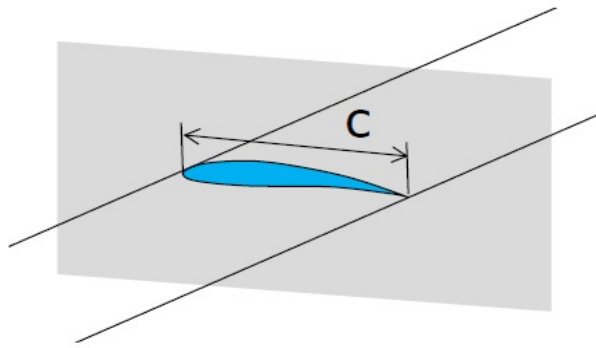
It is the angle between the rotational plane and relative wind velocity.

2.3.5 Twist angle (β_{twist})

The tangential velocity (Ωr) at blade tips is much larger than the wind velocity resulting in a smaller α_{wind} and α_{in} . However, near the blade roots, the tangential velocity is much smaller than wind velocity resulting in a larger α_{wind} and α_{in} and a possibility of **stall**.

Table 2.1: Properties of wind turbine and support structure

Parameter	Value
Rotor, Hub Diameter	126 m, 3 m
Cut in, Rated, Cut-out wind speed	3 m/s, 11.4 m/s , 25 m/s
Cut-in, Rated Rotor speed	6.9 rpm, 12.1 rpm
Overhang	5 m
Rotor Mass (3 Blades)	53220 Kg
Tower Mass	347460 Kg
Hub Mass	56780 Kg
Nacelle Mass	240000 Kg
Transition piece Mass	147000 Kg
Pile Mass	542000 Kg
I_{xx}	21775978.5 Kgm ²
I_{yy}	36748012 Kgm ²
I_{zz}	23079923.5 Kgm ²
Lengths	
Water Depth	25 m
Tower	68 m
Transition Piece (Above water)	5 m
Transition Piece (Under water)	13.7 m
Pile (Above soil)	11.3 m
Pile (Under soil)	24 m
Diameters	
	D_{in}, D_{out}
Tower	4.71 m, 4.80 m
Transition Piece	5.64 m, 5.75 m
Pile	5.53 m, 5.75 m

**Figure 2.3:** Aerofoil and chord length [29]

To optimise the angle of attack, the blade sections near the root are twisted to reduce the α_{wind} . The various angles are depicted in Figure 2.4.

2.3.6 Induction factor a_{in}

As per the BEM (blade element momentum) theory, a_{in} is defined as the fractional decrease in wind velocity between the far field (U_{ff}) and the energy extraction device (U_{turb}) (Figure 2.5). For optimum energy conversion, the value of a_{in} is $\frac{1}{3}$ [29].

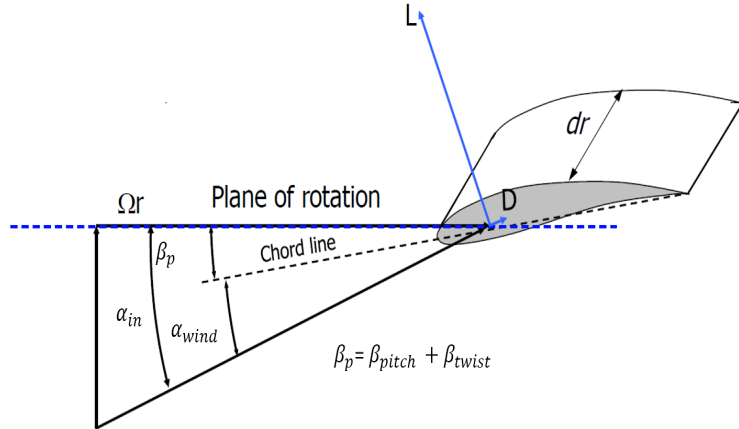
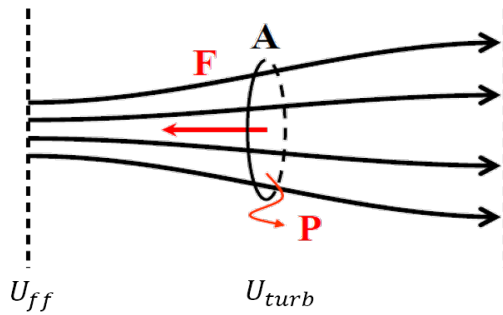


Figure 2.4: Blade angles defined [29]



$$a_{in} = \frac{(U_{ff} - U_{turb})}{U_{ff}}$$

Figure 2.5: Induction factor [29]

2.4 Blade discretization

To capture the large structural gradients at the blade root and the large aerodynamic gradients at the blade tip better, each blade is divided into 17 elements. The 3 inboard and 3 outboard elements are $\frac{2}{3}^{rd}$ of the size of the 11 equally spaced midspan elements.

The properties for various sections of the blade are shown in [Table 2.2](#)

Table 2.2: Properties of blade segments

Node (Root to tip)	Element Length [m]	Twist Angle [Degree]	Chord Length [m]	Element Radius [m]
1	2.73	13.31	3.54	2.87
2	2.73	13.31	3.85	5.60
3	2.73	13.31	4.17	8.33
4	4.10	13.31	4.56	11.75
5	4.10	11.48	4.65	15.85
6	4.10	10.16	4.46	19.95
7	4.10	9.01	4.25	22.55
8	4.10	7.80	4.10	26.65
9	4.10	6.54	3.75	30.75
10	4.10	5.36	3.50	34.85
11	4.10	4.19	3.26	38.95
12	4.10	3.13	3.01	43.05
13	4.10	2.32	2.76	47.15
14	4.10	1.53	2.52	51.25
15	2.73	0.86	2.31	54.67
16	2.73	0.37	2.09	57.40
17	2.73	0.11	1.42	60.13

Chapter 3

Soil Modelling

3.1 Introduction

Soil is a non-linear material, in the sense that its stiffness progressively decreases with an increasing shear stress until, at a sufficiently high stress level, it deforms plastically. A number of approaches exist to model this behaviour such as the *continuum* approach, the *finite element* approach and the *p-y* approach. The last method, i.e. the *p-y* approach is the most commonly applied method in the industry as it is quickly implemented and gives faster results and will be adopted here to model soil as a series of springs. This chapter will deal with the following.

- Introduction to *p-y* curves
- Winkler foundation approach
- Formulation of non-linear and linear soil springs

3.2 *p – y* curves and reaction modulus E_{py}

The differential equation for the equilibrium of a laterally loaded pile as shown in [Figure 3.1](#) is given by [Equation 3.1](#) [24].

$$E_p I_p(z_p) \frac{d^4 y}{dz_p^4} + P_z(z_p) \frac{d^2 y}{dz_p^2} - p(z_p, y) = 0 \quad (3.1)$$

Soil reaction or resistance per unit length p is expressed by [Equation 3.2](#) and can be obtained by the summation of the non-uniform stresses resulting in the soil as a result of the deflection y_1 of the pile ([Figure 3.2](#)) at a given distance z_p along the pile.

$$p(z_p, y) = E_{py}(z_p, y) \cdot y(z_p) \quad (3.2)$$

The reaction modulus E_{py} is defined as the slope of the secant to the curve between p and y ([Equation 3.3](#)). It represents the lateral resistance of the soil (per unit length) at a point along the pile per unit pile deflection y i.e. force/length/deflection and therefore signifies a soil spring stiffness. It is a function of the depth z_p and the lateral deflection y of the pile¹.

$$E_{py} = \frac{p}{y} \quad (3.3)$$

¹It is to be noted that the soil-reaction modulus is not a soil parameter, but it depends on soil resistance and pile deflection.[24]

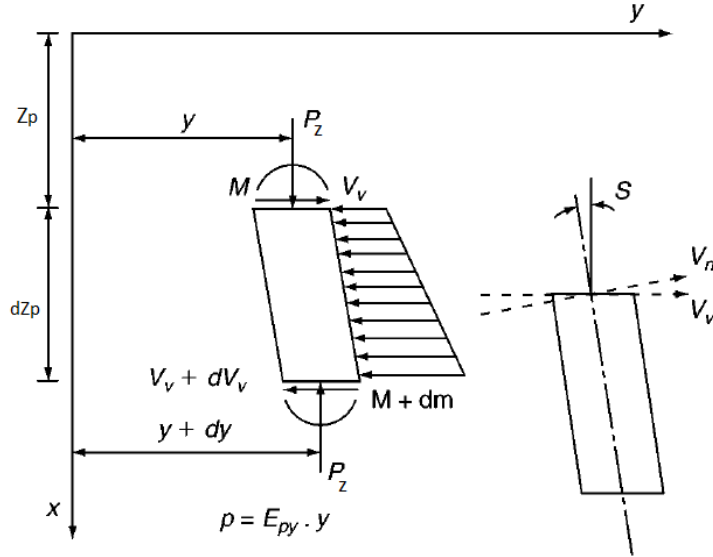


Figure 3.1: Pile equilibrium [24]

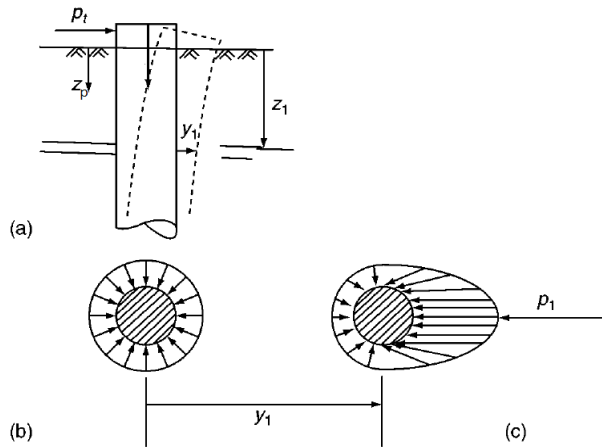


Figure 3.2: Stress distribution on a laterally loaded pile [24]

A p - y curve at an arbitrary depth z_p and its resulting reaction modulus curve is shown in Figure 3.3. Variation of p - y curves with depth is depicted in Figure 3.4. It is to be noted that these curves are for the case of **static loading**. For cyclic or dynamic loading, these curves have to be modified (subsection 3.2.1).

The following points can be observed about the p - y curves from Figure 3.3 and Figure 3.4.

1. The region from origin to point **a** represents the linear behaviour. However, the region between points **a** and **b** denotes non-linear behaviour. The region after point **b** represents plastic deformation [24].
2. The soil resistance is zero at zero depth for all values of deflections y .
3. The initial slopes are linear and increase with depth z_p .
4. The ultimate resistance for each curves approaches a constant value that increases with depth.

The following points are to be noted about the reaction modulus E_{py} [3]

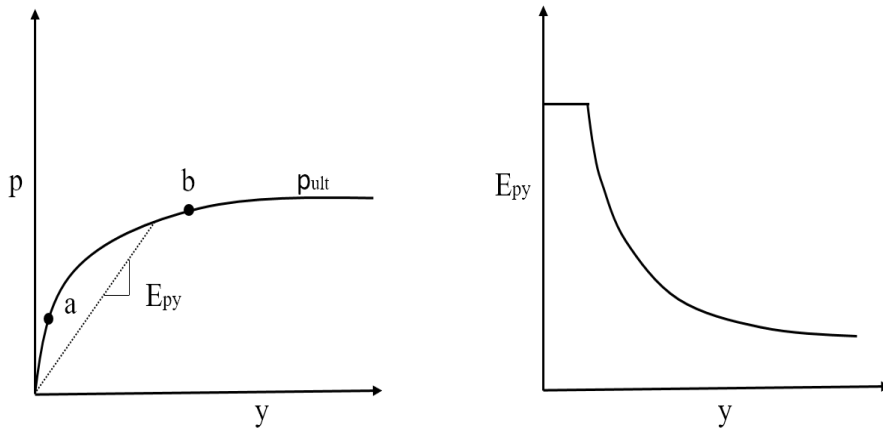


Figure 3.3: Typical $p - y$ curve & resulting soil modulus E_{py} (static loading) (re-created from [24])

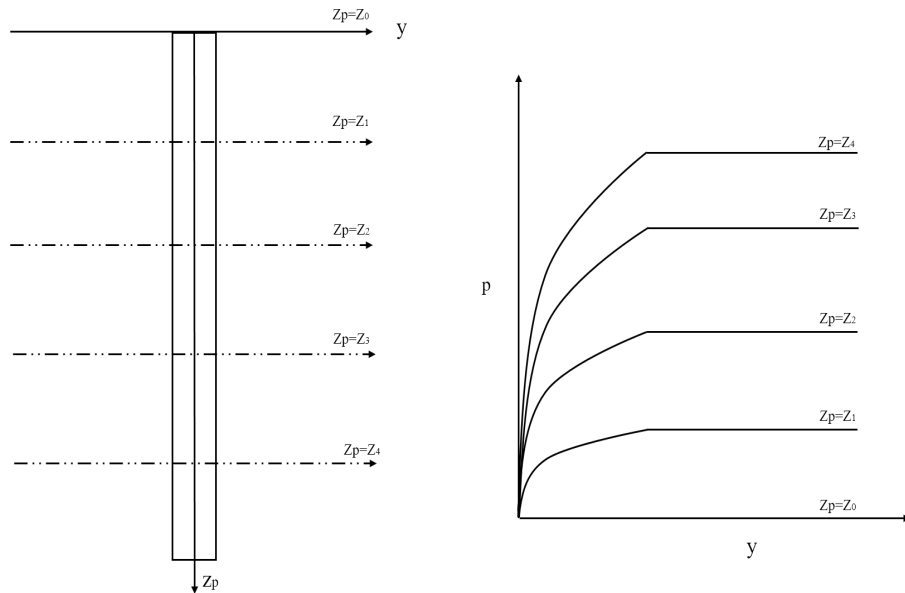


Figure 3.4: Variation of soil lateral resistance p with depth z_p

1. It remains constant for small deflections as no cavity is formed between the pile and the soil.
2. It decreases with increasing deflections y as a cavity between the soil and the pile opens up lowering the stiffness of the soil.
3. It increases with the depth z_p because of the following reasons.
 - The deflections are less likely to produce a larger cavity at increased depth.
 - The overburden pressure increases the stiffness of the soil.
 - The overburden pressure fills up the cavity that is formed.

3.2.1 Modification for cyclic loading

Since the loading on offshore wind turbines is cyclic, the $p-y$ curves have to be modified for such purpose. A modified $p-y$ curve for cyclic loading (**o-a-c-d**) is shown in [Figure 3.5](#).

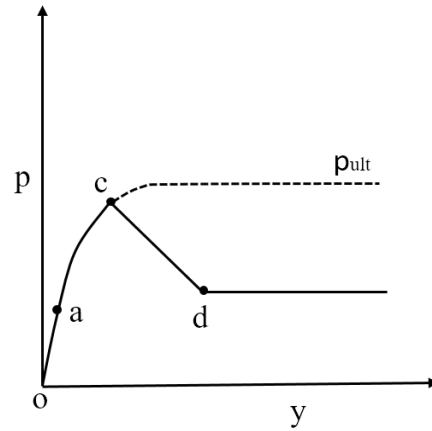


Figure 3.5: Modified p - y curve for cyclic loading

Clearly, the capacity of the soil decreases gradually due to cyclic loading. The change in behaviour can be attributed to the fact that due to cyclic loading, soils such as stiff clays remain pushed away from the pile when large deflections occur due to 2-way cyclic loading thus creating a gap or cavity. This gap causes the change in behaviour of soils as shown in [Figure 3.6](#).

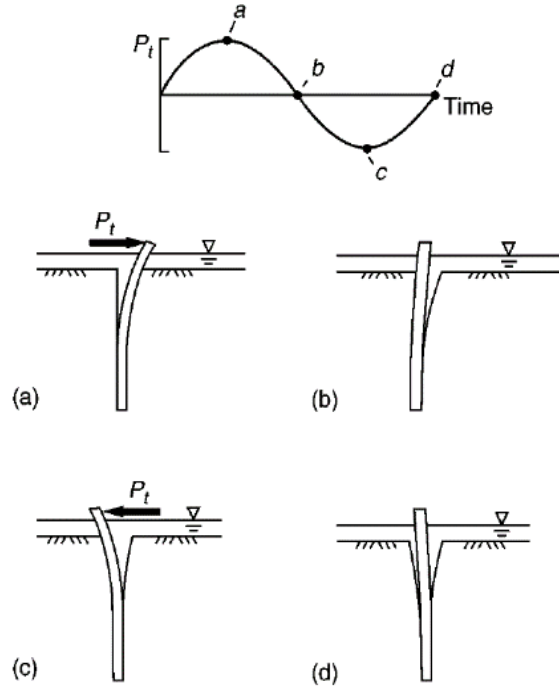


Figure 3.6: Mechanism of soil stiffness reduction [24]

Suppose that the amplitude of vibrations is reduced, then the pile will move in a slack region lowering the resistance. To allow for this effect, Matlock suggested the p - y curve as shown in [Figure 3.7](#) can be used. Thus, the loading history can also be accounted for.

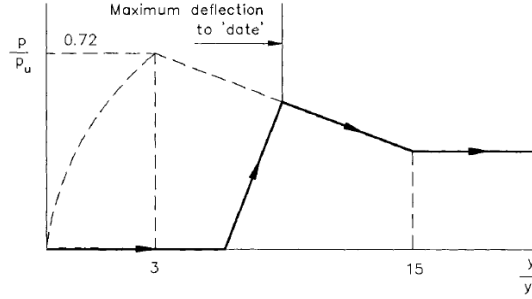


Figure 3.7: Loading history considerations [3]

3.3 Deriving the p - y curves

3.3.1 Experimentally

In order to obtain the p - y curves from experiments, a pile is fitted with closely spaced strain gauges to measure the bending moment along the pile. The following two relations are to be noted

$$\frac{d^2 M_p}{dz_p^2} = E_p I_p(z_p) \frac{d^4 y}{dz_p^4} \quad (3.4)$$

$$p = \frac{dV_p}{dz_p} = \frac{d^2 M_p}{dz_p^2} \quad (3.5)$$

Equation 3.4 and Equation 3.5 imply

1. Deflection y can be obtained by two integrations of the bending moment M_p .
2. Soil lateral resistance p can be obtained by two differentiations of the bending moment M_p .

The differentiations and integrations can be carried out by applying numerical techniques to the bending moment obtained from the measurements. Once the deflections y and lateral resistances p are obtained, a family of p - y curves can be plotted.

3.3.2 Empirically

The p - y curves for practical problems are estimated for a particular type of soil as per the empirical relations given by the DNV and API guidelines. These curves are generated taking soil properties, depth and pile dimensions into account. For this master thesis, p - y curves are generated using DNV guidelines for sand with the following properties.

$$\phi_{sand} = 30^\circ$$

$$\gamma_{sand} = 10 \text{ [KN/m}^3\text{]}$$

3.4 Limitations of p - y curves

Some of the limitations of p - y curves can be summarised as follows [20]

1. The p - y curves are empirical in nature.

2. Pile shape, pile batter and pile installations conditions are not accounted for generating the $p-y$ curves.
3. The traditional $p-y$ curves do not account for the pile EI variation.

3.5 Beam on a Winkler foundation

This approach treats a laterally loaded pile as a beam on elastic foundation and is depicted in [Figure 3.8](#).

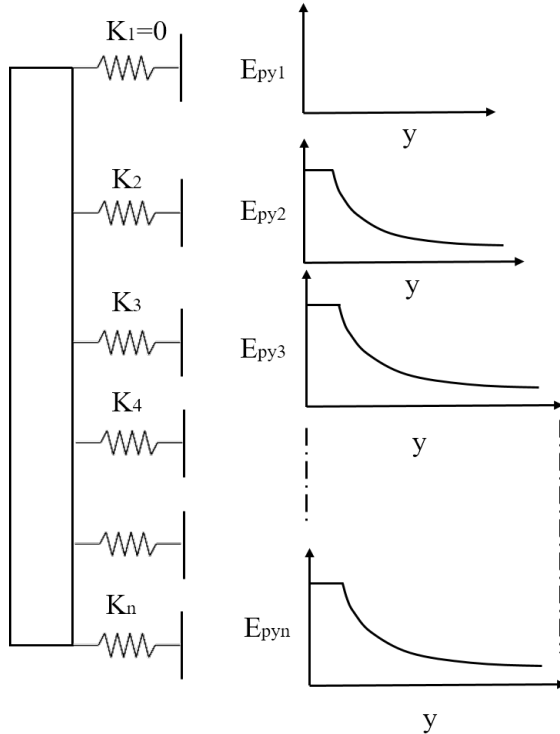


Figure 3.8: Beam on a Winkler foundation

The following are the assumptions used in this approach [3]

1. The beam is supported by a Winkler soil model according to which the elastic soil medium is replaced by a series of infinitely closely spaced “independent”, uncoupled, non-linear and elastic springs. This is shown to be a reasonable approximation by Matlock (1970).
2. The effect of added mass of the soil has negligible effect on the dynamics of the structure.
3. The soil damping need not be calculated. Rough percentage critical damping figures for the complete structure, based on a limited number of tests, can be used instead.

A minimum of 7 springs should be present in the natural deflection wavelength L_p (given by [Equation 3.6](#)) of the beam on elastic foundation [3].

$$L_p = 2\pi \sqrt[4]{\frac{4E_p I_p}{K_s D_{pile}}} \quad (3.6)$$

3.5.1 Advantages of the Winkler foundation approach

The advantages of modelling soil as a Winkler foundation are.

1. It is simple to implement and provides faster problem modelling.
2. Soil non-linearities can be easily modelled.

3.5.2 Dis-advantages of the Winkler foundation approach

The dis-advantages of modelling soil as a Winkler foundation are.

1. This approach, however, does not take the continuity of the soil into account. The approach neglects any coupling effects that may exist amongst adjacent soil layers.
2. Any effects affecting the soil and the pile in 3D space are also neglected in this approach.

3.6 Modelling soil springs

3.6.1 Non-linear springs

The $p-y$ curves for sand with properties mentioned in [subsection 3.3.2](#) can be generated for any depth z_p using the following relation

$$p = 0.9 \cdot p_u \cdot \tanh\left(\frac{K_s \cdot z_p \cdot y}{0.9 \cdot p_u}\right) \quad (3.7)$$

p_u is the ultimate soil resistance and can be evaluated from the following relations

$$p_u = \min \begin{cases} (c_1 \cdot z_p + c_2 \cdot D_{pile}) \gamma_{sand} \cdot z_p \\ c_3 \cdot D_{pile} \cdot \gamma_{sand} \cdot z_p \end{cases} \quad (3.8)$$

The minimum value is used in order to account for the shallow failure (when the soil failure occurs near the sea bed) and deep failure (when the soil is stronger at the upper layers but weaker at the deeper layers) mechanisms of the soil as shown in [Figure 3.9](#). The coefficients c_1 , c_2 and c_3 can be found from graphs given in [9] and are tabulated in [Table 3.1](#).

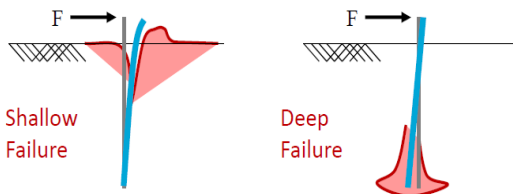


Figure 3.9: Shallow & deep failure soil mechanisms [13]

The values of various parameters used are tabulated in [Table 3.1](#)

Once the $p-y$ curves are known at a particular depth, non-linear soil spring stiffness can be derived by using [Equation 3.9](#) as

$$K_{nl}(z_p, y) = E_{py}(z_p, y) = \frac{p(z_p, y)}{y} \quad (3.9)$$

Table 3.1: Parameters for $p-y$ curve formulation

Parameter	Value	Units
c_1	2	-
c_2	2.7	-
c_3	29	-
K_s	10	MPa/m
γ_{sand}	10	KN/m ³
ϕ_{sand}	30	°
D_{pile}	5.75	m

3.6.2 Linear springs

Cohesionless soils and normally consolidated clays are two kinds of soils where the stiffness is zero at the ground level and increases linearly with depth [24]. Therefore, it is justified to use a linear variation of the soil stiffness. The linear soil spring stiffness is derived using [Equation 3.10](#).

$$K_l(z_p) = \frac{\partial p}{\partial y} \Big|_{y=0} = K_s \cdot z_p \quad (3.10)$$

It is to be noted that the soil spring stiffness defined in [Equation 3.9](#) and [Equation 3.10](#) is per unit length and still needs to be multiplied by length to obtain a spring stiffness in [N/m].

Thus, soil springs having linear and non-linear stiffness characteristics have been defined. Method of implementing them in an integrated model is discussed in [Chapter 6](#).

Chapter 4

Hydrodynamic Loading

4.1 Introduction

In order to simulate the hydrodynamic loads on the OWT, first, a time series of wave surface elevations is required. From this time series, hydrodynamic forces acting on the OWT can then be simulated. This chapter covers the following topics.

- Generating a time series of wave surface elevations using linear wave theory.
- Calculating wave (inertia) forces from the resulting time series of wave surface elevations using Morison's equation ([ME](#)) and MacCamy and Fuchs' equation ([MFE](#)).
- Comparing the two different approaches for accuracy with the diffraction software ANSYS-AQWA.

4.2 Simulation - Wave time series

Waves are stochastic in nature, meaning that they can only be analysed by their statistical properties such as the H_s and T_p . These statistical properties define a *wave spectra*. Two kinds of wave spectra are generally used to define wave statistics at a place namely.

1. Pierson-Moskowitz ([PM](#)) spectra ¹
2. JONSWAP ([JS](#)) spectra

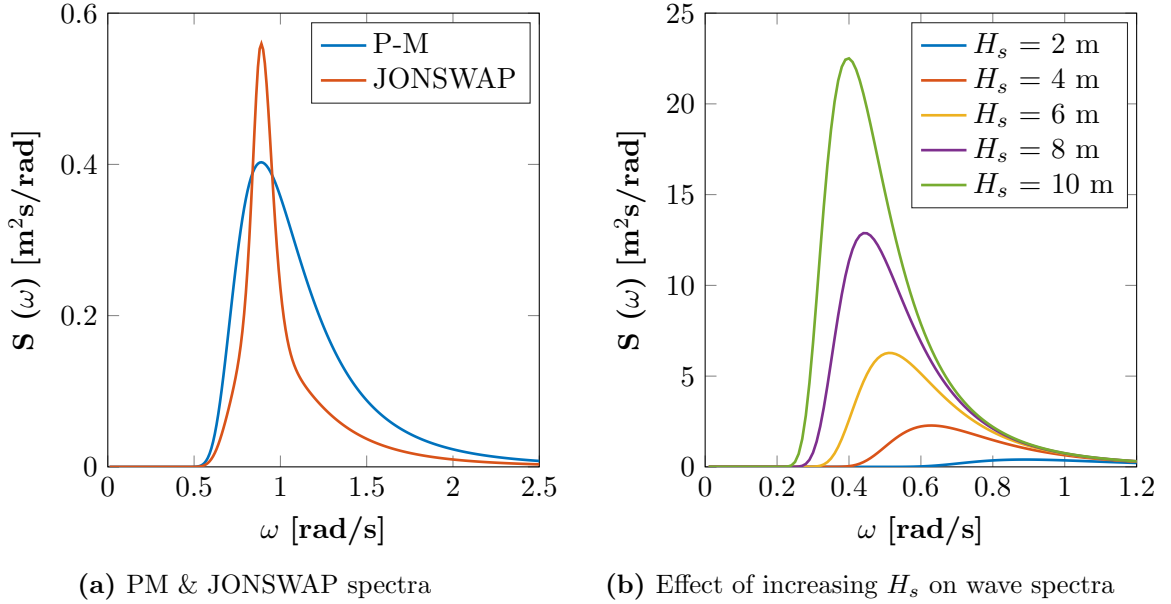
given by the following two relations [28]

$$S(\omega)_{PM} = \alpha_1 g^2 \omega^{-5} \exp\left(\frac{-4g^2 \alpha_1}{H_s^2 \omega^4}\right) \quad (4.1)$$

$$S(\omega)_{JS} = \alpha_1 g^2 \omega^{-5} \exp\left(-1.25(\omega_0/\omega)^4\right) \gamma_w^{a_1} \quad (4.2)$$

A PM spectrum and a JS spectrum are depicted in [Figure 4.1a](#). A PM spectrum for different H_s is depicted in [Figure 4.1b](#). It is to be noted that the tail of the PM spectrum is somewhat higher than that of the JS spectrum, implying that it contains higher energy in that region. For dynamically responding fatigue sensitive structures, higher frequency wave components are more important. Since the OWT is designed to have its 1st natural

¹It is to be noted that [Equation 4.1](#) can be derived from ITTC-Modified Pierson-Moskowitz spectrum by substituting $T_p=5\sqrt{H_s}$ [18]

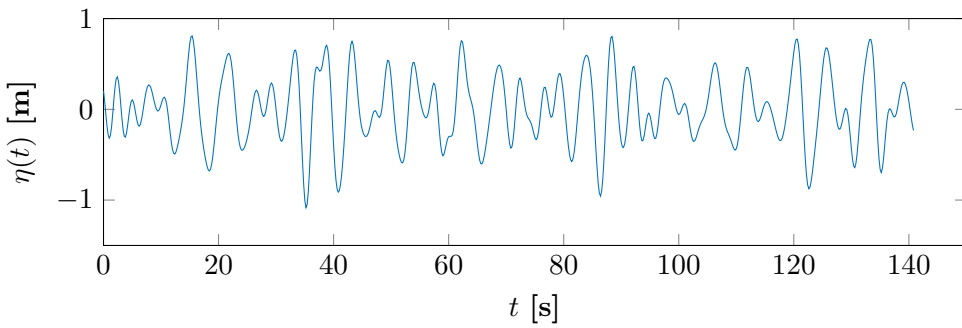
**Figure 4.1:** Wave Spectrum

frequency around this tail, it makes more sense to choose a PM spectrum for response calculations.

Once the spectrum is defined by the H_s , a time series² of sea surface elevation $\eta(t)$ can be generated as a sum of a large number of independent harmonic wave components by using [Equation 4.3](#).

$$\eta(t) = \sum_{i=1}^{N_{f1}} \sqrt{2S_i(\omega)\Delta\omega} \cdot \cos(\omega_i t + \Phi_{waves(i)}) \quad (4.3)$$

A wave time series generated from a PM spectrum with a $H_s = 1.5$ m using 70 frequencies is shown in [Figure 4.2](#).

**Figure 4.2:** Wave time series for $H_s = 1.5$ m

The velocity and acceleration time series at any depth z_w ($z_w=0$ at [MSL](#)) can be obtained using [Equation 4.4](#) and [Equation 4.5](#) respectively:

$$u(z, t) = \sum_{i=1}^{N_{f1}} \sqrt{2S_i(\omega)\Delta\omega} \cdot \omega_i \cdot \frac{\cosh(k_i(d_w + z_w))}{\sinh(k_id)} \cdot \cos(\omega_i t + \Phi_{waves(i)}) \quad (4.4)$$

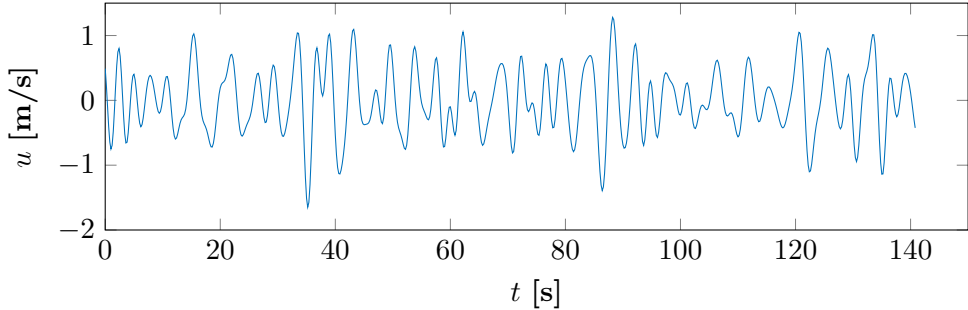
²It is to be noted that the maximum duration of time that can be simulated is dependent on the number of frequencies chosen.

$$\dot{u}(z, t) = - \sum_{i=1}^{N_{f1}} \sqrt{2S_i(\omega)\Delta\omega} \cdot \omega_i^2 \cdot \frac{\cosh(k_i(d_w + z_w))}{\sinh(k_i d)} \cdot \sin(\omega_i t + \Phi_{waves(i)}) \quad (4.5)$$

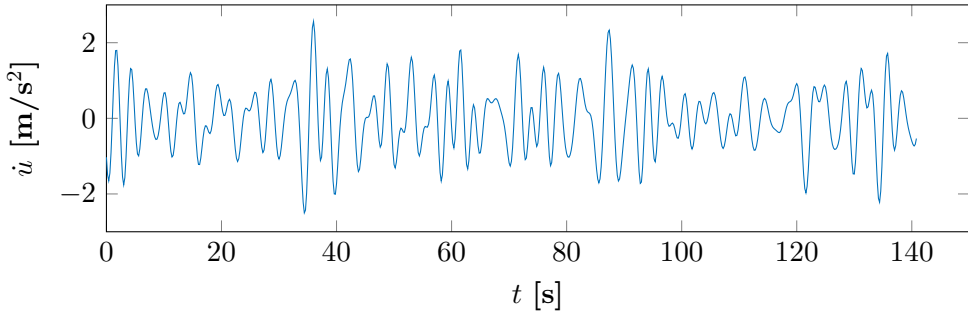
ω_i and k_i are related according to the dispersion [Equation 4.6](#)

$$\omega_i^2 = g \cdot k_i \cdot \tanh(k_i \cdot d_w) \quad (4.6)$$

A time series for u and \dot{u} at $z_w = 0$ based on the surface elevations presented in [Figure 4.2](#) are shown in [Figure 4.3a](#) and [Figure 4.3b](#), respectively.



(a) Water particle velocity time series for $z_w = 0$



(b) Water particle acceleration time series for $z_w = 0$

Figure 4.3: Velocity (a) and acceleration (b) time series

Now that the time series of velocity and accelerations have been defined, the hydrodynamic forces on the OWT support structure can be determined.

Linear wave theory in principle only applies to very small waves, so it does not predict kinematics for the points above the [MSL](#) since they are not in the fluid. To provide predictions of fluid velocity and acceleration (kinematics) at points above the mean water level, **wheeler stretching** is sometimes used ([Figure 4.4](#)). This method is generally applied in the following two ways:

1. By extrapolating the wave velocities and accelerations at the MSL till the point where waves act.
2. By assuming that the wave velocities and accelerations at the point of action of waves are the same as those at the MSL.

In this thesis, however, wheeler's stretching is not used, since this leads to undue complications.

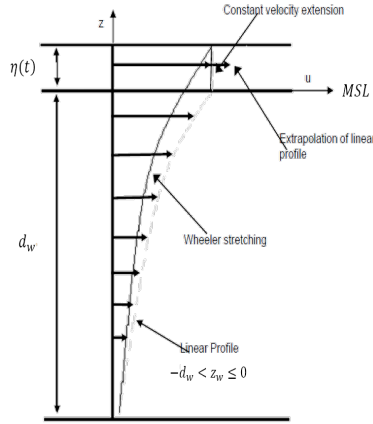


Figure 4.4: Example of Wheeler's stretching

4.3 Morison's Equation (ME)

4.3.1 1-plane structural motions

For structural motions in one plane, the hydrodynamic loads (per unit length) on an element of length dZ_2 (located at a depth z_w) of a flexible cylinder as shown in [Figure 4.5](#), can be written using [ME](#) as

$$dF_{hydro}(z_w, t) = \underbrace{\frac{\pi}{4} \rho_w D_{pile}^2 \dot{u}}_{dF_{in}=dF_k+dF_{diff}} + \underbrace{\frac{\pi}{4} \rho_w D_{pile}^2 C_a (\dot{u} - \ddot{y}_2)}_{dF_{drag,waves}} + \underbrace{\frac{1}{2} \rho_w C_D D_{pile} \cdot (u - \dot{y}_2) |u - \dot{y}_2|}_{dF_{drag,waves}} \quad (4.7)$$

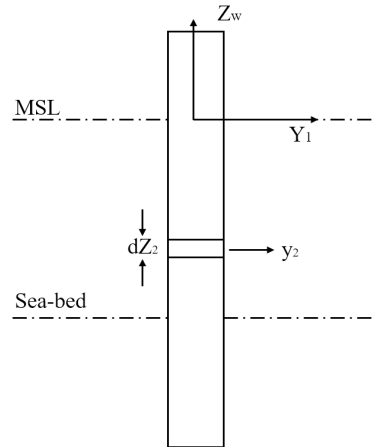


Figure 4.5: Partially submerged pile

The total hydrodynamic force dF_{hydro} given by [Equation 4.7](#) consists of the following three components

1. dF_{fk} : is due to the pressure field induced by the undisturbed incoming waves and is also known as the *Froude-Krylov force*.
2. dF_{diff} : exists because the presence of the structure modifies the incident wave pressure field by forcing the fluid to go around it modifying all the local velocities and thus accelerations.

3. $dF_{drag,waves}$: is caused by the vortices generated in the fluid flow as it passes the structure. Its magnitude is proportional to the (signed) square of fluid velocity relative to the element.

The following three points are to be noted about [Equation 4.7](#):

1. The term $(u - \dot{y}_2)|u - \dot{y}_2|$ maintains a proper sign for the drag term.
2. The drag and inertia force components are 90° out of phase with each other.
3. The non-linear drag term introduces a non-linear term in the system and the non-linearity makes the solution difficult. This equation may be handled in a closed form as long as one linearises the non-linear damping term by the first term of the Fourier series expansion [7].

4.3.2 Value of C_a and C_D

In a steady flow the value of C_D is reasonably well known for most shapes of member. Similarly, in uniformly accelerating flow $C_M (= 1 + C_a)$ values are reasonably well established. In waves (oscillating flow), however, both these coefficients are difficult to select as the re-encounter of the member with its own wake changes the coefficients.

For a regular wave, C_a and C_D are dependent on **KC** (Keulegan Carpenter number) which is defined by [Equation 4.8](#). A sea state is, however, a combination of a number of regular wave components and therefore it becomes very difficult to find exact values for C_a and C_D . For this thesis, C_a is chosen to be 1 [3] and C_D is taken as 0.6.

$$KC = \frac{uT_w}{D_{pile}} \quad (4.8)$$

ME is based on the assumption that the wavelength of the incident wave is much larger than the cylinder diameter $\left(\frac{D_{pile}}{\lambda_w} < 0.2\right)$ (*the diffraction parameter*) and thus the presence of the structure doesn't influence the waves. This value of 0.2 was suggested by Isaacson (1979) in his comprehensive study on the generation mechanism of wave force on circular cylindrical body ([Figure 4.6](#)). However, OWTs have diameters ranging from 6-8 m and can therefore influence the incoming waves. For a general case, therefore, the linear analytical solution proposed by MacCamy and Fuchs (1954) can be used [10].

4.4 MacCamy and Fuchs' (**MFE**) linear diffraction theory

A large diameter pile generates diffracted and reflected waves (diffraction) that can considerably influence the incident waves. The reflected and diffracted waves together are called *scattered waves* and are shown in [Figure 4.7](#).

Diffraction effects become important when $\frac{D_{pile}}{\lambda_w} > 0.2$ or $\lambda_w < 5 \cdot D_{pile}$. For $D_{pile} = 5.75$ m this wavelength comes out to be 28.75 m. At the given water depth of 25 m, the corresponding frequency associated with this wavelength is found to be 1.46 [rad/s] (using [Equation 4.6](#)). Thus diffraction effects will become important for frequencies greater than 1.46 [rad/s].

In 1954, MacCamy and Fuchs applied the known analytical solution for the problem of diffraction of sound waves from an infinite circular cylinder and developed solutions for a circular cylinder in water waves in finite water depth. Full analytical derivation can be found in [25].

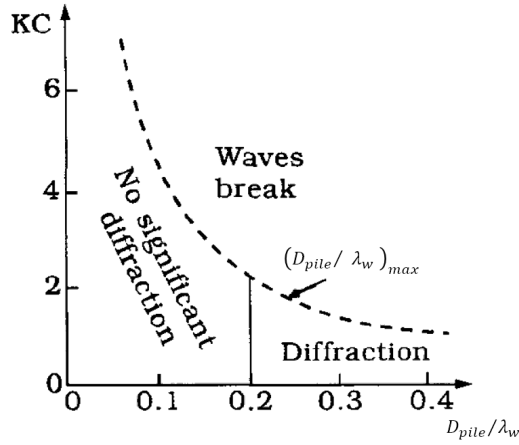


Figure 4.6: Different flow regimes [25]

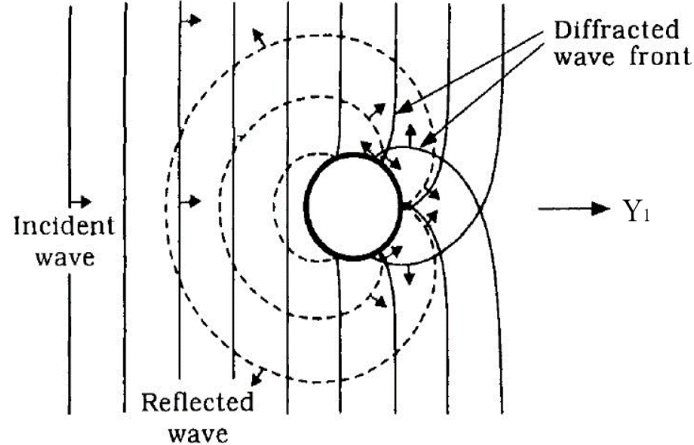


Figure 4.7: Wave diffraction [25]

For a wave travelling in positive Y_1 direction given by [Equation 4.9a](#), they arrived at [Equation 4.9b](#) for wave inertia forces (per unit length) at any depth z_w .

$$\eta_1(t, Y_1) = A_1 \cos(\omega_1 t - k_1 Y_1) \quad (4.9a)$$

$$dF_{in} = \frac{4\rho_w g A_1}{k_1} \cdot \frac{\cosh(k_1(d_w + z_w))}{\cosh(k_1 d_w)} \cdot A(k_1 \cdot r_{pile}) \cdot \cos(\omega_1 t - \delta(k_1 \cdot r_{pile})) \quad (4.9b)$$

The terms $A(k_1 \cdot r_{pile})$ and $\delta(k_1 \cdot r_{pile})$ are defined by [Equation 4.10a](#) and [Equation 4.10b](#)

$$A(k_1 \cdot r_{pile}) = \frac{1}{\sqrt{\{JJ'(k_1 \cdot r_{pile})\}^2 + \{YY'(k_1 \cdot r_{pile})\}^2}} \quad (4.10a)$$

$$\delta(k_1 \cdot r_{pile}) = -\arctan \left\{ \frac{YY'(k_1 \cdot r_{pile})}{JJ'(k_1 \cdot r_{pile})} \right\} \quad (4.10b)$$

For brevity, the terms in the parenthesis are omitted. JJ is the Bessel function of 1st kind (order 1) and JJ' represents its derivative (w.r.t its argument). YY is the Bessel function of 2nd kind (order 1) and YY' represents its derivative (w.r.t its argument). δ represents the phase difference between incident wave and wave force. The following points are to be noted about δ .

1. As $(k_1 \cdot r_{pile})$ approaches 0, δ tends to $-\frac{\pi}{2}$. This is exactly the result obtained in [ME](#).
2. As diffraction starts to play a role, the phase difference starts to diverge from $-\frac{\pi}{2}$.

Both these points are depicted in [Figure 4.8](#).

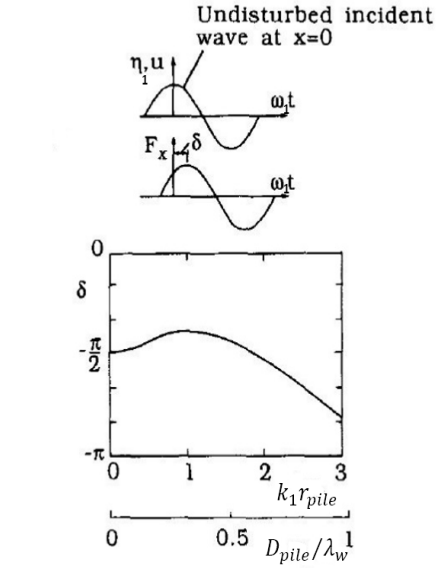


Figure 4.8: Variation of δ with $(k_1 \cdot r_{pile})$ [25]

4.4.1 Corrected C_M

Using MacCamy and Fuchs' solution, it can be shown that the inertia coefficient is given by [Equation 4.11](#) [25], making C_M dependent upon the wave number of the wave and not a constant as is assumed by Morison's equation.

$$C_M = \left[\frac{4A(k_1 \cdot r_{pile})}{\pi(k_1 \cdot r_{pile})^2} \right] \quad (4.11)$$

The variation of C_M with (D_{pile}/λ_w) is shown in [Figure 4.9](#). The following points are to be noted about the corrected C_M .

1. C_M approaches 2 as $(k_1 \cdot r_{pile})$ approaches zero, which is the assumption on which [ME](#) is based.
2. C_M begins to be influenced by diffraction effects after (D_{pile}/λ_w) starts exceeding 0.2.

3. C_M decreases with increasing (D_{pile}/λ_w) . Physically this means that the structure is so big that the acceleration of the flow is maximum over one part of the body while it is not so over the rest of the body.

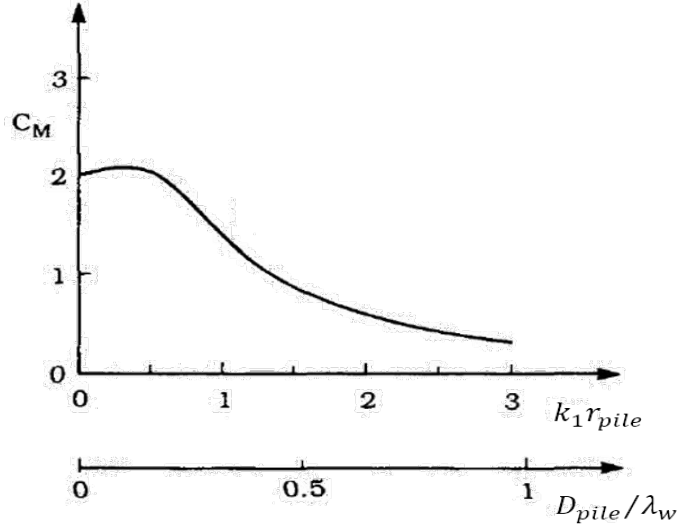


Figure 4.9: Variation of C_M with (D_{pile}/λ_w) [25]

4.5 ME vs MFE

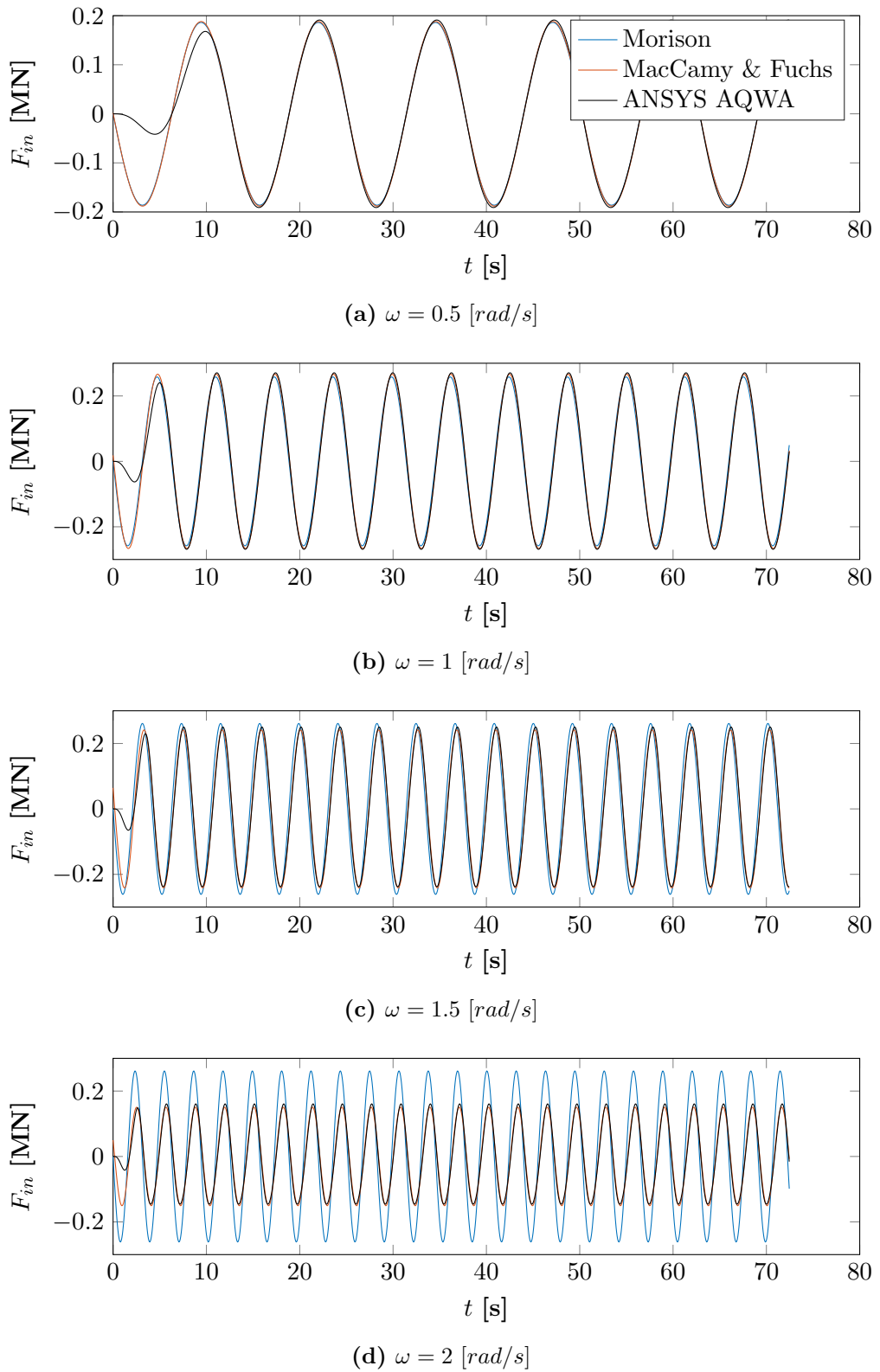
In order to accurately model the hydrodynamic loads on the OWT support structure, both the approaches i.e. **ME** and **MFE** need to be compared with a diffraction software, ANSYS-AQWA. In this comparison only the inertia forces ($dF_{fk} + dF_{diff}$) are compared for a regular wave of amplitude 0.5 m and four different frequencies to evaluate the differences and accuracy.

The results of this comparison are shown in [Figure 4.10](#).

The following points can be noted from these results.

- For lower frequencies (< 1.46 [rad/s]) i.e. $\omega = 0.5$ and 1 [rad/s], both **ME** and **MFE** give similar results ([Figure 4.10a](#) and [Figure 4.10b](#)).
- At $\omega = 1.5$ [rad/s] results from both the approaches start deviating ([Figure 4.10c](#)). This is consistent with the critical frequency of 1.46 [rad/s] found in [section 4.4](#).
- At frequencies greater than 1.5 [rad/s], ([Figure 4.10d](#)), **ME** starts overpredicting the inertia forces while **MFE** remains consistent with the diffraction software.

The sea-state at any general site is composed of a number of independent wave frequencies and it is difficult to predict the exact number of wave frequencies less than the critical frequency (for diffraction limit). To make the OWT model applicable for any wave climate, **MFE** gives more reliable results and is therefore used to calculate the wave inertia loads.

**Figure 4.10:** ME vs MFE vs ANSYS-AQWA

4.6 Two-plane structural motions

For motions in 2 planes with waves approaching the structure as shown in [Figure 4.11](#), the hydrodynamic forces need some modifications. For the inertia forces calculated from MacCamy and Fuchs' equation, the components parallel and perpendicular to X_1Z_w plane are given by [Equation 4.12](#)

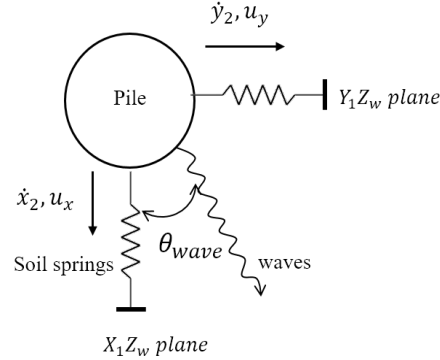


Figure 4.11: Top view of waves approaching a pile

$$\left\{ \overrightarrow{dF}_{in} \right\}_w = dF_{in} \begin{bmatrix} \cos(\theta_{wave}) & \sin(\theta_{wave}) \end{bmatrix}^T \quad (4.12)$$

The drag forces can be modified using [Equation 4.13a](#) and [Equation 4.13b](#).

$$\left\{ \overrightarrow{dF}_{drag} \right\}_w = \frac{1}{2} \rho_w C_D D_{pile} \sqrt{(u_x - \dot{x}_2)^2 + (u_y - \dot{y}_2)^2} \begin{bmatrix} (u_x - \dot{x}_2) & (u_y - \dot{y}_2) \end{bmatrix}^T \quad (4.13a)$$

$$\begin{bmatrix} u_x & u_y \end{bmatrix}^T = u \begin{bmatrix} \cos(\theta_{wave}) & \sin(\theta_{wave}) \end{bmatrix}^T \quad (4.13b)$$

u_x and u_y represent the wave velocities (at a depth z_w) [m/s] resolved parallel and perpendicular to the X_1Z_w plane. \dot{x}_2 and \dot{y}_2 represent velocities [m/s] of the element dZ_2 ([Figure 4.5](#) and [Figure 4.11](#)) (at a depth z_w) in X_1Z_w and Y_1Z_w plane respectively.

It can be seen from [Equation 4.13a](#) that the drag forces in both the planes are coupled.

Chapter 5

Aerodynamic Loading

5.1 Introduction

In order to simulate the aerodynamic loads on the OWT, first, a time series of wind velocities is required. From this time series, aerodynamic forces acting on the OWT can then be simulated. This chapter will cover the following topics.

- Generating a time series of wind velocities.
- Calculating aerodynamic forces on the tower and rotor blades from the resulting wind velocity time series.

5.2 Wind profile

Turbulent wind velocity consists of *longitudinal* (in direction of wind), *lateral* (perpendicular to the wind direction) and *vertical* components as shown in [Figure 5.1](#). The wind velocity is frequently conceived as a sum of the following two components.

1. Mean wind speed $\bar{V}(z_a)$ which is a function of height (z_a) above the sea level.
2. Fluctuating wind speed $v(z_a, t)$ which is a function of both height (z_a) and time (t) and has a zero mean value.

Thus, the total wind velocity vector can be represented by [Equation 5.1](#).

$$\vec{V}_{net} = \begin{Bmatrix} \bar{V}_x \\ \bar{V}_y \\ \bar{V}_z \end{Bmatrix} + \begin{Bmatrix} v_x \\ v_y \\ v_z \end{Bmatrix} \quad (5.1)$$

This thesis, however, is limited only to the longitudinal component i.e. $\bar{V}_x = \bar{V}_z = 0$ and $v_x = v_z = 0$.

Turbulence is a very complex process, and cannot be represented simply in terms of deterministic equations. Owing to its random nature (similar to ocean waves), wind is also defined by its statistical properties and thus the concept of *turbulence spectrum* comes into picture.

5.3 Turbulence spectra

The fluctuations in the wind can be thought of as resulting from a composite of sinusoidally varying winds imposed on the mean steady wind. These sinusoidal variations will have a

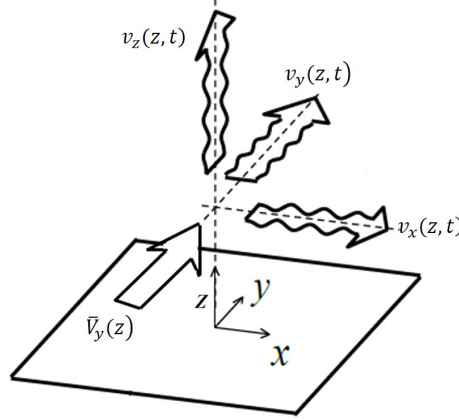


Figure 5.1: The 3 turbulence components [28]

variety of frequencies and amplitudes. These frequencies and amplitudes can be obtained from a *turbulence spectrum* which describes the frequency content of the signal. The two generally used spectrum to simulate wind conditions are

1. Kaimal spectra (**KS**)
2. Von Karman spectra (**VKS**)

given by the following two relations

$$S(f_w)_{\text{KS}} = \frac{4\sigma_v^2 L_{1v}/\bar{V}}{(1 + 6f_w L_{1v}/\bar{V})^{5/3}} \quad (5.2)$$

$$S(f_w)_{\text{VKS}} = \frac{4\sigma_v^2 L_{2v}/\bar{V}}{(1 + 70.8(f_w L_{2v}/\bar{V})^2)^{5/3}} \quad (5.3)$$

$L_{1,2v}$ (Integral scale parameter) is defined by

$$L_{1,2v} = \begin{cases} 5.67z_a & \text{if } z_a < 60m; \\ 340.2 & \text{if } z_a > 60m; \end{cases} \quad (5.4)$$

σ_v is defined by [Equation 5.5](#)

$$\sigma_v = I_{ref}(0.75\bar{V} + 5.6) \quad (5.5)$$

I_{ref} (Expected value of the turbulence intensity at 15 m/s) can take values of 0.16, 0.14 and 0.12 depending upon the turbine class [16].

The **VKS** gives a good description for turbulence in wind tunnels, although the **KS** may give a better fit to empirical observations of atmospheric turbulence [5]. In this thesis, therefore, **KS** is used for generating time series of the wind velocities.

5.4 Simulation - Wind time series

Once the spectrum is defined by the parameters \bar{V} , σ_v and $L_{1,2v}$, a time series of wind speeds can be generated as a sum of a large number of harmonic components by using [Equation 5.6](#).

$$V(t) = \bar{V} + \sum_{j=1}^{N_{f_2}} \sqrt{2S_j(f_w)\Delta f_w} \cdot \sin(2\pi f_{j,w}t + \Phi_{wind(j)}) \quad (5.6)$$

A Kaimal spectrum with $\bar{V}=10.4 \text{ m/s}$, $I_{ref}=0.14$, $N_{f_2}=500$, $\Delta f=0.0033 \text{ Hz}$ ($\frac{\text{Sampling rate}=5}{3 \times N_{f_2} (=500)}$), $L_{1v}=340.2 \text{ m}$ and a time series of wind velocities generated from it are shown in [Figure 5.2a](#) and [Figure 5.2b](#) respectively.

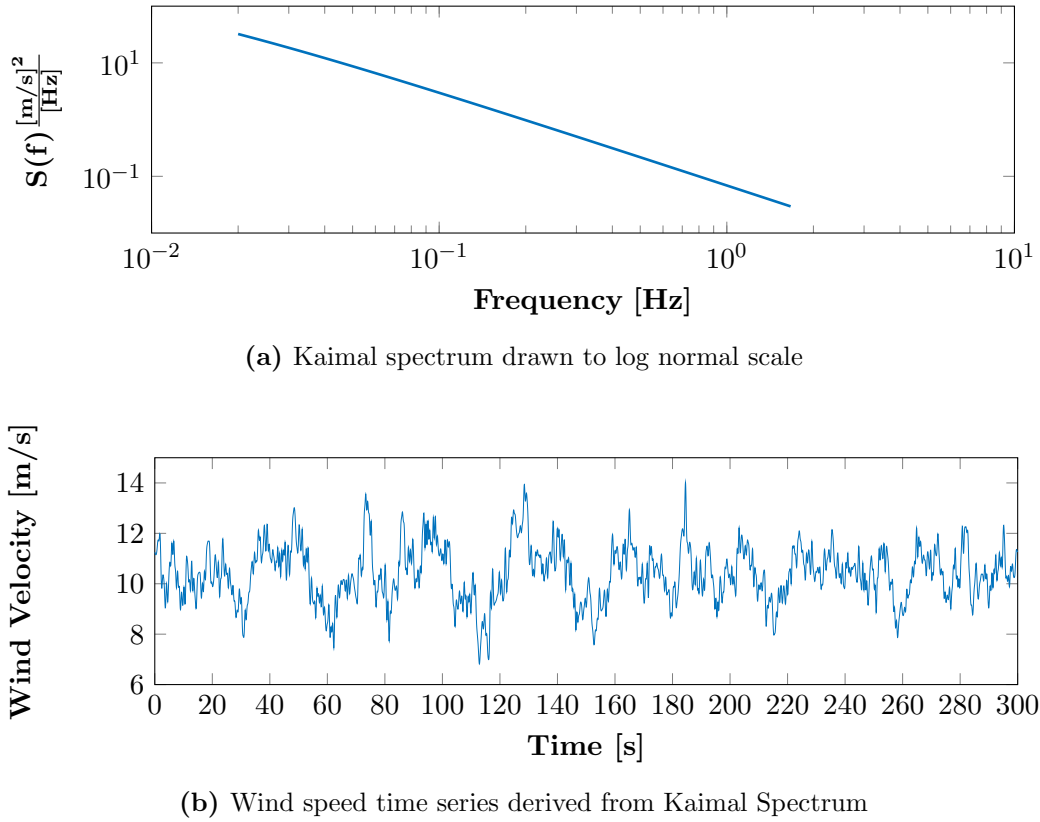


Figure 5.2: Wind Spectrum

The spatial variation of the wind velocity over height can be taken into account using [Equation 5.7](#) [9].

$$V(z_a, t) = V_{hub}(t) \left(\frac{z_a}{z_{hub}} \right)^{\alpha_2} \quad (5.7)$$

5.5 Aerodynamic forces

Aerodynamic loads will act on the following two parts of the OWT

1. Tower + Transition Piece.
2. Rotor blades.

5.5.1 Aerodynamic loads Tower and Transition piece

The presence of the Tower disturbs the flow of air around it and is thus subjected to drag loads. For calculating the forces on the tower and the transition piece, spatial variation of the wind loads is considered i.e. wind shear is **present**. The magnitude of the drag force (per unit length) acting on the exposed part (at height z_a) can be calculated on the

lines of section 4.6 for 2 plane structural motions as demonstrated by [Equation 5.8a](#) and [Equation 5.8b](#)

$$\left\{ \vec{dF}_{drag} \right\}_{wind} = \frac{1}{2} \rho_a C_d D_{t,tp} \sqrt{(V_x - \dot{x}_3)^2 + (V_y - \dot{y}_3)^2} \begin{bmatrix} (V_x - \dot{x}_3) & (V_y - \dot{y}_3) \end{bmatrix}^T \quad (5.8a)$$

$$\begin{bmatrix} V_x & V_y \end{bmatrix}^T = V \begin{bmatrix} \cos(\theta_{wind}) & \sin(\theta_{wind}) \end{bmatrix}^T \quad (5.8b)$$

V_x and V_y represent the wind velocities (at a height z_a) [m/s] resolved parallel and perpendicular to the X_1Z_w plane. \dot{x}_3 and \dot{y}_3 represent velocities [m/s] of the tower element at that height in X_1Z_w and Y_1Z_w planes respectively ([Figure 5.3](#)). Similar to the wave loads, it can be seen from [Equation 5.8a](#) that the wind loads in both planes are coupled.

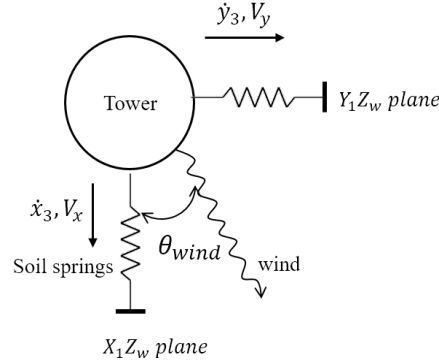


Figure 5.3: Top view of wind approaching the tower

Value of the C_d for smooth cylinder is dependent on the Reynold's number (Re) and can be approximated from [Figure 5.4](#) as 0.6 (for wind speeds of 10-25 [m/s] and diameters of 4-5 [m]).

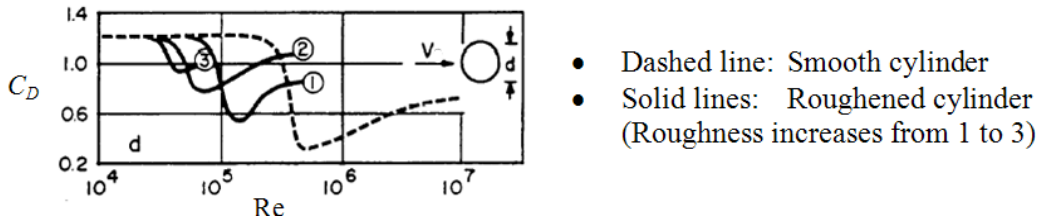


Figure 5.4: Drag coefficient vs Reynold's number
[21]

Thus, having defined all the parameters, aerodynamic loads on the Tower and Transition piece can be calculated.

5.5.2 Aerodynamic loads on rotor blades

Only the general algorithm used for force calculations is given in this section. For detailed explanation of this section, reference is made to [Appendix G](#). For calculating forces on the blades, the rotor blades are assumed to be **rigid**. Moreover, it is assumed that the velocity of wind at the top node V_{hub} acts on all the 3 blades and the spatial variation is disregarded i.e. wind shear is assumed to be **absent**. Each individual blade is divided into 17 segments each having its own blade radius, twist angle, chord length and segment length.

The rotor blades are acted upon by the following 3 forces

1. Drag forces ($F_{d,b}$)
2. Lift forces ($F_{l,b}$)
3. Inertia forces ($F_{i,b}$)

The calculation of these forces is a bit complicated as they act on a rotating blade. The following assumptions are made for calculation of the forces on blades.

1. The flow remains attached.
2. The angle of attack α_{wind} is small ($< 20^\circ$).
3. The velocity of wind at the top node V_{hub} acts on all the 3 blades and the spatial variation is disregarded.

The implications of the 1st two assumptions are

1. The drag coefficient for the blades $C_{d,b}$ can be assumed to be very small. Here it is taken to be 0.01 (Figure 5.5).
2. The lift coefficient can be approximated as $2\pi \sin(\alpha_{wind})$.

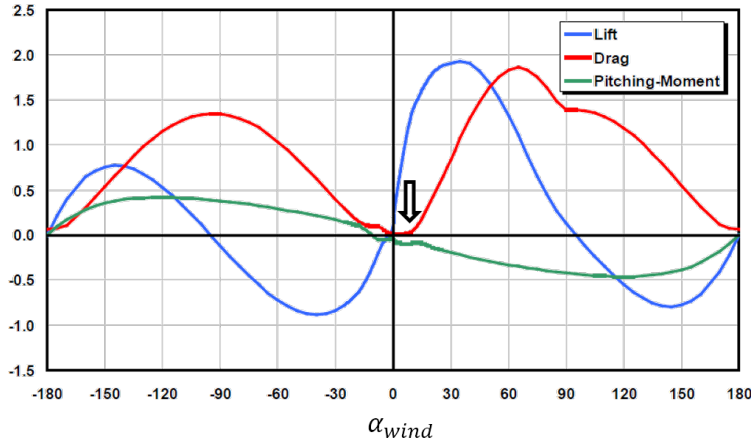


Figure 5.5: Corrected coefficients of the DU40 airfoil [17]

The following procedure is adopted to calculate the 3 forces for each blade segment.

1. A transformation matrix (Equation 5.9) if defined that is used for transforming variables from (and to) global coordinate system (GCS) (located at the top most node of tower) to local rotating coordinate system (LCS) (located at the blade segment) (Figure 5.6).

$$[R]_{trans} = \begin{bmatrix} -\sin \Psi_j & 0 & -\cos \Psi_j \\ 0 & 1 & 0 \\ \cos \Psi_j & 0 & -\sin \Psi_j \end{bmatrix} \begin{bmatrix} 1 & -\theta_{z,t} & \theta_{y,t} \\ \theta_{z,t} & 1 & -\theta_{x,t} \\ -\theta_{y,t} & \theta_{x,t} & 1 \end{bmatrix} \quad (5.9)$$

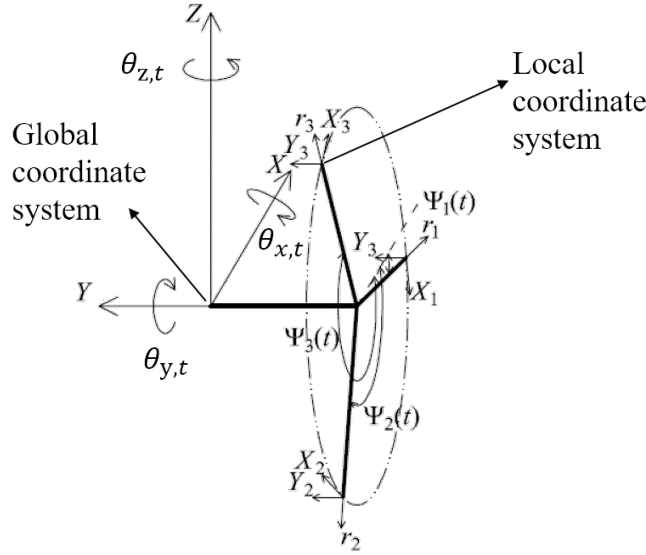


Figure 5.6: Coordinate systems for rotor blades

The blade azimuths Ψ_j are given as

$$\Psi_j = \begin{cases} -\Omega t & \text{for } 1^{\text{st}} \text{ blade;} \\ -\Omega t - \frac{2\pi}{3} & \text{for } 2^{\text{nd}} \text{ blade;} \\ -\Omega t - \frac{4\pi}{3} & \text{for } 3^{\text{rd}} \text{ blade;} \end{cases} \quad (5.10)$$

2. The global wind velocity vector $\begin{bmatrix} V_{hub,x} & V_{hub,y} & 0 \end{bmatrix}^T$ is transformed to local wind velocity vector using [Equation 5.11](#). The radial forces are considered zero here, so the 3^{rd} entry in the local velocity vector is substituted zero.

$$\vec{V}_{loc} = [R]_{trans} \begin{bmatrix} V_{hub,x} & V_{hub,y} & 0 \end{bmatrix}^T + \begin{bmatrix} \Omega * r_j & 0 & 0 \end{bmatrix}^T \quad (5.11)$$

3. The local wind acceleration vector (for inertia forces) are found by [Equation 5.12](#). The 3^{rd} entry in the local acceleration vector is also substituted zero.

$$\dot{\vec{V}}_{loc} = [\dot{R}]_{trans} \begin{bmatrix} V_{hub,x} & V_{hub,y} & 0 \end{bmatrix}^T + [R]_{trans} \begin{bmatrix} \dot{V}_{hub,x} & \dot{V}_{hub,y} & 0 \end{bmatrix}^T \quad (5.12)$$

4. The structural velocities and accelerations in the **LCS** are found from structural translations $\begin{bmatrix} x_t & y_t & 0 \end{bmatrix}^T$ and rotations $\begin{bmatrix} \theta_{x,t} & \theta_{y,t} & \theta_{z,t} \end{bmatrix}^T$ of the top most node of the tower using expressions from [Appendix G](#).
5. The $F_{d,b}$, $F_{l,b}$ and $F_{i,b}$ and their respective torques are calculated in the **LCS** also accounting for the relative motions using complete (for **NLIM**) as well as linearised (for **LIM**) expressions from [Appendix G](#).
6. The forces and torques are translated to **GCS** by multiplication with the *inverse* of $[R]_{trans}$ matrix.
7. The forces and torques are then integrated for each blade (comprising 17 segments) and then the total is found by summing forces and torques from all the 3 blades.

Chapter 6

Model Description

6.1 Introduction

The modelling of soil springs, hydrodynamic and aerodynamic loads was dealt in earlier chapters. This chapter will describe how all the three environmental interactions are integrated to build a mathematical model of the OWT using Finite element method ([FEM](#)). The explanation about the FEM matrices can be found in [Appendix A](#). The following topics are covered:

- Discretizing support structure into parts and selecting the number of elements.
- Application of the external loads on the model and solving the system in time domain.
- A method to reduce the computation time (Mode displacement method) [23].

6.2 Discretization

6.2.1 Support structure

The support structure is divided into following five parts ([Figure 6.1](#) also refer to [Chapter 2](#) [Figure 2.2](#)):

1. Tower (1)
2. Above water transition piece (2)
3. Under water transition piece (3)
4. Embedded pile (4)
5. Un-embedded pile (5)

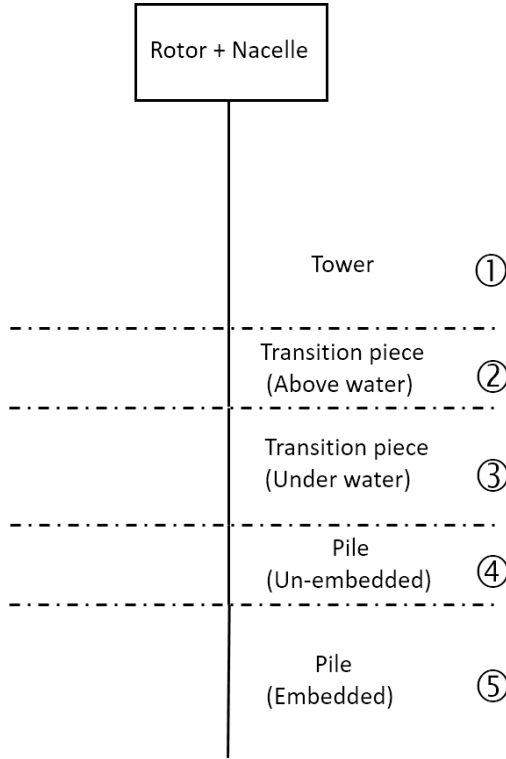


Figure 6.1: Discretization scheme (support structure)

The accuracy of the response increases with decreasing element length (or increasing number of elements). This will, however, increase the computational time. Thus, to obtain a balance between the accuracy and the computational time, the number of elements in each section must be optimised.

This is done by first dividing each part into a large number (≈ 200) of elements and finding out the natural frequencies of the system. Then, the number of elements in the system are reduced and the natural frequencies are again calculated. It is checked every time that the 1st 10 natural frequencies don't deviate by more than 1 %. Doing these iterations leads to the number of elements in each section as shown in [Table 6.1](#).

Table 6.1: Number of elements in each section

Section	Elements
①	15
②	3
③	3
④	3
⑤	10

This gives a total of 34 elements (35 nodes) and since each node has 5 DOF (2 translations and 3 rotations), the total DOF become 175. The last node is, however, assumed to be fixed with respect to the yaw axis ($\theta_z = 0$), so that DOF has to be eliminated. This results in mass and stiffness matrices of order 174×174 (instead of 175×175) and force

vector of order 174×1 . The **odd** entries in the force vector take up the forces and the **even** entries take up the moments acting on the model.

The FEM model is arranged such that the 1st 70 DOF are for the side-side (X-Z) plane motions, the next 70 are for the fore-aft (Y-Z) plane motions and the last 35 (34 after eliminating the last DOF) are for the yaw motions.

The nodal points of application of various forces are tabulated in [Table 6.2](#) and shown in [Figure 6.2](#). The positions where all the three forces are placed in the force vector are shown in [Table 6.3](#).

Table 6.2: Forces and node numbers

	Forces	Nodes
Wind loads		1-19
Wave loads		19-25
Spring forces		25-35

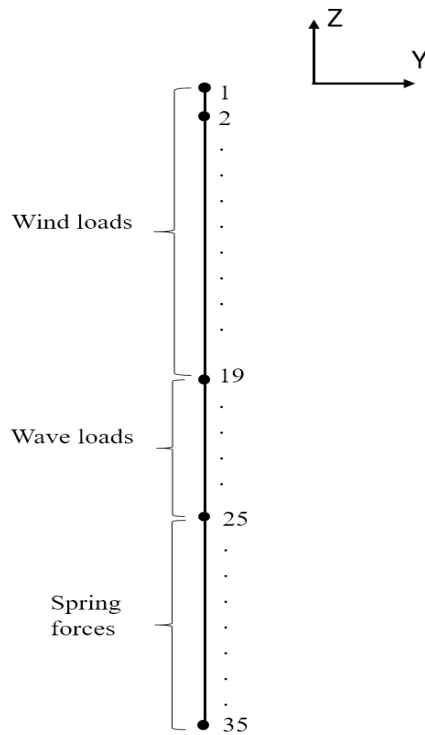


Figure 6.2: Forces and nodes

Table 6.3: Position of forces and moments in the force vector

	X-Z plane		Y-Z plane		Yaw axis	
	Forces	Moments	Forces	Moments	Forces	Moments
Aerodynamic	1,3,5...37	2	71,73...107	72	-	141
Hydrodynamic	37,39,41...49	-	107,109...119	-	-	-
Spring	49,51,53...69	-	119,121...139	-	-	-

6.3 Solution in time domain

The equation of motion for the FEM model under the action of external forces can be written as

$$[M_{sys}] \ddot{\vec{X}} + [C_{sys}] \dot{\vec{X}} + [K_{sys}] \vec{X} = \{ \vec{F}_{sys} \} \quad (6.1)$$

The solution of [Equation 6.1](#) can be obtained using the state space formulation as follows. The acceleration vector of the system can be obtained using [Equation 6.2](#).

$$\ddot{\vec{X}} = [M_{sys}]^{-1} \left(-[K_{sys}] \vec{X} - [C_{sys}] \dot{\vec{X}} + \{ \vec{F}_{sys} \} \right) \quad (6.2)$$

If the initial conditions i.e. $\vec{X}_{t=0}$ and $\dot{\vec{X}}_{t=0}$ are known, then the value of $\ddot{\vec{X}}_{t=0}$ can be determined. The velocity and acceleration vectors can then be integrated in time (using MATLAB's ODE solvers) to obtain displacement and velocity vectors as demonstrated by [Equation 6.3](#).

$$\begin{Bmatrix} \vec{X} \\ \dot{\vec{X}} \\ \ddot{\vec{X}} \end{Bmatrix} \xrightarrow{\int} \begin{Bmatrix} \vec{X} \\ \dot{\vec{X}} \end{Bmatrix} \quad (6.3)$$

In this study, however, system damping is neglected and only the damping effects coming from the external aerodynamic and hydrodynamic forces are considered. Thus the term $[C_{sys}] \dot{\vec{X}}$ is not considered.

6.4 An example

Consider a simplified example of an OWT as shown in [Figure 6.3](#). In this example, bending is considered only in one plane (side-side or X-Z). Also, it is assumed that the mass (m_{rotor}) and the rotary inertia (J_{rotor}) of the rotor and nacelle assembly is concentrated at the top most node. The added mass of water (m_{added}) is assumed to be concentrated on the second node of the tower.

The OWT is divided into 3 beam elements thus having 4 nodes. Each node has 2 DOF ($v_i, \theta_{i=1\dots 4}$). The mass and stiffness matrices of the system are of the order 8×8 .

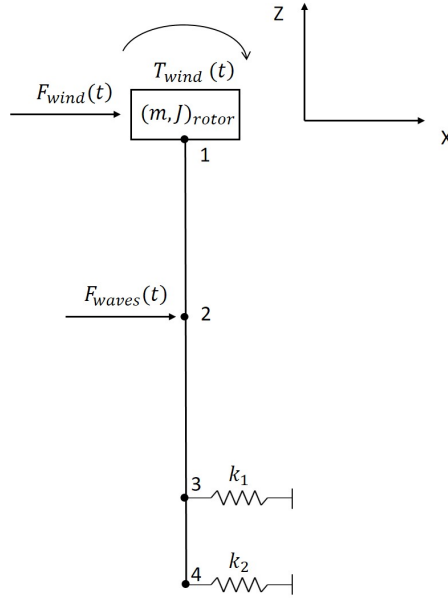


Figure 6.3: Simplified model of an OWT

The equation of motion for such a system as depicted in Figure 6.3 will then be

$$\begin{aligned}
 & \begin{bmatrix} A_1 & B_1 & C_1 & D_1 & 0 & 0 & 0 & 0 \\ A_2 & B_2 & C_2 & D_2 & 0 & 0 & 0 & 0 \\ A_3 & B_3 & C_3 & D_3 & E_1 & F_1 & 0 & 0 \\ A_4 & B_4 & C_4 & D_4 & E_2 & F_2 & 0 & 0 \\ 0 & 0 & C_5 & D_5 & E_3 & F_3 & G_1 & H_1 \\ 0 & 0 & C_6 & D_6 & E_4 & F_4 & G_2 & H_2 \\ 0 & 0 & 0 & 0 & E_5 & F_5 & G_3 & H_3 \\ 0 & 0 & 0 & 0 & E_6 & F_6 & G_4 & H_4 \end{bmatrix} \begin{Bmatrix} \ddot{v}_1 \\ \ddot{\theta}_1 \\ \ddot{v}_2 \\ \ddot{\theta}_2 \\ \ddot{v}_3 \\ \ddot{\theta}_3 \\ \ddot{v}_4 \\ \ddot{\theta}_4 \end{Bmatrix} \\
 + & \begin{bmatrix} a_1 & b_1 & c_1 & d_1 & 0 & 0 & 0 & 0 \\ a_2 & b_2 & c_2 & d_2 & 0 & 0 & 0 & 0 \\ a_3 & b_3 & c_3 & d_3 & e_1 & f_1 & 0 & 0 \\ a_4 & b_4 & c_4 & d_4 & e_2 & f_2 & 0 & 0 \\ 0 & 0 & c_5 & d_5 & e_3 & f_3 & g_1 & h_1 \\ 0 & 0 & c_6 & d_6 & e_4 & f_4 & g_2 & h_2 \\ 0 & 0 & 0 & 0 & e_5 & f_5 & g_3 & h_3 \\ 0 & 0 & 0 & 0 & e_6 & f_6 & g_4 & h_4 \end{bmatrix} \begin{Bmatrix} v_1 \\ \theta_1 \\ v_2 \\ \theta_2 \\ v_3 \\ \theta_3 \\ v_4 \\ \theta_4 \end{Bmatrix} = \begin{Bmatrix} F_{\text{wind}}(t) - m_{\text{rotor}}\ddot{v}_1 \\ T_{\text{wind}}(t) - J_{\text{rotor}}\ddot{\theta}_1 \\ F_{\text{waves}}(t) - m_{\text{added}}\ddot{v}_3 \\ 0 \\ -k_1 v_3 \\ 0 \\ -k_2 v_4 \\ 0 \end{Bmatrix}
 \end{aligned}$$

The terms in the force vector can be transferred on the left hand side of the equation and added to the respective places in the mass matrices. So finally the matrices become

$$\begin{bmatrix} A_1 + m_{\text{rotor}} & B_1 & C_1 & D_1 & 0 & 0 & 0 & 0 \\ A_2 & B_2 + J_{\text{rotor}} & C_2 & D_2 & 0 & 0 & 0 & 0 \\ A_3 & B_3 & C_3 + m_{\text{added}} & D_3 & E_1 & F_1 & 0 & 0 \\ A_4 & B_4 & C_4 & D_4 & E_2 & F_2 & 0 & 0 \\ 0 & 0 & C_5 & D_5 & E_3 & F_3 & G_1 & H_1 \\ 0 & 0 & C_6 & D_6 & E_4 & F_4 & G_2 & H_2 \\ 0 & 0 & 0 & 0 & E_5 & F_5 & G_3 & H_3 \\ 0 & 0 & 0 & 0 & E_6 & F_6 & G_4 & H_4 \end{bmatrix} \begin{Bmatrix} \ddot{v}_1 \\ \ddot{\theta}_1 \\ \ddot{v}_2 \\ \ddot{\theta}_2 \\ \ddot{v}_3 \\ \ddot{\theta}_3 \\ \ddot{v}_4 \\ \ddot{\theta}_4 \end{Bmatrix}$$

$$+ \begin{bmatrix} a_1 & b_1 & c_1 & d_1 & 0 & 0 & 0 & 0 \\ a_2 & b_2 & c_2 & d_2 & 0 & 0 & 0 & 0 \\ a_3 & b_3 & c_3 & d_3 & e_1 & f_1 & 0 & 0 \\ a_4 & b_4 & c_4 & d_4 & e_2 & f_2 & 0 & 0 \\ 0 & 0 & c_5 & d_5 & e_3 & f_3 & g_1 & h_1 \\ 0 & 0 & c_6 & d_6 & e_4 & f_4 & g_2 & h_2 \\ 0 & 0 & 0 & 0 & e_5 & f_5 & g_3 & h_3 \\ 0 & 0 & 0 & 0 & e_6 & f_6 & g_4 & h_4 \end{bmatrix} \begin{Bmatrix} v_1 \\ \theta_1 \\ v_2 \\ \theta_2 \\ v_3 \\ \theta_3 \\ v_4 \\ \theta_4 \end{Bmatrix} = \begin{Bmatrix} F_{wind}(t) \\ T_{wind}(t) \\ F_{waves}(t) \\ 0 \\ -k_1 v_3 \\ 0 \\ -k_2 v_4 \\ 0 \end{Bmatrix}$$

The system of equations can be solved in time domain as described in [section 6.3](#). Note that the natural frequencies of the system can be found by solving the eigenvalue problem represented by [Equation 6.4](#). The mode shape vectors for the corresponding frequencies are given by the eigenvectors of the [Equation 6.4](#).

$$\left([K_{sys}] - \omega_n^2 [M_{sys}] \right) X = 0 \quad (6.4)$$

The number of natural frequencies obtained are equal to the number of DOF in the system. The example shows how a system of equations for motions in X-Z plane can be solved. Similar approach can be used to solve a system for motions in 2 planes.

This approach is, however, computationally very expensive. Therefore, some technique is required in order to reduce the computational time. This leads to the introduction of *mode displacement method*.

6.5 Mode displacement method (Modal Reduction)

The equation of motion for an n degree of freedom (DOF) system under the action of external forces is given by [Equation 6.5](#).

$$[M_{sys}]_{n \times n} \ddot{X}_{n \times 1} + [K_{sys}]_{n \times n} X_{n \times 1} = \{\vec{F}_{sys}\}_{n \times 1} \quad (6.5)$$

The force vector $\{\vec{F}_{sys}\}$ is a function of the acceleration, velocity, displacement and time i.e.

$$\{\vec{F}_{sys}\} = f(\ddot{X}, \dot{X}, X, t)$$

The system of equations represents n coupled 2^{nd} order differential equations and it has n natural frequencies and n corresponding mode shapes. If n is large (174 in this case), however, the computation time required to solve these equations is very long and thus the problem becomes computationally expensive. This problem can be overcome by *mode displacement method* which offers the following advantages.

1. It diagonalises (and thus de-couples) the mass and stiffness matrices of the system.
2. It reduces the order of the mass and stiffness matrices thus reducing the number of equations being solved.

These two points can be explained as follows.

If, instead of n modes, only the 1^{st} r dominant modes are selected ($r < n$) for calculating the response, significant computational resources can be saved.

According to the expansion theorem, the solution vector of [Equation 6.5](#) can be expressed by a linear combination of the normal modes as

$$\vec{X}(t) = q_1(t) \vec{x}^{(1)} + q_2(t) \vec{x}^{(2)} + \dots + q_n(t) \vec{x}^{(n)} \quad (6.6)$$

Here

$q_i(t)$ and $\vec{x}^{(i)}$ ($i = 1 \dots n$) are the generalised time dependent coordinates (also known as the principal coordinates) and the 1^{st} n mode shape vectors of the system respectively.

By defining a modal matrix $[x_{\text{mod}}]_{n \times n}$ in which j^{th} column is the vector $\vec{x}^{(j)}$ (j^{th} modal vector), equation [Equation 6.6](#) can be written in as

$$\vec{X}(t)_{n \times n} = [x_{\text{mod}}]_{n \times n} \vec{q}(t)_{n \times 1} \quad (6.7)$$

Here

$$\vec{q}(t)_{n \times 1} = \begin{Bmatrix} q_1(t) \\ q_2(t) \\ \vdots \\ q_n(t) \end{Bmatrix} \quad (6.8)$$

As $[x_{\text{mod}}]_{n \times n}$ is not a function of time, the velocity and the acceleration vector of the system can be expressed as

$$\vec{\dot{X}}(t)_{n \times n} = [x_{\text{mod}}]_{n \times n} \vec{\dot{q}}(t)_{n \times 1} \quad (6.9a)$$

$$\vec{\ddot{X}}(t)_{n \times n} = [x_{\text{mod}}]_{n \times n} \vec{\ddot{q}}(t)_{n \times 1} \quad (6.9b)$$

Substituting equations [Equation 6.7](#) and [Equation 6.9b](#) into equation [Equation 6.5](#), we obtain

$$[M_{\text{sys}}]_{n \times n} [x_{\text{mod}}]_{n \times n} \vec{q}(t)_{n \times 1} + [K_{\text{sys}}]_{n \times n} [x_{\text{mod}}]_{n \times n} \vec{q}(t)_{n \times 1} = \{ \vec{F} \}_{n \times 1} \quad (6.10)$$

With this substitution, $\{ \vec{F} \}$ which was earlier a function of $(\ddot{X}, \dot{X}, X, t)$ now becomes a function of $(\ddot{q}, \dot{q}, q, t)$. Multiplying both sides by the transpose of the modal vector $[x_{\text{mod}}]_{n \times n}$, we obtain

$$\begin{aligned} & [x_{\text{mod}}]_{n \times n}^T [M_{\text{sys}}]_{n \times n} [x_{\text{mod}}]_{n \times n} \vec{q}(t)_{n \times 1} \\ & \quad + [x_{\text{mod}}]_{n \times n}^T [K_{\text{sys}}]_{n \times n} [x_{\text{mod}}]_{n \times n} \vec{q}(t)_{n \times 1} \\ & = [x_{\text{mod}}]_{n \times n}^T \{ \vec{F} \}_{n \times 1} \end{aligned} \quad (6.11)$$

If, however, only the first r modes are selected instead of n , [Equation 6.11](#) becomes [\[23\]](#)

$$\begin{aligned} & [x_{\text{mod}}]_{r \times n}^T [M_{\text{sys}}]_{n \times n} [x_{\text{mod}}]_{n \times r} \vec{q}(t)_{r \times 1} \\ & \quad + [x_{\text{mod}}]_{r \times n}^T [K_{\text{sys}}]_{n \times n} [x_{\text{mod}}]_{n \times r} \vec{q}(t)_{r \times 1} \\ & \approx [x_{\text{mod}}]_{r \times n}^T \{ \vec{F} \}_{n \times 1} \end{aligned} \quad (6.12)$$

Which on solving yields equation 6.13.

$$\left[M_{diag} \right]_{r \times r} \vec{\ddot{q}}(t)_{r \times 1} + \left[K_{diag} \right]_{r \times r} \vec{q}(t)_{r \times 1} \approx \left\{ \vec{f} \right\}_{r \times 1} \quad (6.13)$$

The following two points are to be noted

1. The right hand side of [Equation 6.12](#) is an approximation because instead of n modes, only r modes have been used. In the case of a continuous system when $n \rightarrow \infty$, this error is further increased.
2. The matrices $\left[M_{diag} \right]_{r \times r}$ and $\left[K_{diag} \right]_{r \times r}$ ([Equation 6.13](#)) are diagonal matrices (using orthogonality) whose i^{th} element represent the generalised mass and stiffness coefficient for the respective mode.

The mass and stiffness matrices are thus reduced to diagonal matrices leading to a system of $r \times r$ instead of $n \times n$ **uncoupled** equations on the left hand side. The equations on the right hand side are, however, still coupled.

6.5.1 Initial conditions

In case of modal analysis, the initial conditions of the system have to be transformed in terms of the natural coordinates. This can be done using [Equation 6.14](#) [8].

$$\left\{ \begin{array}{c} \vec{\dot{q}} \\ \vec{q} \end{array} \right\} = \left[x_{mod} \right]^T \left[M_{sys} \right] \left\{ \begin{array}{c} \vec{X} \\ \vec{X} \end{array} \right\} \quad (6.14)$$

Now the question that remains is that how to select the appropriate number of modes.

6.6 Selecting the number of modes

To minimise the error in the computation and speed up the calculations, an appropriate number of modes must be selected. The frequency content and the spatial distribution of a force signal can give a good insight into selecting the number of modes that give a significant contribution in determining the response of the system. The OWT is subjected to both aerodynamic and hydrodynamic forces. In case of hydrodynamic forces, the frequency content of the signal can be extracted by ([FFT](#)) of the total hydrodynamic force signal.

In case of aerodynamic loading, the frequencies that are important are the ones that correspond to the rotational frequencies of the rotor. For this model, the minimum cut in speed and the maximum rotational speed are 6.9 and 12.1 rpm respectively [17]. This gives a 1P frequency of 0.115 Hz and 0.21 Hz. Also, the blade passing frequencies which depend upon the number of blades (3 in this case) gives 3P frequencies as 0.34 Hz and 0.63 Hz.

The frequency content (obtained by FFT) of the total hydrodynamic force ($H_s = 2$ m), the 1st two natural frequencies of the OWT and the 1P and the 3P frequencies are shown in [Figure 6.4](#). This frequency spectrum has been constructed assuming a wave sampling frequency $f_s = 5$ Hz or samples/second.

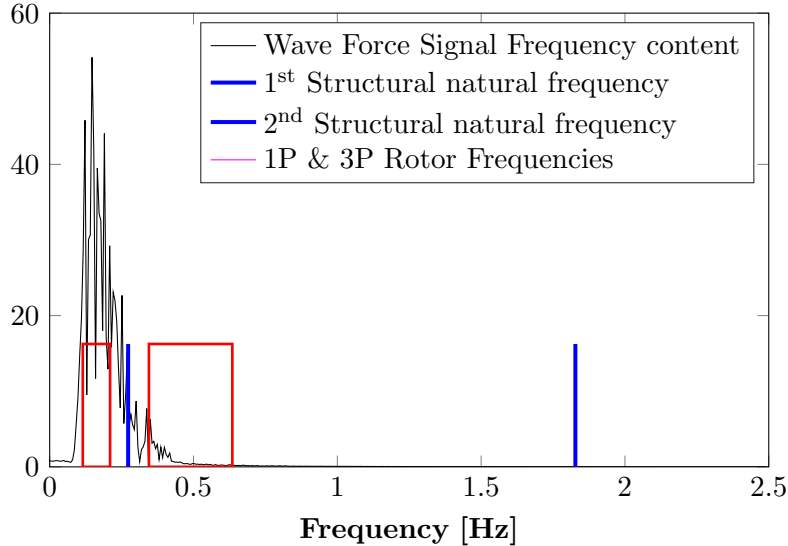


Figure 6.4: Frequency distribution

It can be seen from Figure 6.4 that only the first mode is excited. [8] suggests that the number of modes should atleast be equal to *two times* the highest frequency content in a signal for accurate response prediction of a dynamic system. In case of the OWT, the non-linearities present in the loading conditions can also excite higher modes.

So, the structural response was calculated for number of modes starting from 1 and the number of modes were increased. The results were then compared with the response of the full system. It was found that choosing 10 modes gave good agreement. The first 10 natural frequencies of the whole system in side-side (X-Z), fore-aft (Y-Z) plane and about the yaw axis are shown in Table 6.4. First 10 mode shapes for side-side (X-Z) plane are shown in Figure 6.5 and Figure 6.6.

Table 6.4: First 10 natural frequencies of the OWT [Hz]

Number	XZ plane	YZ plane	Yaw axis
1	0.27	0.27	1.92
2	1.38	1.41	15.55
3	3.13	3.43	24.94
4	6.10	6.67	40.00
5	10.01	10.30	51.98
6	14.90	15.08	67.82
7	18.39	18.45	76.55
8	23.83	23.92	95.12
9	30.17	30.23	108.32
10	37.62	37.66	121.28

The first natural frequency obtained for side-side (X-Z) and fore-aft (Y-Z) plane motions is 0.27 [Hz]. This is in close agreement with [27] which has the first natural frequency defined at 0.29 [Hz] for the mono-pile based OWT.

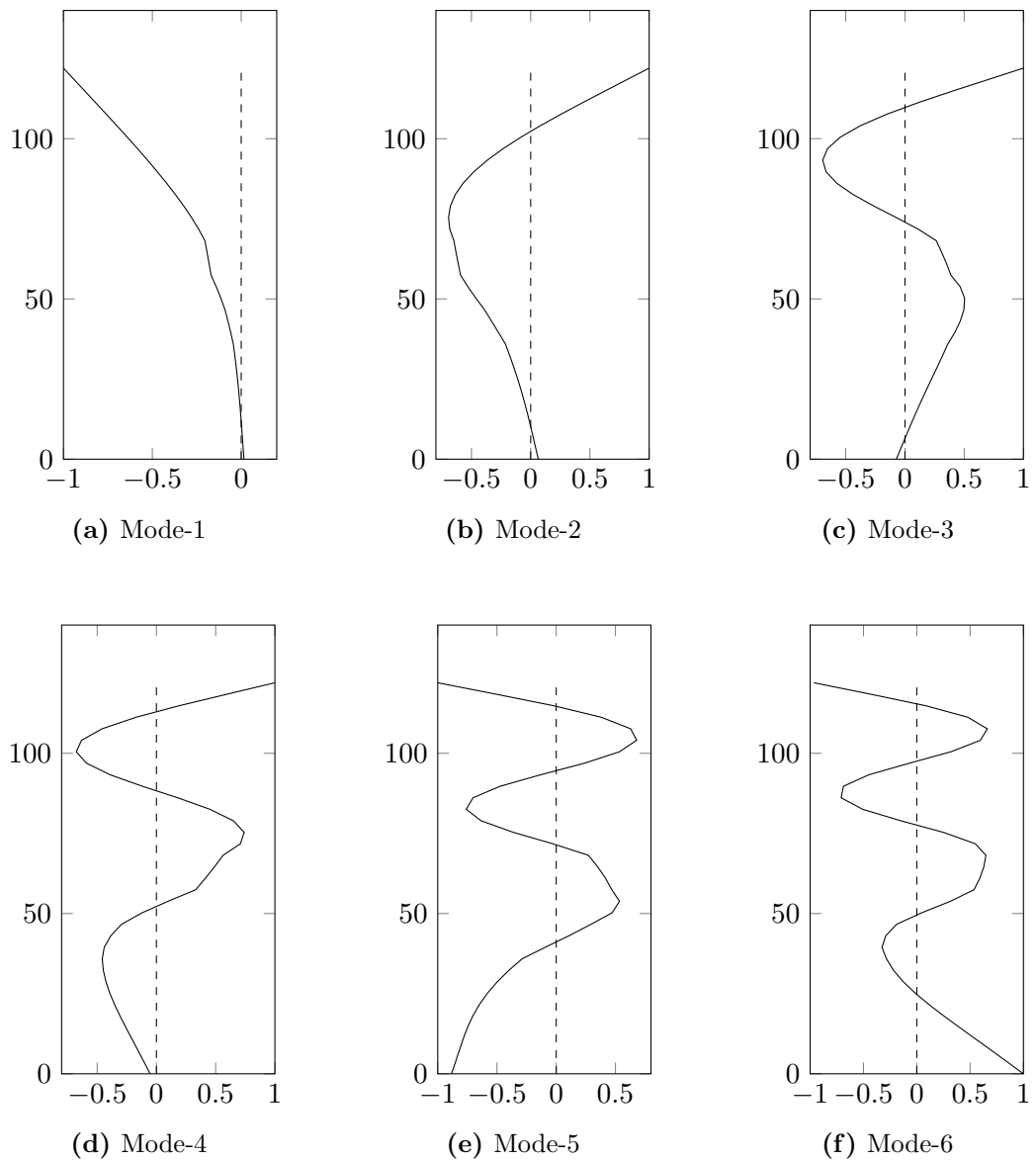


Figure 6.5: Mode shapes 1-6 (Horizontal axis-Modal displacement, Vertical axis-Height of the OWT [m])

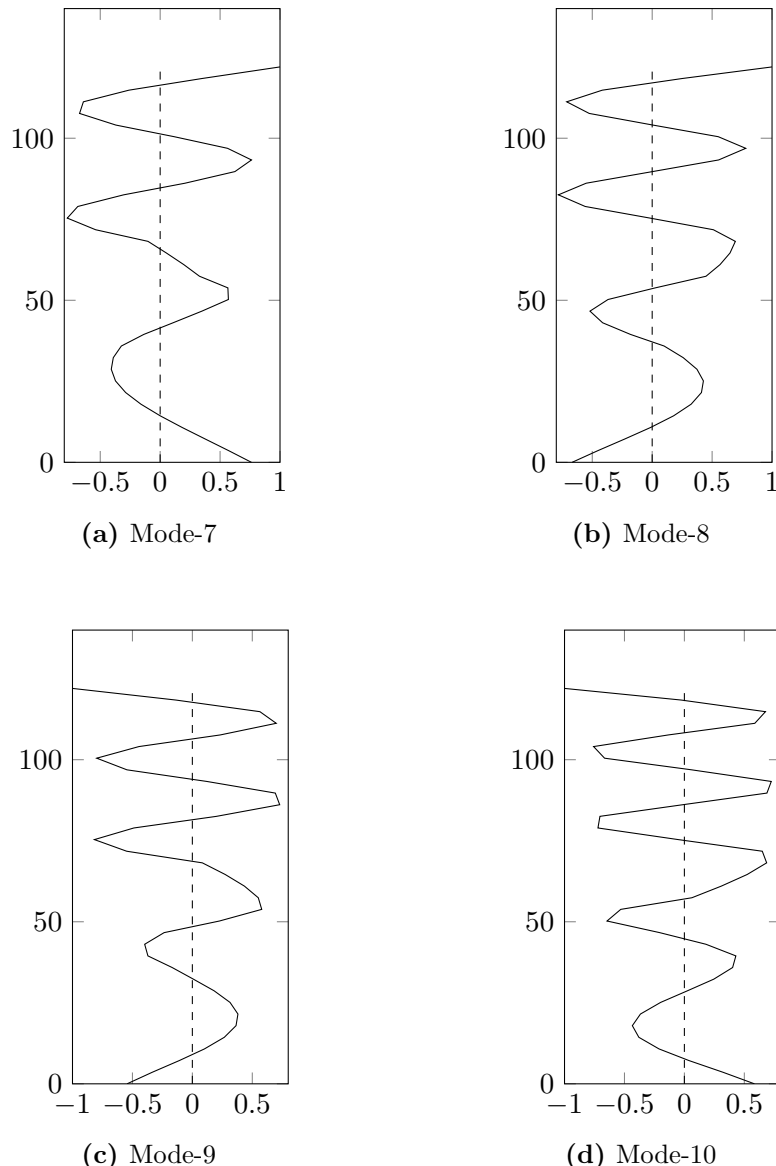


Figure 6.6: Mode shapes 7-10 (Horizontal axis-Modal displacement, Vertical axis-Height of the OWT [m])

Thus choosing 10 modes for each side-side (X-Z), fore-aft (Y-Z) plane and yaw axis gives a total of 30 modes. The equations of motions are then reduced from 175×175 to 30×30 as explained in [section 6.5](#).

Results and Discussions

7.1 Introduction

Now that the mathematical model has been defined, some load cases need to be chosen to compare both the NLIM and LIM. This chapter describes the following.

1. Basic checks to see the behaviour of both NLIM and LIM.
2. Define advanced load cases.
3. Discuss results.

7.2 Simple load case - Regular wave and constant wind

Before going to the more complicated case of turbulent wind and irregular waves, the behaviour of both the models need to be tested for simple conditions. So, both the models are subjected to a constant wind and a regular wave (Figure 7.1) and their responses are calculated. The values of the different parameters used for different load cases are tabulated in [Table 7.1](#) and the physical conditions used for both the models are tabulated in [Table 7.2](#).

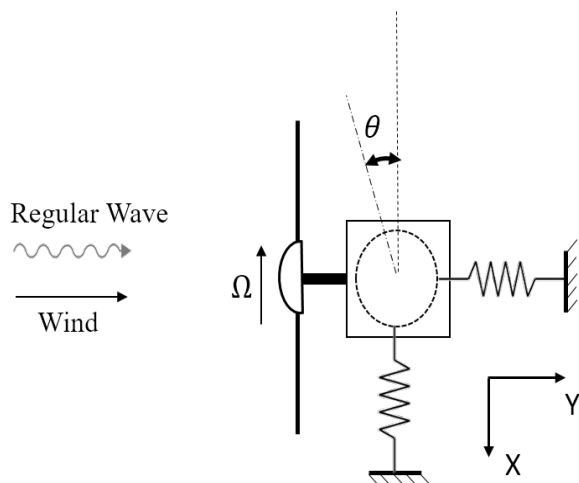


Figure 7.1: Top view-Regular wave, constant wind

Table 7.1: Parameters - (Regular wave-constant wind)

Load case	Wave			Wind			
	$\theta_{wave} [^{\circ}]$	$A_w [\text{m}]$	$\omega_w [\text{rad/s}]$	$\theta_{wind} [^{\circ}]$	$U_{wind} [\text{m/s}]$	a_{in}	$\beta_{pitch} [^{\circ}]$
1	90	1	1	90	12	0.14	3.83
2	90	1	1	90	15	0.07	10.45
3	90	1	1	90	20	0.04	17.47
4	90	1	1	90	24	0.03	22.35

Table 7.2: Physical conditions (Regular wave, constant wind)

Model type	Soil Spring		Wave Conditions		Wind Conditions		Rotor Status
	Linear	Non Linear	Structural motions Excluded	Structural motions Included	Linear	Non Linear	Working
LIM	✓		✓		✓		✓
NLIM		✓		✓		✓	✓

It must be noted that \bar{U}_{wind} defined in [Table 7.1](#) is the far field wind velocity. The wind, however, slows down near the rotor. Using an induction factor a_{in} , the wind velocity near the rotor becomes $(1-a_{in}) \bar{U}_{wind}$.

Since the response of all the load cases show similar patterns, only load case-2 is described here. Load cases 1,3 and 4 can be found in [Appendix B](#).

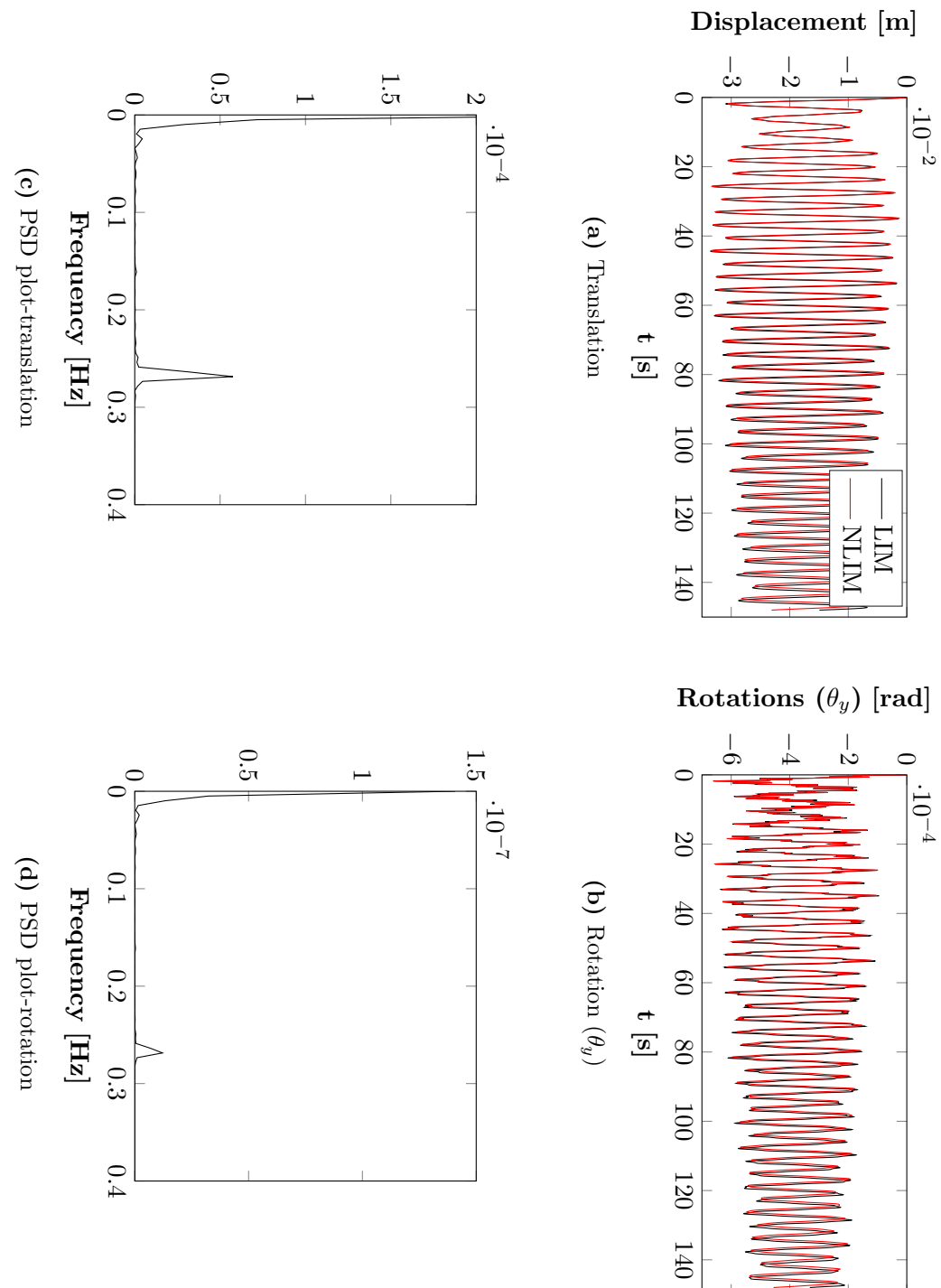


Figure 7.2: Response of the OWT in side-side (X-Z) plane

7.2.1 Discussions - Side-side (X-Z) plane motions and rotation about Y axis

The following points are to be noted for the **translatory** and **rotary** motions ([Figure 7.2](#)).

1. It takes more time for the transient response to die out indicating lower damping (as compared to fore-aft and yaw motions [subsection 7.2.2](#) and [subsection 7.2.3](#)).
2. There is a **DC offset** (a mean displacement from zero) in the time series of both rotary and translatory motions indicating a static deflection. This is also indicated in the power spectrum by the spike in the beginning of the spectrum ([Figure 7.2c](#)) and ([Figure 7.2d](#)). This implies that there must be some constant force or torque causing this deflection. To check this, the tower top is assumed fix (by applying zero displacements and rotations to the rotor model) and a steady wind of 15 m/s is applied to the rotor model. The pitch angle and the rotational speed is set at 10.45° and 12.1 rpm respectively. A constant torque of -2.8 MNm is obtained in the global Y direction ([Figure 7.3](#)). This constant torque causes the structure to lean in - X direction ([Figure 7.4](#)).

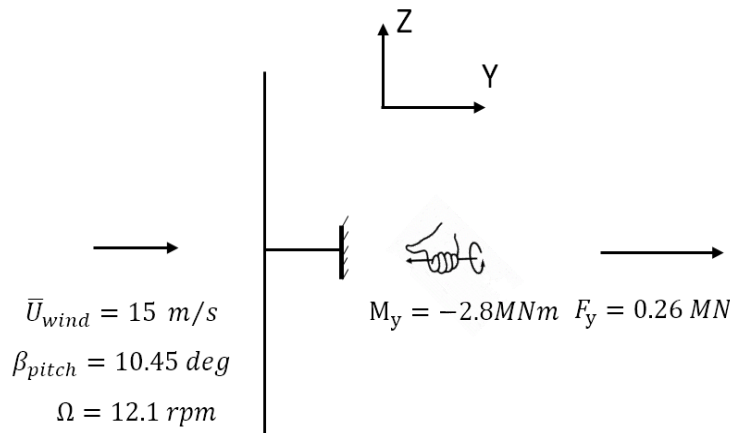


Figure 7.3: Fixed rotor subjected to constant wind

3. There appears a phase lag for both translation and rotation between the NLIM and the LIM where the NLIM seems to lead. This implies that linearising the aerodynamic forces introduces a phase lag between the LIM and the NLIM in side-side direction.
4. The power spectrum density (PSD) plot ([Figure 7.2c](#)) and ([Figure 7.2d](#)) shows a peak at the 1st natural frequency in side-side (X-Z) plane i.e. at 0.27 Hz and a (very small) peak at the incoming wave frequency of 0.16 Hz (in fore-aft or Y-Z plane) indicating that model does capture coupled behaviour.
5. A strange behaviour is seen at a wind speed of 24 m/s. The static rotor test was done at that wind speed and the direction of moment is still found in - Y direction. However, the steady state deflection of the structure is found + X direction which should have deflected in - X direction as in other load cases ([Figure B.1c](#)). To investigate it, pitch settings were varied from 22.35 ° to 40 ° but the results were same.

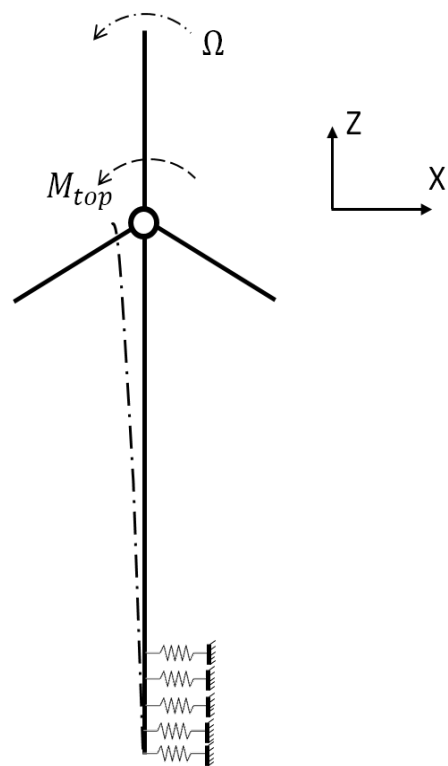


Figure 7.4: Tower top deflection due to constant wind in side-side (X-Z) plane

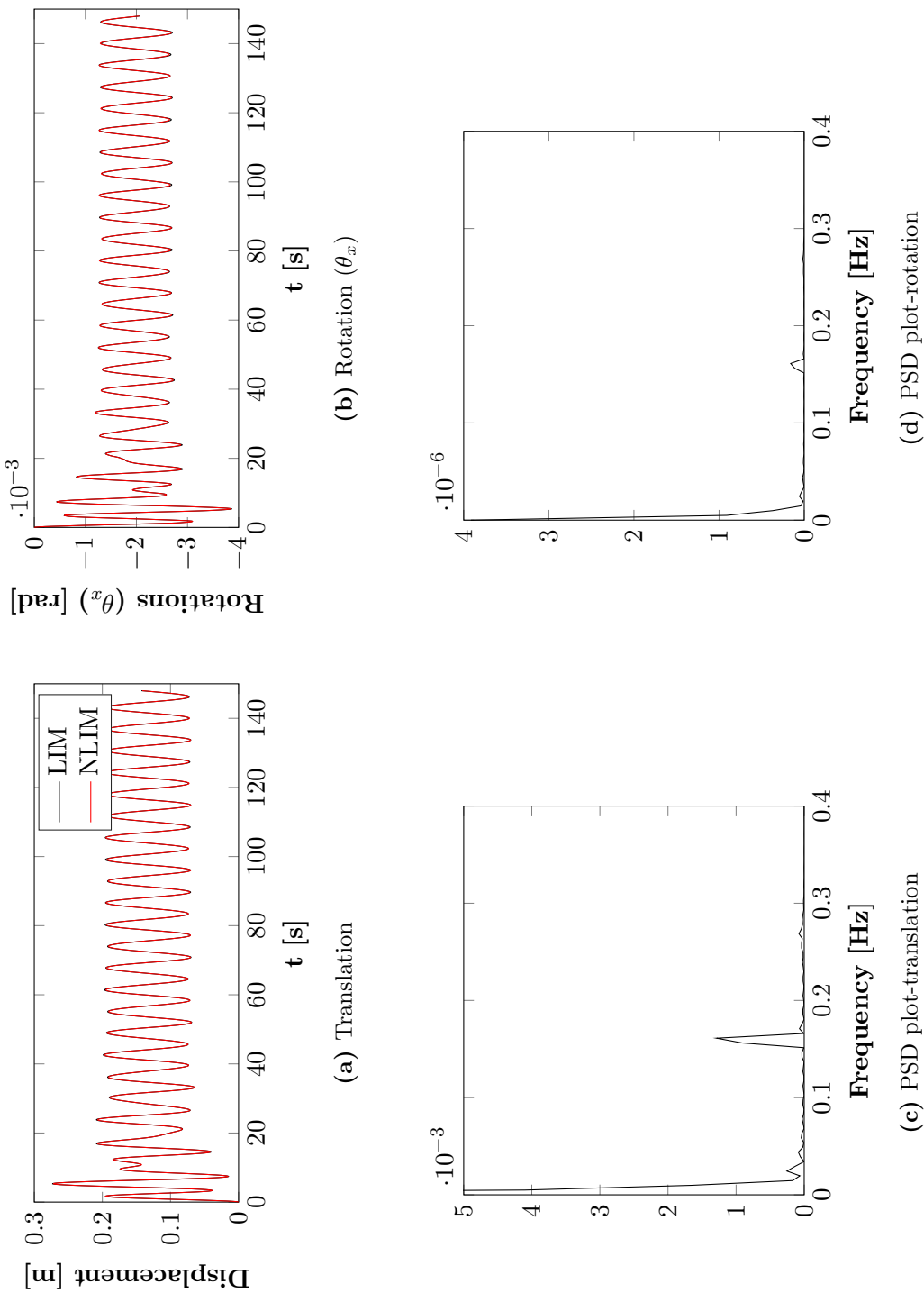


Figure 7.5: Response of the OWT in fore-aft (Y-Z) plane

7.2.2 Discussions - Fore-aft (Y-Z) plane motions and rotation about X axis

The following points are to be noted about the **translatory** and **rotary** motions [Figure 7.5](#)

1. It takes smaller time for the transient response to die out indicating higher damping (as compared to the side-side motions [subsection 7.2.1](#)).
2. There is a DC offset in both the translatory and rotary motions indicating a static deflection. This is also indicated in the power spectrum by the impulse in the beginning of the spectrum ([Figure 7.5c](#)) and ([Figure 7.5d](#)). This implies that there must be some steady force or torque causing this deflection. To check this, the tower top is assumed fix (by applying zero displacements and rotations to the rotor model) and a steady wind of 15 m/s is applied to the rotor model. The pitch angle and the rotational speed is set at 10.45° and 12.1 rpm respectively. A steady force of +0.26 MN is obtained in the global Y direction ([Figure 7.3](#)). This constant force causes the structure to lean to the + Y direction ([Figure 7.6](#)).
3. The response of the LIM is in good agreement with that of the NLIM indicating that linearisation doesn't significantly influence the response in fore-aft direction.
4. The incoming wave frequency of 0.16 Hz and the 1st natural frequency of the structure i.e. 0.27 Hz is clearly visible in the PSD plot [Figure 7.5c](#) and [Figure 7.5d](#).

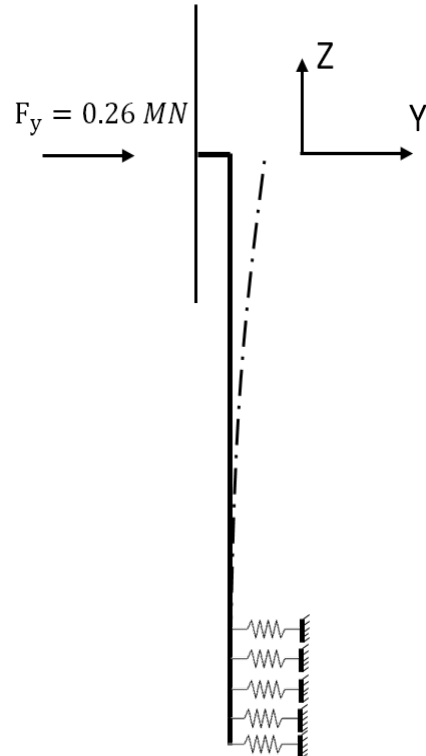


Figure 7.6: Tower top deflection due to constant wind in fore-aft (Y-Z) plane

7.2.3 Discussions - Yaw motions

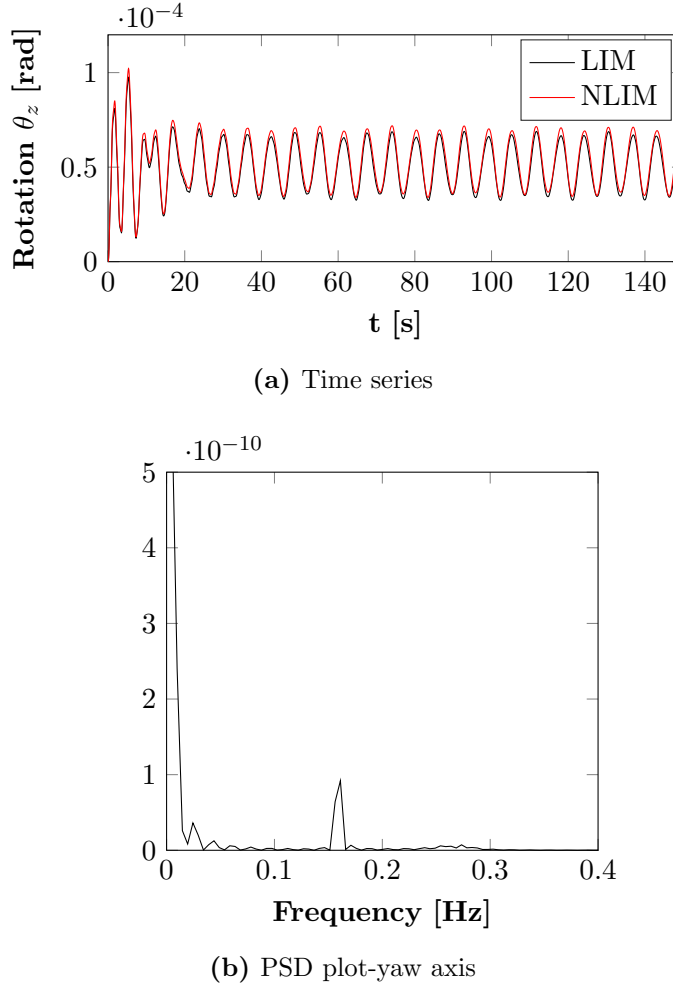


Figure 7.7: Rotations about the yaw (θ_z) axis

The following points are to be noted for the yaw motions (Figure 7.7).

1. It takes smaller time for the yaw transient response to die out indicating higher damping (as compared to side-side motions subsection 7.2.1).
2. A DC offset is also present for the yaw motions (also indicated by a spike in the beginning of Figure 7.7b). This implies that there must be a constant torque that causes this constant rotation. If the tower top is assumed fixed and un-deformed (all DOF set to zero), then the net torque about the yaw axis resulting from the aerodynamic forces on the rotor blades (due to head on wind) is zero due to symmetry of the rotor. However, if the motions (and the deformations) of the tower top are accounted, then a ***strong coupling*** seems to exist between the rotations about global X axis (θ_x) and the yaw motions (θ_z). To check this, the tower top is assumed fixed (by applying zero displacements and rotations to the rotor model) except θ_x which is set to -0.002 radians. The wind speed, rotational velocity and pitch angle are set at 15 m/s, 12.1 rpm and 10.45° respectively. A constant moment of -1.65×10^5 Nm is obtained in the Z direction (Figure 7.8). Since a non-zero offset exists for θ_x (due to normal force in + Y direction), this offset gives a constant torque about the Z axis, giving a non-zero offset for θ_z .

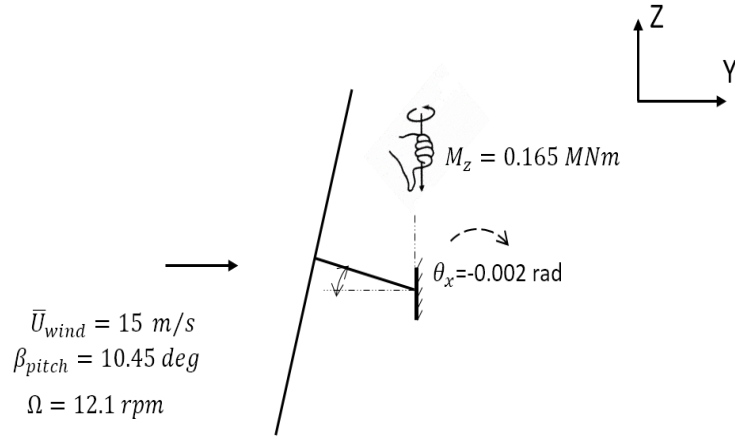


Figure 7.8: Steady yaw moment resulting from a steady rotation about the X axis

3. As the wind and wave loads are applied in the fore-aft (Y-Z) plane, frequencies of 0.16 and 0.27 Hz in the PSD plots of the yaw motions indicate that the model does capture the coupled behaviour.
4. The yaw motions predicted by the LIM agree well with that of the NLIM. Only the DC offset for NLIM is slightly higher than that of the LIM.

These observations suggest that the model agrees well with the expected behaviour and can be subjected to advanced load cases.

7.3 Advanced load cases

Now both the NLIM and LIM have to be compared with respect to the different non-linearities presented by the three environmental conditions. So the following test cases are decided upon.

1. Integrated load case : This load case considers the non-linearities present in the three environmental conditions combined together.
2. Wind : This load case considers the non-linearities present only in the wind loads and ignores those present in the soil and waves.
3. Waves : This load case considers the non-linearities present only in the wave loads and ignores those present in the wind and soil.
4. Soil : This load case considers the non-linearities present only in the soil and ignores those present in the wind and waves.

These load cases are presented and explained in the following sub-sections.

7.3.1 Integrated load case

In this load case, the non-linearities in the three environmental conditions are considered all together. Moreover, the mis-alignments between the wind and the waves are also considered. Since the waves are produced by the winds, increased misalignments are observed at lower wind speeds (and lower H_s). At higher wind speeds (and higher H_s), the wind and waves tend to align themselves. Based on this reasoning the load cases depicted in

Figure 7.9 are decided. The parameters for different load cases and the physical conditions used for both NLIM and LIM are tabulated in [Table 7.3](#) and [Table 7.4](#) respectively.

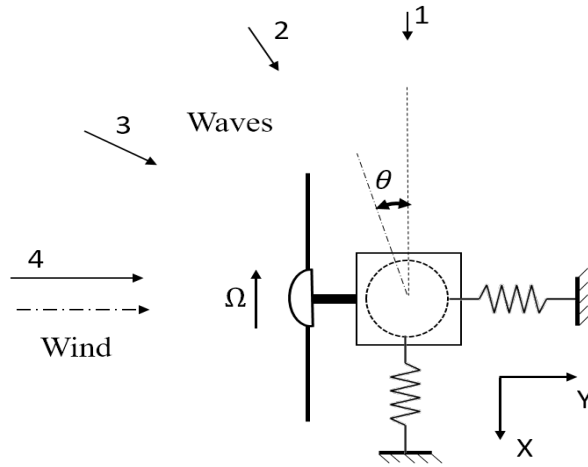


Figure 7.9: Top view-Integrated model

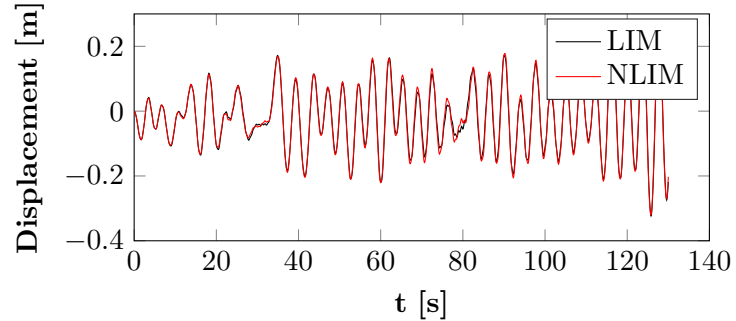
Table 7.3: Parameters (Integrated model)

Load Case	Waves		Wind			
	θ_{wave}	H_s [m]	θ_{wind} [°]	U_{wind} [m/s]	a_{in}	β_{pitch} [°]
1	0	2	90	12	0.14	3.83
2	30	4	90	15	0.07	10.45
3	60	6	90	20	0.04	17.47
4	90	8	90	24	0.03	22.35

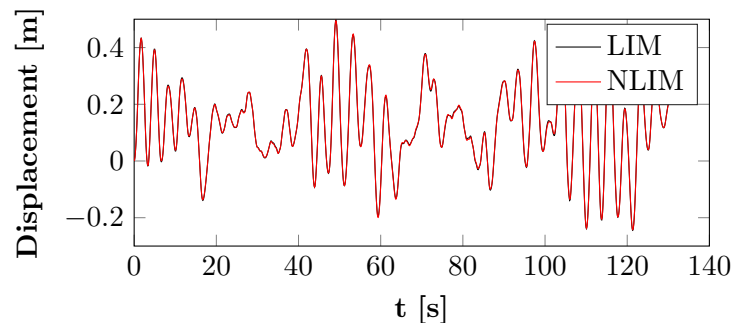
Table 7.4: Physical conditions (Integrated model)

Model type	Soil Spring		Wave Conditions		Wind Conditions		Rotor Status
	Linear	Non Linear	Structural motions Excluded	Structural motions Included	Linear	Non Linear	
LIM	✓		✓		✓		✓
NLIM		✓		✓		✓	✓

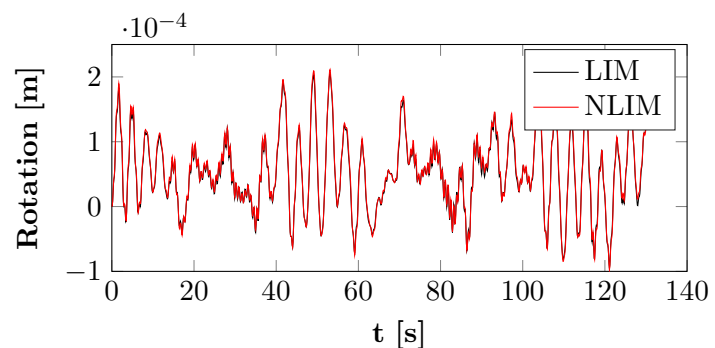
The results of load case-2 are depicted in [Figure 7.10](#) for motion in side-side (X-Z) plane, fore-aft (Y-Z) plane and about the yaw axis. The power spectral density (PSD) of the responses and load spectrum are depicted in [Figure 7.11](#). The PSD plots drawn to log normal scale are depicted in [Figure 7.12](#). The results of all the load cases follow the similar pattern, so only load case-2 is described here. The results of load cases 1,3 and 4 can be found in [Appendix C](#).



(a) Side-side (X-Z) plane motions



(b) Fore-aft (Y-Z) plane motions



(c) Yaw motions

Figure 7.10: Response of the OWT subjected to Load case-2 (Integrated model)

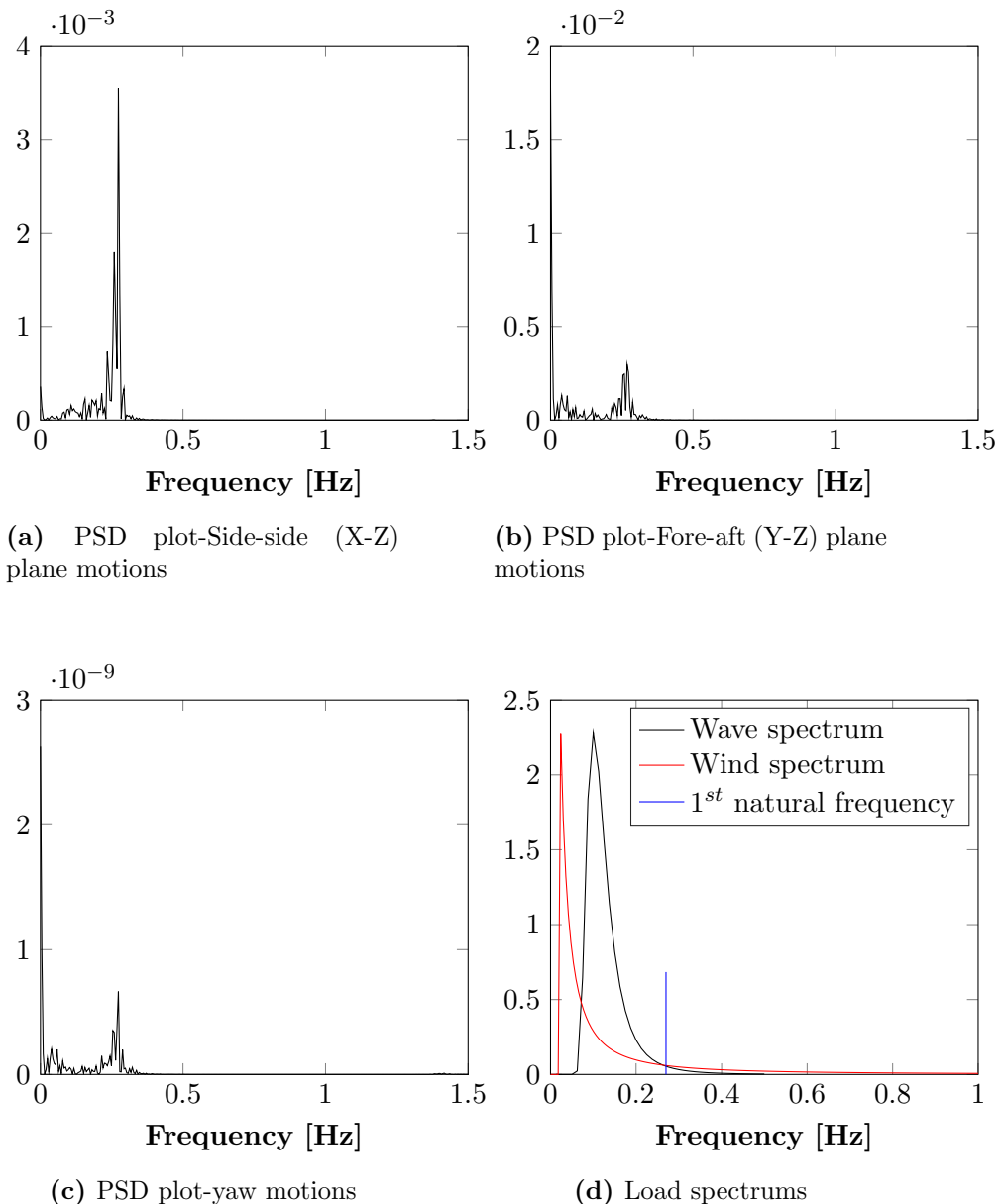


Figure 7.11: Frequency contents of load and responses (Load case-2, Integrated model)

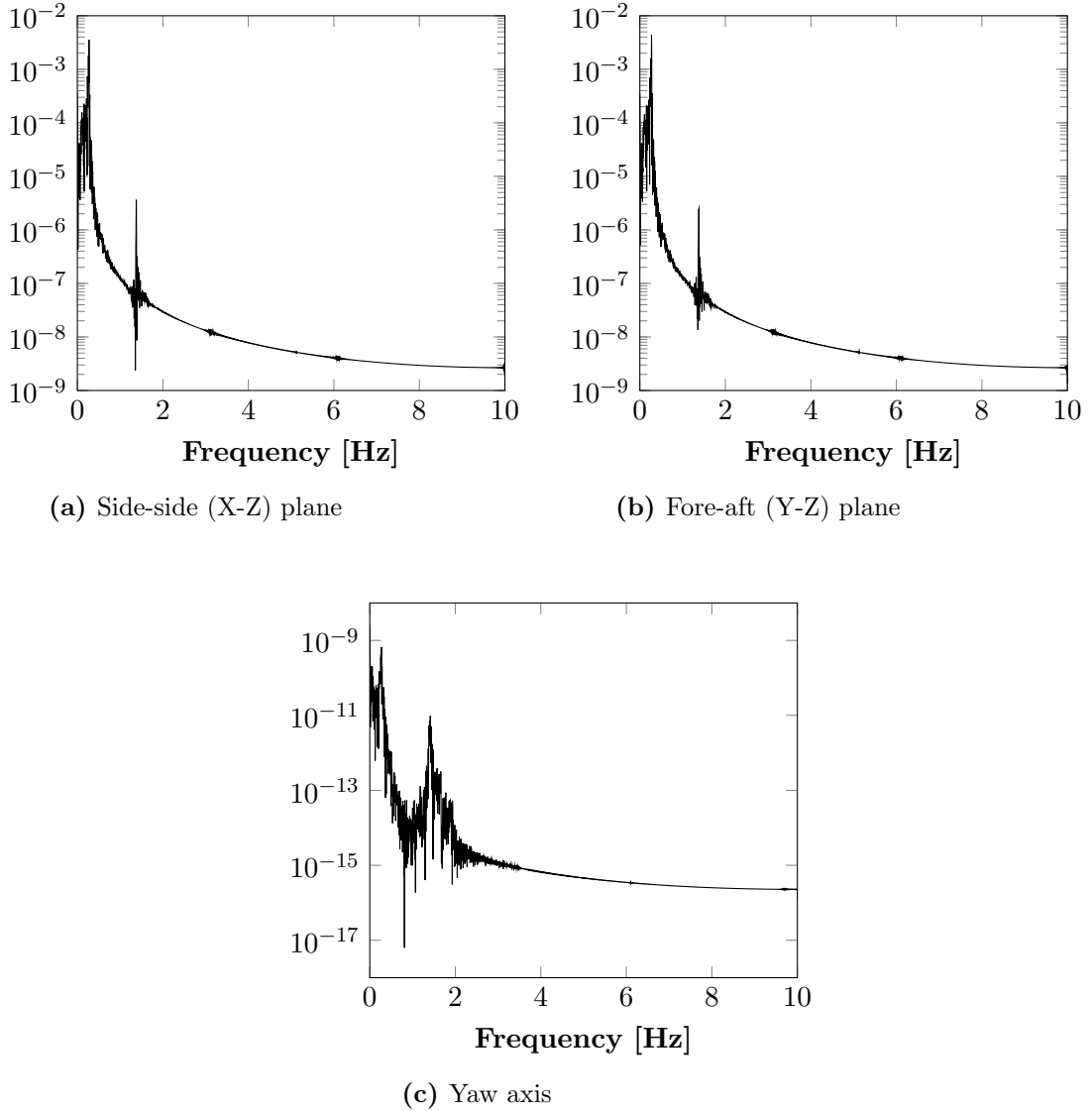


Figure 7.12: PSD plots drawn to semi-log normal scale

Figure 7.10 shows that the LIM and the NLIM are in close agreement with each other. The following points are to be noted.

1. The static deflections are present in all the DOF PSD plots (Figure 7.11).
2. For the motions in side-side (X-Z) plane, high frequency ripples can be observed in the time series (Figure 7.10a), implying that a higher mode is excited. A frequency of 1.38 Hz is clearly visible in the Figure 7.12a which corresponds to the 2nd natural frequency in side-side (X-Z) plane.
3. For the motions in fore-aft (Y-Z) plane, the high frequency ripples are not observed in the time series (Figure 7.10b), implying that contributions from higher modes are not significant. The peak at the 2nd natural frequency in Y-Z plane i.e. 1.41 Hz is very small (Figure 7.12b).
4. For the motions about the yaw axis (θ_z), the high frequency ripples are more dominant in the time series (Figure 7.10c). A close inspection reveals that this contribution comes from a frequency of 1.41 Hz which is the 2nd natural frequency for motions in fore-aft (Y-Z) plane (Figure 7.12c). This is in line with the discussions in

subsection 7.2.3, confirming that a strong coupling exists between fore-aft (rotations about X axis, θ_x) and yaw motions.

5. Even though the energy of the frequencies in the wind and the wave spectra near their tails is low (Figure 7.11d)¹, their contribution to the dynamic response of the tower top is considerably large as they are located near the 1st (and 2nd) natural frequency of the OWT structure making the transfer of energy between the structure and the external forces much easier.
6. For frequencies to the left of the 1st natural frequency, even though their energy content is high, the transfer of energy between the structure and the external forces is not very efficient and thus their contribution to the dynamic response of the OWT structure is not very significant.

¹It is to be noted that the values on the Y axis are not drawn to scale

7.3.2 Load case - Wind

In this load case, only the non-linearities in the wind loading are considered. Soil is modelled as linear springs and wave loads are absent. The situation is depicted in Figure 7.13 and the parameters and the physical conditions used for this load case are tabulated in Table 7.5 and Table 7.5. The results of load case-1 are depicted in Figure 7.14a, Figure 7.14b and Figure 7.14c for motion in side-side (X-Z) plane, fore-aft (Y-Z) plane and about the yaw axis respectively. The results of all the load cases follow the similar pattern, so only load case-1 is described here. The results of load cases 2,3 and 4 can be found in Appendix D.

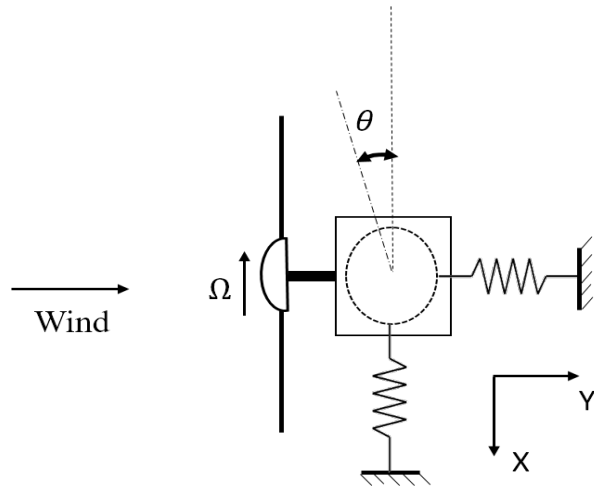


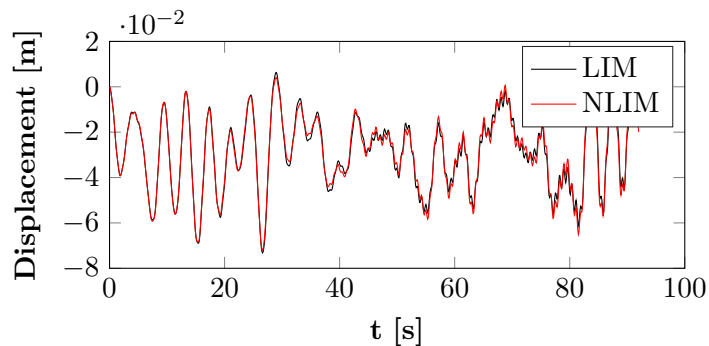
Figure 7.13: Top view-(Wind model)

Table 7.5: Parameters (Wind)

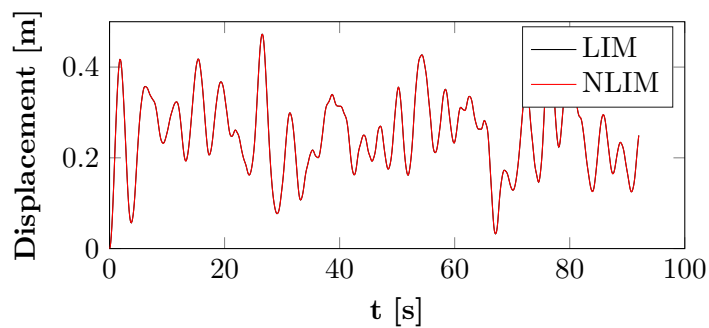
Load Case	θ_{wind} [°]	\bar{U}_{wind} [m/s]	a_{in}	β_{pitch} [°]
1	90	12	0.14	3.83
2	90	15	0.07	10.45
3	90	20	0.04	17.47
4	90	24	0.03	22.35

Table 7.6: Physical Conditions (Wind)

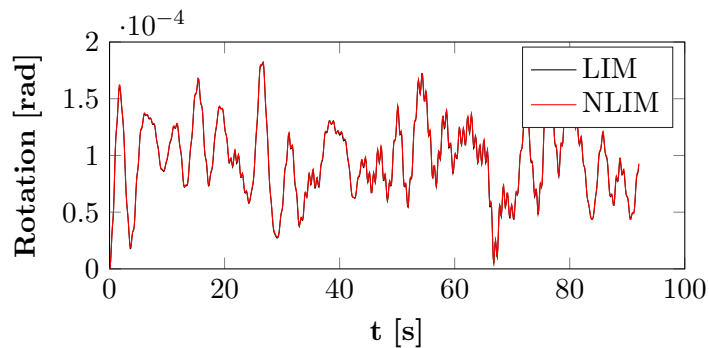
Model Type	Soil Springs		Wind Conditions		Rotor
	Linear	Non Linear	Linear	Non Linear	Status
LIM	✓		✓		✓
NLIM	✓			✓	✓



(a) Side-side (X-Z) plane motions



(b) Fore-aft (Y-Z) plane motions



(c) Yaw axis motions

Figure 7.14: Response of the OWT subjected to Load case-1 (Wind Model)

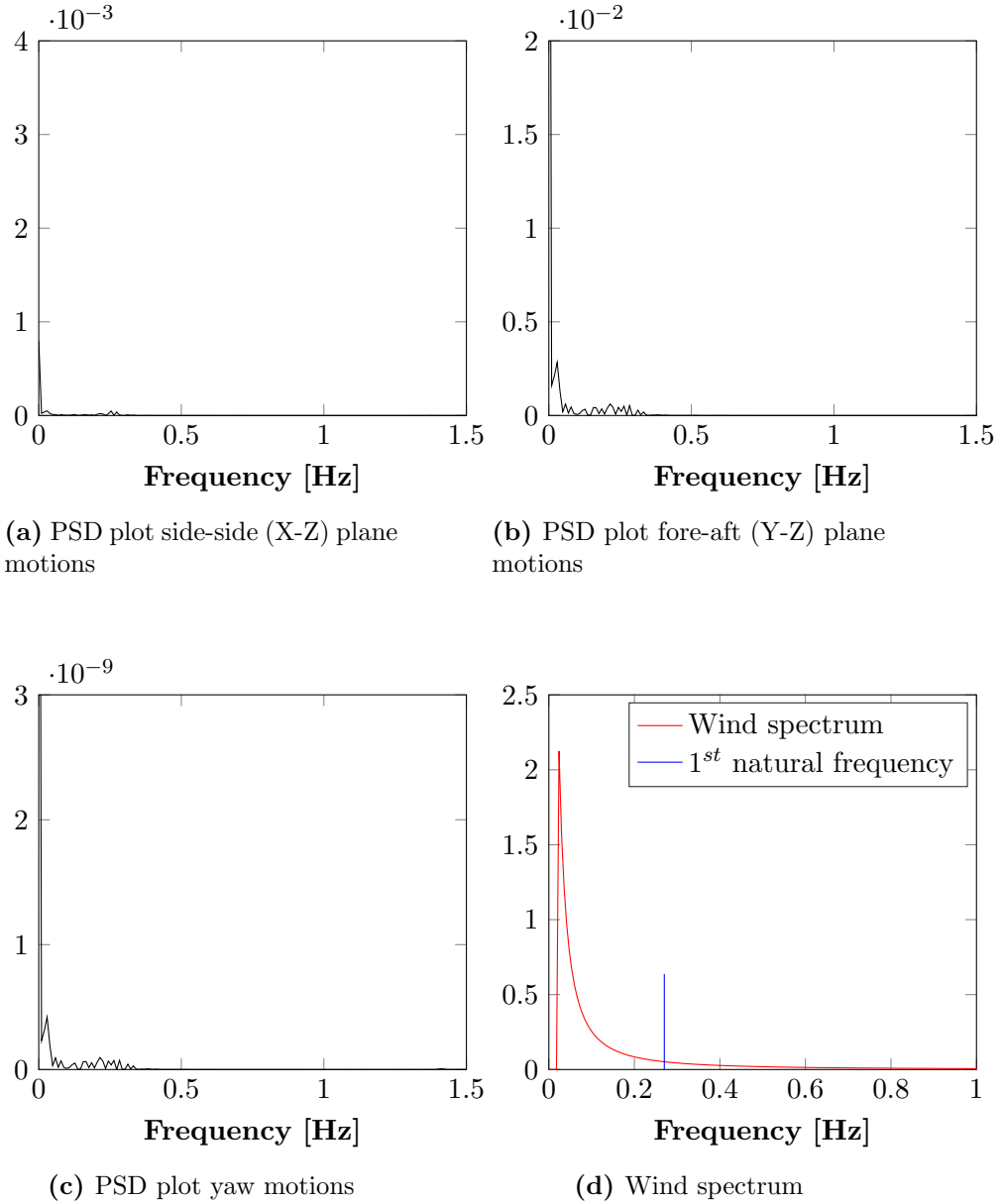


Figure 7.15: Frequency contents of load and responses (Load case-1, Wind model)

From [Figure 7.14b](#) and [Figure 7.14c](#) it can be seen that the agreement between the LIM and the NLIM is particularly good for fore-aft (Y-Z) plane and Yaw motions. [Figure 7.14a](#) shows that the agreement between LIM and NLIM is good for most of the time instants. Only at a few time instants, there is a slight disagreement between them.

[Figure 7.15](#) shows static components in the responses (spikes at very low frequencies). The high frequency ripples can also be observed in the side-side plane ([Figure 7.15a](#)) and the yaw motions ([Figure 7.15c](#)). These can be explained on the lines of [subsection 7.3.1](#).

7.3.3 Load case - Waves

In this load case, only the non-linearities in the wave loading are considered. Soil is modelled as linear springs and wind loads are absent. Also, the rotor is assumed to be non-rotating i.e. $\Omega = 0$. The situation is depicted in [Figure 7.16](#), and the parameters and the physical conditions used for this load case are tabulated in [Table 7.7](#) and [Table 7.8](#). The response of the top most node for load case-1 in side-side (X-Z) plane and fore-aft (Y-Z) plane is shown in [Figure 7.17a](#) and [Figure 7.17b](#) respectively. The yaw motions are zero as no force or torque is applied at the top most node. The results of all the load cases follow the similar pattern, so only load case-1 is described here. The results of load cases 2,3 and 4 can be found in [Appendix E](#).

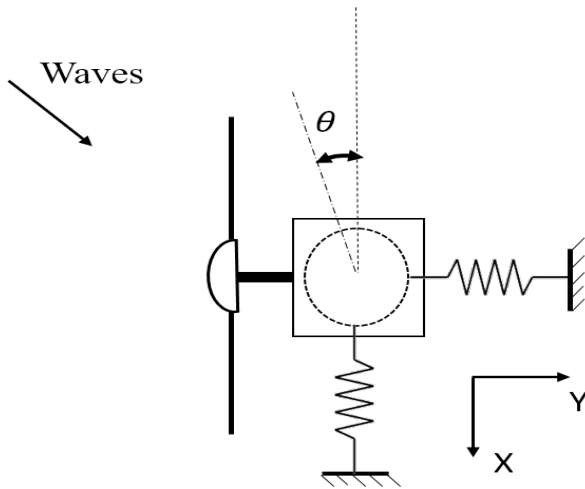


Figure 7.16: Top view-(Waves-model)

Table 7.7: Parameters (Waves)

Load Case	θ_{wave} [°]	H_s [m]
1	45	2
2	45	4
3	45	6
4	45	8

Table 7.8: Physical Conditions (Waves)

Model Type	Soil Springs		Wave Conditions	
	Linear	Non Linear	Structural Motions Excluded	Structural Motions Included
LIM	✓		✓	
NLIM	✓			✓

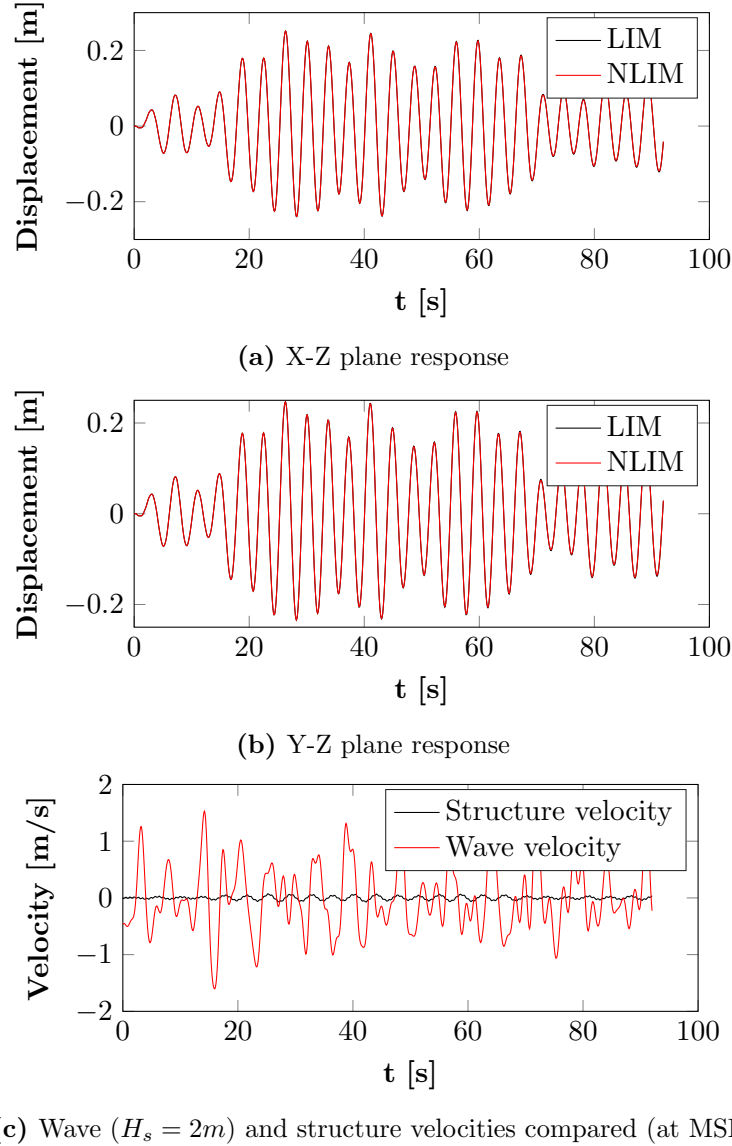


Figure 7.17: Response of the OWT subjected Load case-1 (Waves model)

It can be seen from [Figure 7.17a](#) and [Figure 7.17b](#) that the there is hardly any difference between the responses of LIM and NLIM. This can be explained from the fact that the structural velocities are small as compared to the wave velocities as shown in [Figure 7.17c](#).

The relative velocities ($U - \dot{x}$) only become important when the wave velocities are very small. However, such occurrences are less frequent. This implies that the hydrodynamic damping is not very significant.

7.3.4 Load case - Soil

In this load case, only the non-linearities in soil are considered. Wind loads are absent and the rotor is assumed to be non-rotating i.e. $\Omega=0$. The wave loads are considered without any structural motions. The parameters and the physical conditions used for this load case are tabulated in [Table 7.9](#) and [Table 7.9](#).

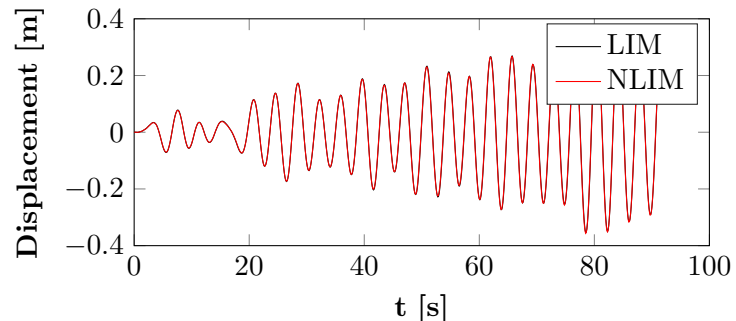
The response of the top most node in side-side (X-Z) plane and fore-aft (Y-Z) plane is shown in [Figure 7.18a](#) and [Figure 7.18b](#) respectively. The yaw motions are zero as no force or torque is applied at the top most node. The results of all the load cases follow the similar pattern, so only load case-1 is described here. The results of load cases 2,3 and 4 can be found in [Appendix F](#).

Table 7.9: Parameters (Soil)

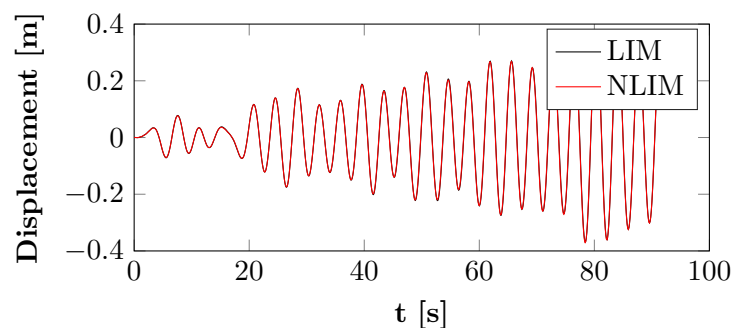
Load Case	θ_{wave} [°]	H_s [m]
1	45	2
2	45	4
3	45	6
4	45	8

Table 7.10: Physical Conditions (Soil)

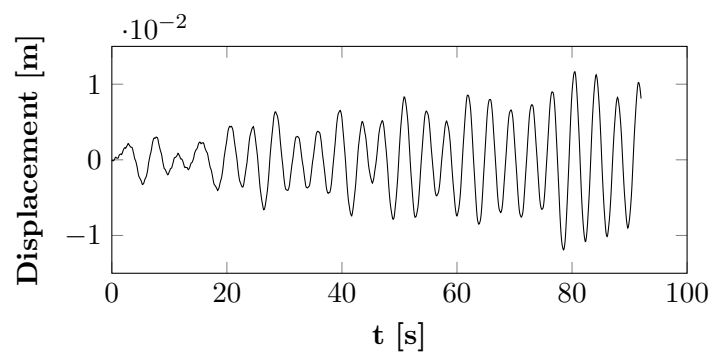
Model Type	Soil Spring		Waves Structure motions Excluded
	Linear	Non Linear	
LIM	✓		✓
NLIM		✓	✓



(a) Load case-1



(b) Load case-1

(c) Displacement of the 2nd embedded node ($H_s = 2m$)**Figure 7.18:** Response of the OWT subjected to Load case-1 (Soil Model)

It can be seen from [Figure 7.18a](#) and [Figure 7.18b](#) that there is hardly any difference between the responses of LIM and NLIM. This can be explained from the fact that the structural displacements of the nodes in the soil are very small (a few millimetres) as shown in [Figure 7.18c](#).

[Figure 7.19](#) shows the maximum displacement of the 2nd node of the pile embedded in soil plotted along the non-linear soil spring stiffness at various depths. The displacements of the nodes located deeper in the soil are even less. Thus the stiffness does not enter far into the non-linear regime of the p - y curves.

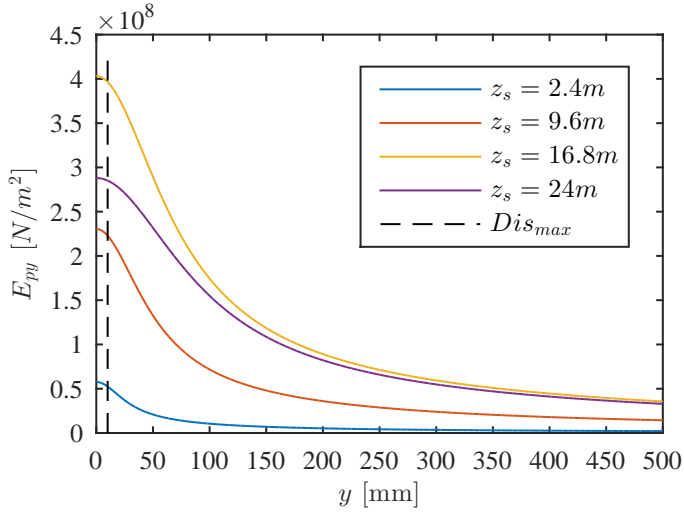


Figure 7.19: E_{py} vs Deflection and maximum displacement of the 2nd node (from sea bed) in soil

This also suggests that p - y curves do not represent the non-linearities present in the soil correctly and instead, it will make more sense to use a hysteresis curve that can account for the soil loading history.

7.4 Modal damping

From the linearised equations of the aerodynamic forces, a 5×5 damping matrix can be identified. Using this (aerodynamic) damping matrix, a global system damping matrix (174×174) can be defined. Using this system damping matrix, damping ratios of different modes can be calculated by solving the eigenvalue problem represented by [Equation 7.1](#).

$$\left\{ \begin{bmatrix} \begin{bmatrix} 0 \end{bmatrix}_{n \times n} & \begin{bmatrix} I \end{bmatrix}_{n \times n} \\ \begin{bmatrix} -M^{-1}K \end{bmatrix}_{n \times n} & \begin{bmatrix} -M^{-1}C \end{bmatrix}_{n \times n} \end{bmatrix} - \lambda_{sys} \begin{bmatrix} I \end{bmatrix}_{2n \times 2n} \right\} X = 0 \quad (7.1)$$

Here, M, K and C are the system mass, stiffness and damping matrices respectively. $n=174$ represents the total DOF of the system. The natural frequencies and eigenvectors obtained from [Equation 7.1](#) are complex valued and exist as conjugate pairs.

The complex eigenvalue for the i^{th} mode is given by [Equation 7.2](#)

$$\lambda_{sys,i} = -\zeta_i \omega_i - j \omega_i \sqrt{1 - \zeta_i^2} \quad (7.2)$$

Here, $j=\sqrt{-1}$ and ζ_i represents the damping ratio of the i^{th} mode. From [Equation 7.2](#), the natural frequency and the damping ratio of the i^{th} can be found by using [Equation 7.3a](#)

and Equation 7.3b respectively.

$$\omega_i = \sqrt{(\Re(\lambda_{sys,i}))^2 + (\Im(\lambda_{sys,i}))^2} \quad (7.3a)$$

$$\zeta_i = \frac{-\Re(\lambda_{sys,i})}{|\lambda_{sys,i}|} \quad (7.3b)$$

Here, \Re and \Im represent the real and imaginary parts of a complex number.

The modal damping values are calculated for the 1st 10 modes for wind speeds of 12, 15 and 20 m/s and depicted in Figure 7.20. The modal damping ratios for 15 m/s are tabulated in Table 7.11.

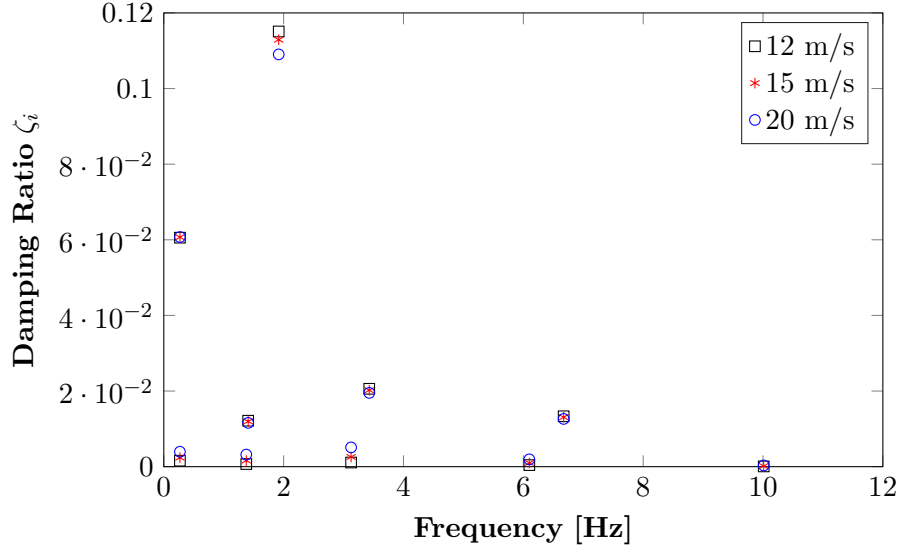


Figure 7.20: Modal damping ratios for different wind speeds

Table 7.11: Modal damping ratios for different planes for wind speed of 15 m/s

Mode number	Plane / mode number	ζ_i
1	(side-side)/1	0.24
2	(fore-aft)/1	6.1
3	(side-side)/2	0.16
4	(fore-aft)/2	1.2
5	(yaw axis)/1	11.3
6	(side-side)/3	0.25
7	(fore-aft)/3	1.9
8	(side-side)/4	0.19
9	(fore-aft)/4	1.2
10	(side-side)/5	0.03

Chapter 8

Conclusions and Recommendations

8.1 Conclusions

Two 3D finite element models of an OWT capable of fore-aft, side-side and yaw motions were constructed and their responses were compared for different load cases (in time domain). The 1st model (**NLIM**) took the non-linearities in soil, hydrodynamic and aerodynamic loading into account. The 2nd model (**LIM**) used linearised expressions for soil, hydrodynamic and aerodynamic loading. The following conclusions are made from this comparative study.

1. Morison's equation and MacCamy and Fuchs' equation are compared with a diffraction software for calculating hydrodynamic (inertia) loads on a submerged cylinder of 5.75 m diameter. It is found that for higher frequencies, Morison's equation over-predicts the wave inertia forces. MacCamy and Fuchs' equation, however, remains consistent with ANSYS-AQWA. This indicates that MacCamy and Fuchs' equation is more accurate for modelling wave inertia loads on submerged cylinders.
2. It is observed that for the pile diameter of 5.75 m, the structural velocities are too small when compared to the wave velocities. Thus omitting the structural velocities in the drag expression terms do not significantly influence the structural motions.
3. The deflections of the pile in the soil are found to be in the order of a few millimetres indicating that the soil stiffness does not enter the non-linear region. Thus, the $p-y$ curves are not very effective in capturing the non-linear soil behaviour.
4. The model does capture the physical behaviour of the OWT till mean wind speeds of 20 m/s. At 24 m/s, however, the side-side plane motion behaviour needs further investigation.
5. The response obtained from the **LIM** closely followed that obtained from the **NLIM** for most load cases. However, a phase difference is observed between them for the side-side motions in case of a constant wind in which the **NLIM** leads the **LIM**.
6. A strong coupling is observed between the rotations about the global X axis (θ_x , fore-aft direction) and the yaw motions (θ_z).
7. Modal damping ratios are calculated from the linearised aerodynamic damping matrix derived from the rotor aerodynamic loads. A plot of modal damping ratios as a function of natural frequencies is generated for different wind speeds.

8.2 Recommendations for further work

This master thesis was carried out within a limited time frame of 8-9 months. Consequently, its scope was limited and this leaves a room for further improvements. In this thesis, a basic 3D finite element model of an OWT was created that provides easy access to the source code making it convenient to manipulate the parameters that influence the dynamic behaviour of the OWT. However, for further improvements, the following recommendations are made.

1. As the $p-y$ curves are not very accurate in predicting the non-linear soil behaviour, hysteresis should be used to model soil springs that take the loading and un-loading history of the soil into account. Also, torsional resistance of the soil needs to be modelled.
2. The present model assumes the blades to be rigid. In reality, the rotor blades are flexible. Thus, the next step to bring the model close to reality would be to impart flexibility to the blades.
3. More insight is needed to look into the behaviour of side-side plane motions for constant wind speed of 24 m/s.
4. Spatial variation of the wind profile for wind loads on the blades can be modelled. Also, the present model assumes constant induction factor. For more accuracy in the model, it can be made to vary along the blade radius.
5. Tower shadow effect needs to be incorporated.
6. The present model applies hydrodynamic loads from [MSL](#) till sea-bed. Thus incorporation of wave profile stretching (Wheeler's stretching) will make it more accurate.
7. To assess the credibility of the present model, validation with a commercial software is still required.

Appendix A

Finite Element Formulation

A.1 Introduction

The analytical solution of a boundary value problem can be very difficult if not impossible. Therefore a computational technique is required to obtain an approximate solution. The *finite element method* ([FEM](#)) is one such numerical technique. This chapter will deal with the following topics:

- Formulation of mass and stiffness matrices for a beam element for single plane motions.
- Extension of those matrices to two plane motions with torsion capability.
- Response calculations.

A.2 Timoshenko Beam Elements (single plane)

The derivation of mass and stiffness matrices will not be dealt here. It can, however, be found in [\[11\]](#). The mass and stiffness matrices for a Timoshenko beam element are of the order 4×4 . Each node has 2 [DOF](#), one translation perpendicular to the length of the beam ($v_{1,2}$) and one rotation ($\theta_{1,2}$) as shown in [Figure A.1](#). It is to be noted, that the coordinate system shown here is element coordinate system ([ECS](#)) and [NOT](#) ([GCS](#)).

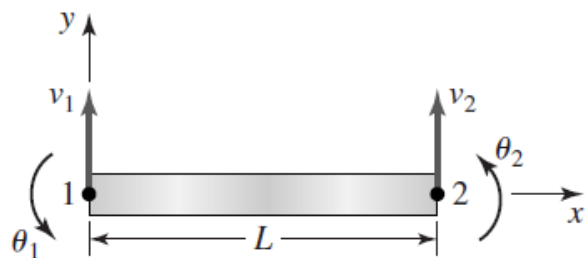


Figure A.1: DOF of a beam element [\[15\]](#)

The mass [M] and bending stiffness [K_b] matrices of a Timoshenko beam element for

bending in X-Z plane are

$$[M]_{XZ} = \frac{\rho_s A_b L}{(1 + \phi)^2} \begin{bmatrix} a & c & b & -d \\ c & e & d & -f \\ b & d & a & -c \\ -d & -f & -c & e \end{bmatrix} \quad (\text{A.1})$$

$$[K_b]_{XZ} = \frac{EI_b}{L^3(1 + \phi)} \begin{bmatrix} 12 & 6L & -12 & 6L \\ 6L & (4 + \phi)L^2 & -6L & (2 - \phi)L^2 \\ -12 & -6L & 12 & -6L \\ 6L & (2 - \phi)L^2 & -6L & (4 + \phi)L^2 \end{bmatrix} \quad (\text{A.2})$$

The terms a, b, c, d, e and f are given by the following relations [2]

$$\begin{aligned} a &= \frac{13}{35} + \frac{7\phi}{10} + \frac{\phi^2}{3} + \frac{6}{5} \left(\frac{r_g}{L}\right)^2; b = \frac{9}{70} + \frac{3\phi}{10} + \frac{\phi^2}{6} - \frac{6}{5} \left(\frac{r_g}{L}\right)^2; c = \left(\frac{11}{210} + \frac{11\phi}{120} + \frac{\phi^2}{24} + \left(\frac{1}{10} - \frac{\phi}{2}\right) \left(\frac{r_g}{L}\right)^2\right) L; \\ d &= \left(\frac{13}{420} + \frac{3\phi}{40} + \frac{\phi^2}{24} - \left(\frac{1}{10} - \frac{\phi}{2}\right) \left(\frac{r_g}{L}\right)^2\right) L; e = \left(\frac{1}{105} + \frac{\phi}{60} + \frac{\phi^2}{120} + \left(\frac{2}{15} + \frac{\phi}{6} + \frac{\phi^2}{3}\right) \left(\frac{r_g}{L}\right)^2\right) L^2; \\ f &= \left(\frac{1}{140} + \frac{\phi}{60} + \frac{\phi^2}{120} + \left(\frac{1}{30} + \frac{\phi}{6} - \frac{\phi^2}{6}\right) \left(\frac{r_g}{L}\right)^2\right) L^2; \end{aligned}$$

The term ϕ ¹ gives the relative importance of the shear deformations to the bending deformations and is given by Equation A.3 [11].

$$\phi = \frac{24(1 + \nu)}{k_{sc}} \left(\frac{r_g}{L}\right)^2 \quad (\text{A.3})$$

k_{sc} is the shear coefficient and is given by Equation A.4 [14]

$$k_{sc} = \frac{6(r_{in}^2 + r_{ext}^2)(1 + \nu)^2}{7r_{in}^4 + 34r_{in}^2r_{ext}^2 + 7r_{ext}^4 + \nu(12r_{in}^4 + 48r_{in}^2r_{ext}^2 + 12r_{ext}^4) + \nu^2(4r_{in}^4 + 16r_{in}^2r_{ext}^2 + 4r_{ext}^4)} \quad (\text{A.4})$$

To account for the loss of stiffness due to compressive axial loading on the beam, the stiffness matrix needs to be adjusted. This is done by the $[K_g]$ matrix as [11]

$$[K_g]_{XZ} = \frac{-P_{ax}}{L(1 + \phi)^2} \begin{bmatrix} \left(\frac{6}{5} + 2\phi + \phi^2\right) & \frac{L}{10} & -\left(\frac{6}{5} + 2\phi + \phi^2\right) & \frac{L}{10} \\ \frac{L}{10} & \left(\frac{2}{15} + \frac{\phi}{6} + \frac{\phi^2}{12}\right)L^2 & -\frac{L}{10} & -\left(\frac{1}{30} + \frac{\phi}{6} + \frac{\phi^2}{12}\right)L^2 \\ -\left(\frac{6}{5} + 2\phi + \phi^2\right) & -\frac{L}{10} & \left(\frac{6}{5} + 2\phi + \phi^2\right) & -\frac{L}{10} \\ \frac{L}{10} & -\left(\frac{1}{30} + \frac{\phi}{6} + \frac{\phi^2}{12}\right)L^2 & -\frac{L}{10} & \left(\frac{2}{15} + \frac{\phi}{6} + \frac{\phi^2}{12}\right)L^2 \end{bmatrix} \quad (\text{A.5})$$

Thus, the net beam element stiffness matrix can be written as

$$[K]_{XZ} = [K_b]_{XZ} + [K_g]_{XZ} \quad (\text{A.6})$$

A.3 2-Plane bending with torsional capability

To account for 2 plane bending, i.e. motions in X-Z and Y-Z plane, the beam element of section A.2 is first extended to include 2-plane bending, and then torsional capability is added to it.

Figure A.2 shows a beam element with an attached 3-dimensional ECS in which the x axis corresponds to the longitudinal axis of the beam and is assumed to pass through the centroid of the beam cross section. The y and z axes are assumed to correspond to

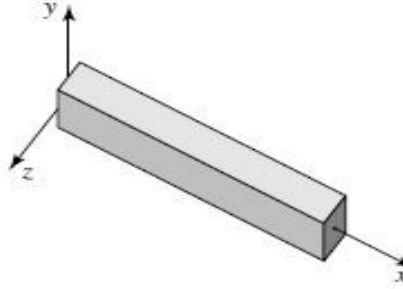


Figure A.2: Beam element in 3D ECS [15]

the principal axes for area moments of inertia of the cross section. If this is not the case, treatment of simultaneous bending in two planes and superposition of the results as in the following element development will not produce correct results [15].

The mass and stiffness matrices for motions in X-Z plane have been shown in [section A.2](#). The only differences between the Y-Z plane bending stiffness and mass matrices and that for X-Z plane bending stiffness and mass matrices are the sign changes in the off-diagonal terms. This is done in order to be consistent with the right hand rule.

Thus the mass matrix $[M]_{YZ}$ for bending in Y-Z plane becomes

$$[M]_{YZ} = \frac{\rho_s A_b L}{(1 + \phi)^2} \begin{bmatrix} a & -c & b & d \\ -c & e & -d & -f \\ b & -d & a & c \\ d & -f & c & e \end{bmatrix} \quad (\text{A.7})$$

The stiffness matrix $[K]_{YZ}$ for bending in Y-Z plane can also be found out by changing the signs of the corresponding terms.

Finally, the torsion mass and stiffness matrices can be written as [2].

$$[M]_{torsion} = \rho_s L J_b \begin{bmatrix} 1/3 & 1/6 \\ 1/6 & 1/3 \end{bmatrix} \quad (\text{A.8})$$

$$[K]_{torsion} = \frac{J_b G_s}{L} \begin{bmatrix} 1 & -1 \\ -1 & 1 \end{bmatrix} \quad (\text{A.9})$$

Thus, a beam element with 2-plane bending and torsion capabilities as shown in [Figure A.3](#) can be defined by the mass and stiffness matrices given by [Equation A.10a](#) and [Equation A.10b](#) respectively.

$$[M]_{system} = \begin{bmatrix} [M]_{XZ} & [0] & [0] \\ [0] & [M]_{YZ} & [0] \\ [0] & [0] & [M]_{torsion} \end{bmatrix} \quad (\text{A.10a})$$

$$[K]_{system} = \begin{bmatrix} [K]_{XZ} & [0] & [0] \\ [0] & [K]_{YZ} & [0] \\ [0] & [0] & [K]_{torsion} \end{bmatrix} \quad (\text{A.10b})$$

¹It is to be noted that if $\phi = 0$, the matrices are reduced to those of an Euler-Bernoulli beam.

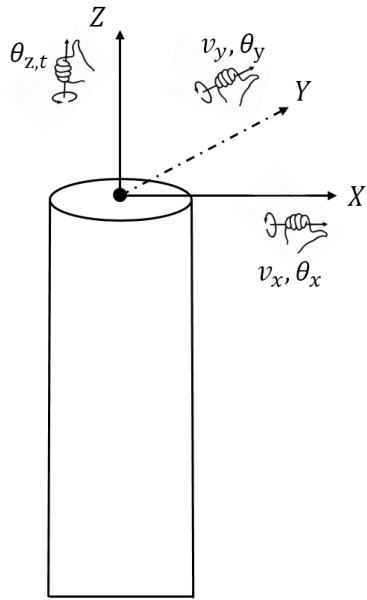


Figure A.3: Beam element with two plane motion and torsion capability

The equations of motion for a beam element whose mass and stiffness matrices have been assembled in [section A.3](#) can be defined as

$$[M]_{system} \ddot{X} + [K]_{system} X = \left\{ \vec{F} \right\}_{system} \quad (\text{A.11})$$

Appendix B

Results-Regular wave-Constant wind

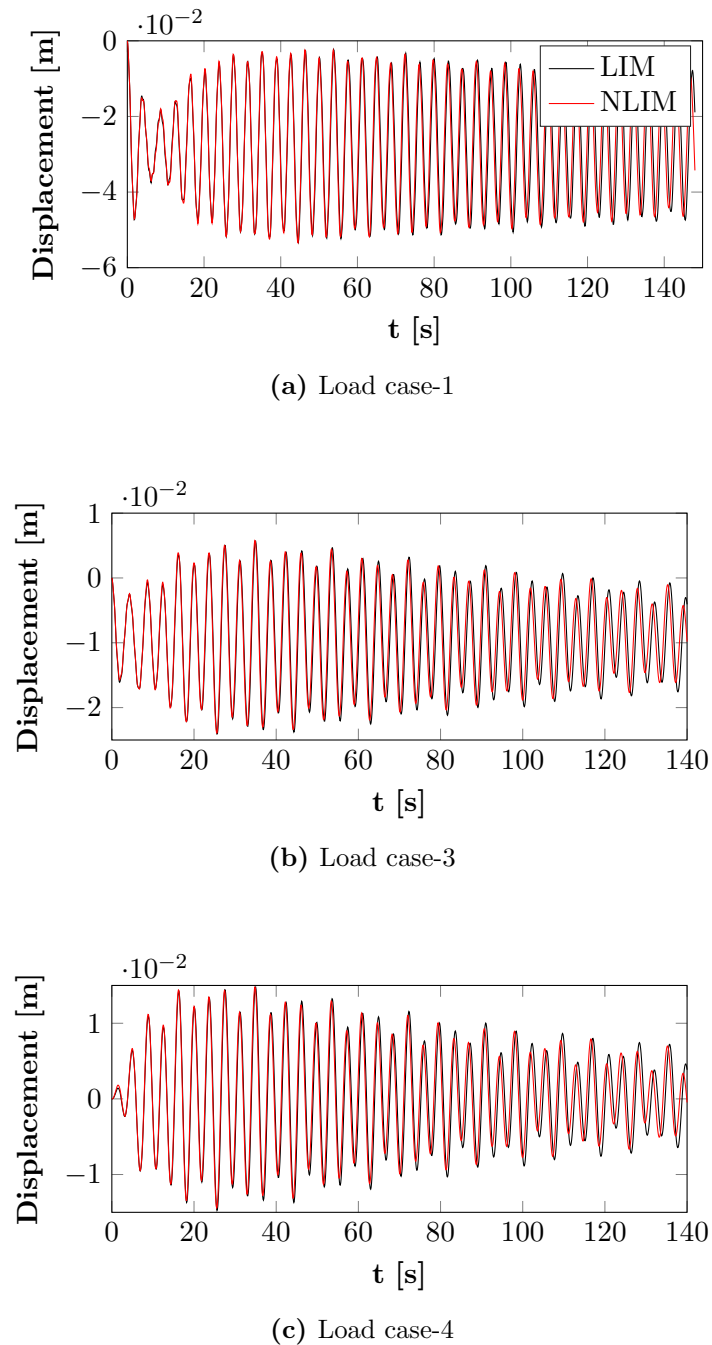
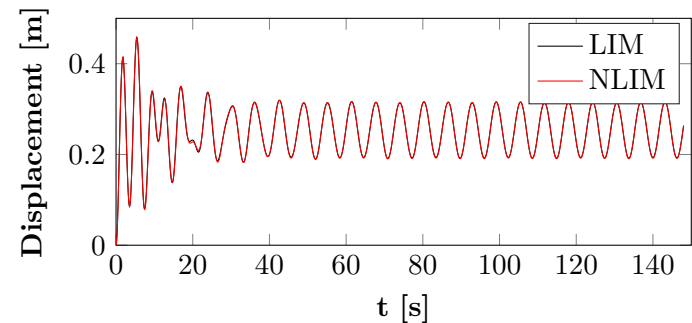
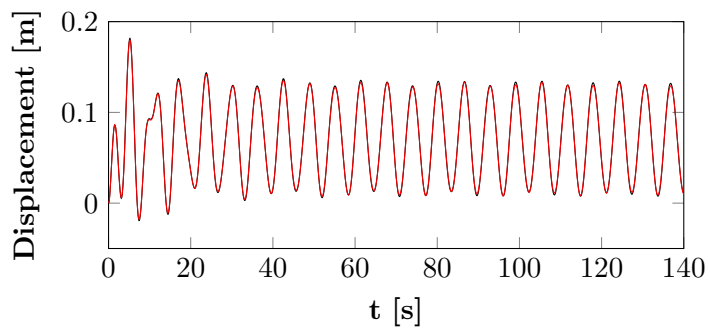


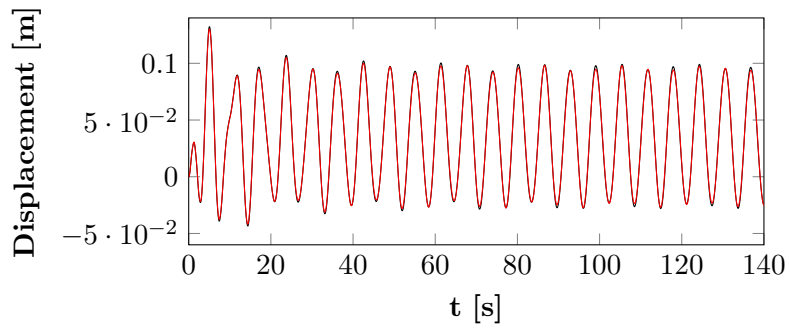
Figure B.1: Response of the OWT subjected in X-Z (side-side) plane for different load cases (Regular wave-constant wind)



(a) Load case-1

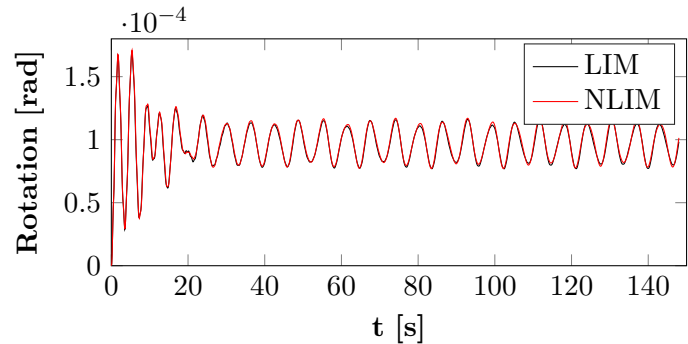


(b) Load case-3

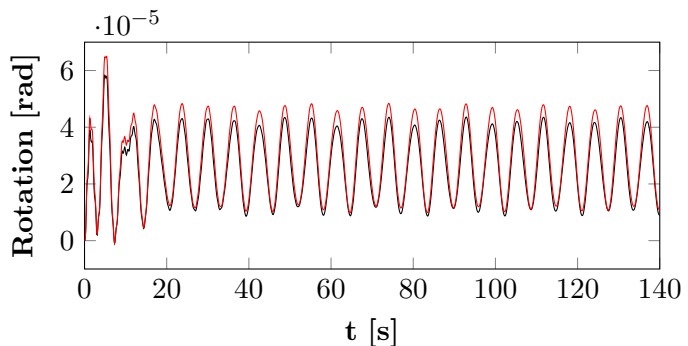


(c) Load case-4

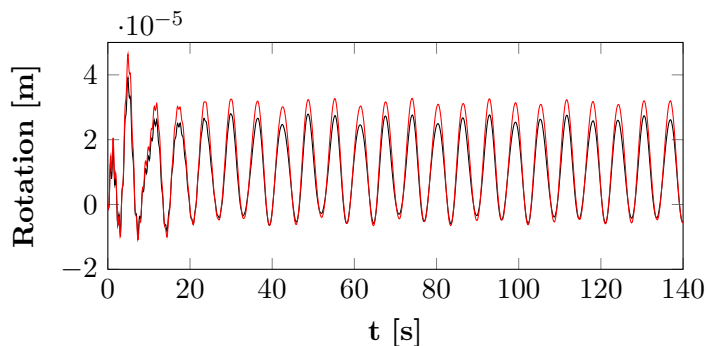
Figure B.2: Response of the OWT subjected in Y-Z (fore-aft) plane for different load cases (Regular wave-constant wind)



(a) Load case-1



(b) Load case-3

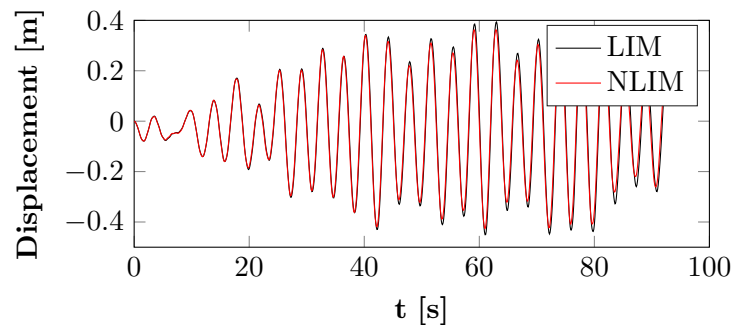


(c) Load case-4

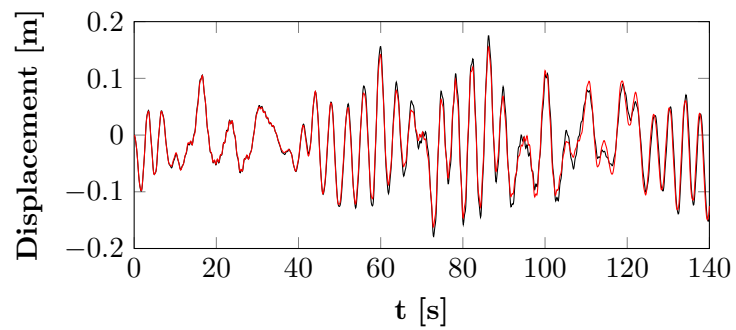
Figure B.3: Response of the OWT about the Yaw axis for different load cases (Regular wave-constant wind)

Appendix C

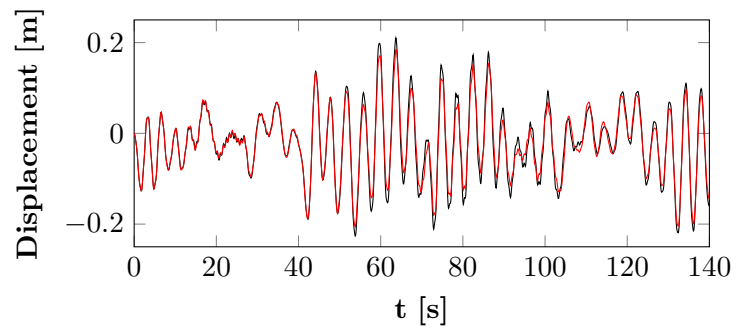
Results-Integrated



(a) Load case-1

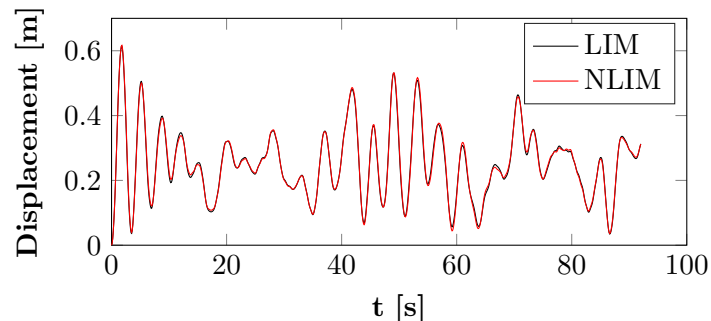


(b) Load case-3

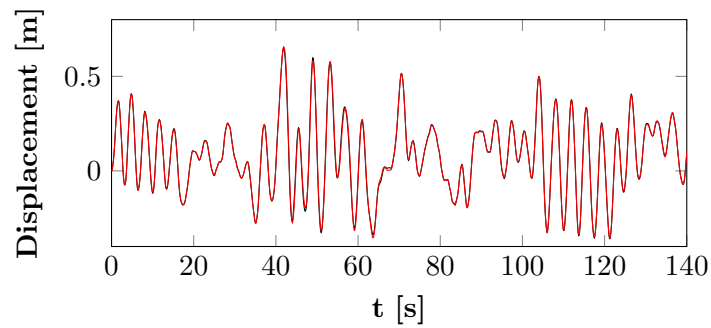


(c) Load case-4

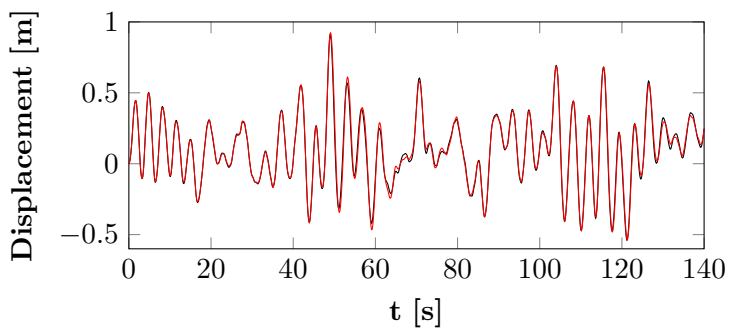
Figure C.1: Response of the OWT subjected in X-Z plane for different load cases (Integrated model)



(a) Load case-1

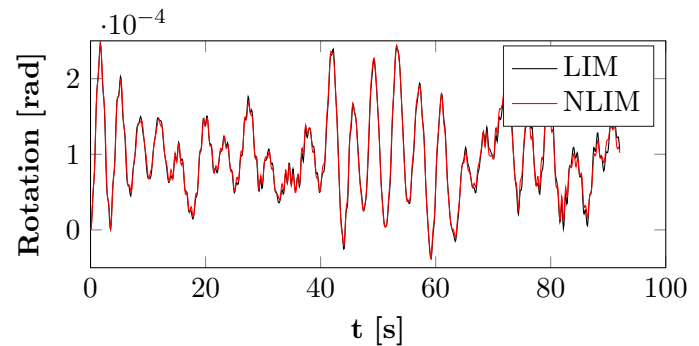


(b) Load case-3

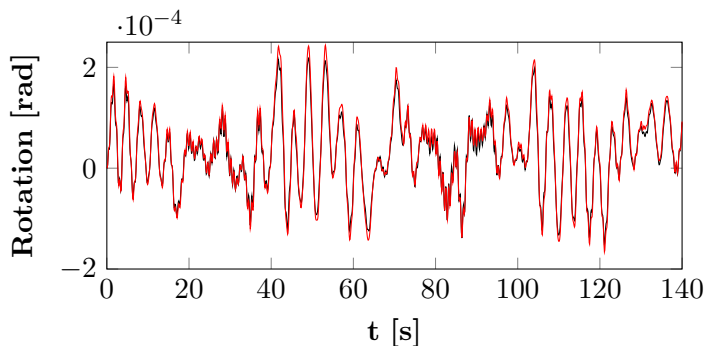


(c) Load case-4

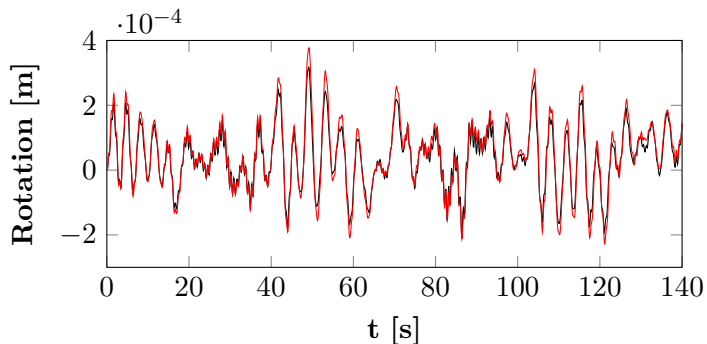
Figure C.2: Response of the OWT subjected in Y-Z plane for different load cases (Integrated model)



(a) Load case-1



(b) Load case-3

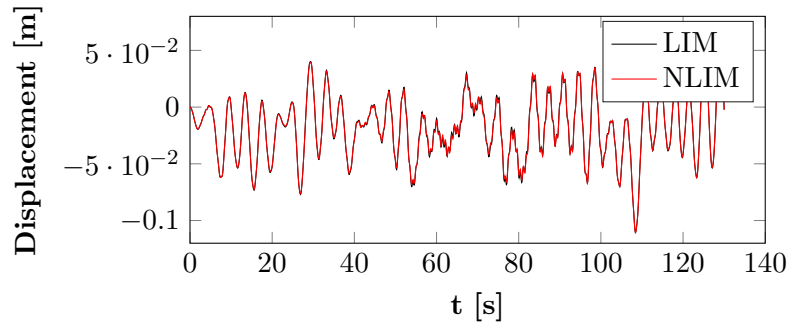


(c) Load case-4

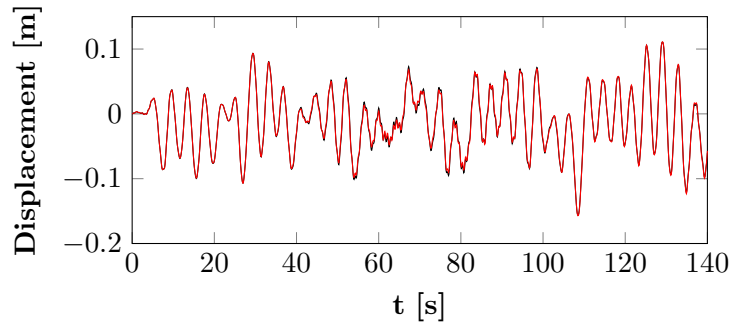
Figure C.3: Response of the OWT about the Yaw axis for different load cases (Integrated model)

Appendix D

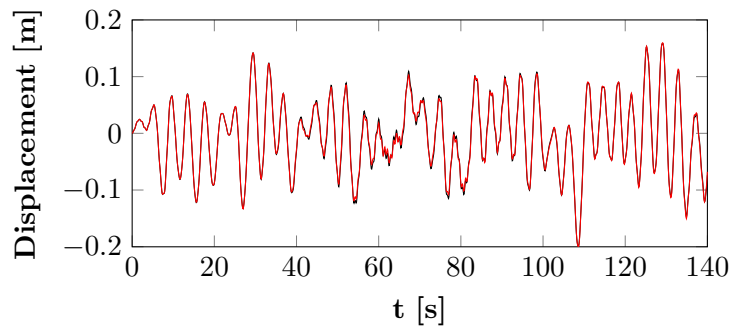
Results-Wind



(a) Load case-2

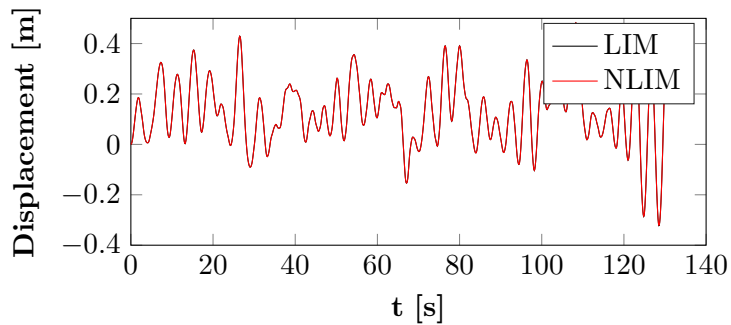


(b) Load case-3

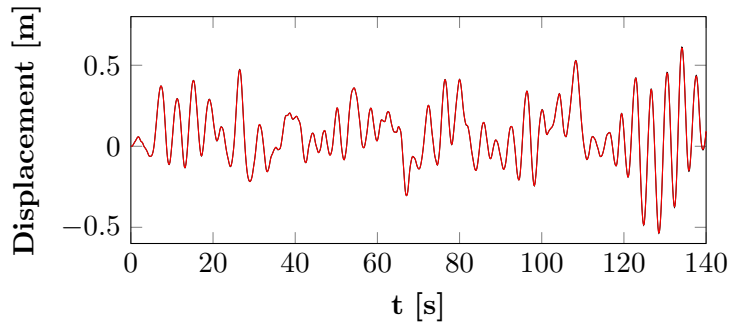


(c) Load case-4

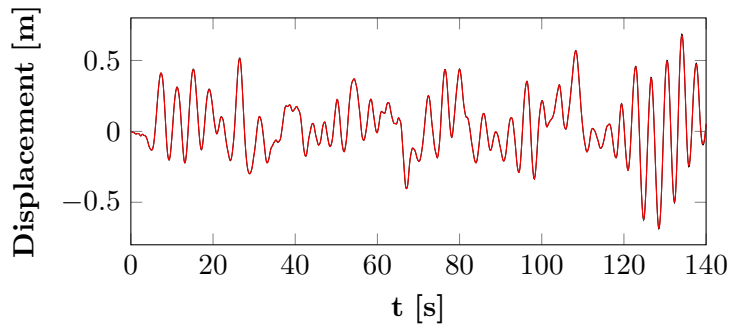
Figure D.1: Response of the OWT subjected in side-side (X-Z) plane for different load cases (Wind)



(a) Load case-2



(b) Load case-3



(c) Load case-4

Figure D.2: Response of the OWT subjected in fore-aft (Y-Z) plane for different load cases (Wind)

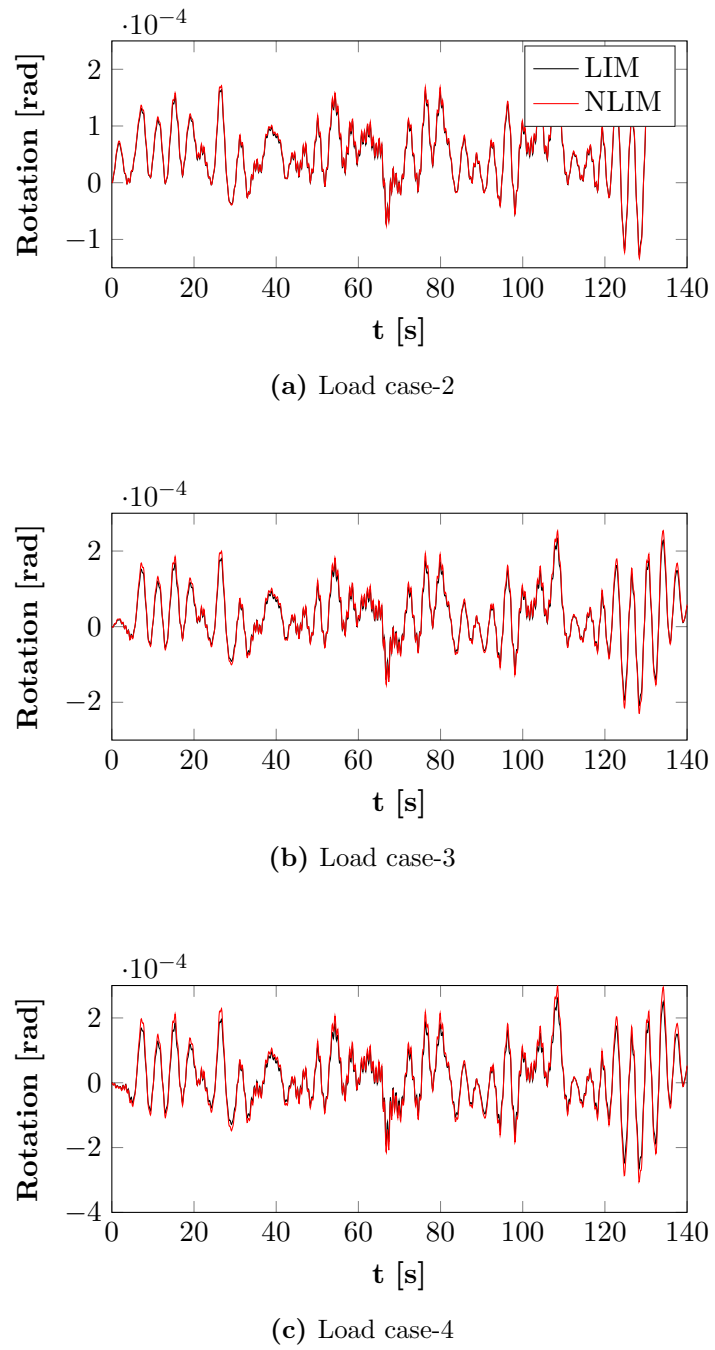
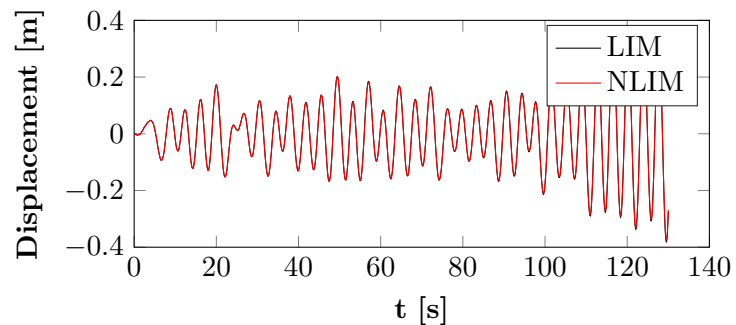


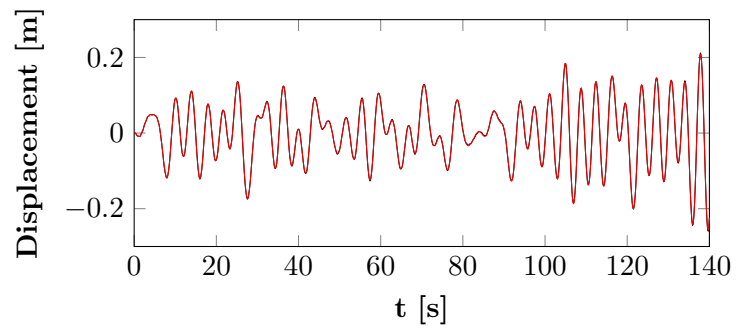
Figure D.3: Response of the OWT about the Yaw axis for different load cases (Wind)

Appendix E

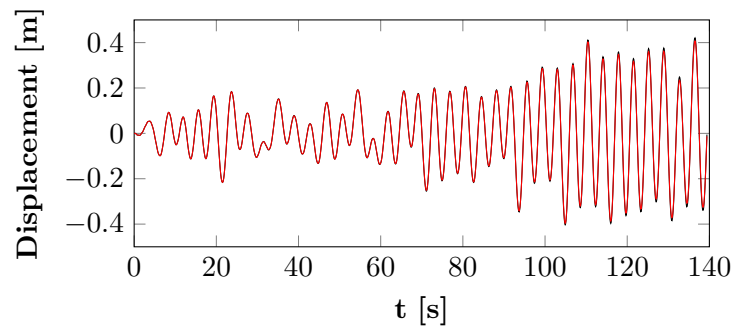
Results-Waves



(a) Load case-2

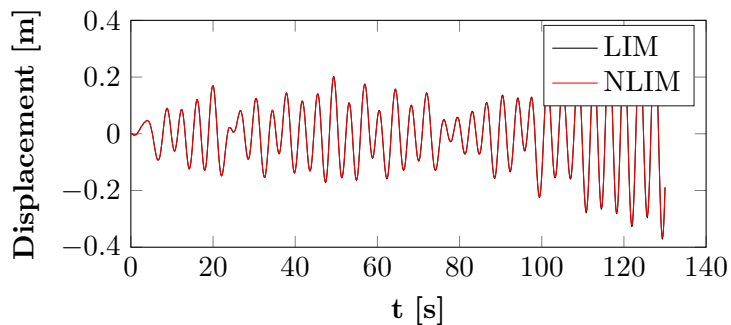


(b) Load case-3

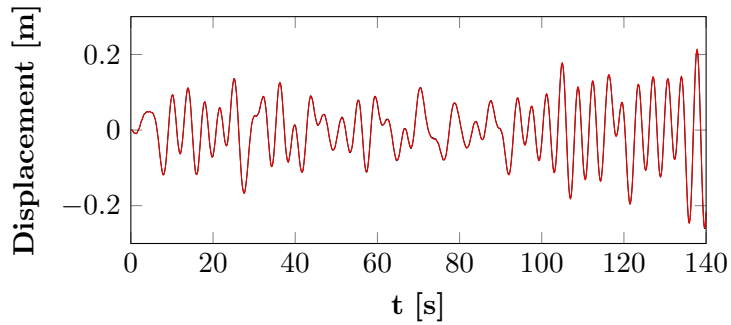


(c) Load case-4

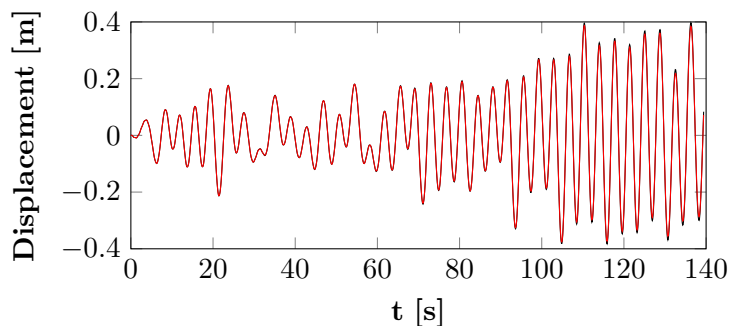
Figure E.1: Response of the OWT subjected in side-side (X-Z) plane for different load cases (Waves)



(a) Load case-2



(b) Load case-3

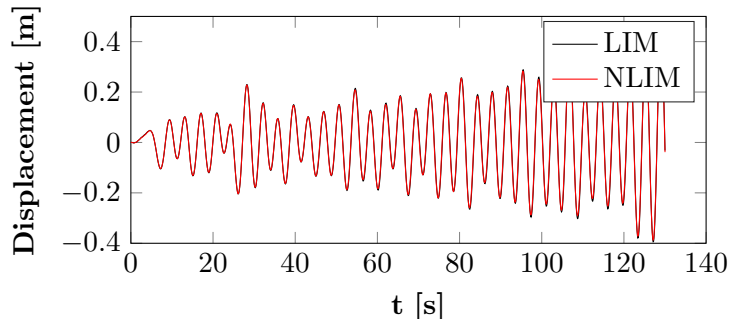


(c) Load case-4

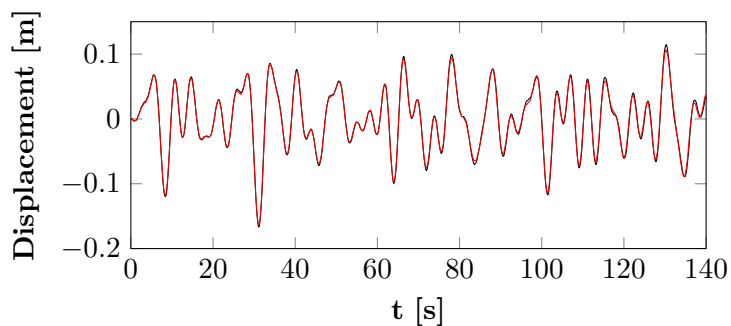
Figure E.2: Response of the OWT subjected in fore-aft (Y-Z) plane for different load cases (Waves)

Appendix F

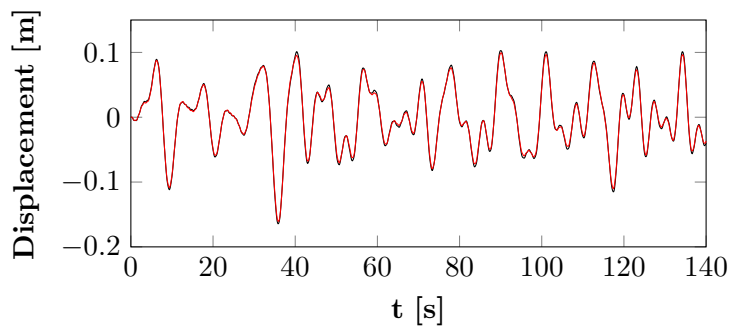
Results-Soil



(a) Load case-2



(b) Load case-3



(c) Load case-4

Figure F.1: Response of the OWT in side-side (X-Z) plane for different load cases (Soil)

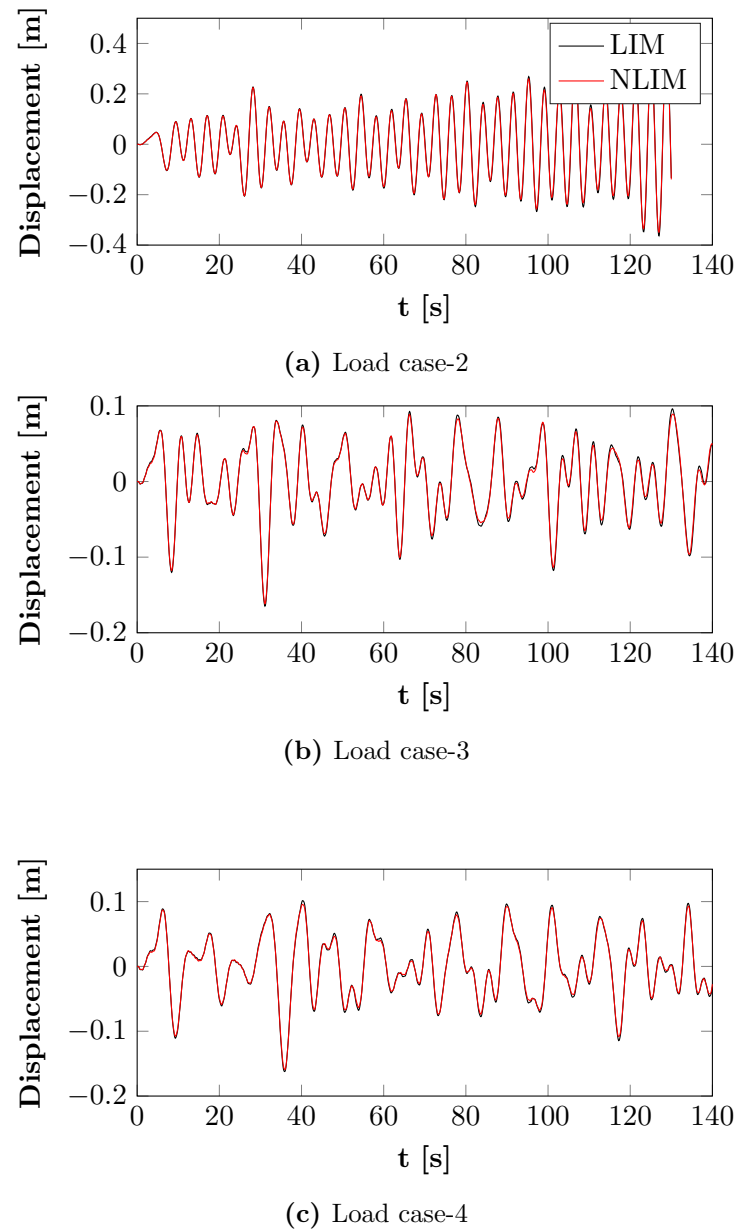


Figure F.2: Response of the OWT in fore-aft (Y-Z) plane for different load cases (Soil)

Appendix G

Aerodynamic model for blade loading

The following is taken from [19] and is not my original work.

1. Introduction

1.1. Background

The added damping of rotating rotors on a flexible support through aerodynamic action in fore-aft direction is known to relevant in the dynamic analysis of, for instance, wind turbine structures. This relevance is even more pronounced for offshore wind turbines, for which the dynamic response to wave actions is importantly reduced by this added damping. The contribution in side-to-side direction of the added damping is much less, and therefore generally neglected. This would imply that in case of wind-wave misalignments, the dynamic response to wave actions is only damped slightly. Still, the effect of side-to-side damping may be substantial, especially if the coupling between fore-aft and side-to-side motion is considered.

10 2. Aerodynamic interaction

2.1. Fore-aft aerodynamic damping

In the offshore-wind industry, the importance of fore-aft aerodynamic damping is already widely recognized. The aerodynamic forcing depends on the relative wind velocity, implying that a structural motion induces a counteracting force, which reduces the dynamic amplification of the motion. This damping effect requires that the aerodynamic force increases with an increase in the relative velocity, i.e., the interaction may become unstable when the added damping is negative and the interactive force amplifies the dynamic motion.

A simple model to understand the aerodynamic damping of a rotating rotor was developed by [?]. As a starting point, Figure 1(a) presents a three-bladed rotor in a fixed global $X_0Y_0Z_0$ frame of reference. The origin of the reference frame is located at the centre of rotation and the Y_0 axis coincides with the rotational axis. The figure illustrates the azimuths of the three blades $\Psi_j(t)$, for $j = 1, 2, 3$, with respect to the X_0 axis, which are related to the rotational velocity Ω :

$$\Psi_1(t) = -\Omega t, \Psi_2(t) = -\Omega t + \frac{2}{3}\pi, \Psi_3(t) = -\Omega t + \frac{4}{3}\pi. \quad (1)$$

Figure 1(b) depicts a cross-section of the j -th aerofoil, subjected to an air flow field $\mathbf{W}_j(r, t)$. The cross-section is defined within the rotating global reference frame $X_jY_0r_j$, with r_j corresponding to the longitudinal blade axis and X_jr_j defining the plane of rotation. The local configuration of the aerofoil is indicated by the local $x_jy_jr_j$ coordinate system, where the principal axes vary with twist $\beta(r_j)$ about the r_j axis. Furthermore, the aerofoil can be pitched, introducing a constant pitch $\beta_{0;j}$ in addition to $\beta(r_j)$. $c(r_j)$ represents the chord width of the aerofoil, and $\alpha(r_j, t)$ the angle between the flow vector and the local x_j axis, the so-called angle of attack. The force experienced by an aerofoil situated in an air flow can be decomposed into a force component parallel to the direction of the flow and a force component perpendicular to the flow direction – drag $\mathbf{F}_D(r_j, t)$ and lift $\mathbf{F}_L(r_j, t)$, respectively – as presented in Figure 1(c). Both drag and lift can be defined as a function of the air flow vector $\mathbf{W}(r_j, t)$, which is positioned under an angle $\alpha(r_j, t)$ with respect to the local x_j axis of the aerofoil and the angle $\phi(r_j, t)$ with respect to the plane of rotation, see Figure 1(b).

Assuming attached flow conditions, and neglecting time dependencies, the effective forcing in Y_0 direction of the j -th blade can be approximated as

$$\frac{dF_{Y_0}(r_j)}{dr_j} = \frac{1}{2}\rho c(r_j) |\mathbf{W}(r_j)|^2 (C_L(r_j) \cos \phi(r_j) + C_D(r_j) \sin \phi(r_j)), \quad (2)$$

where ρ is the air density and $C_D(r_j)$ and $C_L(r_j)$ representing a static drag and lift coefficient, respectively. By neglecting time dependencies, it is assumed that the effective wind velocity $\mathbf{W}(r_j)$ is constant in time. This implies that only the rotational velocity Ωr_j and the mean wind velocity $\bar{W}_{Y_0}(r_j)$ are accounted for, i.e., $\mathbf{W}(r_j) = [\Omega r_j \bar{W}_{Y_0}(r_j)]^T$. Moreover, it is assumed that Ωr_j is much larger than $\bar{W}_{Y_0}(r_j)$ – an assumption that is generally valid at the tip of the blade – and that $C_L(r_j) \gg C_D(r_j)$ – implying attached flow conditions. On this basis, Eq. (2) can be approximated as

$$\frac{dF_{Y_0}(r_j)}{dr_j} = \frac{1}{2}\rho c(r_j) C_L(r_j) (\Omega r_j)^2. \quad (3)$$

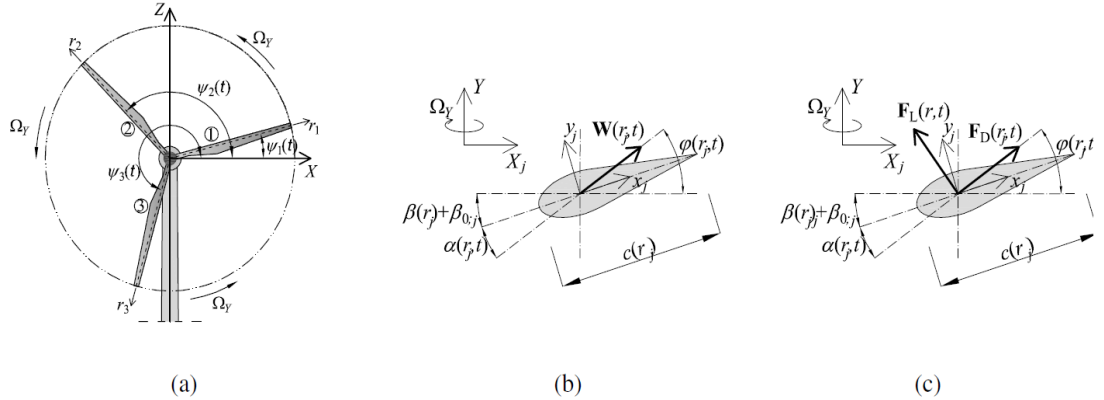


Figure 1: Aerodynamic configuration, with (a) the definition of the rotor blade azimuths, (b) the definition of the angle of attack, and (c) the definition of the drag and the lift forces.

- 40 For attached flow conditions, the lift coefficient $C_L(r_j)$ is proportional to the governing angle of attack $\alpha(r_j)$, and can be approximated as $C_L(r_j) = 2\pi \sin \alpha(r_j) \approx 2\pi \alpha(r_j)$. From Figure 1(b) it can be deduced that $\alpha(r_j) = \phi(r_j) - (\beta(r_j) + \beta_{0,j})$, with

$$\phi(r_j) \approx \frac{\bar{W}_{Y_0}(r_j)}{\Omega r_j}. \quad (4)$$

At this point, the time dependency of the relative out-of-plane wind velocity is recognized, and $\bar{W}_{Y_0}(r_j)$ is replaced by $W_{Y_0}(r_j, t) = \bar{W}_{Y_0}(r_j) + w_{Y_0}(r_j, t) - \dot{u}_{Y_0}(r_j, t)$, with $w_{Y_0}(r_j, t)$ being the time-dependent component of the ambient wind field and $\dot{u}_{Y_0}(r_j, t)$ the structural response velocity in Y_0 direction. Substitution of Eq. (4), with $W_{Y_0}(r_j, t)$ instead of $\bar{W}_{Y_0}(r_j)$, into Eq. (3) allows for the extraction of an added damping coefficient $C_{aero;j}$ per blade, from which for a three-bladed rotor a total damping can be derived as

$$C_{aero} = \rho \pi \Omega \sum_{j=1}^3 \int_{r_0}^R c(r_j) r_j dr_j, \quad (5)$$

with R and r_0 being the rotor and hub radius, respectively.

This simple approximation shows the aerodynamic damping in fore-aft direction to be linearly dependent on the 55 rotational velocity Ω . Moreover, for a stand-still rotor, this damping vanishes completely. In practise, this aerodynamic damping is often presented as a percentage of the critical damping of the first fore-aft mode of the wind turbine, i.e. modal damping of the first mode. Typically, this aerodynamic damping can amount up to 4 to 5% of modal damping.

2.2. Quasi-stationary aerodynamics

The aerodynamic damping as given by Eq. (5) was derived on the basis of a number of crude approximations with respect to the aerodynamic interaction. In order to find a general definition of the added damping, a more elaborated aerodynamic model is adopted. To this end, the lift and drag forces are defined separately, and the contribution of the inertia force is accounted for too.

Considering first the drag force, only skin friction is accounted for. This, because the current analysis is restricted to attached flows, implying that the angle of attack is relatively small, and the contribution of the pressure drag is negligible. Based on this assumption, the drag force can be estimated by determining the viscous drag only:

$$\mathbf{F}_D(r_j, t) = \frac{1}{2} \rho c(r_j) C_D(r_j) \mathbf{W}(r_j, t) |\mathbf{W}(r_j, t)|, \quad (6)$$

The lift force $\mathbf{F}_L(r_j, t)$ acting on an aerofoil in an inviscid incompressible flow can be derived from the Kutta-Joukowski theorem:

$$\mathbf{F}_L(r_j, t) = \rho (\mathbf{\Gamma}(r_j, t) \times \mathbf{W}(r_j, t)), \quad (7)$$

where $\mathbf{\Gamma}(r_j, t)$ represents the circulatory flow round the body. Adopting the analogy of a thin plate, and assuming the static angle of attack $\alpha(r_j, t)$ to be small – a valid assumption if the analysis is limited to attached flows, the circulatory flow can be expressed as:

$$\mathbf{\Gamma}(r_j, t) = \pi c(r_j) \sin \alpha(r_j, t) |\mathbf{W}(r_j, t)| \mathbf{e}_{r_j}, \quad (8)$$

from which the static lift coefficient $C_L(r_j, t) = 2\pi \sin \alpha(r_j, t)$ can be identified. The circulatory flow is defined round the r_j axis, by means of the unit vector $\mathbf{e}_{r_j} = [0 \ 0 \ 1]^T$. The attack $\alpha(r_j, t)$ adheres the following definition:

$$\sin \alpha(r_j, t) = \frac{W_{y_j}(r_j, t)}{|\mathbf{W}(r_j, t)|}, \quad (9)$$

with $W_{y_j}(r_j, t)$ representing the relative flow velocity perpendicular to the symmetry axis of the aerofoil:

$$W_{y_j}(r_j, t) = \{\boldsymbol{\beta}_j(r_j)\}^T \mathbf{W}(r_j, t), \quad (10)$$

where

$$\boldsymbol{\beta}_j(r_j) = [-\sin(\beta(r_j) + \beta_{0;j}) \ \cos(\beta(r_j) + \beta_{0;j}) \ 0]^T, \quad (11)$$

70 with which the lift force $\mathbf{F}_L(r_j, t)$ can be expressed as:

$$\mathbf{F}_L(r_j, t) = \rho \pi c(r_j) \{\boldsymbol{\beta}_j(r_j)\}^T \mathbf{W}(r_j, t) (\mathbf{e}_{r_j} \times \mathbf{W}(r_j, t)). \quad (12)$$

In addition, an inertia force should be accounted for. This inertia force $\mathbf{F}_I(r_j, t)$ is aligned with the acceleration vector of the effective air flow field and can be derived from:

$$\mathbf{F}_I(r_j, t) = \rho \pi c(r_j)^2 \dot{\mathbf{W}}(r_j, t) \quad (13)$$

The vector $\mathbf{W}(r_j, t)$ can be thought of as a summation of vectors:

$$\mathbf{W}(r_j, t) = r_j (\mathbf{e}_{r_j} \times \boldsymbol{\Omega}) + \mathbf{W}_{X_j}(r_j, t) - \dot{\mathbf{u}}_{X_j}(r_j, t), \quad (14)$$

where $\boldsymbol{\Omega}$ represents the rotating of the aerofoil round the Y axis, $\mathbf{W}_{X_j}(r_j, t)$ the ambient airflow velocity, as experienced by the rotating rotor blades, and $\mathbf{u}_{X_j}(r_j, t)$ the structural displacement within the rotating local $X_j Y_j$ plane:

$$\boldsymbol{\Omega} = [0 \ -\Omega_Y \ 0]^T. \quad (15)$$

$$\mathbf{W}_{X_j}(r_j, t) = [W_{X_j}(r_j, t) \ W_{Y_j}(r_j, t) \ W_{r_j}(r_j, t)]^T. \quad (16)$$

$$\mathbf{u}_{X_j}(r_j, t) = [u_{X_j}(r_j, t) \ u_{Y_j}(r_j, t) \ u_{r_j}(r_j, t)]^T. \quad (17)$$

The overdot indicates a derivative with respect to time. By inclusion of this response term, the dependency of the aerodynamic forces on the structural response is explicitly accounted for.

80 The validity of the original expression is essentially restricted to 2D flows. Moreover, the presented force equations are in principle only valid for stationary flow conditions, implying that these expression do not account for the loss of the aerodynamic equilibrium after a disturbance of the flow. It should be noted, as was mentioned before, that the presented theory is only valid for attached flow conditions.

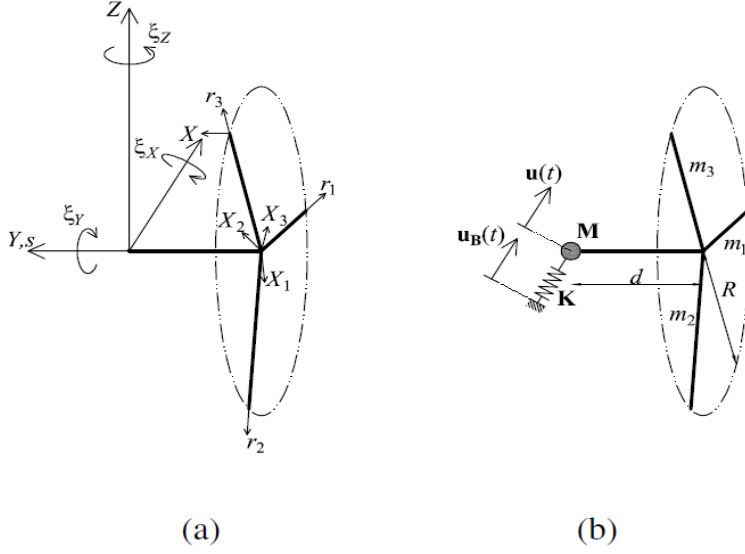


Figure 2: One-degree-of-freedom three-bladed rotor model, with (a) the definition of the model coefficients, and (b) the definition of the in-plane velocity components.

3. Model definition

85 3.1. Rigid rotor model

A model is defined to describe the dynamics of a rotating rotor of a wind turbine, accounting for the eccentricity of the rotational plane with respect to the longitudinal axis of the turbine tower. Figure 2 presents the model of a turbine rotor with radius R , while the hub has radius r_0 . In Figure 2(a), the geometry is presented within the fixed XYZ reference frame. By means of ξ_X , ξ_Y and ξ_Z , the rotations round each of the axis is indicated. The origin of the reference frame is located at the centre line of the turbine tower and the rotational axis of the rotor. The centre of rotation of the rotor is located at a distance d from the origin of the reference frame and lies under undeformed conditions on the Y axis. The three blades of the rotor are each described by the azimuth positions $\Psi_j(t)$ and the rotating reference frames X_j , Y_j and r_j , for $j = 1, 2, 3$.

Figure 2(b) shows the degree-of-freedom vector $\mathbf{u}(t)$, composed of the vectors $\mathbf{u}_X(t)$ and $\boldsymbol{\theta}(t)$:

$$\mathbf{u}(t) = [\mathbf{u}_X(t)^T \quad \boldsymbol{\theta}(t)^T]^T, \quad (18)$$

95 where $\mathbf{u}_X(t)$ contains the translations $u_X(t)$, $u_Y(t)$ and $u_Z(t)$ in the indicated directions, and $\boldsymbol{\theta}(t)$ the rotations $\theta_X(t)$, $\theta_Y(t)$ and $\theta_Z(t)$ round the indicated axes:

$$\mathbf{u}_X(t) = [u_X(t) \quad u_Y(t) \quad u_Z(t)]^T, \quad (19)$$

$$\boldsymbol{\theta}(t) = [\theta_X(t) \quad \theta_Y(t) \quad \theta_Z(t)]^T. \quad (20)$$

The stiffness matrix \mathbf{K}_T represents the static stiffness of the tower structure corresponding to the freedom of motion given by $\mathbf{u}(t)$. The 6×6 matrix, therefore, contains terms coupling the lateral and rotational motion:

$$\mathbf{K}_T = \begin{bmatrix} K_{XX} & 0 & 0 & 0 & R_{XY} & 0 \\ 0 & K_{YY} & 0 & R_{YX} & 0 & 0 \\ 0 & 0 & K_{ZZ} & 0 & 0 & 0 \\ 0 & K_{YX} & 0 & R_{XX} & 0 & 0 \\ K_{YX} & 0 & 0 & 0 & R_{YY} & 0 \\ 0 & 0 & 0 & 0 & 0 & R_{ZZ} \end{bmatrix}, \quad (21)$$

100 with the lateral stiffnesses K_{XX} , K_{YY} and K_{ZZ} corresponding to a lateral resistance to a lateral deflection in the indicated directions, and the rotational stiffnesses R_{XX} , R_{YY} and R_{ZZ} , corresponding to a rotational resistance to a rotation in the indicated directions. The coupling terms K_{XY} , K_{YX} define the lateral resistance to a rotation and R_{XY} , R_{YX} the rotational resistance to a lateral deflection, all with respect to the indicated directions. It can be seen that the motion in Z direction and the rotation round the Z axis are uncoupled. The inertia matrix \mathbf{M}_N defines the effective mass and mass moment of inertia of the nacelle and tower, corresponding to the principal vibrational modes that define the six degree-of-freedom system. It is assumed that the centre of gravity of the nacelle is positioned on the centre axis of the tower, implying that the matrix \mathbf{M}_N is diagonal:

$$\mathbf{M}_N = \begin{bmatrix} M_X & 0 & 0 & 0 & 0 & 0 \\ 0 & M_Y & 0 & 0 & 0 & 0 \\ 0 & 0 & M_Z & 0 & 0 & 0 \\ 0 & 0 & 0 & J_X & 0 & 0 \\ 0 & 0 & 0 & 0 & J_Y & 0 \\ 0 & 0 & 0 & 0 & 0 & J_Z \end{bmatrix}, \quad (22)$$

with M_X , M_Y and M_Z as the effective mass in the indicated direction and J_X , J_Y and J_Z the mass moment of inertia round the indicated axis.

110 The masses of the blades are considered separately as $m_j(r_j)$, being distributed along the blade axes r_j . The mass moment of inertia of the blades is neglected. Since the first natural frequency of the blades is generally much higher than the natural frequencies corresponding to the first bending modes of the complete structure, the blades can be assumed as rigid.

115 In the derivation of the equations of motion of the six degree-of-freedom system, base motions is accounted for. These motions are defined by the vector $\mathbf{u}_B(t)$ describe the imposed motions at the base of the model:

$$\mathbf{u}_B(t) = [u_{B;X}(t) \ u_{B;Y}(t) \ u_{B;Z}(t) \ \theta_{B;X}(t) \ \theta_{B;Y}(t) \ \theta_{B;Z}(t)]^T. \quad (23)$$

3.2. Equations of motion

The geometry of the turbine rotor as depicted in Figure 2(a) can be expressed in terms of the vector superposition $\mathbf{x}_0(t)$:

$$\begin{aligned} \mathbf{x}_0(t) &= \begin{bmatrix} 0 \\ s \\ 0 \end{bmatrix} + \sum_{j=1}^3 \begin{bmatrix} r_j \cos \Psi_j(t) \\ -d \\ -r_j \sin \Psi_j(t) \end{bmatrix} \\ &= \mathbf{x}_{N_0} + \mathbf{x}_{R_0}(t), \end{aligned} \quad (24)$$

120 defining the X , Y and Z coordinates, respectively, \mathbf{x}_{N_0} and $\mathbf{x}_{R_0}(t)$ define the geometry of the undeformed nacelle and rotor. The vector $\mathbf{x}(t)$ describes the deformed geometry of the turbine rotor, and results from translation and rotation of the initial geometry, making use of Eqs. (19) and (20):

$$\begin{aligned} \mathbf{x}(t) &= \mathbf{u}(t) + \mathbf{x}_0(t) + (\boldsymbol{\theta}(t) \times \mathbf{x}_0(t)) \\ &= \mathbf{x}_{N_0}(t) + \mathbf{x}_{R_0}(t). \end{aligned} \quad (25)$$

Here, $\mathbf{x}_N(t)$ defines the deformed geometry of the nacelle and $\mathbf{x}_R(t)$ the deformed geometry of the rotor:

$$\mathbf{x}_N(t) = \mathbf{u}_X(t) + \mathbf{x}_{N_0} + (\boldsymbol{\theta}(t) \times \mathbf{x}_{N_0}(t)), \quad (26)$$

$$\mathbf{x}_R(t) = \mathbf{u}_X(t) + \mathbf{x}_{R_0} + (\boldsymbol{\theta}(t) \times \mathbf{x}_{R_0}(t)). \quad (27)$$

Since rotations defined in a three-dimensional frame of reference are non-commutative, the small-angle assumption is adopted from the beginning, implying that $\sin x \approx x$, $\cos x \approx 1$ and $x^2 \ll x$.

From $\mathbf{x}(t)$, the potential energy $P(t)$ and the kinematic energy $T(t)$ of the system can be defined straightforwardly:

$$P(t) = \frac{1}{2} [\{\mathbf{u}(t)\}^T - \{\mathbf{u}_B(t)\}^T] \mathbf{K}_T [\mathbf{u}(t) - \mathbf{u}_B(t)], \quad (28)$$

$$T(t) = \frac{1}{2} \{\dot{\mathbf{u}}(t)\}^T \mathbf{M}_N \dot{\mathbf{u}}(t) + \sum_{j=1}^3 \int_{r_0}^R \{\dot{\mathbf{x}}_R(t)\}^T \dot{\mathbf{x}}_R(t) m_j(r_j) dr_j, \quad (29)$$

where use has been made of the concentrated definitions of \mathbf{K}_T and \mathbf{M}_N . The overdots in Eq. (29) indicate a derivative to time. Hamilton's principle [?] allows for the derivation of the equations of motion from the potential energy and the kinematic energy from the Lagrangian $L(t) = T(t) - P(t)$:

$$\left[\mathbf{M}_N + \sum_{j=1}^3 \mathbf{M}_j \right] \ddot{\mathbf{u}}(t) + \sum_{j=1}^3 \mathbf{C}_j \dot{\mathbf{u}}(t) + \left[\mathbf{K}_T + \sum_{j=1}^3 \mathbf{K}_j \right] \mathbf{u}(t) = \mathbf{K}_T \mathbf{u}_B(t), \quad (30)$$

with

$$\mathbf{M}_j = \int_{r_0}^R m_j r_j \begin{bmatrix} \frac{1}{r_j} & 0 & 0 & 0 & \sin \Psi_j(t) & \frac{d}{r_j} \\ 0 & \frac{1}{r_j} & 0 & -\sin \Psi_j(t) & 0 & \cos \Psi_j(t) \\ 0 & 0 & \frac{1}{r_j} & -\frac{d}{r_j} & -\cos \Psi_j(t) & 0 \\ 0 & -\sin \Psi_j(t) & -\frac{d}{r_j} & r_j \sin^2 \Psi_j(t) + \frac{d^2}{r_j} & d \cos \Psi_j(t) & -r_j \sin \Psi_j(t) \cos \Psi_j(t) \\ \sin \Psi_j(t) & 0 & -\cos \Psi_j(t) & d \cos \Psi_j(t) & r_j & d \sin \Psi_j(t) \\ \frac{d}{r_j} & \cos \Psi_j(t) & 0 & -r_j \sin \Psi_j(t) \cos \Psi_j(t) & d \sin \Psi_j(t) & r_j \cos^2 \Psi_j(t) + \frac{d^2}{r_j} \end{bmatrix} dr_j, \quad (31)$$

$$\mathbf{C}_j = \int_{r_0}^R m_j \Omega r_j \begin{bmatrix} 0 & 0 & 0 & 0 & 2 \cos \Psi_j(t) & 0 \\ 0 & 0 & 0 & -2 \cos \Psi_j(t) & 0 & -2 \sin \Psi_j(t) \\ 0 & 0 & 0 & 0 & 2 \sin \Psi_j(t) & 0 \\ 0 & -\cos \Psi_j(t) & 0 & 3r_j \sin \Psi_j(t) \cos \Psi_j(t) & -2d \sin \Psi_j(t) & r_j (2 \sin^2 \Psi_j(t) - \cos^2 \Psi_j(t)) \\ \cos \Psi_j(t) & 0 & \sin \Psi_j(t) & -d \sin \Psi_j(t) & 0 & d \cos \Psi_j(t) \\ 0 & -\sin \Psi_j(t) & 0 & r_j (\sin^2 \Psi_j(t) - 2 \cos^2 \Psi_j(t)) & 2d \cos \Psi_j(t) & -3r_j \sin \Psi_j(t) \cos \Psi_j(t) \end{bmatrix} dr_j, \quad (32)$$

$$\mathbf{K}_j = \int_{r_0}^R m_j \Omega^2 r_j \begin{bmatrix} 0 & 0 & 0 & 0 & -\sin \Psi_j(t) & 0 \\ 0 & 0 & 0 & \sin \Psi_j(t) & 0 & -\cos \Psi_j(t) \\ 0 & 0 & 0 & 0 & \cos \Psi_j(t) & 0 \\ 0 & 0 & 0 & r_j (2 \cos^2 \Psi_j(t) - 1) & -d \cos \Psi_j(t) & 2r_j \sin \Psi_j(t) \cos \Psi_j(t) \\ 0 & 0 & 0 & 0 & 0 & 0 \\ 0 & 0 & 0 & 2r_j \sin \Psi_j(t) \cos \Psi_j(t) & -d \sin \Psi_j(t) & -r_j (2 \cos^2 \Psi_j(t) - 1) 0 \end{bmatrix} dr_j. \quad (33)$$

The matrices C_j and K_j correspond to the Coriolis and the centrifugal force components, respectively. These matrices are asymmetric because of the description of the rotating blade elements in a fixed frame of reference and both matrices vanish if the rotor is not rotating. For a rotating rotor, the three rotor matrices are time-dependent. This time dependency disappears if the three blades are identical:

$$\sum_{j=1}^3 \mathbf{M}_j = \int_{r_0}^R m_j r_j \begin{bmatrix} \frac{3}{r_j} & 0 & 0 & 0 & 0 & 3 \frac{d}{r_j} \\ 0 & \frac{3}{r_j} & 0 & 0 & 0 & 0 \\ 0 & 0 & \frac{3}{r_j} & -3 \frac{d}{r_j} & 0 & 0 \\ 0 & 0 & -3 \frac{d}{r_j} & \frac{3}{2} r_j + 3 \frac{d^2}{r_j} & 0 & 0 \\ 0 & 0 & 0 & 0 & 3r_j & 0 \\ 3 \frac{d}{r_j} & 0 & 0 & 0 & 0 & \frac{3}{2} r_j + 3 \frac{d^2}{r_j} \end{bmatrix} dr_j, \quad (34)$$

$$\sum_{j=1}^3 \mathbf{C}_j = \int_{r_0}^R m_j \Omega r_j \begin{bmatrix} 0 & 0 & 0 & 0 & 0 & 0 \\ 0 & 0 & 0 & 0 & 0 & 0 \\ 0 & 0 & 0 & 0 & 0 & 0 \\ 0 & 0 & 0 & 0 & 0 & \frac{3}{2}r_j \\ 0 & 0 & 0 & 0 & 0 & 0 \\ 0 & 0 & 0 & -\frac{3}{2}r_j & 0 & 0 \end{bmatrix} dr_j, \quad (35)$$

$$\sum_{j=1}^3 \mathbf{K}_j = \mathbf{0}_{6 \times 6}. \quad (36)$$

140 *3.3. Aerodynamic excitation*

Figure 1(c) defined the drag and lift force contributions $\mathbf{F}_D(r_j, t)$ and $\mathbf{F}_L(r_j, t)$, acting on a blade section, within the rotating $X_j Y_j r_j$ reference frame of the j th blade. The inertia force $\mathbf{F}_I(r_j, t)$ can be depicted in this frame too, as it acts in line with the relative wind acceleration $\dot{\mathbf{W}}(r_j, t)$. These forces are defined such, that they contain X_j and Y_j components, while the r_j component equals zero:

$$\mathbf{F}_{X_j}(r_j, t) = \begin{bmatrix} F_{D;X_j}(r_j, t) + F_{L;X_j}(r_j, t) + F_{I;X_j}(r_j, t) \\ F_{D;Y_j}(r_j, t) + F_{L;Y_j}(r_j, t) + F_{I;Y_j}(r_j, t) \\ 0 \end{bmatrix} = \begin{bmatrix} F_{X_j}(r_j, t) \\ F_{Y_j}(r_j, t) \\ 0 \end{bmatrix}. \quad (37)$$

145 The rotating reference frames in Figure 1(c) correspond with the rotating frames $X_j Y_j r_j$ in Figure 2. The orientation of these local reference frames depends on the deformation of the structure. In absence of such deformations, the local reference frames, denoted by \mathbf{X}_{j_0} , can be obtained from the global reference frame through the translation $\mathbf{T}_{\mathbf{X} \rightarrow \mathbf{X}_{j_0}}$ and the rotation $\mathbf{R}_{\mathbf{X} \rightarrow \mathbf{X}_{j_0}}(t)$:

$$\begin{aligned} \mathbf{X}_{j_0}(t) &= \mathbf{R}_{\mathbf{X} \rightarrow \mathbf{X}_{j_0}}(t) (\mathbf{T}_{\mathbf{X} \rightarrow \mathbf{X}_{j_0}} + \mathbf{X}) = \\ &= \begin{bmatrix} 0 \\ d \\ 0 \end{bmatrix} + \begin{bmatrix} -\sin \Psi_j(t) & 0 & -\cos \Psi_j(t) \\ 0 & 1 & 0 \\ \cos \Psi_j(t) & 0 & -\sin \Psi_j(t) \end{bmatrix} \begin{bmatrix} X \\ Y \\ Z \end{bmatrix} \\ &= \mathbf{T}_{\mathbf{X} \rightarrow \mathbf{X}_{j_0}} + \mathbf{R}_{\mathbf{X} \rightarrow \mathbf{X}_{j_0}}(t) \mathbf{X}. \end{aligned} \quad (38)$$

Adopting the rotor geometry $\mathbf{x}_{R_0}(t)$ from Eq. (24), the transformation to the rotating frames of reference brings:

$$\begin{aligned} \mathbf{x}_{R_{j_0}}(t) &= \mathbf{T}_{\mathbf{X} \rightarrow \mathbf{X}_{j_0}} + \mathbf{R}_{\mathbf{X} \rightarrow \mathbf{X}_{j_0}}(t) \mathbf{x}_{R_0}(t) \\ &= \begin{bmatrix} 0 \\ d \\ 0 \end{bmatrix} + \begin{bmatrix} -\sin \Psi_j(t) & 0 & -\cos \Psi_j(t) \\ 0 & 1 & 0 \\ \cos \Psi_j(t) & 0 & -\sin \Psi_j(t) \end{bmatrix} \begin{bmatrix} r_j \cos \Psi_j(t) \\ -d \\ -r_j \sin \Psi_j(t) \end{bmatrix} = \begin{bmatrix} 0 \\ 0 \\ r_j \end{bmatrix}, \end{aligned} \quad (39)$$

150 describing the rotor geometry in the rotating frames of reference.

The model of the rotating rotor is defined in the global frame of reference, see Eq. (30), and therefore requires the formulation of the aerodynamic forces within this global coordinate system. Apart from the rotor rotation, the orientation of the local reference frames, and likewise the aerodynamic forces by the structural deformation too. With the application of the transformations defined by Eqs. (19) and (20), the orientations of the local rotating reference frames can be obtained:

$$\begin{aligned} \mathbf{x}_{R_j}(t) &= \mathbf{R}_{\mathbf{X} \rightarrow \mathbf{X}_{j_0}}(t) (\mathbf{T}_{\mathbf{X} \rightarrow \mathbf{X}_{j_0}} + \mathbf{x}_R(t)) \\ &= \mathbf{R}_{\mathbf{X} \rightarrow \mathbf{X}_{j_0}}(t) (\mathbf{T}_{\mathbf{X} \rightarrow \mathbf{X}_{j_0}} + \mathbf{u}(t) + \mathbf{x}_{R_0}(t) + (\boldsymbol{\theta}(t) \times \mathbf{x}_{R_0}(t))) \\ &= \mathbf{R}_{\mathbf{X} \rightarrow \mathbf{X}_{j_0}}(t) \mathbf{u}(t) + \mathbf{T}_{\mathbf{X} \rightarrow \mathbf{X}_{j_0}} + \mathbf{R}_{\mathbf{X} \rightarrow \mathbf{X}_j}(t) \mathbf{x}_{R_0}(t), \end{aligned} \quad (40)$$

with

$$\begin{aligned}\mathbf{R}_{\mathbf{X} \rightarrow \mathbf{x}_j}(t) &= \mathbf{R}_{\mathbf{X} \rightarrow \mathbf{x}_{j_0}}(t) + \mathbf{R}_{\mathbf{X} \rightarrow \mathbf{x}_{j_0}}(t)\mathbf{Q}_\theta(t) \\ &= \mathbf{R}_{\mathbf{X} \rightarrow \mathbf{x}_{j_0}}(t)(\mathbf{I}_{3 \times 3} + \mathbf{Q}_\theta(t)),\end{aligned}\quad (41)$$

where $\mathbf{I}_{3 \times 3}$ is the 3×3 identity matrix. The cross product is replaced by the matrix multiplication of \mathbf{x}_{R_0} with the skew-symmetric matrix $\mathbf{Q}_\theta(t)$:

$$\mathbf{Q}_\theta(t) = [\boldsymbol{\theta}(t)]_\times = \begin{bmatrix} 0 & -\theta_Z(t) & \theta_Y(t)(t) \\ \theta_Z(t) & 0 & -\theta_X(t) \\ -\theta_Y(t) & \theta_X(t) & 0 \end{bmatrix}. \quad (42)$$

The matrix $\mathbf{R}_{\mathbf{X} \rightarrow \mathbf{x}_j}(t)$ defines the orientation of the local rotating reference frames \mathbf{X}_j , including the effect of the structural deformation. This matrix provides a basis to express the locally-defined aerodynamic forces in terms of the global XYZ reference frame:

$$\begin{aligned}\mathbf{F}_X(r_j, t) &= \left\{ \mathbf{R}_{\mathbf{X} \rightarrow \mathbf{x}_j}(t) \right\}^{-1} \mathbf{F}_{X_j}(r_j, t) \\ &= \left\{ \mathbf{R}_{\mathbf{X} \rightarrow \mathbf{x}_{j_0}}(t)(\mathbf{I}_{3 \times 3} + \mathbf{Q}_\theta(t)) \right\}^{-1} \mathbf{F}_{X_j}(r_j, t) \\ &= \{(\mathbf{I}_{3 \times 3} + \mathbf{Q}_\theta(t))\}^{-1} \left\{ \mathbf{R}_{\mathbf{X} \rightarrow \mathbf{x}_{j_0}}(t) \right\}^{-1} \mathbf{F}_{X_j}(r_j, t) \\ &= (\mathbf{I}_{3 \times 3} + \{\mathbf{Q}_\theta(t)\}^T) \left\{ \mathbf{R}_{\mathbf{X} \rightarrow \mathbf{x}_{j_0}}(t) \right\}^{-1} \mathbf{F}_{X_j}(r_j, t) \\ &= \left[\left\{ \mathbf{R}_{\mathbf{X} \rightarrow \mathbf{x}_{j_0}}(t) \right\}^{-1} + \{\mathbf{Q}_\theta(t)\}^T \left\{ \mathbf{R}_{\mathbf{X} \rightarrow \mathbf{x}_{j_0}}(t) \right\}^{-1} \right] \mathbf{F}_{X_j}(r_j, t) \\ &= \left[\left\{ \mathbf{R}_{\mathbf{X} \rightarrow \mathbf{x}_{j_0}}(t) \right\}^{-1} - \{\mathbf{Q}_\theta(t)\} \left\{ \mathbf{R}_{\mathbf{X} \rightarrow \mathbf{x}_{j_0}}(t) \right\}^{-1} \right] \mathbf{F}_{X_j}(r_j, t),\end{aligned}\quad (43)$$

in which use is made of the assumption of small angles. The moment round the origin $\mathbf{T}_O(r_j, t)$ can subsequently be obtained from:

$$\mathbf{T}_O(r_j, t) = \mathbf{x}_R(t) \times \mathbf{F}_X(r_j, t). \quad (44)$$

The total resulting aerodynamic excitation $\mathbf{F}(t)$ can be found from integrating the separate blade contributions over the blade length and adding each contribution:

$$\mathbf{F}(t) = \sum_{j=1}^3 \int_{r_0}^R \left[\mathbf{F}_X(r_j, t) \right] d r_j. \quad (45)$$

The aerodynamic forces are a function of the relative wind velocity $\mathbf{W}(r_j, t)$, as defined by Eq. (14). First, this requires the formulation of the ambient wind field in terms of the local rotating reference frames:

$$\begin{aligned}\mathbf{W}_{X_j}(r_j, t) &= \mathbf{R}_{\mathbf{X} \rightarrow \mathbf{x}_j}(t)\mathbf{W}_X(r_j, t) \\ &= \mathbf{R}_{\mathbf{X} \rightarrow \mathbf{x}_{j_0}}(t)\mathbf{W}_X(r_j, t) + (\boldsymbol{\theta}(t) \times \mathbf{W}_X(r_j, t))\end{aligned}\quad (46)$$

Second, taking $\mathbf{x}_{R_{j_0}}(r_j, t)$ from Eq. (39), the structural velocity can be found from the deformation $\mathbf{u}_{X_j}(r_j, t)$, defined within the local rotating frames of reference:

$$\begin{aligned}\mathbf{u}_{X_j}(r_j, t) &= \mathbf{x}_{R_j}(r_j, t) - \mathbf{x}_{R_{j_0}}(r_j, t) \\ &= \mathbf{R}_{\mathbf{X} \rightarrow \mathbf{x}_{j_0}}(t)\mathbf{u}_X(t) + \mathbf{T}_{\mathbf{X} \rightarrow \mathbf{x}_{j_0}} + \mathbf{R}_{\mathbf{X} \rightarrow \mathbf{x}_j}(t)\mathbf{x}_{R_0}(t) - (\mathbf{T}_{\mathbf{X} \rightarrow \mathbf{x}_{j_0}} + \mathbf{R}_{\mathbf{X} \rightarrow \mathbf{x}_{j_0}}(t)\mathbf{x}_{R_0}(t)) \\ &= \mathbf{R}_{\mathbf{X} \rightarrow \mathbf{x}_{j_0}}(t)\mathbf{u}_X(t) + (\mathbf{R}_{\mathbf{X} \rightarrow \mathbf{x}_j}(t) - \mathbf{R}_{\mathbf{X} \rightarrow \mathbf{x}_{j_0}}(t))\mathbf{x}_{R_0}(t) \\ &= \mathbf{R}_{\mathbf{X} \rightarrow \mathbf{x}_{j_0}}(t)\mathbf{u}_X(t) + (\mathbf{R}_{\mathbf{X} \rightarrow \mathbf{x}_{j_0}}(t) + \mathbf{R}_{\mathbf{X} \rightarrow \mathbf{x}_{j_0}}(t)\mathbf{Q}_\theta(t) - \mathbf{R}_{\mathbf{X} \rightarrow \mathbf{x}_{j_0}}(t))\mathbf{x}_{R_0}(t) \\ &= \mathbf{R}_{\mathbf{X} \rightarrow \mathbf{x}_{j_0}}(t)\mathbf{u}_X(t) + \mathbf{R}_{\mathbf{X} \rightarrow \mathbf{x}_{j_0}}(t)\mathbf{Q}_\theta(t)\mathbf{x}_{R_0}(t) \\ &= \mathbf{R}_{\mathbf{X} \rightarrow \mathbf{x}_{j_0}}(t)\mathbf{u}_X(t) + \mathbf{R}_{\mathbf{X} \rightarrow \mathbf{x}_{j_0}}(t)(\boldsymbol{\theta}(t) \times \mathbf{x}_{R_0}(t)) \\ &= \mathbf{R}_{\mathbf{X} \rightarrow \mathbf{x}_{j_0}}(t)\mathbf{u}_X(t) - \mathbf{R}_{\mathbf{X} \rightarrow \mathbf{x}_{j_0}}(t)\mathbf{Q}_{x_{R_0}}(t)\boldsymbol{\theta}(t),\end{aligned}\quad (47)$$

¹⁷⁰ with the skew-symmetric matrix $\mathbf{Q}_{x_{R_0}}(t)$ replacing the cross product:

$$\mathbf{Q}_{x_{R_0}}(t) = [\mathbf{x}_{R_0}(t)]_x = \begin{bmatrix} 0 & r_j \sin \Psi_j(t) & -d \\ -r_j \sin \Psi_j(t) & 0 & -r_j \cos \Psi_j(t) \\ d & r_j \cos \Psi_j(t) & 0 \end{bmatrix}. \quad (48)$$

The structural velocity $\dot{\mathbf{u}}_{X_j}(r_j, t)$ and acceleration $\ddot{\mathbf{u}}_{X_j}(r_j, t)$ can subsequently be obtained from

$$\begin{aligned} \dot{\mathbf{u}}_{X_j}(r_j, t) &= \dot{\mathbf{R}}_{X \rightarrow X_{j_0}}(t)\mathbf{u}_X(t) + \mathbf{R}_{X \rightarrow X_{j_0}}(t)\dot{\mathbf{u}}_X(t) \\ &\quad + \dot{\mathbf{R}}_{X \rightarrow X_{j_0}}(t)(\boldsymbol{\theta}(t) \times \mathbf{x}_{R_0}(t)) + \mathbf{R}_{X \rightarrow X_{j_0}}(t)[(\dot{\boldsymbol{\theta}}(t) \times \mathbf{x}_{R_0}(t)) + (\boldsymbol{\theta}(t) \times \dot{\mathbf{x}}_{R_0}(t))] \\ &= \dot{\mathbf{R}}_{X \rightarrow X_{j_0}}(t)\mathbf{u}_X(t) + \mathbf{R}_{X \rightarrow X_{j_0}}(t)\dot{\mathbf{u}}_X(t) - [\dot{\mathbf{R}}_{X \rightarrow X_{j_0}}(t)\mathbf{Q}_{x_{R_0}}(t) + \mathbf{R}_{X \rightarrow X_{j_0}}(t)\dot{\mathbf{Q}}_{x_{R_0}}(t)]\boldsymbol{\theta}(t) - \mathbf{R}_{X \rightarrow X_{j_0}}(t)\mathbf{Q}_{x_{R_0}}(t)\dot{\boldsymbol{\theta}}(t), \end{aligned} \quad (49)$$

$$\begin{aligned} \ddot{\mathbf{u}}_{X_j}(r_j, t) &= \ddot{\mathbf{R}}_{X \rightarrow X_{j_0}}(t)\mathbf{u}_X(t) + 2\dot{\mathbf{R}}_{X \rightarrow X_{j_0}}(t)\dot{\mathbf{u}}_X(t) + \mathbf{R}_{X \rightarrow X_{j_0}}(t)\ddot{\mathbf{u}}_X(t) \\ &\quad + \ddot{\mathbf{R}}_{X \rightarrow X_{j_0}}(t)(\boldsymbol{\theta}(t) \times \mathbf{x}_{R_0}(t)) + 2\dot{\mathbf{R}}_{X \rightarrow X_{j_0}}(t)[(\dot{\boldsymbol{\theta}}(t) \times \mathbf{x}_{R_0}(t)) + (\boldsymbol{\theta}(t) \times \dot{\mathbf{x}}_{R_0}(t))] \\ &\quad + \mathbf{R}_{X \rightarrow X_{j_0}}(t)[(\ddot{\boldsymbol{\theta}}(t) \times \mathbf{x}_{R_0}(t)) + 2(\dot{\boldsymbol{\theta}}(t) \times \dot{\mathbf{x}}_{R_0}(t)) + (\boldsymbol{\theta}(t) \times \ddot{\mathbf{x}}_{R_0}(t))] \\ &= \ddot{\mathbf{R}}_{X \rightarrow X_{j_0}}(t)\mathbf{u}_X(t) + 2\dot{\mathbf{R}}_{X \rightarrow X_{j_0}}(t)\dot{\mathbf{u}}_X(t) + \mathbf{R}_{X \rightarrow X_{j_0}}(t)\ddot{\mathbf{u}}_X(t) \\ &\quad - [\ddot{\mathbf{R}}_{X \rightarrow X_{j_0}}(t)\mathbf{Q}_{x_{R_0}}(t) + 2\dot{\mathbf{R}}_{X \rightarrow X_{j_0}}(t)\dot{\mathbf{Q}}_{x_{R_0}}(t) + \mathbf{R}_{X \rightarrow X_{j_0}}(t)\ddot{\mathbf{Q}}_{x_{R_0}}(t)]\boldsymbol{\theta}(t) \\ &\quad - 2[\dot{\mathbf{R}}_{X \rightarrow X_{j_0}}(t)\mathbf{Q}_{x_{R_0}}(t) + \mathbf{R}_{X \rightarrow X_{j_0}}(t)\dot{\mathbf{Q}}_{x_{R_0}}(t)]\dot{\boldsymbol{\theta}}(t) - [\mathbf{R}_{X \rightarrow X_{j_0}}(t)\mathbf{Q}_{x_{R_0}}(t)]\ddot{\boldsymbol{\theta}}(t). \end{aligned} \quad (50)$$

For the further analysis of the aerodynamic excitation, the third entries of $\mathbf{W}_{X_j}(r_j, t)$ and $\mathbf{u}_{X_j}(r_j, t)$ can be set to zero.

3.4. Added mass and damping

¹⁷⁵ The drag and lift forces, as introduced in Section 2.2 by Eqs. (6) and Eqs. (12), depend non-linearly on the relative velocity $\mathbf{W}(r_j, t)$, including the structural motion $\mathbf{u}(r_j, t)$. The contribution of the structural motion to the aerodynamic excitation can be assessed by deriving added mass and damping matrices. This assessment requires linearization of the forcing expressions.

3.4.1. Drag force linearization

¹⁸⁰ Substitution of Eqs. (14) and (46) into the non-linear drag force given by Eq. (6), brings

$$\begin{aligned} \mathbf{F}_{D;X_j}(r_j, t) &= \frac{1}{2}\rho c(r_j)C_D(r_j)\mathbf{W}(r_j, t)|\mathbf{W}(r_j, t)| \\ &= \frac{1}{2}\rho c(r_j)C_D(r_j)\left(r_j(\mathbf{e}_{r_j} \times \boldsymbol{\Omega}) + \mathbf{W}_{X_j}(r_j, t) - \dot{\mathbf{u}}_{X_j}(r_j, t)\right)|r_j(\mathbf{e}_{r_j} \times \boldsymbol{\Omega}) + \mathbf{W}_{X_j}(r_j, t) - \dot{\mathbf{u}}_{X_j}(r_j, t)| \\ &= \frac{1}{2}\rho c(r_j)C_D(r_j)\left(r_j(\mathbf{e}_{r_j} \times \boldsymbol{\Omega}) + \mathbf{R}_{X \rightarrow X_{j_0}}(t)\mathbf{W}_X(r_j, t) + (\boldsymbol{\theta}(t) \times \mathbf{W}_X(r_j, t)) - \dot{\mathbf{u}}_{X_j}(r_j, t)\right) \\ &\quad |r_j(\mathbf{e}_{r_j} \times \boldsymbol{\Omega}) + \mathbf{R}_{X \rightarrow X_{j_0}}(t)\mathbf{W}_X(r_j, t) + (\boldsymbol{\theta}(t) \times \mathbf{W}_X(r_j, t)) - \dot{\mathbf{u}}_{X_j}(r_j, t)|. \end{aligned} \quad (51)$$

Linearization of a function $\mathbf{f} = (\mathbf{c} + \mathbf{x} + \mathbf{y})|\mathbf{c} + \mathbf{x} + \mathbf{y}|$ with respect to \mathbf{x} and \mathbf{y} , where $\mathbf{c} = [c_1 \quad c_2]^T$, $\mathbf{x} = [x_1 \quad x_2]^T$ and $\mathbf{y} = [y_1 \quad y_2]^T$, gives

$$\begin{aligned} \mathbf{f} &= (\mathbf{c} + \mathbf{x} + \mathbf{y})|\mathbf{c} + \mathbf{x} + \mathbf{y}| \\ &\approx |\mathbf{c}|\mathbf{c} + |\mathbf{c}|(\mathbf{x} + \mathbf{y}) + \{\mathbf{c}\}^T \frac{\mathbf{x} + \mathbf{y}}{|\mathbf{c}|}\mathbf{c}. \end{aligned} \quad (52)$$

In addition, $\mathbf{W}_{X_{j_0}}(r_j, t)$ is derived from

$$\mathbf{W}_{X_{j_0}}(r_j, t) = \mathbf{R}_{X \rightarrow X_{j_0}}(t)\mathbf{W}_X(r_j, t). \quad (53)$$

From here, the vector $\mathbf{V}_{X_{j0}}(r_j, t)$ is adopted to refer to the air flow resulting from the rotational velocity and the ambient wind field:

$$\mathbf{V}_{X_{j0}}(r_j, t) = r_j (\mathbf{e}_{r_j} \times \boldsymbol{\Omega}) + \mathbf{W}_{X_{j0}}(r_j, t). \quad (54)$$

On this basis, linearization of $\mathbf{F}_{D;X_j}(r_j, t)$ gives

$$\begin{aligned} \mathbf{F}_{D;X_j}(r_j, t) &\approx \frac{1}{2} \rho c(r_j) C_D(r_j) \left[|\mathbf{V}_{X_{j0}}(r_j, t)| \mathbf{V}_{X_{j0}}(r_j, t) \right. \\ &\quad + |\mathbf{V}_{X_{j0}}(r_j, t)| \{(\boldsymbol{\theta}(t) \times \mathbf{W}_X(r_j, t)) - \dot{\mathbf{u}}_{X_j}(r_j, t)\} \\ &\quad \left. + \{\mathbf{V}_{X_{j0}}(r_j, t)\}^T \frac{(\boldsymbol{\theta}(t) \times \mathbf{W}_X(r_j, t)) - \dot{\mathbf{u}}_{X_j}(r_j, t)}{|\mathbf{V}_{X_{j0}}(r_j, t)|} \mathbf{V}_{X_{j0}}(r_j, t) \right] \\ &\approx \frac{1}{2} \rho c(r_j) C_D(r_j) \left[|\mathbf{V}_{X_{j0}}(r_j, t)| \{\mathbf{V}_{X_{j0}}(r_j, t)\} \right. \\ &\quad + \left\{ \frac{\mathbf{V}_{X_{j0}}(r_j, t) \{\mathbf{V}_{X_{j0}}(r_j, t)\}^T}{|\mathbf{V}_{X_{j0}}(r_j, t)|} + |\mathbf{V}_{X_{j0}}(r_j, t)| \mathbf{I}_{3 \times 3} \right\} (\boldsymbol{\theta}(t) \times \mathbf{W}_X(r_j, t)) \\ &\quad \left. - \left\{ \frac{\mathbf{V}_{X_{j0}}(r_j, t) \{\mathbf{V}_{X_{j0}}(r_j, t)\}^T}{|\mathbf{V}_{X_{j0}}(r_j, t)|} + |\mathbf{V}_{X_{j0}}(r_j, t)| \mathbf{I}_{3 \times 3} \right\} \dot{\mathbf{u}}_{X_j}(r_j, t) \right]. \end{aligned} \quad (55)$$

In order to isolate the vector $\boldsymbol{\theta}(t)$, the skew-symmetric matrix $\mathbf{Q}_W(r_j, t)$ is introduced:

$$\mathbf{Q}_W(r_j, t) = [\mathbf{W}_X(r_j, t)]_x = \begin{bmatrix} 0 & -W_Z(r_j, t) & W_Y(r_j, t) \\ W_Z(r_j, t) & 0 & -W_X(r_j, t) \\ -W_Y(r_j, t) & W_X(r_j, t) & 0 \end{bmatrix}, \quad (56)$$

allowing for the following reformulation of $\mathbf{F}_{D;X_j}(r_j, t)$:

$$\begin{aligned} \mathbf{F}_{D;X_j}(r_j, t) &\approx \frac{1}{2} \rho c(r_j) C_D(r_j) \left[|\mathbf{V}_{X_{j0}}(r_j, t)| \mathbf{V}_{X_{j0}}(r_j, t) \right. \\ &\quad - \left\{ \frac{\mathbf{V}_{X_{j0}}(r_j, t) \{\mathbf{V}_{X_{j0}}(r_j, t)\}^T}{|\mathbf{V}_{X_{j0}}(r_j, t)|} + |\mathbf{V}_{X_{j0}}(r_j, t)| \mathbf{I}_{3 \times 3} \right\} \mathbf{Q}_W(r_j, t) \boldsymbol{\theta}(t) \\ &\quad \left. - \left\{ \frac{\mathbf{V}_{X_{j0}}(r_j, t) \{\mathbf{V}_{X_{j0}}(r_j, t)\}^T}{|\mathbf{V}_{X_{j0}}(r_j, t)|} + |\mathbf{V}_{X_{j0}}(r_j, t)| \mathbf{I}_{3 \times 3} \right\} \dot{\mathbf{u}}_{X_j}(r_j, t) \right], \end{aligned} \quad (57)$$

Within the global frame of reference, the drag force $\mathbf{F}_{D;X}(r_j, t)$ is given by

$$\begin{aligned} \mathbf{F}_{D;X}(r_j, t) &= \frac{1}{2} \rho c(r_j) C_D(r_j) \{\mathbf{R}_{X \rightarrow X_j}(t)\}^{-1} \mathbf{W}(r_j, t) |\mathbf{W}(r_j, t)| \\ &\approx \frac{1}{2} \rho c(r_j) C_D(r_j) \left[\{\mathbf{R}_{X \rightarrow X_{j0}}(t)\}^{-1} - \mathbf{Q}_\theta(t) \{\mathbf{R}_{X \rightarrow X_{j0}}(t)\}^{-1} \right] \\ &\quad \left[|\mathbf{V}_{X_{j0}}(r_j, t)| \mathbf{V}_{X_{j0}}(r_j, t) - \left\{ \frac{\mathbf{V}_{X_{j0}}(r_j, t) \{\mathbf{V}_{X_{j0}}(r_j, t)\}^T}{|\mathbf{V}_{X_{j0}}(r_j, t)|} + |\mathbf{V}_{X_{j0}}(r_j, t)| \mathbf{I}_{3 \times 3} \right\} \mathbf{Q}_W(r_j, t) \boldsymbol{\theta}(t) \right. \\ &\quad \left. - \left\{ \frac{\mathbf{V}_{X_{j0}}(r_j, t) \{\mathbf{V}_{X_{j0}}(r_j, t)\}^T}{|\mathbf{V}_{X_{j0}}(r_j, t)|} + |\mathbf{V}_{X_{j0}}(r_j, t)| \mathbf{I}_{3 \times 3} \right\} \dot{\mathbf{u}}_{X_j}(r_j, t) \right]. \end{aligned} \quad (58)$$

¹⁹⁰ Omitting the non-linear terms with respect to $\boldsymbol{\theta}(t)$ and $\dot{\mathbf{u}}_{X_j}(t)$, the expression for $\mathbf{F}_{D;X}(r_j, t)$ reduces to

$$\begin{aligned} \mathbf{F}_{D;X}(r_j, t) &\approx \frac{1}{2} \rho c(r_j) C_D(r_j) \\ &\left[|\mathbf{V}_{X_{j;0}}(r_j, t)| \left\{ \mathbf{R}_{X \rightarrow X_{j_0}}(t) \right\}^{-1} \mathbf{V}_{X_{j;0}}(r_j, t) - \left\{ \mathbf{R}_{X \rightarrow X_{j_0}}(t) \right\}^{-1} \left\{ \frac{\mathbf{V}_{X_{j;0}}(r_j, t) \left\{ \mathbf{V}_{X_{j;0}}(r_j, t) \right\}^T}{|\mathbf{V}_{X_{j;0}}(r_j, t)|} + |\mathbf{V}_{X_{j;0}}(r_j, t)| \mathbf{I}_{3 \times 3} \right\} \mathbf{Q}_W(r_j, t) \boldsymbol{\theta}(t) \right. \\ &- \left. \left\{ \mathbf{R}_{X \rightarrow X_{j_0}}(t) \right\}^{-1} \left\{ \frac{\mathbf{V}_{X_{j;0}}(r_j, t) \left\{ \mathbf{V}_{X_{j;0}}(r_j, t) \right\}^T}{|\mathbf{V}_{X_{j;0}}(r_j, t)|} + |\mathbf{V}_{X_{j;0}}(r_j, t)| \mathbf{I}_{3 \times 3} \right\} \dot{\mathbf{u}}_{X_j}(r_j, t) \right. \\ &- \left. \left. - |\mathbf{V}_{X_{j;0}}(r_j, t)| \mathbf{Q}_\theta(t) \left\{ \mathbf{R}_{X \rightarrow X_{j_0}}(t) \right\}^{-1} \mathbf{V}_{X_{j;0}}(r_j, t) \right] \right. \end{aligned} \quad (59)$$

$\boldsymbol{\theta}(t)$ is isolated from the $\mathbf{Q}_\theta(t)$ matrix multiplication in the following manner:

$$\begin{aligned} -\mathbf{Q}_\theta(t) \left\{ \mathbf{R}_{X \rightarrow X_{j_0}}(t) \right\}^{-1} \mathbf{V}_{X_{j;0}}(r_j, t) &= -\boldsymbol{\theta}(t) \times \left(\left\{ \mathbf{R}_{X \rightarrow X_{j_0}}(t) \right\}^{-1} \mathbf{V}_{X_{j;0}}(r_j, t) \right) \\ &= \left(\left\{ \mathbf{R}_{X \rightarrow X_{j_0}}(t) \right\}^{-1} \mathbf{V}_{X_{j;0}}(r_j, t) \right) \times \boldsymbol{\theta}(t) \\ &= \mathbf{Q}_{1;j}(r_j, t) \boldsymbol{\theta}(t), \end{aligned} \quad (60)$$

where the skew-symmetric matrix $\mathbf{Q}_{1;j}(r_j, t)$ is given by

$$\mathbf{Q}_{1;j}(r_j, t) = \left[\left\{ \mathbf{R}_{X \rightarrow X_{j_0}}(t) \right\}^{-1} \mathbf{V}_{X_{j;0}}(r_j, t) \right]_\times, \quad (61)$$

The vector $\boldsymbol{\theta}(t)$ can now as follows be isolated:

$$\begin{aligned}
\mathbf{F}_{D;X}(r_j, t) &\approx \frac{1}{2} \rho c(r_j) C_D(r_j) \\
&\left[\left| \mathbf{V}_{X_{j,0}}(r_j, t) \right| \left\{ \mathbf{R}_{X \rightarrow X_{j,0}}(t) \right\}^{-1} \mathbf{V}_{X_{j,0}}(r_j, t) - \left\{ \mathbf{R}_{X \rightarrow X_{j,0}}(t) \right\}^{-1} \left\{ \frac{\mathbf{V}_{X_{j,0}}(r_j, t) \left\{ \mathbf{V}_{X_{j,0}}(r_j, t) \right\}^T}{\left| \mathbf{V}_{X_{j,0}}(r_j, t) \right|} + \left| \mathbf{V}_{X_{j,0}}(r_j, t) \right| \mathbf{I}_{3 \times 3} \right\} \mathbf{Q}_W(r_j, t) \boldsymbol{\theta}(t) \right. \\
&\quad \left. - \left\{ \mathbf{R}_{X \rightarrow X_{j,0}}(t) \right\}^{-1} \left\{ \frac{\mathbf{V}_{X_{j,0}}(r_j, t) \left\{ \mathbf{V}_{X_{j,0}}(r_j, t) \right\}^T}{\left| \mathbf{V}_{X_{j,0}}(r_j, t) \right|} + \left| \mathbf{V}_{X_{j,0}}(r_j, t) \right| \mathbf{I}_{3 \times 3} \right\} \dot{\mathbf{u}}_{X_j}(r_j, t) + \left| \mathbf{V}_{X_{j,0}}(r_j, t) \right| \mathbf{Q}_{1;j}(r_j, t) \boldsymbol{\theta}(t) \right] \\
&\approx \frac{1}{2} \rho c(r_j) C_D(r_j) \\
&\left[\left| \mathbf{V}_{X_{j,0}}(r_j, t) \right| \left\{ \mathbf{R}_{X \rightarrow X_{j,0}}(t) \right\}^{-1} \mathbf{V}_{X_{j,0}}(r_j, t) \right. \\
&\quad \left. - \left\{ \mathbf{R}_{X \rightarrow X_{j,0}}(t) \right\}^{-1} \left\{ \frac{\mathbf{V}_{X_{j,0}}(r_j, t) \left\{ \mathbf{V}_{X_{j,0}}(r_j, t) \right\}^T}{\left| \mathbf{V}_{X_{j,0}}(r_j, t) \right|} + \left| \mathbf{V}_{X_{j,0}}(r_j, t) \right| \mathbf{I}_{3 \times 3} \right\} \dot{\mathbf{u}}_{X_j}(r_j, t) \right. \\
&\quad \left. - \left\{ \mathbf{R}_{X \rightarrow X_{j,0}}(t) \right\}^{-1} \left\{ \frac{\mathbf{V}_{X_{j,0}}(r_j, t) \left\{ \mathbf{V}_{X_{j,0}}(r_j, t) \right\}^T}{\left| \mathbf{V}_{X_{j,0}}(r_j, t) \right|} + \left| \mathbf{V}_{X_{j,0}}(r_j, t) \right| \mathbf{I}_{3 \times 3} \right\} \mathbf{Q}_W(r_j, t) \boldsymbol{\theta}(t) + \left| \mathbf{V}_{X_{j,0}}(r_j, t) \right| \mathbf{Q}_{1;j}(r_j, t) \boldsymbol{\theta}(t) \right] \\
&\approx \frac{1}{2} \rho c(r_j) C_D(r_j) \\
&\left[\left| \mathbf{V}_{X_{j,0}}(r_j, t) \right| \left\{ \mathbf{R}_{X \rightarrow X_{j,0}}(t) \right\}^{-1} \mathbf{V}_{X_{j,0}}(r_j, t) \right. \\
&\quad \left. - \left\{ \mathbf{R}_{X \rightarrow X_{j,0}}(t) \right\}^{-1} \left\{ \frac{\mathbf{V}_{X_{j,0}}(r_j, t) \left\{ \mathbf{V}_{X_{j,0}}(r_j, t) \right\}^T}{\left| \mathbf{V}_{X_{j,0}}(r_j, t) \right|} + \left| \mathbf{V}_{X_{j,0}}(r_j, t) \right| \mathbf{I}_{3 \times 3} \right\} \dot{\mathbf{u}}_{X_j}(r_j, t) \right. \\
&\quad \left. - \left\{ \mathbf{R}_{X \rightarrow X_{j,0}}(t) \right\}^{-1} \left\{ \frac{\mathbf{V}_{X_{j,0}}(r_j, t) \left\{ \mathbf{V}_{X_{j,0}}(r_j, t) \right\}^T}{\left| \mathbf{V}_{X_{j,0}}(r_j, t) \right|} \mathbf{Q}_W(r_j, t) + \left| \mathbf{V}_{X_{j,0}}(r_j, t) \right| (\mathbf{Q}_W(r_j, t) - \mathbf{R}_{X \rightarrow X_{j,0}}(t) \mathbf{Q}_{1;j}(r_j, t)) \right\} \boldsymbol{\theta}(t) \right]. \tag{62}
\end{aligned}$$

Subsequent substitution of Eq. (49) results into the full formulation of the linearized drag force $\mathbf{F}_{D;X}(r_j, t)$ within the global frame of reference:

$$\begin{aligned}
\mathbf{F}_{D;X}(r_j, t) &\approx \frac{1}{2} \rho c(r_j) C_D(r_j) \left[\left| \mathbf{V}_{X_{j,0}}(r_j, t) \right| \left\{ \mathbf{R}_{X \rightarrow X_{j,0}}(t) \right\}^{-1} \mathbf{V}_{X_{j,0}}(r_j, t) \right. \\
&\quad - \left\{ \mathbf{R}_{X \rightarrow X_{j,0}}(t) \right\}^{-1} \left\{ \frac{\mathbf{V}_{X_{j,0}}(r_j, t) \left\{ \mathbf{V}_{X_{j,0}}(r_j, t) \right\}^T}{\left| \mathbf{V}_{X_{j,0}}(r_j, t) \right|} \mathbf{Q}_W(r_j, t) + \left| \mathbf{V}_{X_{j,0}}(r_j, t) \right| (\mathbf{Q}_W(r_j, t) - \mathbf{R}_{X \rightarrow X_{j,0}}(t) \mathbf{Q}_{1;j}(r_j, t)) \right\} \boldsymbol{\theta}(t) \\
&\quad - \left\{ \mathbf{R}_{X \rightarrow X_{j,0}}(t) \right\}^{-1} \left\{ \frac{\mathbf{V}_{X_{j,0}}(r_j, t) \left\{ \mathbf{V}_{X_{j,0}}(r_j, t) \right\}^T}{\left| \mathbf{V}_{X_{j,0}}(r_j, t) \right|} + \left| \mathbf{V}_{X_{j,0}}(r_j, t) \right| \mathbf{I}_{3 \times 3} \right\} \\
&\quad \left. \left\{ \dot{\mathbf{R}}_{X \rightarrow X_{j,0}}(t) \mathbf{u}_X(t) + \mathbf{R}_{X \rightarrow X_{j,0}}(t) \dot{\mathbf{u}}_X(t) - (\dot{\mathbf{R}}_{X \rightarrow X_{j,0}}(t) \mathbf{Q}_{x_{R_{0;j}}}(r_j, t) + \mathbf{R}_{X \rightarrow X_{j,0}}(t) \dot{\mathbf{Q}}_{x_{R_{0;j}}}(r_j, t)) \boldsymbol{\theta}(t) - \mathbf{R}_{X \rightarrow X_{j,0}}(t) \mathbf{Q}_{x_{R_{0;j}}}(r_j, t) \dot{\boldsymbol{\theta}}(t) \right\} \right] \\
&\approx \frac{1}{2} \rho c(r_j) C_D(r_j) \left[\left\{ \mathbf{R}_{X \rightarrow X_{j,0}}(t) \right\}^{-1} \left| \mathbf{V}_{X_{j,0}}(r_j, t) \right| \mathbf{V}_{X_{j,0}}(r_j, t) \right. \\
&\quad - \left\{ \mathbf{R}_{X \rightarrow X_{j,0}}(t) \right\}^{-1} \left\{ \frac{\mathbf{V}_{X_{j,0}}(r_j, t) \left\{ \mathbf{V}_{X_{j,0}}(r_j, t) \right\}^T}{\left| \mathbf{V}_{X_{j,0}}(r_j, t) \right|} \mathbf{Q}_W(r_j, t) + \left| \mathbf{V}_{X_{j,0}}(r_j, t) \right| (\mathbf{Q}_W(r_j, t) - \mathbf{R}_{X \rightarrow X_{j,0}}(t) \mathbf{Q}_{1;j}(r_j, t)) \right\} \boldsymbol{\theta}(t) \\
&\quad - \left\{ \mathbf{R}_{X \rightarrow X_{j,0}}(t) \right\}^{-1} \left\{ \frac{\mathbf{V}_{X_{j,0}}(r_j, t) \left\{ \mathbf{V}_{X_{j,0}}(r_j, t) \right\}^T}{\left| \mathbf{V}_{X_{j,0}}(r_j, t) \right|} + \left| \mathbf{V}_{X_{j,0}}(r_j, t) \right| \mathbf{I}_{3 \times 3} \right\} \dot{\mathbf{R}}_{X \rightarrow X_{j,0}}(t) \mathbf{u}_X(t) \\
&\quad - \left\{ \left\{ \mathbf{R}_{X \rightarrow X_{j,0}}(t) \right\}^{-1} \frac{\mathbf{V}_{X_{j,0}}(r_j, t) \left\{ \mathbf{V}_{X_{j,0}}(r_j, t) \right\}^T}{\left| \mathbf{V}_{X_{j,0}}(r_j, t) \right|} \mathbf{R}_{X \rightarrow X_{j,0}}(t) + \left| \mathbf{V}_{X_{j,0}}(r_j, t) \right| \mathbf{I}_{3 \times 3} \right\} \dot{\mathbf{u}}_X(t) \\
&\quad + \left\{ \mathbf{R}_{X \rightarrow X_{j,0}}(t) \right\}^{-1} \left\{ \frac{\mathbf{V}_{X_{j,0}}(r_j, t) \left\{ \mathbf{V}_{X_{j,0}}(r_j, t) \right\}^T}{\left| \mathbf{V}_{X_{j,0}}(r_j, t) \right|} + \left| \mathbf{V}_{X_{j,0}}(r_j, t) \right| \mathbf{I}_{3 \times 3} \right\} (\dot{\mathbf{R}}_{X \rightarrow X_{j,0}}(t) \mathbf{Q}_{x_{R_{0;j}}}(t) + \mathbf{R}_{X \rightarrow X_{j,0}}(t) \dot{\mathbf{Q}}_{x_{R_{0;j}}}(t)) \boldsymbol{\theta}(t) \\
&\quad \left. + \left\{ \left\{ \mathbf{R}_{X \rightarrow X_{j,0}}(t) \right\}^{-1} \frac{\mathbf{V}_{X_{j,0}}(r_j, t) \left\{ \mathbf{V}_{X_{j,0}}(r_j, t) \right\}^T}{\left| \mathbf{V}_{X_{j,0}}(r_j, t) \right|} \mathbf{R}_{X \rightarrow X_{j,0}}(t) + \left| \mathbf{V}_{X_{j,0}}(r_j, t) \right| \mathbf{I}_{3 \times 3} \right\} \mathbf{Q}_{x_{R_{0;j}}}(t) \dot{\boldsymbol{\theta}}(t) \right]. \tag{63}
\end{aligned}$$

Adopting the matrices $\mathbf{K}_{F_D}(r_j, t)$ and $\mathbf{C}_{F_D}(r_j, t)$, the linearized drag force can be rewritten as

$$\mathbf{F}_{D;X}(r_j, t) \approx \frac{1}{2} \rho c(r_j) C_D(r_j) \left[\left| \mathbf{V}_{X_{j,0}}(r_j, t) \right| \left\{ \mathbf{R}_{X \rightarrow X_{j,0}}(t) \right\}^{-1} \mathbf{V}_{X_{j,0}}(r_j, t) + \mathbf{K}_{F_D}(r_j, t) \mathbf{u}(t) + \mathbf{C}_{F_D}(r_j, t) \dot{\mathbf{u}}(t) \right], \tag{64}$$

with

$$\mathbf{K}_{F_D}(r_j, t) = \left[\begin{array}{c} \left(-\left\{ \mathbf{R}_{X \rightarrow X_{j,0}}(t) \right\}^{-1} \frac{\mathbf{V}_{X_{j,0}}(r_j, t) \left\{ \mathbf{V}_{X_{j,0}}(r_j, t) \right\}^T}{\left| \mathbf{V}_{X_{j,0}}(r_j, t) \right|} \dot{\mathbf{R}}_{X \rightarrow X_{j,0}}(t) - \left| \mathbf{V}_{X_{j,0}}(r_j, t) \right| \left\{ \mathbf{R}_{X \rightarrow X_{j,0}}(t) \right\}^{-1} \dot{\mathbf{R}}_{X \rightarrow X_{j,0}}(t) \right)^T \\ -\left\{ \mathbf{R}_{X \rightarrow X_{j,0}}(t) \right\}^{-1} \frac{\mathbf{V}_{X_{j,0}}(r_j, t) \left\{ \mathbf{V}_{X_{j,0}}(r_j, t) \right\}^T}{\left| \mathbf{V}_{X_{j,0}}(r_j, t) \right|} \mathbf{Q}_W(r_j, t) \\ -\left| \mathbf{V}_{X_{j,0}}(r_j, t) \right| \left\{ \mathbf{R}_{X \rightarrow X_{j,0}}(t) \right\}^{-1} (\mathbf{Q}_W(r_j, t) - \mathbf{R}_{X \rightarrow X_{j,0}}(t) \mathbf{Q}_{1;j}(r_j, t)) \\ +\left\{ \mathbf{R}_{X \rightarrow X_{j,0}}(t) \right\}^{-1} \frac{\mathbf{V}_{X_{j,0}}(r_j, t) \left\{ \mathbf{V}_{X_{j,0}}(r_j, t) \right\}^T}{\left| \mathbf{V}_{X_{j,0}}(r_j, t) \right|} (\dot{\mathbf{R}}_{X \rightarrow X_{j,0}}(t) \mathbf{Q}_{x_{R_{0;j}}}(t) + \mathbf{R}_{X \rightarrow X_{j,0}}(t) \dot{\mathbf{Q}}_{x_{R_{0;j}}}(t)) \\ +\left| \mathbf{V}_{X_{j,0}}(r_j, t) \right| \left(\left\{ \mathbf{R}_{X \rightarrow X_{j,0}}(t) \right\}^{-1} \dot{\mathbf{R}}_{X \rightarrow X_{j,0}}(t) \mathbf{Q}_{x_{R_{0;j}}}(r_j, t) + \dot{\mathbf{Q}}_{x_{R_{0;j}}}(r_j, t) \right) \end{array} \right]^T \tag{65}$$

$$\mathbf{C}_{F_D}(r_j, t) = \begin{bmatrix} -\left(\{\mathbf{R}_{X \rightarrow X_{j_0}}(t)\}^{-1} \frac{\mathbf{V}_{X_{j_0}}(r_j, t) \{\mathbf{V}_{X_{j_0}}(r_j, t)\}^T}{|\mathbf{V}_{X_{j_0}}(r_j, t)|} \mathbf{R}_{X \rightarrow X_{j_0}}(t) + |\mathbf{V}_{X_{j_0}}(r_j, t)| \mathbf{I}_{3 \times 3}\right)^T \\ \left(\{\mathbf{R}_{X \rightarrow X_{j_0}}(t)\}^{-1} \frac{\mathbf{V}_{X_{j_0}}(r_j, t) \{\mathbf{V}_{X_{j_0}}(r_j, t)\}^T}{|\mathbf{V}_{X_{j_0}}(r_j, t)|} \mathbf{R}_{X \rightarrow X_{j_0}}(t) \mathbf{Q}_{X_{R_{0,j}}}(r_j, t) + |\mathbf{V}_{X_{j_0}}(r_j, t)| \mathbf{Q}_{X_{R_{0,j}}}(r_j, t)\right)^T \end{bmatrix}^T \quad (66)$$

These resulting matrices $\mathbf{K}_{F_D}(r_j, t)$ and $\mathbf{C}_{F_D}(r_j, t)$ contain time-dependent coefficients. In the resulting force expression, Eq. (45), these matrices appear as $\sum_{j=1}^3 \mathbf{K}_{F_D}(r_j, t)$ and $\sum_{j=1}^3 \mathbf{C}_{F_D}(r_j, t)$. It can be shown that for a symmetric rotor with identical blades, and a time-independent ambient wind field $\mathbf{W}_X(r_j, t) = [0 \quad W_Y \quad 0]^T = \mathbf{W}_Y$, where W_Y is a constant wind velocity in the global Y direction, these matrix summations render time-independent. After adopting $r_j = r$, the time-dependent vector $\mathbf{V}_{X_{j_0}}(r, t)$ can now be expressed as

$$\begin{aligned} \mathbf{V}_{X_{j_0}}(r, t) &= r(\mathbf{e}_r \times \boldsymbol{\Omega}) + \mathbf{W}_{X_{j_0}}(r_j, t) \\ &= r(\mathbf{e}_r \times \boldsymbol{\Omega}) + \mathbf{W}_Y \\ &= [\Omega_Y r \quad W_Y \quad 0]^T \\ &= \mathbf{V}_{X_0}(r). \end{aligned} \quad (67)$$

On this basis,

$$\frac{\mathbf{V}_{X_j}(r) \{\mathbf{V}_{X_j}(r)\}^T}{|\mathbf{V}_{X_j}(r)|} = \frac{1}{\sqrt{(\Omega_Y r)^2 + W_Y^2}} \begin{bmatrix} \Omega_Y^2 r^2 & \Omega_Y r W_Y & 0 \\ \Omega_Y r W_Y & W_Y^2 & 0 \\ 0 & 0 & 0 \end{bmatrix}. \quad (68)$$

and

$$\mathbf{Q}_W(r, t) = \begin{bmatrix} 0 & 0 & W_Y \\ 0 & 0 & 0 \\ -W_Y & 0 & 0 \end{bmatrix}, \quad (69)$$

$$\mathbf{Q}_1(r, t) = \begin{bmatrix} 0 & \Omega_Y r \sin \Psi_j(t) & W_Y \\ -\Omega_Y r \sin \Psi_j(t) & 0 & -\Omega_Y r \cos \Psi_j(t) \\ -W_Y & \Omega_Y r \cos \Psi_j(t) & 0 \end{bmatrix}. \quad (70)$$

The matrix summations $\sum_{j=1}^3 \mathbf{K}_{F_D}(r, t)$ and $\sum_{j=1}^3 \mathbf{C}_{F_D}(r, t)$ can now be rendered time-independent into

$$\begin{aligned} \sum_{j=1}^3 \mathbf{K}_{F_D}(r, t) &= \frac{3}{2 \sqrt{(\Omega_Y r)^2 + W_Y^2}} \left[\begin{pmatrix} 0 & 0 & \Omega_Y^3 r^2 \\ 0 & 0 & 0 \\ -\Omega_Y^3 r^2 & 0 & -\Omega_Y^2 r^2 W_Y \end{pmatrix} \begin{pmatrix} -\Omega_Y^3 r_j^2 d & 0 & 0 \\ 0 & 0 & -2\Omega_Y r W_Y^2 \\ \Omega_Y^2 r^2 W_Y & 0 & -\Omega_Y^3 r^2 d \end{pmatrix} \right. \\ &\quad \left. + 3 \sqrt{(\Omega_Y r)^2 + W_Y^2} \left[\begin{pmatrix} 0 & 0 & \Omega_Y \\ 0 & 0 & 0 \\ -\Omega_Y & 0 & 0 \end{pmatrix} \begin{pmatrix} -\Omega_Y d & 0 & 0 \\ 0 & 0 & 0 \\ 0 & 0 & -\Omega_Y d \end{pmatrix} \right] \right], \end{aligned} \quad (71)$$

$$\begin{aligned} \sum_{j=1}^3 \mathbf{C}_{F_D}(r, t) &= \frac{3}{2 \sqrt{(\Omega_Y r)^2 + W_Y^2}} \left[\begin{pmatrix} -\Omega_Y^2 r^2 & 0 & 0 \\ 0 & -2W_Y^2 & 0 \\ 0 & 0 & -\Omega_Y^2 r^2 \end{pmatrix} \begin{pmatrix} \Omega_Y r^2 W_Y & 0 & -\Omega_Y^2 r^2 d \\ 0 & -2\Omega_Y r^2 W_Y & 0 \\ \Omega_Y^2 r^2 d & 0 & \Omega_Y r^2 W_Y \end{pmatrix} \right. \\ &\quad \left. + 3 \sqrt{(\Omega_Y r)^2 + W_Y^2} \left[-\mathbf{I}_{3 \times 3} \begin{pmatrix} -\Omega_Y d & 0 & -d \\ 0 & 0 & 0 \\ d & \Omega_Y r & -\Omega_Y d \end{pmatrix} \right] \right], \end{aligned} \quad (72)$$

3.4.2. Drag moment linearization

From the drag force, defined in the global frame of reference, the moment round the origin can be expressed as follows:

$$\begin{aligned}
\mathbf{T}_{O;D}(r_j, t) &= \mathbf{x}_{R;j}(r_j, t) \times \mathbf{F}_{D;X}(r_j, t) \\
&\approx \frac{1}{2} \rho c(r_j) C_D(r_j) \left\{ \mathbf{u}_X(t) + \mathbf{x}_{R_{0;j}}(r_j, t) + (\boldsymbol{\theta}(t) \times \mathbf{x}_{R_{0;j}}(r_j, t)) \right\} \\
&\quad \times \left[|\mathbf{V}_{X_{j;0}}(r_j, t)| \left\{ \mathbf{R}_{X \rightarrow X_{j;0}}(t) \right\}^{-1} \mathbf{V}_{X_{j;0}}(r_j, t) + \mathbf{K}_{FD}(r_j, t) \mathbf{u}(t) + \mathbf{C}_{FD}(r_j, t) \dot{\mathbf{u}}(t) \right] \\
&\approx \frac{1}{2} \rho c(r_j) C_D(r_j) \left\{ \mathbf{u}_X(t) + \mathbf{x}_{R_{0;j}}(r_j, t) - \mathbf{Q}_{x_{R_{0;j}}}(r_j, t) \boldsymbol{\theta}(t) \right\} \\
&\quad \times \left[|\mathbf{V}_{X_{j;0}}(r_j, t)| \left\{ \mathbf{R}_{X \rightarrow X_{j;0}}(t) \right\}^{-1} \mathbf{V}_{X_{j;0}}(r_j, t) + \mathbf{K}_{FD}(r_j, t) \mathbf{u}(t) + \mathbf{C}_{FD}(r_j, t) \dot{\mathbf{u}}(t) \right]
\end{aligned} \tag{73}$$

Omitting the non-linear terms with respect to $\mathbf{u}(t)$ and $\dot{\mathbf{u}}(t)$, the expression for $\mathbf{T}_{O;D}(r_j, t)$ reduces to

$$\begin{aligned}
\mathbf{T}_{O;D}(r_j, t) &\approx \frac{1}{2} \rho c(r_j) C_D(r_j) \left(\mathbf{u}_X(t) \times \left[|\mathbf{V}_{X_{j;0}}(r_j, t)| \left\{ \mathbf{R}_{X \rightarrow X_{j;0}}(t) \right\}^{-1} \mathbf{V}_{X_{j;0}}(r_j, t) \right] \right) \\
&\quad + \frac{1}{2} \rho c(r_j) C_D(r_j) \left(\mathbf{x}_{R_{0;j}}(r_j, t) \times \left[|\mathbf{V}_{X_{j;0}}(r_j, t)| \left\{ \mathbf{R}_{X \rightarrow X_{j;0}}(t) \right\}^{-1} \mathbf{V}_{X_{j;0}}(r_j, t) + \mathbf{K}_{FD}(r_j, t) \mathbf{u}(t) + \mathbf{C}_{FD}(r_j, t) \dot{\mathbf{u}}(t) \right] \right) \\
&\quad - \frac{1}{2} \rho c(r_j) C_D(r_j) \left(\mathbf{Q}_{x_{R_{0;j}}}(r_j, t) \boldsymbol{\theta}(t) \times \left[|\mathbf{V}_{X_{j;0}}(r_j, t)| \left\{ \mathbf{R}_{X \rightarrow X_{j;0}}(t) \right\}^{-1} \mathbf{V}_{X_{j;0}}(r_j, t) \right] \right).
\end{aligned} \tag{74}$$

Isolation of $\mathbf{u}_X(t)$ and $\boldsymbol{\theta}(t)$ requires the introduction of the skew-symmetric matrix $\mathbf{Q}_{1;j}(r_j, t)$, with which $\mathbf{T}_{O;D}(r_j, t)$ can be rewritten as

$$\begin{aligned}
\mathbf{T}_{O;D}(r_j, t) &\approx -\frac{1}{2} \rho c(r_j) C_D(r_j) |\mathbf{V}_{X_{j;0}}(r_j, t)| \mathbf{Q}_{1;j}(r_j, t) \mathbf{u}_X(t) \\
&\quad + \frac{1}{2} \rho c(r_j) C_D(r_j) \left[-|\mathbf{V}_{X_{j;0}}(r_j, t)| \mathbf{Q}_{1;j}(r_j, t) \mathbf{x}_{R_{0;j}}(r_j, t) + (\mathbf{x}_{R_{0;j}}(r_j, t) \times \mathbf{K}_{FD}(r_j, t) \mathbf{u}(t)) + (\mathbf{x}_{R_{0;j}}(r_j, t) \times \mathbf{C}_{FD}(r_j, t) \dot{\mathbf{u}}(t)) \right] \\
&\quad + \frac{1}{2} \rho c(r_j) C_D(r_j) |\mathbf{V}_{X_{j;0}}(r_j, t)| \mathbf{Q}_{1;j}(r_j, t) \mathbf{Q}_{x_{R_{0;j}}}(r_j, t) \boldsymbol{\theta}(t) \\
&\approx -\frac{1}{2} \rho c(r_j) C_D(r_j) |\mathbf{V}_{X_{j;0}}(r_j, t)| \mathbf{Q}_{1;j}(r_j, t) \mathbf{u}_X(t) \\
&\quad + \frac{1}{2} \rho c(r_j) C_D(r_j) \left[-|\mathbf{V}_{X_{j;0}}(r_j, t)| \mathbf{Q}_{1;j}(r_j, t) \mathbf{x}_{R_{0;j}} + \mathbf{Q}_{x_{R_{0;j}}}(r_j, t) \mathbf{K}_{FD}(r_j, t) \mathbf{u}(t) + \mathbf{Q}_{x_{R_{0;j}}}(r_j, t) \mathbf{C}_{FD}(r_j, t) \dot{\mathbf{u}}(t) \right] \\
&\quad + \frac{1}{2} \rho c(r_j) C_D(r_j) |\mathbf{V}_{X_{j;0}}(r_j, t)| \mathbf{Q}_{1;j}(r_j, t) \mathbf{Q}_{x_{R_{0;j}}}(r_j, t) \boldsymbol{\theta}(t) \\
&\approx \frac{1}{2} \rho c(r_j) C_D(r_j) \left[-|\mathbf{V}_{X_{j;0}}(r_j, t)| \mathbf{Q}_{1;j}(r_j, t) \mathbf{x}_{R_{0;j}}(r_j, t) \right. \\
&\quad \left. + \mathbf{Q}_{x_{R_{0;j}}}(r_j, t) \mathbf{K}_{FD}(r_j, t) \mathbf{u}(t) + \mathbf{Q}_{x_{R_{0;j}}}(r_j, t) \mathbf{C}_{FD}(r_j, t) \dot{\mathbf{u}}(t) - |\mathbf{V}_{X_{j;0}}(r_j, t)| \mathbf{Q}_{1;j}(r_j, t) \mathbf{u}_X(t) + |\mathbf{V}_{X_{j;0}}(r_j, t)| \mathbf{Q}_{1;j}(r_j, t) \mathbf{Q}_{x_{R_{0;j}}}(r_j, t) \boldsymbol{\theta}(t) \right].
\end{aligned} \tag{75}$$

Adopting the matrices $\mathbf{K}_{TD}(r_j, t)$ and $\mathbf{C}_{TD}(r_j, t)$, the linearized moment from the drag force can be rewritten as

$$\begin{aligned}
\mathbf{T}_{O;D}(r_j, t) &\approx \frac{1}{2} \rho c(r_j) C_D(r_j) \left[-|\mathbf{V}_{X_{j;0}}(r_j, t)| \mathbf{Q}_1(r_j, t) \mathbf{x}_{R_{0;j}}(r_j, t) + \mathbf{K}_{TD}(r_j, t) \mathbf{u}(t) + \mathbf{C}_{TD}(r_j, t) \dot{\mathbf{u}}(t) \right] \\
&\approx \frac{1}{2} \rho c(r_j) C_D(r_j) \left[\mathbf{Q}_{x_{R_{0;j}}}(r_j, t) \left\{ \mathbf{R}_{X \rightarrow X_{j;0}}(t) \right\}^{-1} |\mathbf{V}_{X_{j;0}}(r_j, t)| \mathbf{V}_{X_{j;0}}(r_j, t) + \mathbf{K}_{TD}(r_j, t) \mathbf{u}(t) + \mathbf{C}_{TD}(r_j, t) \dot{\mathbf{u}}(t) \right],
\end{aligned} \tag{76}$$

with

$$\mathbf{K}_{T_D}(r_j, t) = \mathbf{Q}_{x_{R_0}}(t) \mathbf{K}_{F_D}(r_j, t) + |\mathbf{V}_{X_{j,0}}(r_j, t)| \begin{bmatrix} -\mathbf{Q}_{1,j}(r_j, t) & \mathbf{Q}_{1,j}(r_j, t) \mathbf{Q}_{x_{R_0,j}}(r_j, t) \end{bmatrix}, \quad (77)$$

$$\mathbf{C}_{T_D}(r_j, t) = \mathbf{Q}_{x_{R_0,j}}(r_j, t) \mathbf{C}_{F_D}(r_j, t). \quad (78)$$

For a symmetric rotor with identical blades and a time-independent ambient wind field, the matrix multiplications $\sum_{j=1}^3 \mathbf{K}_{T_D}(r, t)$ and $\sum_{j=1}^3 \mathbf{C}_{T_D}(r, t)$ can be rendered time-independent:

$$\begin{aligned} \sum_{j=1}^3 \mathbf{K}_{T_D}(r, t) &= \frac{3}{2\sqrt{(\Omega_Y r)^2 + W_Y^2}} \left[\begin{pmatrix} \Omega_Y^3 r^2 d & 0 & -\Omega_Y^2 r^2 W_Y \\ 0 & 0 & 0 \\ \Omega_Y^2 r^2 W_Y & 0 & \Omega_Y^3 r^2 d \end{pmatrix} \begin{pmatrix} 0 & 0 & \Omega_Y^3 r^2 d^2 + \Omega_Y r^2 W_Y^2 \\ 0 & 0 & -2\Omega_Y^2 r^3 W_Y \\ -\Omega_Y^3 r^2 d^2 - \Omega_Y r^2 W_Y^2 & 0 & 0 \end{pmatrix} \right] \\ &\quad + 3\sqrt{(\Omega_Y r)^2 + W_Y^2} \left[\begin{pmatrix} \Omega_Y d & 0 & -W_Y \\ 0 & 0 & 0 \\ W_Y & 0 & \Omega_Y d \end{pmatrix} \begin{pmatrix} W_Y d & 0 & \frac{3}{2}\Omega_Y r^2 + \Omega_Y d^2 \\ 0 & 0 & 0 \\ -\frac{3}{2}\Omega_Y r^2 - \Omega_Y d^2 & 0 & W_Y d \end{pmatrix} \right], \end{aligned} \quad (79)$$

$$\begin{aligned} \sum_{j=1}^3 \mathbf{C}_{T_D}(r, t) &= \frac{3}{2\sqrt{(\Omega_Y r)^2 + W_Y^2}} \left[\begin{pmatrix} \Omega_Y r^2 W_Y & 0 & \Omega_Y^2 r^2 d \\ 0 & -2\Omega_Y r^2 W_Y & 0 \\ -\Omega_Y^2 r^2 d & 0 & \Omega_Y r^2 W_Y \end{pmatrix} \begin{pmatrix} r_j^2 (\Omega_Y^2 d^2 + W_Y^2) & 0 & 0 \\ 0 & -2\Omega_Y^2 r^4 & 0 \\ 0 & 0 & r^2 (\Omega_Y^2 d^2 + W_Y^2) \end{pmatrix} \right] \\ &\quad + 3\sqrt{(\Omega_Y r)^2 + W_Y^2} \left[\begin{pmatrix} 0 & 0 & d \\ 0 & 0 & 0 \\ -d & 0 & 0 \end{pmatrix} \begin{pmatrix} -\frac{1}{2}r^2 - d^2 & 0 & 0 \\ 0 & -r^2 & 0 \\ 0 & 0 & -\frac{1}{2}r^2 - d^2 \end{pmatrix} \right]. \end{aligned} \quad (80)$$

The resulting drag excitation $\mathbf{F}_D(t)$, accounting for both forces and moments, can be expressed as

$$\mathbf{F}_D(t) \approx \sum_{j=1}^3 \int_{r_0}^R \frac{1}{2} \rho c(r_j) C_D(r_j) \left\{ |\mathbf{V}_{X_{j,0}}(r_j, t)| \begin{bmatrix} \mathbf{I}_{3 \times 3} \\ \mathbf{Q}_{x_{R_0,j}}(r_j, t) \end{bmatrix} \{\mathbf{R}_{x \rightarrow x_{j,0}}(t)\}^{-1} \mathbf{V}_{X_{j,0}}(r_j, t) \right. \quad (81)$$

$$\left. + \mathbf{K}_D(r_j, t) \mathbf{u}(t) + \mathbf{C}_D(r_j, t) \dot{\mathbf{u}}(t) \right\} dr_j, \quad (82)$$

with

$$\mathbf{K}_D(r_j, t) = \begin{bmatrix} \mathbf{K}_{F_D}(r_j, t) \\ \mathbf{K}_{T_D}(r_j, t) \end{bmatrix} = \begin{bmatrix} \mathbf{K}_{F_D}(r_j, t) \\ \mathbf{Q}_{x_{R_0,j}}(r_j, t) \mathbf{K}_{F_D}(r_j, t) \end{bmatrix} + |\mathbf{V}_{X_{j,0}}(r_j, t)| \begin{bmatrix} \mathbf{0}_{3 \times 3} \\ -\mathbf{Q}_{1,j}(r_j, t) & \mathbf{Q}_{1,j}(r_j, t) \mathbf{Q}_{x_{R_0,j}}(r_j, t) \end{bmatrix} \quad (83)$$

$$\mathbf{C}_D(r_j, t) = \begin{bmatrix} \mathbf{C}_{F_D}(r_j, t) \\ \mathbf{C}_{T_D}(r_j, t) \end{bmatrix} = \begin{bmatrix} \mathbf{C}_{F_D}(r_j, t) \\ \mathbf{Q}_{x_{R_0,j}}(t) \mathbf{C}_{F_D}(r_j, t) \end{bmatrix}. \quad (84)$$

3.4.3. Lift force linearization

Substitution of Eqs. (14) and (46) into the non-linear lift force given by Eq. (12), brings

$$\begin{aligned} \mathbf{F}_{L;x_j}(r_j, t) &= \rho \pi c(r_j) \{\boldsymbol{\beta}_j(r_j)\}^T \mathbf{W}(r_j, t) (\mathbf{e}_{r_j} \times \mathbf{W}(r_j, t)) \\ &= \rho \pi c(r_j) \{\boldsymbol{\beta}_j(r_j)\}^T \{r_j (\mathbf{e}_{r_j} \times \boldsymbol{\Omega}) + \mathbf{W}_{X_j}(r_j, t) - \dot{\mathbf{u}}_{X_j}(r_j, t)\} (\mathbf{e}_{r_j} \times \{r_j (\mathbf{e}_{r_j} \times \boldsymbol{\Omega}) + \mathbf{W}_{X_j}(r_j, t) - \dot{\mathbf{u}}_{X_j}(r_j, t)\}) \\ &= \rho \pi c(r_j) \{\boldsymbol{\beta}_j(r_j)\}^T \{r_j (\mathbf{e}_{r_j} \times \boldsymbol{\Omega}) + \mathbf{R}_{x \rightarrow x_{j,0}}(t) \mathbf{W}_X(r_j, t) + (\boldsymbol{\theta}(t) \times \mathbf{W}_X(r_j, t)) - \dot{\mathbf{u}}_{X_j}(r_j, t)\} \\ &\quad (\mathbf{e}_{r_j} \times \{r_j (\mathbf{e}_{r_j} \times \boldsymbol{\Omega}) + \mathbf{R}_{x \rightarrow x_{j,0}}(t) \mathbf{W}_X(r_j, t) + (\boldsymbol{\theta}(t) \times \mathbf{W}_X(r_j, t)) - \dot{\mathbf{u}}_{X_j}(r_j, t)\}) \\ &= \rho \pi c(r_j) \{\boldsymbol{\beta}_j(r_j)\}^T \{\mathbf{V}_{X_{j,0}}(r_j, t) + (\boldsymbol{\theta}(t) \times \mathbf{W}_X(r_j, t)) - \dot{\mathbf{u}}_{X_j}(r_j, t)\} (\mathbf{e}_{r_j} \times \{\mathbf{V}_{X_{j,0}}(r_j, t) + (\boldsymbol{\theta}(t) \times \mathbf{W}_X(r_j, t)) - \dot{\mathbf{u}}_{X_j}(r_j, t)\}) \end{aligned} \quad (85)$$

Linearization of $\mathbf{F}_{L;X_j}(r_j, t)$ with respect to $\dot{\mathbf{u}}_{X_j}(r_j, t)$ and $\boldsymbol{\theta}(t)$ gives

$$\begin{aligned}
\mathbf{F}_{L;X_j}(r_j, t) &\approx \rho\pi c(r_j) \left\{ \boldsymbol{\beta}_j(r_j) \right\}^T \mathbf{V}_{X_{j,0}}(r_j, t) \left(\mathbf{e}_{r_j} \times \left\{ \mathbf{V}_{X_{j,0}}(r_j, t) + (\boldsymbol{\theta}(t) \times \mathbf{W}_X(r_j, t)) - \dot{\mathbf{u}}_{X_j}(r_j, t) \right\} \right) \\
&\quad + \rho\pi c(r_j) \left\{ \boldsymbol{\beta}_j(r_j) \right\}^T \left\{ (\boldsymbol{\theta}(t) \times \mathbf{W}_X(r_j, t)) \right\} \left(\mathbf{e}_{r_j} \times \mathbf{V}_{X_{j,0}}(r_j, t) \right) - \rho\pi c(r_j) \left\{ \boldsymbol{\beta}_j(r_j) \right\}^T \dot{\mathbf{u}}_{X_j}(r_j, t) \left(\mathbf{e}_{r_j} \times \mathbf{V}_{X_{j,0}}(r_j, t) \right) \\
&\approx \rho\pi c(r_j) \left[\left\{ \boldsymbol{\beta}_j(r_j) \right\}^T \mathbf{V}_{X_{j,0}}(r_j, t) \left(\mathbf{e}_{r_j} \times \mathbf{V}_{X_{j,0}}(r_j, t) \right) \right. \\
&\quad + \left\{ \boldsymbol{\beta}_j(r_j) \right\}^T \mathbf{V}_{X_{j,0}}(r_j, t) \left\{ \mathbf{e}_{r_j} \times (\boldsymbol{\theta}(t) \times \mathbf{W}_X(r_j, t)) \right\} - \left\{ \boldsymbol{\beta}_j(r_j) \right\}^T \mathbf{V}_{X_{j,0}}(r_j, t) \left\{ \mathbf{e}_{r_j} \times \dot{\mathbf{u}}_{X_j}(r_j, t) \right\} \\
&\quad \left. + \left\{ \boldsymbol{\beta}_j(r_j) \right\}^T \left\{ (\boldsymbol{\theta}(t) \times \mathbf{W}_X(r_j, t)) \right\} \left(\mathbf{e}_{r_j} \times \mathbf{V}_{X_{j,0}}(r_j, t) \right) - \left\{ \boldsymbol{\beta}_j(r_j) \right\}^T \dot{\mathbf{u}}_{X_j}(r_j, t) \left(\mathbf{e}_{r_j} \times \mathbf{V}_{X_{j,0}}(r_j, t) \right) \right] \\
&\approx \rho\pi c(r_j) \left[\left\{ \boldsymbol{\beta}_j(r_j) \right\}^T \mathbf{V}_{X_{j,0}}(r_j, t) \left(\mathbf{e}_{r_j} \times \mathbf{V}_{X_{j,0}}(r_j, t) \right) \right. \\
&\quad + \left\{ \boldsymbol{\beta}_j(r_j) \right\}^T \mathbf{V}_{X_{j,0}}(r_j, t) \left\{ \mathbf{e}_{r_j} \times (\boldsymbol{\theta}(t) \times \mathbf{W}_X(r_j, t)) \right\} - \left\{ \boldsymbol{\beta}_j(r_j) \right\}^T \mathbf{V}_{X_{j,0}}(r_j, t) \left\{ \mathbf{e}_{r_j} \times \dot{\mathbf{u}}_{X_j}(r_j, t) \right\} \\
&\quad \left. + \left(\mathbf{e}_{r_j} \times \mathbf{V}_{X_{j,0}}(r_j, t) \right) \left\{ \boldsymbol{\beta}_j(r_j) \right\}^T \left\{ (\boldsymbol{\theta}(t) \times \mathbf{W}_X(r_j, t)) \right\} - \left(\mathbf{e}_{r_j} \times \mathbf{V}_{X_{j,0}}(r_j, t) \right) \left\{ \boldsymbol{\beta}_j(r_j) \right\}^T \dot{\mathbf{u}}_{X_j}(r_j, t) \right] \\
&\quad (86)
\end{aligned}$$

Introduction of the skew-symmetric matrix \mathbf{Q}_{r_j} allows for the isolation of $\dot{\mathbf{u}}_{X_j}(r_j, t)$ and $\boldsymbol{\theta}(t)$:

$$\mathbf{Q}_{r_j} = [\mathbf{e}_{r_j}]_\times, \quad (87)$$

resulting into

$$\begin{aligned}
\mathbf{F}_{L;X_j}(r_j, t) &\approx \rho\pi c(r_j) \left[\left\{ \boldsymbol{\beta}_j(r_j) \right\}^T \mathbf{V}_{X_{j,0}}(r_j, t) \left(\mathbf{e}_{r_j} \times \mathbf{V}_{X_{j,0}}(r_j, t) \right) \right. \\
&\quad + \left\{ \boldsymbol{\beta}_j(r_j) \right\}^T \mathbf{V}_{X_{j,0}}(r_j, t) \mathbf{Q}_{r_j} (\boldsymbol{\theta}(t) \times \mathbf{W}_X(r_j, t)) - \left\{ \boldsymbol{\beta}_j(r_j) \right\}^T \mathbf{V}_{X_{j,0}}(r_j, t) \mathbf{Q}_{r_j} \dot{\mathbf{u}}_{X_j}(r_j, t) \\
&\quad \left. + \left(\mathbf{e}_{r_j} \times \mathbf{V}_{X_{j,0}}(r_j, t) \right) \left\{ \boldsymbol{\beta}_j(r_j) \right\}^T (\boldsymbol{\theta}(t) \times \mathbf{W}_X(r_j, t)) - \left(\mathbf{e}_{r_j} \times \mathbf{V}_{X_{j,0}}(r_j, t) \right) \left\{ \boldsymbol{\beta}_j(r_j) \right\}^T \dot{\mathbf{u}}_{X_j}(r_j, t) \right] \\
&\approx \rho\pi c(r_j) \left[\left\{ \boldsymbol{\beta}_j(r_j) \right\}^T \mathbf{V}_{X_{j,0}}(r_j, t) \left(\mathbf{e}_{r_j} \times \mathbf{V}_{X_{j,0}}(r_j, t) \right) \right. \\
&\quad - \left\{ \boldsymbol{\beta}_j(r_j) \right\}^T \mathbf{V}_{X_{j,0}}(r_j, t) \mathbf{Q}_{r_j} \mathbf{Q}_W(r_j, t) \boldsymbol{\theta}(t) - \left\{ \boldsymbol{\beta}_j(r_j) \right\}^T \mathbf{V}_{X_{j,0}}(r_j, t) \mathbf{Q}_{r_j} \dot{\mathbf{u}}_{X_j}(r_j, t) \\
&\quad \left. - \left(\mathbf{e}_{r_j} \times \mathbf{V}_{X_{j,0}}(r_j, t) \right) \left\{ \boldsymbol{\beta}_j(r_j) \right\}^T \mathbf{Q}_W(r_j, t) \boldsymbol{\theta}(t) - \left(\mathbf{e}_{r_j} \times \mathbf{V}_{X_{j,0}}(r_j, t) \right) \left\{ \boldsymbol{\beta}_j(r_j) \right\}^T \dot{\mathbf{u}}_{X_j}(r_j, t) \right] \\
&\approx \rho\pi c(r_j) \left[\left\{ \boldsymbol{\beta}_j(r_j) \right\}^T \mathbf{V}_{X_{j,0}}(r_j, t) \left(\mathbf{e}_{r_j} \times \mathbf{V}_{X_{j,0}}(r_j, t) \right) \right. \\
&\quad - \left\{ \left\{ \boldsymbol{\beta}_j(r_j) \right\}^T \mathbf{V}_{X_{j,0}}(r_j, t) \mathbf{Q}_{r_j} \mathbf{Q}_W(r_j, t) + \left(\mathbf{e}_{r_j} \times \mathbf{V}_{X_{j,0}}(r_j, t) \right) \left\{ \boldsymbol{\beta}_j(r_j) \right\}^T \mathbf{Q}_W(r_j, t) \right\} \boldsymbol{\theta}(t) \\
&\quad \left. - \left\{ \left\{ \boldsymbol{\beta}_j(r_j) \right\}^T \mathbf{V}_{X_{j,0}}(r_j, t) \mathbf{Q}_{r_j} + \left(\mathbf{e}_{r_j} \times \mathbf{V}_{X_{j,0}}(r_j, t) \right) \left\{ \boldsymbol{\beta}_j(r_j) \right\}^T \right\} \dot{\mathbf{u}}_{X_j}(r_j, t) \right]
\end{aligned}
\quad (88)$$

Within the global frame of reference, the lift force $\mathbf{F}_{L;X}(r_j, t)$ is given by

$$\begin{aligned}
\mathbf{F}_{L;X}(r_j, t) &= \rho\pi c(r_j) \left\{ \mathbf{R}_{X \rightarrow X_j}(t) \right\}^{-1} \left\{ \boldsymbol{\beta}_j(r_j) \right\}^T \mathbf{W}(r_j, t) (\mathbf{e}_{r_j} \times \mathbf{W}(r_j, t)) \\
&\approx \rho\pi c(r_j) \left[\left\{ \mathbf{R}_{X \rightarrow X_{j0}}(t) \right\}^{-1} - \mathbf{R}_\theta(t) \left\{ \mathbf{R}_{X \rightarrow X_{j0}}(t) \right\}^{-1} \right] \left[\left\{ \boldsymbol{\beta}_j(r_j) \right\}^T \mathbf{V}_{X_{j0}}(r_j, t) (\mathbf{e}_{r_j} \times \mathbf{V}_{X_{j0}}(r_j, t)) \right. \\
&\quad \left. - \left\{ \left\{ \boldsymbol{\beta}_j(r_j) \right\}^T \mathbf{V}_{X_{j0}}(r_j, t) \mathbf{Q}_{r_j} \mathbf{Q}_W(r_j, t) + (\mathbf{e}_{r_j} \times \mathbf{V}_{X_{j0}}(r_j, t)) \left\{ \boldsymbol{\beta}_j(r_j) \right\}^T \mathbf{Q}_W(r_j, t) \right\} \boldsymbol{\theta}(t) \right. \\
&\quad \left. - \left\{ \left\{ \boldsymbol{\beta}_j(r_j) \right\}^T \mathbf{V}_{X_{j0}}(r_j, t) \mathbf{Q}_{r_j} + (\mathbf{e}_{r_j} \times \mathbf{V}_{X_{j0}}(r_j, t)) \left\{ \boldsymbol{\beta}_j(r_j) \right\}^T \right\} \dot{\mathbf{u}}_{X_j}(r_j, t) \right]
\end{aligned} \tag{89}$$

²³⁰ Omitting the non-linear terms with respect to $\boldsymbol{\theta}(t)$ and $\dot{\mathbf{u}}_{X_j}(t)$, the expression for $\mathbf{F}_{L;X}(r_j, t)$ reduces to

$$\begin{aligned}
\mathbf{F}_{L;X}(r_j, t) &\approx \rho\pi c(r_j) \left[\left\{ \mathbf{R}_{X \rightarrow X_{j0}}(t) \right\}^{-1} \left\{ \boldsymbol{\beta}_j(r_j) \right\}^T \mathbf{V}_{X_{j0}}(r_j, t) (\mathbf{e}_{r_j} \times \mathbf{V}_{X_{j0}}(r_j, t)) \right. \\
&\quad - \left\{ \mathbf{R}_{X \rightarrow X_{j0}}(t) \right\}^{-1} \left\{ \left\{ \boldsymbol{\beta}_j(r_j) \right\}^T \mathbf{V}_{X_{j0}}(r_j, t) \mathbf{Q}_{r_j} \mathbf{Q}_W(r_j, t) + (\mathbf{e}_{r_j} \times \mathbf{V}_{X_{j0}}(r_j, t)) \left\{ \boldsymbol{\beta}_j(r_j) \right\}^T \mathbf{Q}_W(r_j, t) \right\} \boldsymbol{\theta}(t) \right. \\
&\quad - \left\{ \mathbf{R}_{X \rightarrow X_{j0}}(t) \right\}^{-1} \left\{ \left\{ \boldsymbol{\beta}_j(r_j) \right\}^T \mathbf{V}_{X_{j0}}(r_j, t) \mathbf{Q}_{r_j} + (\mathbf{e}_{r_j} \times \mathbf{V}_{X_{j0}}(r_j, t)) \left\{ \boldsymbol{\beta}_j(r_j) \right\}^T \right\} \dot{\mathbf{u}}_{X_j}(r_j, t) \\
&\quad \left. - \mathbf{R}_\theta(t) \left\{ \mathbf{R}_{X \rightarrow X_{j0}}(t) \right\}^{-1} \left\{ \boldsymbol{\beta}_j(r_j) \right\}^T \mathbf{V}_{X_{j0}}(r_j, t) (\mathbf{e}_{r_j} \times \mathbf{V}_{X_{j0}}(r_j, t)) \right].
\end{aligned} \tag{90}$$

$\boldsymbol{\theta}(t)$ is isolated from the $\mathbf{Q}_\theta(t)$ matrix multiplication in the following manner:

$$\begin{aligned}
-\mathbf{R}_\theta(t) \left\{ \mathbf{R}_{X \rightarrow X_{j0}}(t) \right\}^{-1} \left\{ \boldsymbol{\beta}_j(r_j) \right\}^T \mathbf{V}_{X_{j0}}(r_j, t) (\mathbf{e}_{r_j} \times \mathbf{V}_{X_{j0}}(r_j, t)) &= - \left\{ \boldsymbol{\beta}_j(r_j) \right\}^T \mathbf{V}_{X_{j0}}(r_j, t) \mathbf{R}_\theta(t) \left\{ \mathbf{R}_{X \rightarrow X_{j0}}(t) \right\}^{-1} (\mathbf{e}_{r_j} \times \mathbf{V}_{X_{j0}}(r_j, t)) \\
&= - \left\{ \boldsymbol{\beta}_j(r_j) \right\}^T \mathbf{V}_{X_{j0}}(r_j, t) [\boldsymbol{\theta}(t) \times \left\{ \mathbf{R}_{X \rightarrow X_{j0}}(t) \right\}^{-1} (\mathbf{e}_{r_j} \times \mathbf{V}_{X_{j0}}(r_j, t))] \\
&= \left\{ \boldsymbol{\beta}_j(r_j) \right\}^T \mathbf{V}_{X_{j0}}(r_j, t) \left[\left\{ \mathbf{R}_{X \rightarrow X_{j0}}(t) \right\}^{-1} (\mathbf{e}_{r_j} \times \mathbf{V}_{X_{j0}}(r_j, t)) \times \boldsymbol{\theta}(t) \right] \\
&= \left\{ \boldsymbol{\beta}_j(r_j) \right\}^T \mathbf{V}_{X_{j0}}(r_j, t) \mathbf{Q}_{2;j}(r_j, t) \boldsymbol{\theta}(t),
\end{aligned} \tag{91}$$

where the skew-symmetric matrix $\mathbf{Q}_{2;j}(r_j, t)$ is given by

$$\mathbf{Q}_{2;j}(r_j, t) = \left[\left\{ \mathbf{R}_{X \rightarrow X_{j0}}(t) \right\}^{-1} (\mathbf{e}_{r_j} \times \mathbf{V}_{X_{j0}}(r_j, t)) \right]_x, \tag{92}$$

The vector $\boldsymbol{\theta}(t)$ can now as follows be isolated:

$$\begin{aligned}
\mathbf{F}_{L;X}(r_j, t) &\approx \rho\pi c(r_j) \left[\left\{ \mathbf{R}_{X \rightarrow X_{j_0}}(t) \right\}^{-1} \left\{ \boldsymbol{\beta}_j(r_j) \right\}^T \mathbf{V}_{X_{j_0}}(r_j, t) (\mathbf{e}_{r_j} \times \mathbf{V}_{X_{j_0}}(r_j, t)) \right. \\
&\quad - \left\{ \mathbf{R}_{X \rightarrow X_{j_0}}(t) \right\}^{-1} \left\{ \left\{ \boldsymbol{\beta}_j(r_j) \right\}^T \mathbf{V}_{X_{j_0}}(r_j, t) \mathbf{Q}_{r_j} \mathbf{Q}_W(r_j, t) + (\mathbf{e}_{r_j} \times \mathbf{V}_{X_{j_0}}(r_j, t)) \left\{ \boldsymbol{\beta}_j(r_j) \right\}^T \mathbf{Q}_W(r_j, t) \right\} \boldsymbol{\theta}(t) \\
&\quad - \left\{ \mathbf{R}_{X \rightarrow X_{j_0}}(t) \right\}^{-1} \left\{ \left\{ \boldsymbol{\beta}_j(r_j) \right\}^T \mathbf{V}_{X_{j_0}}(r_j, t) \mathbf{Q}_{r_j} + (\mathbf{e}_{r_j} \times \mathbf{V}_{X_{j_0}}(r_j, t)) \left\{ \boldsymbol{\beta}_j(r_j) \right\}^T \right\} \dot{\mathbf{u}}_{X_j}(r_j, t) \\
&\quad \left. + \left\{ \boldsymbol{\beta}_j(r_j) \right\}^T \mathbf{V}_{X_{j_0}}(r_j, t) \mathbf{Q}_{2_j}(r_j, t) \boldsymbol{\theta}(t) \right] \\
&\approx \rho\pi c(r_j) \left[\left\{ \mathbf{R}_{X \rightarrow X_{j_0}}(t) \right\}^{-1} \left\{ \boldsymbol{\beta}_j(r_j) \right\}^T \mathbf{V}_{X_{j_0}}(r_j, t) (\mathbf{e}_{r_j} \times \mathbf{V}_{X_{j_0}}(r_j, t)) \right. \\
&\quad - \left\{ \mathbf{R}_{X \rightarrow X_{j_0}}(t) \right\}^{-1} \left\{ \left\{ \boldsymbol{\beta}_j(r_j) \right\}^T \mathbf{V}_{X_{j_0}}(r_j, t) \mathbf{Q}_{r_j} \mathbf{Q}_W(r_j, t) + (\mathbf{e}_{r_j} \times \mathbf{V}_{X_{j_0}}(r_j, t)) \left\{ \boldsymbol{\beta}_j(r_j) \right\}^T \mathbf{Q}_W(r_j, t) \right\} \boldsymbol{\theta}(t) \\
&\quad + \left\{ \boldsymbol{\beta}_j(r_j) \right\}^T \mathbf{V}_{X_{j_0}}(r_j, t) \mathbf{Q}_{2_j}(r_j, t) \boldsymbol{\theta}(t) \\
&\quad - \left\{ \mathbf{R}_{X \rightarrow X_{j_0}}(t) \right\}^{-1} \left\{ \left\{ \boldsymbol{\beta}_j(r_j) \right\}^T \mathbf{V}_{X_{j_0}}(r_j, t) \mathbf{Q}_{r_j} + (\mathbf{e}_{r_j} \times \mathbf{V}_{X_{j_0}}(r_j, t)) \left\{ \boldsymbol{\beta}_j(r_j) \right\}^T \right\} \dot{\mathbf{u}}_{X_j}(r_j, t) \Big] \\
&\approx \rho\pi c(r_j) \left[\left\{ \mathbf{R}_{X \rightarrow X_{j_0}}(t) \right\}^{-1} \left\{ \boldsymbol{\beta}_j(r_j) \right\}^T \mathbf{V}_{X_{j_0}}(r_j, t) (\mathbf{e}_{r_j} \times \mathbf{V}_{X_{j_0}}(r_j, t)) \right. \\
&\quad - \left\{ \mathbf{R}_{X \rightarrow X_{j_0}}(t) \right\}^{-1} \left\{ \left\{ \boldsymbol{\beta}_j(r_j) \right\}^T \mathbf{V}_{X_{j_0}}(r_j, t) \mathbf{Q}_{r_j} \mathbf{Q}_W(r_j, t) + (\mathbf{e}_{r_j} \times \mathbf{V}_{X_{j_0}}(r_j, t)) \left\{ \boldsymbol{\beta}_j(r_j) \right\}^T \mathbf{Q}_W(r_j, t) \right. \\
&\quad \left. \left. - \left\{ \boldsymbol{\beta}_j(r_j) \right\}^T \mathbf{V}_{X_{j_0}}(r_j, t) \mathbf{R}_{X \rightarrow X_{j_0}}(t) \mathbf{Q}_{2_j}(r_j, t) \right\} \boldsymbol{\theta}(t) \right. \\
&\quad \left. - \left\{ \mathbf{R}_{X \rightarrow X_{j_0}}(t) \right\}^{-1} \left\{ \left\{ \boldsymbol{\beta}_j(r_j) \right\}^T \mathbf{V}_{X_{j_0}}(r_j, t) \mathbf{Q}_{r_j} + (\mathbf{e}_{r_j} \times \mathbf{V}_{X_{j_0}}(r_j, t)) \left\{ \boldsymbol{\beta}_j(r_j) \right\}^T \right\} \dot{\mathbf{u}}_{X_j}(r_j, t) \right]. \tag{93}
\end{aligned}$$

Subsequent substitution of Eq. (49) results into the full formulation of the linearized lift force $\mathbf{F}_{L;X}(r_j, t)$ within the

²³⁵ global frame of reference:

$$\begin{aligned}
\mathbf{F}_{L;X}(r_j, t) &\approx \rho\pi c(r_j) \left[\left\{ \mathbf{R}_{X \rightarrow X_{j_0}}(t) \right\}^{-1} \left\{ \boldsymbol{\beta}_j(r_j) \right\}^T \mathbf{V}_{X_{j_0}}(r_j, t) (\mathbf{e}_{r_j} \times \mathbf{V}_{X_{j_0}}(r_j, t)) \right. \\
&\quad - \left\{ \mathbf{R}_{X \rightarrow X_{j_0}}(t) \right\}^{-1} \left\{ \left\{ \boldsymbol{\beta}_j(r_j) \right\}^T \mathbf{V}_{X_{j_0}}(r_j, t) \mathbf{Q}_{r_j} \mathbf{Q}_W(r_j, t) + (\mathbf{e}_{r_j} \times \mathbf{V}_{X_{j_0}}(r_j, t)) \left\{ \boldsymbol{\beta}_j(r_j) \right\}^T \mathbf{Q}_W(r_j, t) \right. \\
&\quad \left. - \left\{ \boldsymbol{\beta}_j(r_j) \right\}^T \mathbf{V}_{X_{j_0}}(r_j, t) \mathbf{R}_{X \rightarrow X_{j_0}}(t) \mathbf{Q}_{2j}(r_j, t) \right\} \boldsymbol{\theta}(t) \\
&\quad - \left\{ \mathbf{R}_{X \rightarrow X_{j_0}}(t) \right\}^{-1} \left\{ \left\{ \boldsymbol{\beta}_j(r_j) \right\}^T \mathbf{V}_{X_{j_0}}(r_j, t) \mathbf{Q}_{r_j} + (\mathbf{e}_{r_j} \times \mathbf{V}_{X_{j_0}}(r_j, t)) \left\{ \boldsymbol{\beta}_j(r_j) \right\}^T \right\} \\
&\quad \left. \left\{ \dot{\mathbf{R}}_{X \rightarrow X_{j_0}}(t) \mathbf{u}_X(t) + \mathbf{R}_{X \rightarrow X_{j_0}}(t) \dot{\mathbf{u}}_X(t) - (\dot{\mathbf{R}}_{X \rightarrow X_{j_0}}(t) \mathbf{Q}_{x_{R_0}}(t) + \mathbf{R}_{X \rightarrow X_{j_0}}(t) \dot{\mathbf{Q}}_{x_{R_0}}(t)) \boldsymbol{\theta}(t) - \mathbf{R}_{X \rightarrow X_{j_0}}(t) \mathbf{Q}_{x_{R_0}}(t) \dot{\boldsymbol{\theta}}(t) \right\} \right] \\
&\approx \rho\pi c(r_j) \left[\left\{ \mathbf{R}_{X \rightarrow X_{j_0}}(t) \right\}^{-1} \left\{ \boldsymbol{\beta}_j(r_j) \right\}^T \mathbf{V}_{X_{j_0}}(r_j, t) (\mathbf{e}_{r_j} \times \mathbf{V}_{X_{j_0}}(r_j, t)) \right. \\
&\quad - \left\{ \mathbf{R}_{X \rightarrow X_{j_0}}(t) \right\}^{-1} \left\{ \left\{ \boldsymbol{\beta}_j(r_j) \right\}^T \mathbf{V}_{X_{j_0}}(r_j, t) \mathbf{Q}_{r_j} \mathbf{Q}_W(r_j, t) + (\mathbf{e}_{r_j} \times \mathbf{V}_{X_{j_0}}(r_j, t)) \left\{ \boldsymbol{\beta}_j(r_j) \right\}^T \mathbf{Q}_W(r_j, t) \right. \\
&\quad \left. - \left\{ \boldsymbol{\beta}_j(r_j) \right\}^T \mathbf{V}_{X_{j_0}}(r_j, t) \mathbf{R}_{X \rightarrow X_{j_0}}(t) \mathbf{Q}_{2j}(r_j, t) \right\} \boldsymbol{\theta}(t) \\
&\quad - \left\{ \mathbf{R}_{X \rightarrow X_{j_0}}(t) \right\}^{-1} \left\{ \left\{ \boldsymbol{\beta}_j(r_j) \right\}^T \mathbf{V}_{X_{j_0}}(r_j, t) \mathbf{Q}_{r_j} + (\mathbf{e}_{r_j} \times \mathbf{V}_{X_{j_0}}(r_j, t)) \left\{ \boldsymbol{\beta}_j(r_j) \right\}^T \right\} \dot{\mathbf{R}}_{X \rightarrow X_{j_0}}(t) \mathbf{u}_X(t) \\
&\quad - \left\{ \mathbf{R}_{X \rightarrow X_{j_0}}(t) \right\}^{-1} \left\{ \left\{ \boldsymbol{\beta}_j(r_j) \right\}^T \mathbf{V}_{X_{j_0}}(r_j, t) \mathbf{Q}_{r_j} + (\mathbf{e}_{r_j} \times \mathbf{V}_{X_{j_0}}(r_j, t)) \left\{ \boldsymbol{\beta}_j(r_j) \right\}^T \right\} \mathbf{R}_{X \rightarrow X_{j_0}}(t) \dot{\mathbf{u}}_X(t) \\
&\quad + \left\{ \mathbf{R}_{X \rightarrow X_{j_0}}(t) \right\}^{-1} \left\{ \left\{ \boldsymbol{\beta}_j(r_j) \right\}^T \mathbf{V}_{X_{j_0}}(r_j, t) \mathbf{Q}_{r_j} + (\mathbf{e}_{r_j} \times \mathbf{V}_{X_{j_0}}(r_j, t)) \left\{ \boldsymbol{\beta}_j(r_j) \right\}^T \right\} (\dot{\mathbf{R}}_{X \rightarrow X_{j_0}}(t) \mathbf{Q}_{x_{R_0}}(t) + \mathbf{R}_{X \rightarrow X_{j_0}}(t) \dot{\mathbf{Q}}_{x_{R_0}}(t)) \boldsymbol{\theta}(t) \\
&\quad \left. + \left\{ \mathbf{R}_{X \rightarrow X_{j_0}}(t) \right\}^{-1} \left\{ \left\{ \boldsymbol{\beta}_j(r_j) \right\}^T \mathbf{V}_{X_{j_0}}(r_j, t) \mathbf{Q}_{r_j} + (\mathbf{e}_{r_j} \times \mathbf{V}_{X_{j_0}}(r_j, t)) \left\{ \boldsymbol{\beta}_j(r_j) \right\}^T \right\} (\mathbf{R}_{X \rightarrow X_{j_0}}(t) \mathbf{Q}_{x_{R_0}}(t)) \dot{\boldsymbol{\theta}}(t) \right]. \tag{94}
\end{aligned}$$

Adopting the matrices $\mathbf{K}_{FL}(r_j, t)$ and $\mathbf{C}_{FL}(r_j, t)$, the linearized lift force can be rewritten as

$$\mathbf{F}_{L;X}(r_j, t) \approx \rho\pi c(r_j) \left[\left\{ \mathbf{R}_{X \rightarrow X_{j_0}}(t) \right\}^{-1} \left\{ \boldsymbol{\beta}_j(r_j) \right\}^T \mathbf{V}_{X_{j_0}}(r_j, t) (\mathbf{e}_{r_j} \times \mathbf{V}_{X_{j_0}}(r_j, t)) + \mathbf{K}_{FL}(r_j, t) \mathbf{u}(t) + \mathbf{C}_{FL}(r_j, t) \dot{\mathbf{u}}(t) \right], \tag{95}$$

with

$$\mathbf{K}_{FL}(r_j, t) = \left[\begin{array}{c} - \left\{ \mathbf{R}_{X \rightarrow X_{j_0}}(t) \right\}^{-1} \left\{ \boldsymbol{\beta}_j(r_j) \right\}^T \mathbf{V}_{X_{j_0}}(r_j, t) \mathbf{Q}_{r_j} \dot{\mathbf{R}}_{X \rightarrow X_{j_0}}(t) \\ - \left\{ \mathbf{R}_{X \rightarrow X_{j_0}}(t) \right\}^{-1} (\mathbf{e}_{r_j} \times \mathbf{V}_{X_{j_0}}(r_j, t)) \left\{ \boldsymbol{\beta}_j(r_j) \right\}^T \dot{\mathbf{R}}_{X \rightarrow X_{j_0}}(t) \\ - \left\{ \mathbf{R}_{X \rightarrow X_{j_0}}(t) \right\}^{-1} \left\{ \left\{ \boldsymbol{\beta}_j(r_j) \right\}^T \mathbf{V}_{X_{j_0}}(r_j, t) \mathbf{Q}_{r_j} \mathbf{Q}_W(r_j, t) \right\} \\ - \left\{ \mathbf{R}_{X \rightarrow X_{j_0}}(t) \right\}^{-1} \left\{ (\mathbf{e}_{r_j} \times \mathbf{V}_{X_{j_0}}(r_j, t)) \left\{ \boldsymbol{\beta}_j(r_j) \right\}^T \mathbf{Q}_W(r_j, t) \right\} \\ \left\{ \boldsymbol{\beta}_j(r_j) \right\}^T \mathbf{V}_{X_{j_0}}(r_j, t) \mathbf{Q}_{2j}(r_j, t) \\ + \left\{ \mathbf{R}_{X \rightarrow X_{j_0}}(t) \right\}^{-1} \left\{ \left\{ \boldsymbol{\beta}_j(r_j) \right\}^T \mathbf{V}_{X_{j_0}}(r_j, t) \mathbf{Q}_{r_j} + (\mathbf{e}_{r_j} \times \mathbf{V}_{X_{j_0}}(r_j, t)) \left\{ \boldsymbol{\beta}_j(r_j) \right\}^T \right\} \\ \left. \dot{\mathbf{R}}_{X \rightarrow X_{j_0}}(t) \mathbf{Q}_{x_{R_0}}(t) + \mathbf{R}_{X \rightarrow X_{j_0}}(t) \dot{\mathbf{Q}}_{x_{R_0}}(t) \right] \end{array} \right]^T \tag{96}$$

$$\mathbf{C}_{F_L}(r_j, t) = \begin{bmatrix} -\{\mathbf{R}_{X \rightarrow X_{j_0}}(t)\}^{-1} \{\boldsymbol{\beta}_j(r_j)\}^T \mathbf{V}_{X_{j_0}}(r_j, t) \mathbf{Q}_{r_j} \mathbf{R}_{X \rightarrow X_{j_0}}(t) \\ -\{\mathbf{R}_{X \rightarrow X_{j_0}}(t)\}^{-1} (\mathbf{e}_{r_j} \times \mathbf{V}_{X_{j_0}}(r_j, t)) \{\boldsymbol{\beta}_j(r_j)\}^T \mathbf{R}_{X \rightarrow X_{j_0}}(t) \\ \{\mathbf{R}_{X \rightarrow X_{j_0}}(t)\}^{-1} \{\boldsymbol{\beta}_j(r_j)\}^T \mathbf{V}_{X_{j_0}}(r_j, t) \mathbf{Q}_{r_j} \mathbf{R}_{X \rightarrow X_{j_0}}(t) \mathbf{Q}_{x_{R_0}}(t) \\ + \{\mathbf{R}_{X \rightarrow X_{j_0}}(t)\}^{-1} (\mathbf{e}_{r_j} \times \mathbf{V}_{X_{j_0}}(r_j, t)) \{\boldsymbol{\beta}_j(r_j)\}^T \mathbf{R}_{X \rightarrow X_{j_0}}(t) \mathbf{Q}_{x_{R_0}}(t) \end{bmatrix}^T \quad (97)$$

For a symmetric rotor with identical blades and a time-independent ambient wind field, the matrix multiplications $\sum_{j=1}^3 \mathbf{K}_{F_L}(r, t)$ and $\sum_{j=1}^3 \mathbf{C}_{F_L}(r, t)$ can be rendered time-independent :

$$\begin{aligned} \sum_{j=1}^3 \mathbf{K}_{F_L}(r, t) &= \frac{3}{2} \sin(\beta(r) + \beta_0) \left[\begin{pmatrix} 0 & 0 & W_Y \Omega_Y \\ 0 & 0 & 0 \\ -W_Y \Omega_Y & 0 & 0 \end{pmatrix} \begin{pmatrix} -W_Y \Omega_Y d & 0 & -\Omega_Y^2 r^2 \\ 0 & 0 & 2W_Y \Omega_Y r \\ \Omega_Y^2 r^2 & 0 & -W_Y \Omega_Y d \end{pmatrix} \right] \\ &\quad + \frac{3}{2} \cos(\beta(r) + \beta_0) \left[\begin{pmatrix} 0 & 0 & 0 \\ 0 & 0 & 0 \\ 0 & 0 & 0 \end{pmatrix} \begin{pmatrix} 0 & 0 & 2W_Y \Omega_Y r \\ 0 & 0 & 0 \\ -2W_Y \Omega_Y r & 0 & 0 \end{pmatrix} \right], \end{aligned} \quad (98)$$

$$\begin{aligned} \sum_{j=1}^3 \mathbf{C}_{F_L}(r, t) &= \frac{3}{2} \sin(\beta(r) + \beta_0) \left[\begin{pmatrix} -W_Y & 0 & 0 \\ 0 & 0 & 0 \\ 0 & 0 & -W_Y \end{pmatrix} \begin{pmatrix} \Omega_Y r^2 & 0 & -W_Y d \\ 0 & 4\Omega_Y r_j^2 & 0 \\ W_Y d & 0 & -\Omega_Y r^2 \end{pmatrix} \right] \\ &\quad + \frac{3}{2} \cos(\beta(r) + \beta_0) \left[\begin{pmatrix} 0 & 0 & 0 \\ 0 & -2\Omega_Y r & 0 \\ 0 & 0 & 0 \end{pmatrix} \begin{pmatrix} -2W_Y r & 0 & 0 \\ 0 & -2W_Y r & 0 \\ 0 & 0 & 0 \end{pmatrix} \right]. \end{aligned} \quad (99)$$

3.4.4. Lift moment linearization

From the lift force, defined in the global frame of reference, the moment round the origin can be expressed as follows:

$$\begin{aligned} \mathbf{T}_{O;L}(r_j, t) &= \mathbf{x}_{R_j}(t) \times \mathbf{F}_{L;X}(r_j, t) \\ &\approx \rho \pi c(r_j) \left\{ \mathbf{u}_X(t) + \mathbf{x}_{R_{0;j}} + (\boldsymbol{\theta}(t) \times \mathbf{x}_{R_{0;j}}(t)) \right\} \\ &\quad \times \left[\{\mathbf{R}_{X \rightarrow X_{j_0}}(t)\}^{-1} \{\boldsymbol{\beta}_j(r_j)\}^T \mathbf{V}_{X_{j_0}}(r_j, t) (\mathbf{e}_{r_j} \times \mathbf{V}_{X_{j_0}}(r_j, t)) + \mathbf{K}_{F_L}(r_j, t) \mathbf{u}(t) + \mathbf{C}_{F_L}(r_j, t) \dot{\mathbf{u}}(t) \right] \\ &\approx \rho \pi c(r_j) \left\{ \mathbf{u}_X(t) + \mathbf{x}_{R_{0;j}} - \mathbf{Q}_{x_{R_{0;j}}}(t) \boldsymbol{\theta}(t) \right\} \\ &\quad \times \left[\{\mathbf{R}_{X \rightarrow X_{j_0}}(t)\}^{-1} \{\boldsymbol{\beta}_j(r_j)\}^T \mathbf{V}_{X_{j_0}}(r_j, t) (\mathbf{e}_{r_j} \times \mathbf{V}_{X_{j_0}}(r_j, t)) + \mathbf{K}_{F_L}(r_j, t) \mathbf{u}(t) + \mathbf{C}_{F_L}(r_j, t) \dot{\mathbf{u}}(t) \right] \end{aligned} \quad (100)$$

Omitting the non-linear terms with respect to $\mathbf{u}(t)$ and $\dot{\mathbf{u}}(t)$, the expression for $\mathbf{T}_{O;L}(r_j, t)$ reduces to

$$\begin{aligned} \mathbf{T}_{O;L}(r_j, t) &\approx \rho \pi c(r_j) \left(\mathbf{u}_X(t) \times \left[\{\boldsymbol{\beta}_j(r_j)\}^T \mathbf{V}_{X_{j_0}}(r_j, t) \{\mathbf{R}_{X \rightarrow X_{j_0}}(t)\}^{-1} (\mathbf{e}_{r_j} \times \mathbf{V}_{X_{j_0}}(r_j, t)) \right] \right) \\ &\quad + \rho \pi c(r_j) \left(\mathbf{x}_{R_0} \times \left[\{\boldsymbol{\beta}_j(r_j)\}^T \mathbf{V}_{X_{j_0}}(r_j, t) \{\mathbf{R}_{X \rightarrow X_{j_0}}(t)\}^{-1} (\mathbf{e}_{r_j} \times \mathbf{V}_{X_{j_0}}(r_j, t)) + \mathbf{K}_{F_L}(r_j, t) \mathbf{u}(t) + \mathbf{C}_{F_L}(r_j, t) \dot{\mathbf{u}}(t) \right] \right) \\ &\quad - \rho \pi c(r_j) \left(\mathbf{Q}_{x_{R_0}}(t) \boldsymbol{\theta}(t) \times \left[\{\boldsymbol{\beta}_j(r_j)\}^T \mathbf{V}_{X_{j_0}}(r_j, t) \{\mathbf{R}_{X \rightarrow X_{j_0}}(t)\}^{-1} (\mathbf{e}_{r_j} \times \mathbf{V}_{X_{j_0}}(r_j, t)) \right] \right). \end{aligned} \quad (101)$$

Isolation of $\mathbf{u}_X(t)$ and $\boldsymbol{\theta}(t)$ requires the introduction of the skew-symmetric matrix $\mathbf{Q}_{2;j}(r_j, t)$, with which $\mathbf{T}_{O;L}(r_j, t)$ can be rewritten as

$$\begin{aligned}
\mathbf{T}_{O;L}(r_j, t) &\approx -\rho\pi c(r_j) \left\{ \boldsymbol{\beta}_j(r_j) \right\}^T \mathbf{V}_{X_{j;0}}(r_j, t) \mathbf{Q}_{2;j}(r_j, t) \mathbf{u}_X(t) \\
&\quad + \rho\pi c(r_j) \left[-\left\{ \boldsymbol{\beta}_j(r_j) \right\}^T \mathbf{V}_{X_{j;0}}(r_j, t) \mathbf{Q}_{2;j}(r_j, t) \mathbf{x}_{R_0} + (\mathbf{x}_{R_0} \times \mathbf{K}_{F_L}(r_j, t) \mathbf{u}(t)) + (\mathbf{x}_{R_0} \times \mathbf{C}_{F_L}(r_j, t) \dot{\mathbf{u}}(t)) \right] \\
&\quad + \rho\pi c(r_j) \left\{ \boldsymbol{\beta}_j(r_j) \right\}^T \mathbf{V}_{X_{j;0}}(r_j, t) \mathbf{Q}_{2;j}(r_j, t) \mathbf{Q}_{x_{R_0}}(t) \boldsymbol{\theta}(t) \\
&\approx -\rho\pi c(r_j) \left\{ \boldsymbol{\beta}_j(r_j) \right\}^T \mathbf{V}_{X_{j;0}}(r_j, t) \mathbf{Q}_{2;j}(r_j, t) \mathbf{u}_X(t) \\
&\quad + \rho\pi c(r_j) \left[-\left\{ \boldsymbol{\beta}_j(r_j) \right\}^T \mathbf{V}_{X_{j;0}}(r_j, t) \mathbf{Q}_{2;j}(r_j, t) \mathbf{x}_{R_0} + \mathbf{Q}_{x_{R_0}}(t) \mathbf{K}_{F_L}(r_j, t) \mathbf{u}(t) + \mathbf{Q}_{x_{R_0}}(t) \mathbf{C}_{F_L}(r_j, t) \dot{\mathbf{u}}(t) \right] \quad (102) \\
&\quad + \rho\pi c(r_j) \left\{ \boldsymbol{\beta}_j(r_j) \right\}^T \mathbf{V}_{X_{j;0}}(r_j, t) \mathbf{Q}_{2;j}(r_j, t) \mathbf{Q}_{x_{R_0}}(t) \boldsymbol{\theta}(t) \\
&\approx \rho\pi c(r_j) \left[-\left\{ \boldsymbol{\beta}_j(r_j) \right\}^T \mathbf{V}_{X_{j;0}}(r_j, t) \mathbf{Q}_{2;j}(r_j, t) \mathbf{x}_{R_0} + \mathbf{Q}_{x_{R_0}}(t) \mathbf{K}_{F_L}(r_j, t) \mathbf{u}(t) + \mathbf{Q}_{x_{R_0}}(t) \mathbf{C}_{F_L}(r_j, t) \dot{\mathbf{u}}(t) \right. \\
&\quad \left. - \left\{ \boldsymbol{\beta}_j(r_j) \right\}^T \mathbf{V}_{X_{j;0}}(r_j, t) \mathbf{Q}_{2;j}(r_j, t) \mathbf{u}_X(t) + \left\{ \boldsymbol{\beta}_j(r_j) \right\}^T \mathbf{V}_{X_{j;0}}(r_j, t) \mathbf{Q}_{2;j}(r_j, t) \mathbf{Q}_{x_{R_0}}(t) \boldsymbol{\theta}(t) \right].
\end{aligned}$$

Adopting the matrices $\mathbf{K}_{T_L}(r_j, t)$ and $\mathbf{C}_{T_L}(r_j, t)$, the linearized moment from the lift force can be rewritten as

$$\begin{aligned}
\mathbf{T}_{O;L}(r_j, t) &\approx \rho\pi c(r_j) \left[-\left\{ \boldsymbol{\beta}_j(r_j) \right\}^T \mathbf{V}_{X_{j;0}}(r_j, t) \mathbf{Q}_{2;j}(r_j, t) \mathbf{x}_{R_0} + \mathbf{K}_{T_L}(r_j, t) \mathbf{u}(t) + \mathbf{C}_{T_L}(r_j, t) \dot{\mathbf{u}}(t) \right] \\
&\approx \rho\pi c(r_j) \left[\left\{ \boldsymbol{\beta}_j(r_j) \right\}^T \mathbf{V}_{X_{j;0}}(r_j, t) \mathbf{x}_{R_0} \times \left\{ \mathbf{R}_{X \rightarrow X_{j;0}}(t) \right\}^{-1} (\mathbf{e}_{r_j} \times \{ \mathbf{V}_{X_{j;0}}(r_j, t) \}) \right. \\
&\quad \left. + \mathbf{K}_{T_L}(r_j, t) \mathbf{u}(t) + \mathbf{C}_{T_L}(r_j, t) \dot{\mathbf{u}}(t) \right], \quad (103)
\end{aligned}$$

with

$$\mathbf{K}_{T_L}(r_j, t) = \mathbf{Q}_{x_{R_0}}(t) \mathbf{K}_{F_L}(r_j, t) + \left\{ \boldsymbol{\beta}_j(r_j) \right\}^T \mathbf{V}_{X_{j;0}}(r_j, t) \left[-\mathbf{Q}_{2;j}(r_j, t) \quad \mathbf{Q}_{2;j}(r_j, t) \mathbf{Q}_{x_{R_0}}(t) \right], \quad (104)$$

250

$$\mathbf{C}_{T_L}(r_j, t) = \mathbf{Q}_{x_{R_0}}(t) \mathbf{C}_{F_L}(r_j, t). \quad (105)$$

For a symmetric rotor with identical blades and a time-independent ambient wind field, the matrix multiplications $\sum_{j=1}^3 \mathbf{K}_{T_L}(r_j, t)$ and $\sum_{j=1}^3 \mathbf{C}_{T_L}(r_j, t)$ can be rendered time-independent:

$$\begin{aligned}
\sum_{j=1}^3 \mathbf{K}_{T_L}(r_j, t) &= \frac{3}{2} \sin(\beta(r) + \beta_0) \left[\begin{pmatrix} W_Y \Omega_Y d & 0 & 4\Omega_Y^2 r^2 \\ 0 & 0 & 0 \\ -4\Omega_Y^2 r^2 & 0 & W_Y \Omega_Y d \end{pmatrix} \begin{pmatrix} -5\Omega_Y^2 r^2 d & 0 & -W_Y \Omega_Y (r^2 - d^2) \\ 0 & 0 & -2(\Omega_Y^2 r^3 + W_Y^2) \\ W_Y \Omega_Y (r^2 - d^2) & 0 & -5\Omega_Y^2 r^2 d \end{pmatrix} \right. \\
&\quad \left. + \frac{3}{2} \cos(\beta(r) + \beta_0) \begin{pmatrix} 0 & 0 & -3W_Y \Omega_Y r \\ 0 & 0 & 0 \\ 3W_Y \Omega_Y r & 0 & 0 \end{pmatrix} \begin{pmatrix} 5W_Y \Omega_Y r d & 0 & r(\Omega_Y^2 r^2 W_Y^2) \\ 0 & 0 & 2W_Y \Omega_Y r^2 \\ -r(\Omega_Y^2 r^2 W_Y^2) & 0 & 5W_Y \Omega_Y r d \end{pmatrix} \right], \quad (106)
\end{aligned}$$

$$\begin{aligned}
\sum_{j=1}^3 \mathbf{C}_{T_L}(r_j, t) &= \frac{3}{2} \sin(\beta(r_j) + \beta_{0;j}) \left[\begin{pmatrix} -2\Omega_Y r^2 & 0 & W_Y d \\ 0 & -2\Omega_Y r^2 & 0 \\ -W_Y d & 0 & \Omega_Y r^2 W_Y \end{pmatrix} \begin{pmatrix} -W_Y d^2 & 0 & -\Omega_Y r^2 d \\ 0 & -2W_Y r^2 & \Omega_Y r^3 \\ 3\Omega_Y r^2 d & 0 & -W_Y d^2 \end{pmatrix} \right. \\
&\quad \left. + \frac{3}{2} \cos(\beta(r) + \beta_0) \begin{pmatrix} W_Y r & 0 & 0 \\ 0 & 4W_Y r & 0 \\ 0 & 0 & W_Y r \end{pmatrix} \begin{pmatrix} -\Omega_Y r^3 & 0 & W_Y r d \\ 0 & -r^2 & -W_Y r^2 \\ -3W_Y r d & 0 & -\Omega_Y r^3 \end{pmatrix} \right]. \quad (107)
\end{aligned}$$

The resulting lift excitation $\mathbf{F}_L(t)$, accounting for both forces and moments, can now be expressed as

$$\mathbf{F}_L(t) \approx \sum_{j=1}^3 \int_{r_0}^R \rho \pi c(r_j) \left\{ \left\{ \boldsymbol{\beta}_j(r_j) \right\}^T \mathbf{V}_{X_{j0}}(r_j, t) \begin{bmatrix} \left\{ \mathbf{R}_{X \rightarrow X_{j0}}(t) \right\}^{-1} (\mathbf{e}_{r_j} \times \{ \mathbf{V}_{X_{j0}}(r_j, t) \}) \\ \mathbf{x}_{R_0} \times \left\{ \mathbf{R}_{X \rightarrow X_{j0}}(t) \right\}^{-1} (\mathbf{e}_{r_j} \times \{ \mathbf{V}_{X_{j0}}(r_j, t) \}) \end{bmatrix} \right\} \quad (108)$$

$$+ \mathbf{K}_L(r_j, t) \mathbf{u}(t) + \mathbf{C}_L(r_j, t) \dot{\mathbf{u}}(t) \} dr_j, \quad (109)$$

with

$$\mathbf{K}_L(r_j, t) = \begin{bmatrix} \mathbf{K}_{F_L}(r_j, t) \\ \mathbf{K}_{T_L}(r_j, t) \end{bmatrix} = \begin{bmatrix} \mathbf{Q}_{x_{R_0}}(t) \mathbf{K}_{F_L}(r_j, t) \\ \mathbf{Q}_{T_L}(r_j, t) \end{bmatrix} + \left\{ \boldsymbol{\beta}_j(r_j) \right\}^T \mathbf{V}_{X_{j0}}(r_j, t) \left\{ \mathbf{R}_{X \rightarrow X_{j0}}(t) \right\}^{-1} \begin{bmatrix} \mathbf{0}_{3 \times 3} & \mathbf{0}_{3 \times 3} \\ -\mathbf{Q}_{2;j}(r_j, t) & \mathbf{Q}_{2;j}(r_j, t) \mathbf{Q}_{x_{R_0}}(t) \end{bmatrix} \quad (110)$$

$$\mathbf{C}_L(r_j, t) = \begin{bmatrix} \mathbf{C}_{F_L}(r_j, t) \\ \mathbf{C}_{T_L}(r_j, t) \end{bmatrix} = \begin{bmatrix} \mathbf{Q}_{x_{R_0}}(t) \mathbf{C}_{F_L}(r_j, t) \\ \mathbf{Q}_{T_L}(r_j, t) \end{bmatrix}. \quad (111)$$

3.4.5. Inertia force linearization

The inertia force, as defined in the local rotating reference frames is given by Eq. (13). Transformation to the global frame of reference brings

$$\begin{aligned} \mathbf{F}_{I;X}(r_j, t) &= \rho \pi c(r_j)^2 \left\{ \mathbf{R}_{X \rightarrow X_j}(t) \right\}^{-1} \dot{\mathbf{W}}(r_j, t) \\ &= \rho \pi c(r_j)^2 \left\{ \mathbf{R}_{X \rightarrow X_j}(t) \right\}^{-1} (\dot{\mathbf{W}}_{X_j}(r_j, t) - \ddot{\mathbf{u}}_{X_j}(t)) \\ &= \rho \pi c(r_j)^2 \left\{ \mathbf{R}_{X \rightarrow X_j}(t) \right\}^{-1} (\dot{\mathbf{V}}_{X_{j0}}(r_j, t) + (\dot{\boldsymbol{\theta}}(t) \times \mathbf{W}_X(r_j, t)) + (\boldsymbol{\theta}(t) \times \dot{\mathbf{W}}_X(r_j, t)) - \ddot{\mathbf{u}}_{X_j}(t)) \\ &= \rho \pi c(r_j)^2 \left[\left\{ \mathbf{R}_{X \rightarrow X_{j0}}(t) \right\}^{-1} - \mathbf{R}_{\theta}(t) \left\{ \mathbf{R}_{X \rightarrow X_{j0}}(t) \right\}^{-1} \right] (\dot{\mathbf{V}}_{X_{j0}}(r_j, t) + (\dot{\boldsymbol{\theta}}(t) \times \mathbf{W}_X(r_j, t)) + (\boldsymbol{\theta}(t) \times \dot{\mathbf{W}}_X(r_j, t)) - \ddot{\mathbf{u}}_{X_j}(t)). \end{aligned} \quad (112)$$

Omitting the non-linear terms with respect to $\boldsymbol{\theta}(t)$ and $\dot{\mathbf{u}}_{X_j}(t)$, the expression for $\mathbf{F}_{I;X}(r_j, t)$ reduces to

$$\begin{aligned} \mathbf{F}_{I;X}(r_j, t) &\approx \rho \pi c(r_j)^2 \left[\left\{ \mathbf{R}_{X \rightarrow X_{j0}}(t) \right\}^{-1} \dot{\mathbf{V}}_{X_{j0}}(r_j, t) - \mathbf{R}_{\theta}(t) \left\{ \mathbf{R}_{X \rightarrow X_{j0}}(t) \right\}^{-1} \dot{\mathbf{V}}_{X_{j0}}(r_j, t) \right. \\ &\quad \left. + \left\{ \mathbf{R}_{X \rightarrow X_{j0}}(t) \right\}^{-1} (\dot{\boldsymbol{\theta}}(t) \times \mathbf{W}_X(r_j, t)) + \left\{ \mathbf{R}_{X \rightarrow X_{j0}}(t) \right\}^{-1} (\boldsymbol{\theta}(t) \times \dot{\mathbf{W}}_X(r_j, t)) - \left\{ \mathbf{R}_{X \rightarrow X_{j0}}(t) \right\}^{-1} \ddot{\mathbf{u}}_{X_j}(t) \right]. \end{aligned} \quad (113)$$

$\boldsymbol{\theta}(t)$ is isolated from the $\mathbf{Q}_{\theta}(t)$ matrix multiplication in the following manner:

$$\begin{aligned} -\mathbf{R}_{\theta}(t) \left\{ \mathbf{R}_{X \rightarrow X_{j0}}(t) \right\}^{-1} \dot{\mathbf{V}}_{X_{j0}}(r_j, t) &= -\boldsymbol{\theta}(t) \times \left(\left\{ \mathbf{R}_{X \rightarrow X_{j0}}(t) \right\}^{-1} \dot{\mathbf{V}}_{X_{j0}}(r_j, t) \right) \\ &= \left(\left\{ \mathbf{R}_{X \rightarrow X_{j0}}(t) \right\}^{-1} \dot{\mathbf{V}}_{X_{j0}}(r_j, t) \right) \times \boldsymbol{\theta}(t) \\ &= \mathbf{Q}_{3;j}(r_j, t) \boldsymbol{\theta}(t), \end{aligned} \quad (114)$$

where the skew-symmetric matrix $\mathbf{Q}_{3;j}(r_j, t)$ is given by

$$\mathbf{Q}_{3;j}(r_j, t) = \left[\left\{ \mathbf{R}_{X \rightarrow X_{j0}}(t) \right\}^{-1} \dot{\mathbf{V}}_{X_{j0}}(r_j, t) \right]_{\times}, \quad (115)$$

The vector $\boldsymbol{\theta}(t)$ can now as follows be isolated:

$$\begin{aligned}
\mathbf{F}_{\text{I};X}(r_j, t) &\approx \rho\pi c(r_j)^2 \left[\left\{ \mathbf{R}_{\mathbf{X} \rightarrow \mathbf{X}_{j_0}}(t) \right\}^{-1} \dot{\mathbf{V}}_{X_{j;0}}(r_j, t) + \mathbf{Q}_{3;j}(r_j, t) \boldsymbol{\theta}(t) \right. \\
&\quad \left. - \left\{ \mathbf{R}_{\mathbf{X} \rightarrow \mathbf{X}_{j_0}}(t) \right\}^{-1} \mathbf{Q}_W(r_j, t) \dot{\boldsymbol{\theta}}(t) - \left\{ \mathbf{R}_{\mathbf{X} \rightarrow \mathbf{X}_{j_0}}(t) \right\}^{-1} \dot{\mathbf{Q}}_W(r_j, t) \boldsymbol{\theta}(t) - \left\{ \mathbf{R}_{\mathbf{X} \rightarrow \mathbf{X}_{j_0}}(t) \right\}^{-1} \ddot{\mathbf{u}}_{X_j}(t) \right] \\
&\approx \rho\pi c(r_j)^2 \left[\left\{ \mathbf{R}_{\mathbf{X} \rightarrow \mathbf{X}_{j_0}}(t) \right\}^{-1} \dot{\mathbf{V}}_{X_{j;0}}(r_j, t) - \left\{ \mathbf{R}_{\mathbf{X} \rightarrow \mathbf{X}_{j_0}}(t) \right\}^{-1} \dot{\mathbf{Q}}_W(r_j, t) \boldsymbol{\theta}(t) + \mathbf{Q}_{3;j}(r_j, t) \boldsymbol{\theta}(t) \right. \\
&\quad \left. - \left\{ \mathbf{R}_{\mathbf{X} \rightarrow \mathbf{X}_{j_0}}(t) \right\}^{-1} \mathbf{Q}_W(r_j, t) \dot{\boldsymbol{\theta}}(t) - \left\{ \mathbf{R}_{\mathbf{X} \rightarrow \mathbf{X}_{j_0}}(t) \right\}^{-1} \ddot{\mathbf{u}}_{X_j}(t) \right] \\
&\approx \rho\pi c(r_j)^2 \left[\left\{ \mathbf{R}_{\mathbf{X} \rightarrow \mathbf{X}_{j_0}}(t) \right\}^{-1} \dot{\mathbf{V}}_{X_{j;0}}(r_j, t) - \left\{ \mathbf{R}_{\mathbf{X} \rightarrow \mathbf{X}_{j_0}}(t) \right\}^{-1} (\dot{\mathbf{Q}}_W(r_j, t) - \mathbf{R}_{\mathbf{X} \rightarrow \mathbf{X}_{j_0}}(t) \mathbf{Q}_{3;j}(r_j, t)) \boldsymbol{\theta}(t) \right. \\
&\quad \left. - \left\{ \mathbf{R}_{\mathbf{X} \rightarrow \mathbf{X}_{j_0}}(t) \right\}^{-1} \mathbf{Q}_W(r_j, t) \dot{\boldsymbol{\theta}}(t) - \left\{ \mathbf{R}_{\mathbf{X} \rightarrow \mathbf{X}_{j_0}}(t) \right\}^{-1} \ddot{\mathbf{u}}_{X_j}(t) \right]. \tag{116}
\end{aligned}$$

Subsequent substitution of Eq. (50) results into the full formulation of the linearized inertia force $\mathbf{F}_{\text{I};\mathbf{X}}(r_j, t)$ within the global frame of reference:

Adopting the matrices $\mathbf{K}_{\text{F}_i}(r_j, t)$, $\mathbf{C}_{\text{F}_i}(r_j, t)$ and $\mathbf{M}_{\text{F}_i}(r_j, t)$, the linearized inertia force can be rewritten as

$$\mathbf{F}_{\text{I};X}(r_j, t) \approx \rho\pi c(r_j)^2 \left[\left\{ \mathbf{R}_{\mathbf{X} \rightarrow \mathbf{X}_{j_0}}(t) \right\}^{-1} \dot{\mathbf{V}}_{\mathbf{X}_{j_0}}(r_j, t) + \mathbf{K}_{\text{F}_i}(r_j, t)\mathbf{u}(t) + \mathbf{C}_{\text{F}_i}(r_j, t)\dot{\mathbf{u}}(t) + \mathbf{M}_{\text{F}_i}(r_j, t)\ddot{\mathbf{u}}(t) \right], \quad (118)$$

with

$$\mathbf{K}_{\text{F}_i}(r_j, t) = \begin{bmatrix} \left(-\left\{ \mathbf{R}_{\mathbf{X} \rightarrow \mathbf{X}_{j_0}}(t) \right\}^{-1} \ddot{\mathbf{R}}_{\mathbf{X} \rightarrow \mathbf{X}_{j_0}}(t) \right)^T \\ \left(\left\{ \mathbf{R}_{\mathbf{X} \rightarrow \mathbf{X}_{j_0}}(t) \right\}^{-1} \left[2\dot{\mathbf{R}}_{\mathbf{X} \rightarrow \mathbf{X}_{j_0}}(t)\dot{\mathbf{Q}}_{\mathbf{x}_{R_0}}(t) + \mathbf{R}_{\mathbf{X} \rightarrow \mathbf{X}_{j_0}}(t)\ddot{\mathbf{Q}}_{\mathbf{x}_{R_0}}(t) \right] \right)^T \\ -\left\{ \mathbf{R}_{\mathbf{X} \rightarrow \mathbf{X}_{j_0}}(t) \right\}^{-1} \left(\dot{\mathbf{Q}}_{\mathbf{W}}(r_j, t) - \mathbf{R}_{\mathbf{X} \rightarrow \mathbf{X}_{j_0}}(t)\mathbf{Q}_{3;j}(r_j, t) \right) \end{bmatrix}^T, \quad (119)$$

$$\mathbf{C}_{\text{F}_i}(r_j, t) = \begin{bmatrix} \left(-2\left\{ \mathbf{R}_{\mathbf{X} \rightarrow \mathbf{X}_{j_0}}(t) \right\}^{-1} \dot{\mathbf{R}}_{\mathbf{X} \rightarrow \mathbf{X}_{j_0}}(t) \right)^T \\ \left(\left\{ \mathbf{R}_{\mathbf{X} \rightarrow \mathbf{X}_{j_0}}(t) \right\}^{-1} \left[2\dot{\mathbf{R}}_{\mathbf{X} \rightarrow \mathbf{X}_{j_0}}(t)\mathbf{Q}_{\mathbf{x}_{R_0}}(t) + 2\mathbf{R}_{\mathbf{X} \rightarrow \mathbf{X}_{j_0}}(t)\dot{\mathbf{Q}}_{\mathbf{x}_{R_0}}(t) - \mathbf{Q}_{\mathbf{W}}(r_j, t) \right] \right)^T \end{bmatrix}^T, \quad (120)$$

$$\mathbf{M}_{\text{F}_i}(r_j, t) = \begin{bmatrix} -\mathbf{I}_{3 \times 3} \\ \mathbf{Q}_{\mathbf{x}_{R_0}}(t) \end{bmatrix}^T. \quad (121)$$

²⁷⁰ For a symmetric rotor with identical blades and a time-independent ambient wind field, the matrix multiplications $\sum_{j=1}^3 \mathbf{K}_{\text{F}_i}(r, t)$, $\sum_{j=1}^3 \mathbf{C}_{\text{F}_i}(r, t)$ and $\sum_{j=1}^3 \mathbf{M}_{\text{F}_i}(r, t)$ can be rendered time-independent :

$$\sum_{j=1}^3 \mathbf{K}_{\text{F}_i}(r, t) = \begin{bmatrix} 0 & 0 & W_Y \Omega_Y \\ 0 & 0 & 0 \\ -W_Y \Omega_Y & 0 & 0 \end{bmatrix} \begin{bmatrix} -W_Y \Omega_Y d & 0 & -\Omega_Y^2 r^2 \\ 0 & 0 & 2W_Y \Omega_Y r \\ \Omega_Y^2 r^2 & 0 & -W_Y \Omega_Y d \end{bmatrix}, \quad (122)$$

$$\sum_{j=1}^3 \mathbf{C}_{\text{F}_i}(r, t) = \begin{bmatrix} -W_Y & 0 & 0 \\ 0 & 0 & 0 \\ 0 & 0 & -W_Y \end{bmatrix} \begin{bmatrix} \Omega_Y r^2 & 0 & -W_Y d \\ 0 & 4\Omega_Y r_j^2 & 0 \\ W_Y d & 0 & -\Omega_Y r^2 \end{bmatrix}. \quad (123)$$

$$\sum_{j=1}^3 \mathbf{M}_{\text{F}_i}(r, t) = \begin{bmatrix} -W_Y & 0 & 0 \\ 0 & 0 & 0 \\ 0 & 0 & -W_Y \end{bmatrix} \begin{bmatrix} \Omega_Y r^2 & 0 & -W_Y d \\ 0 & 4\Omega_Y r_j^2 & 0 \\ W_Y d & 0 & -\Omega_Y r^2 \end{bmatrix}. \quad (124)$$

3.4.6. Inertia moment linearization

²⁷⁵ From the inertia force, defined in the global frame of reference, the moment round the origin can be expressed as follows:

$$\begin{aligned} \mathbf{T}_{\text{O};\text{I}}(r_j, t) &= \mathbf{x}_R(t) \times \mathbf{F}_{\text{I};X}(r_j, t) \\ &\approx \rho\pi c(r_j)^2 \left\{ \mathbf{u}_X(t) + \mathbf{x}_{R_{0;j}} + (\boldsymbol{\theta}(t) \times \mathbf{x}_{R_{0;j}}(t)) \right\} \times \left[\left\{ \mathbf{R}_{\mathbf{X} \rightarrow \mathbf{X}_{j_0}}(t) \right\}^{-1} \dot{\mathbf{V}}_{\mathbf{X}_{j_0}}(r_j, t) + \mathbf{K}_{\text{F}_i}(r_j, t)\mathbf{u}(t) + \mathbf{C}_{\text{F}_i}(r_j, t)\dot{\mathbf{u}}(t) + \mathbf{M}_{\text{F}_i}(r_j, t)\ddot{\mathbf{u}}(t) \right] \\ &\approx \rho\pi c(r_j)^2 \left\{ \mathbf{u}_X(t) + \mathbf{x}_{R_{0;j}} - \mathbf{Q}_{\mathbf{x}_{R_{0;j}}}(t)\boldsymbol{\theta}(t) \right\} \times \left[\left\{ \mathbf{R}_{\mathbf{X} \rightarrow \mathbf{X}_{j_0}}(t) \right\}^{-1} \dot{\mathbf{V}}_{\mathbf{X}_{j_0}}(r_j, t) + \mathbf{K}_{\text{F}_i}(r_j, t)\mathbf{u}(t) + \mathbf{C}_{\text{F}_i}(r_j, t)\dot{\mathbf{u}}(t) + \mathbf{M}_{\text{F}_i}(r_j, t)\ddot{\mathbf{u}}(t) \right]. \end{aligned} \quad (125)$$

Omitting the non-linear terms with respect to $\mathbf{u}(t)$ and $\dot{\mathbf{u}}(t)$, the expression for $\mathbf{T}_{O;L}(r_j, t)$ reduces to

$$\begin{aligned}
\mathbf{T}_{O;I}(r_j, t) &\approx \rho\pi c(r_j)^2 \left(\mathbf{u}_X(t) \times \left\{ \mathbf{R}_{X \rightarrow X_{j_0}}(t) \right\}^{-1} \dot{\mathbf{V}}_{X_{j_0}}(r_j, t) \right) \\
&\quad + \rho\pi c(r_j)^2 \left(\mathbf{x}_{R_{0;j}} \times \left[\left\{ \mathbf{R}_{X \rightarrow X_{j_0}}(t) \right\}^{-1} \dot{\mathbf{V}}_{X_{j_0}}(r_j, t) + \mathbf{K}_{F_I}(r_j, t)\mathbf{u}(t) + \mathbf{C}_{F_I}(r_j, t)\dot{\mathbf{u}}(t) + \mathbf{M}_{F_I}(r_j, t)\ddot{\mathbf{u}}(t) \right] \right) \\
&\quad - \rho\pi c(r_j)^2 \left(\mathbf{Q}_{x_{R_{0;j}}}(t)\boldsymbol{\theta}(t) \times \left\{ \mathbf{R}_{X \rightarrow X_{j_0}}(t) \right\}^{-1} \dot{\mathbf{V}}_{X_{j_0}}(r_j, t) \right) \\
&\approx -\rho\pi c(r_j)^2 \left(\left\{ \mathbf{R}_{X \rightarrow X_{j_0}}(t) \right\}^{-1} \dot{\mathbf{V}}_{X_{j_0}}(r_j, t) \times \mathbf{u}_X(t) \right) \\
&\quad + \rho\pi c(r_j)^2 \left(-\left\{ \mathbf{R}_{X \rightarrow X_{j_0}}(t) \right\}^{-1} \dot{\mathbf{V}}_{X_{j_0}}(r_j, t) \times \mathbf{x}_{R_{0;j}} + \mathbf{x}_{R_{0;j}} \times \left[\mathbf{K}_{F_I}(r_j, t)\mathbf{u}(t) + \mathbf{C}_{F_I}(r_j, t)\dot{\mathbf{u}}(t) + \mathbf{M}_{F_I}(r_j, t)\ddot{\mathbf{u}}(t) \right] \right) \\
&\quad + \rho\pi c(r_j)^2 \left(\left\{ \mathbf{R}_{X \rightarrow X_{j_0}}(t) \right\}^{-1} \dot{\mathbf{V}}_{X_{j_0}}(r_j, t) \times \mathbf{Q}_{x_{R_{0;j}}}(t)\boldsymbol{\theta}(t) \right).
\end{aligned} \tag{126}$$

With the introduction of the skew-symmetric matrix $\mathbf{Q}_{3;j}(r_j, t)$, $\mathbf{u}_X(t)$ and $\boldsymbol{\theta}(t)$ can be isolated:

$$\begin{aligned}
\mathbf{T}_{O;I}(r_j, t) &\approx -\rho\pi c(r_j)^2 \left(\mathbf{Q}_{3;j}(r_j, t)\mathbf{u}_X(t) \right) \\
&\quad + \rho\pi c(r_j)^2 \left(-\mathbf{Q}_{3;j}(r_j, t)\mathbf{x}_{R_{0;j}} + \mathbf{x}_{R_{0;j}} \times \left[\mathbf{K}_{F_I}(r_j, t)\mathbf{u}(t) + \mathbf{C}_{F_I}(r_j, t)\dot{\mathbf{u}}(t) + \mathbf{M}_{F_I}(r_j, t)\ddot{\mathbf{u}}(t) \right] \right) \\
&\quad + \rho\pi c(r_j)^2 \left(\mathbf{Q}_{3;j}(r_j, t)\mathbf{Q}_{x_{R_{0;j}}}(t)\boldsymbol{\theta}(t) \right).
\end{aligned} \tag{127}$$

Adopting the matrices $\mathbf{K}_{T_L}(r_j, t)$ and $\mathbf{C}_{T_L}(r_j, t)$, the linearized moment from the lift force can be rewritten as

$$\mathbf{T}_{O;I}(r_j, t) \approx \rho\pi c(r_j)^2 \left[\mathbf{x}_{R_{0;j}} \times \left\{ \mathbf{R}_{X \rightarrow X_{j_0}}(t) \right\}^{-1} \dot{\mathbf{V}}_{X_{j_0}}(r_j, t) + \mathbf{K}_{T_I}(r_j, t)\mathbf{u}(t) + \mathbf{C}_{T_I}(r_j, t)\dot{\mathbf{u}}(t) + \mathbf{M}_{T_I}(r_j, t)\ddot{\mathbf{u}}(t) \right], \tag{128}$$

²⁸⁰ with

$$\mathbf{K}_{T_I}(r_j, t) = \mathbf{Q}_{x_{R_{0;j}}}(t)\mathbf{K}_{F_I}(r_j, t) + \begin{bmatrix} -\mathbf{Q}_{3;j}(r_j, t) & \mathbf{Q}_{3;j}(r_j, t)\mathbf{Q}_{x_{R_{0;j}}}(t) \end{bmatrix}, \tag{129}$$

$$\mathbf{C}_{T_I}(r_j, t) = \mathbf{Q}_{x_{R_{0;j}}}(t)\mathbf{C}_{F_I}(r_j, t), \tag{130}$$

$$\mathbf{M}_{T_I}(r_j, t) = \mathbf{Q}_{x_{R_{0;j}}}(t)\mathbf{M}_{F_I}(r_j, t). \tag{131}$$

The resulting inertia excitation $\mathbf{F}_I(t)$, accounting for both forces and moments, can now be expressed as

$$\mathbf{F}_I(t) \approx \sum_{j=1}^3 \int_{r_0}^R \rho\pi c(r_j)^2 \left\{ \left[\mathbf{x}_{R_{0;j}} \times \left\{ \mathbf{R}_{X \rightarrow X_{j_0}}(t) \right\}^{-1} \dot{\mathbf{V}}_{X_{j_0}}(r_j, t) \right] + \mathbf{K}_I(r_j, t)\mathbf{u}(t) + \mathbf{C}_I(r_j, t)\dot{\mathbf{u}}(t) + \mathbf{M}_I(r_j, t)\ddot{\mathbf{u}}(t) \right\} dr_j, \tag{132}$$

with

$$\mathbf{K}_I(r_j, t) = \begin{bmatrix} \mathbf{K}_{F_I}(r_j, t) \\ \mathbf{K}_{T_I}(r_j, t) \end{bmatrix} = \begin{bmatrix} \mathbf{K}_{F_I}(r_j, t) \\ \mathbf{Q}_{x_{R_{0;j}}}(t)\mathbf{K}_{F_I}(r_j, t) \end{bmatrix} + \begin{bmatrix} \mathbf{0}_{3 \times 3} \\ -\mathbf{Q}_{3;j}(r_j, t) \end{bmatrix} \mathbf{Q}_{x_{R_{0;j}}}(t) \mathbf{Q}_{x_{R_{0;j}}}(t)^T \tag{133}$$

$$\mathbf{C}_I(r_j, t) = \begin{bmatrix} \mathbf{C}_{F_I}(r_j, t) \\ \mathbf{C}_{T_I}(r_j, t) \end{bmatrix} = \begin{bmatrix} \mathbf{C}_{F_I}(r_j, t) \\ \mathbf{Q}_{x_{R_{0;j}}}(t)\mathbf{C}_{F_I}(r_j, t) \end{bmatrix}, \tag{134}$$

$$\mathbf{M}_I(r_j, t) = \begin{bmatrix} \mathbf{M}_{F_I}(r_j, t) \\ \mathbf{M}_{T_I}(r_j, t) \end{bmatrix} = \begin{bmatrix} \mathbf{M}_{F_I}(r_j, t) \\ \mathbf{Q}_{x_{R_{0;j}}}(t)\mathbf{M}_{F_I}(r_j, t) \end{bmatrix}. \tag{135}$$

²⁸⁵

Bibliography

- [1] K.A Abhinav and Nilanjan Saha. Dynamic analysis of an offshore wind turbine including soil effects. In *8th International Conference on Asian and Pacific Coasts (APAC 2015)*.
- [2] ANSYS. *Theory reference for the mechanical APDL and Mechanical Applications*, 2009.
- [3] N DP Barltrop and A J Adams. *Dynamics of fixed offshore structures*. Butterworth Heinemann, 1991.
- [4] Swagata Bisoi and Sumanta Haldar. Dynamic analysis of offshore wind turbine in clay considering soil–monopile–tower interaction. *Soil Dynamics and Earthquake Engineering*, 63:19–35, 2014.
- [5] Tony Burton, David Sharpe, Nick Jenkins, and Ervin Bossanyi. *WIND ENERGY HANDBOOK*. JOHN WILEY and SONS, LTD, 2001.
- [6] Erica Bush and Lance Manuel. Foundation models for offshore wind turbines. American Institute of Aeronautics and Astronautics, January 2009.
- [7] Subrata K Chakrabarti. *HANDBOOK OF OFFSHORE ENGINEERING*. Elsevier, 2005.
- [8] Robert D. Cook, David S. Malkus, Michael E. Plesha, and Robert J. Witt. *Concepts and applications of finite element analysis*. John Wiley and Sons Inc., 2002.
- [9] DNV. Design of offshore wind turbine structures. Technical report, DNV, 2014.
- [10] O M Faltinsen. *Sea loads on ships and offshore structures*. Cambridge University Press, 1990.
- [11] H.P Gavin. Structural element stiffness, mass and damping matrices, 2014.
- [12] LEO H. HOLTHUIJSEN. *Waves in oceanic and coastal waters*. Cambridge University Press, 2007.
- [13] Ir. J.S Hoving. Offshore foundation design theory-lecture notes-bottom founded structures-tu delft, 2015.
- [14] J.R Hutchinson. Shear coefficients for timoshenko beam theory. *Journal of Applied Mechanics*, 68:89–91, 2001.
- [15] David V Hutton. *Fundamentals of Finite Element Analysis*. McGraw-Hill, 2003.
- [16] IEC. International standards for wind turbines. Technical report, International Electrotechnical Commission, 2005-08.

- [17] J. Jonkman, S. Butterfield, W. Musial, and G. Scott. Definition of a 5-mw reference wind turbine for offshore system development nrel/tp-500-38060. Technical report, 2009.
- [18] J MJ Journee and W W Massie. *Offshore Hydromechanics*. TU Delft, 2001.
- [19] P. van der Male, K.N. van Dalen, and A.V. Metrikine. Definition of the lateral damping of a rotating turbine rotor. 2016, To be published.
- [20] Pango A Miguel. Analyses of lateral loaded piles with p-y curves - observations on the effect of pile flexural stiffness and cyclic loading, 2013.
- [21] Ricardo Pereira. Aerodynamic loading-lecture notes-tu delft, 2015.
- [22] Francesco Petrini, Hui Li, and Franco Bontempi. Basis of design and numerical modeling of offshore wind turbines. *Structural Engineering and Mechanics*, 2010.
- [23] Singiresu S Rao. *Mechanical Vibrations*. Peritence Hall, 2011.
- [24] Lymon C Reese and William Van Impe. *Single piles and pile groups under lateral loading*. CRC Press, 2011.
- [25] B Mutlu Somer and Jorgen Fredsoe. *Hydrodynamics around cylindrical structures*. World Scientific, 2006.
- [26] Jan Van Der Tempel. *Design of Support Structures for Offshore Wind Turbines*. PhD thesis, TU Delft, 2006.
- [27] Wybren de Vries, Vermula, Naveen Kumar, (Rambøll) Patrik.Passon, Tim Fischer, Daniel Kaufer, Denis Matha, Björn Schmidt, and Fabian Vorpahl. Upwind – integrated wind turbine design project no. 019945 (ses6). Technical report, TU Delft, 2011.
- [28] Prof.ir. A.C.W.M. Vrouwenvelder. Random vibrations-lecture notes-tu delft, 2015.
- [29] Michiel Zaaijer. Introduction to wind energy (aerodynamic theory)-lecture notes-tu delft, 2015.